INTERFACIAL INSTABILITY AND SPRAY HEAT TRANSFER PROBLEMS OF TWO PHASE FLOW

JAN VALHA

A thesis submitted to Middlesex University in partial fulfillment of the requirements for the degree of Doctor of Philosophy.

April 1996

The work was carried out at the Energy Technology Centre, Middlesex University, School of Mechanical and Manufacturing Engineering, Bounds Green Road, London N11 2NQ

ABSTRACT

This thesis describes detailed investigations of two different problems in gas-liquid two-phase flow, namely, a study of interfacial stability in a partially filled cylinder subjected to vertical oscillations and a study of heat and mass transfer from hot spray droplets injected into an closed vessel.

The interfacial instability study considers experimental data taken from the author's previous work. Cylinders of various diameters, partially filled with water, ethanol or glycerol were subjected to a sinusoidal vertical motion. The critical acceleration, causing the interfacial wave to grow unstable, was found to be approximately constant for a given cylinder diameter, independent on the amplitude of the forcing oscillations. The experiments also indicate that the critical acceleration always decreases with increasing cylinder diameter. A mathematical analysis of the interfacial instability is based on a stability investigation of a Mathieu equation. It is shown that the experimental data fall into unstable regions for a single, first mode of oscillations. This finding is supported by the experimental analysis given by Cilliberto and Gollub. The analysis shows the effects of the liquid column height on the interfacial instability to be dependent on $\tanh(k_m l)$. This multiplier is equal to 1 for the column heights of 250 mm, 500 mm and 750 mm, investigated, and a given cylinder diameter, thus having no effect on the results. Computational analysis of the interfacial problem is developed which is based on the simplified MAC method incorporating the Continuum Surface Force (CSF) model for simulating the effects of surface tension. Computational experiments were run for water and glycerol, the two liquids of significantly different properties. The results are presented in the form of time sequenced plots showing the interfacial positions and graphs relating the interfacial wave amplitude and time. Stability of the interface is found to be dependent on the initial surface disturbance. Growth of the interfacial wave is observed in some cases. In the range of situations investigated, surface tension effects are found to have only a small influence both on the stability and frequency of the interfacial oscillations. The period of interfacial oscillations with no forcing vibrations is found to be in good agreement with the period predicted by mathematical analysis. Influence of the initial disturbance profile was also investigated. The results indicate that the interfacial wave adopts oscillatory behaviour similar to the other cases. The oscillation frequency of the interfacial wave undergoing forcing vibrations is found to match the findings of the mathematical analysis. The wave oscillates with an angular velocity equal to the multiples of the half the forcing vibration angular velocity, $\omega/2$.

In the second investigation a testing rig was constructed to investigate the heat and mass transfer processes in dense hot sprays injected into an enclosed cylindrical vessel. Heat and mass transfer rates were investigated indirectly from the measurements of the gas - vapour mixture pressure rise in the cylinder. The experiments covered different combinations of the parameters influencing the processes. The number and size of spray nozzles, the vessel volume, the type of gas and the initial pressure level in the cylinder were investigated. The experimental results indicate that, for the range of solid cone nozzles tested, the heat and mass transfer characteristics are, to a first approximation independent of the size of the nozzles. The results also show that the rise of spray chamber internal pressure is directly proportional to liquid temperature and flowrate. An analysis, based on energy balances for the whole cylinder, has yielded a new dimensionless group incorporating the important parameters of droplet heat transfer namely the droplet velocity and radius, spray chamber dimensions, gravity, conductivity and convectivity. A good match has been found between the analytical results and experimental findings. An improved analysis, incorporating the effect of evaporation from drops, is also presented. It is based on simultaneous solution of energy and mass balance equations for a single droplet. Again, good agreement with the experimental results is found. Both analyses indicate that, for this particular case of dense, evaporative spray, the Nusselt number tends to have a value equal to 1.

ACKNOWLEDGMENTS

I wish to express my gratitude to my director of studies Prof. J. Kubie for his guidance during my study, organising my funds and his friendly words that supported me during the years of my stay at Middlesex University. My special thanks also go to my supervisor

Dr. J. S. Lewis who has been a great help to me by assessing my progress along the way and for correcting the manuscript of this thesis. I shall certainly miss our discussions on the subjects of aerodynamics and heat transfer.

I wish to acknowledge the National Power Plc. for the financial support of my study.

I would also like to extend my thanks to all my colleagues at the Energy Technology Centre for their support, and to the technical staff of the Energy Technology Centre, Machine Tools and Fluid Laboratories.

Thanks are also due to the WordPerfect Corporation for the development of their spellchecker, this thesis needed it.

Finally I would like to thank my family for their support and patience.

LIST OF CONTENTS

LIST OF FIGURES

CHAPTER 1

CHAPTER 2

LIST OF TABLES

NOMENCLATURE

NOMENCLATURE FOR CHAPTER 2

a	oscillatory acceleration (m s^{-2})
A	amplitude of oscillatory motion (m)
c	wave velocity (m s^{-1})
C	integration constant
D	continuity function (s^{-1})
F	volume of fluid function
F_b	body force source (m s^{-2})
F_{sv}	continuum surface force (N m^{-3})
g	gravitational acceleration (m s^{-2})
i	horizontal unit vector
j	vertical unit vector
J	first order Bessel function
k	wavenumber (m^{-1})
l	height of liquid column (m)
n	direction vector
p	parameter given by equation (2.22)
p	pressure (Pa)
q	parameter given by equation (2.23)
r	horizontal coordinate (m)
R	cylinder radius (m)
S	spatially dependent component of η (m)
s	variable defined as $s = k_m.r$
t	time (s)
u	function given by $u = \omega t/2$
u	velocity in r direction (m s^{-1})
v	velocity in z direction (m s^{-2})
Y	second order Bessel function

z vertical coordinate (m)

Z spatially dependent component of Ψ (m)

Greek symbols

α zero of the Bessel function

α overrelaxation coefficient

ϵ iteration condition

η interface displacement measured from equilibrium position (m)

θ arbitrary pressure (Pa)

κ curvature of the interface (m^{-1})

μ dynamic viscosity (kg $m^{-1}s^{-1}$)

ρ density (kg m^{-3})

σ surface tension (N m^{-1})

Φ pressure normalised to unity density (m^2s^{-2})

Ψ velocity potential (m^2 s^{-1})

ω angular velocity of the oscillatory motion (rad s^{-1})

Ω vorticity (s^{-1})

Subscripts

b body force

d damped conditions

i,j mesh position

m order of mode of oscillation

o undamped conditions

r horizontal direction

v vapour

z vertical direction

Superscripts

α	coordinate exponent
$\sim$	tilde velocity notation
$\rightarrow$	vector
$\hat{}$	unit vector
n	nth time step

NOMENCLATURE FOR CHAPTER 3

a	droplet radius	(μm)
B_H	heat transfer number	
B_M	mass transfer number	
c_p	specific heat at constant pressure	(J $kg^{-1}K^{-1}$)
c_v	specific heat at constant volume	(J $kg^{-1}K^{-1}$)
C_D	drag coefficient	
D_{ab}	diffusivity	(m^2s^{-1})
D	spray chamber diameter	(m)
h	specific enthalpy	(J kg^{-1})
h	convective heat transfer coefficient	(W m^{-2} K^{-1})
H	expression given by equation (3.41)	
k	conductivity	(W $m^{-1}K^{-1}$)
k_c	convective mass transfer coefficient	(m s^{-1})
K	mass flowrate coefficient	
$K_{1,2,3}$	derived nondimensional groups	
l_T	typical droplet trajectory	
L	latent heat of vaporisation	(J kg^{-1})
m	masses related to a single droplet	(kg)
$\dot{m}_L$	liquid mass flowrate	(kg s^{-1})
M	overall masses in the spray chamber	(kg)
n	number of droplets	

N_D	average number of droplets present in heat transfer zone
Nu	Nusselt number
p	pressure (Pa)
P	nondimensional pressure
q	sensible heat (W)
R	gas constant (J $kg^{-1}K^{-1}$)
Re	Reynolds number
S_D	droplet surface
Sc	Schmidt number
Sh	Sherwood number
SMD	Sauter mean diameter
t	time (s)
t^*	nondimensional time
T	temperature (K)
u	velocity (m s^{-1})
u	specific internal energy (J kg^{-1})
U	internal energy (J)
v	specific volume (m^3 kg^{-1})
V	volume (m^3)
We	Weber number
x	partial pressure
Y	mass ratio

Greek symbols

Γ	general conductivity
θ	spray angle (°)
μ	dynamic viscosity (kg $m^{-1}s^{-1}$)
ρ	density (kg m^{-3})

σ	surface tension (N m^{-1})
Φ	relative humidity
ω	specific humidity

Subscripts

CV	control volume
D	droplet
G	gas
i	ith time step
L	liquid
m	mixture
o	initial
S	still zone
T	transfer zone
V	vapour

CHAPTER 1 : INTRODUCTION

1.1 FOREWORD

Two phase fluid flows are common in nature and in industrial processes. The flow of blood, the drift of clouds in the atmosphere, the waves on the ocean are only a few examples from the natural world. Humankind has employed two phase flows for its own benefit, for instance in boilers, refrigeration and heat pump systems, fuel injectors or absorption and bubble columns.

As implied above two phase flows play an important role in power production and many other energy related processes. Furthermore, the situation has changed over the last two decades as a result of the energy crisis beginning in the 1970s, which opened a wide range of opportunities for researches into new types of clean and cheap power generation. This is reflected by the continuing interest in studies aimed at obtaining a detailed understanding of two phase flows.

Two phase flow phenomena in general can be subdivided into two large groups [1]:

(i) Interfacial phenomena, where no or very little mixing between the phases occurs. Typical examples would be interfacial waves, flow of bubbles and free surface pipe flow.

(ii) Mixing phenomena, where mass transfer between phases is of great importance. Representatives of these types of flow are, for example, film condensation, convective boiling and evaporating sprays.

The work reported in this thesis deals with two different areas of study, one representative from each of the above two groups, namely

- an investigation of interfacial wave phenomena in a partially filled vertical cylinder subject to longitudinal sinusoidal oscillations,
- an investigation of heat and mass transfer from spray droplets injected into a gas filled vessel.

The two problems investigated are connected, in the sense that they both address perceived research needs in the development of a novel type of liquid piston heat pump operating on a Stirling cycle. Notwithstanding this specific motivation, it is believed that the findings of this work will be of more general interest. The purposes of the following sections of this chapter are to give a brief introduction and to define objectives for the two areas studied.

1.2 INTERFACIAL WAVES

Surface waves are characterised by a phase interface, that is a region separating two phases - usually liquid and gas - in which the properties and behaviour undergo a step change. Although complex molecular models have been developed to describe interfacial regions [2] most studies of phase interface stability are based on two continuum models.

Of primary concern in the study of interfacial waves is the motion of common lines. A common line is the curve formed by the intersection of two dividing surfaces. In general, hydrodynamic and surface - tension forces govern the motion and deformation of the common line. When waves become unstable, the energy transfer between the phases becomes critical. There are several possible mechanisms for energy transfer across an interface. Based on the dominant hydrodynamic and gravity forces involved, the following causes for the generation of surface waves can be identified: inviscid flow pressure (Kelvin - Helmholz instability) [1], viscous shear stress [3], inviscid Reynolds stress [4], viscous Reynolds stress [5] and turbulent fluctuations of pressure [6].

It has been stated [1] that turbulent fluctuations of pressure and inviscid Reynolds stress are important for the generation of longer waves on deep water. On the other hand, for viscous fluids, wave formation is well predicted by the Kelvin - Helmholz instability. Capillary and short gravity waves, which are important for thin liquid film flows, appear to be generated initially by viscous Reynolds stress.

When gas velocity above liquid surface is increased an initially stable interface becomes wavy, and as the relative velocity is increased further the waves become irregular. At a sufficiently high gas velocity, large amplitude waves appear and at a still higher gas velocity, the onset of entrainment can occur. Under certain conditions, the forces acting on the interface lead to an extreme deformation, which results in entrainment of liquid in the gas phase due to the breakup of a portion of a wave into several droplets. The forces acting on the wave crests depend on the flow pattern around them as well as on the shape of the interface. In general, the five basic types of entrainment mechanism shown in Figure 1.1 can be considered.

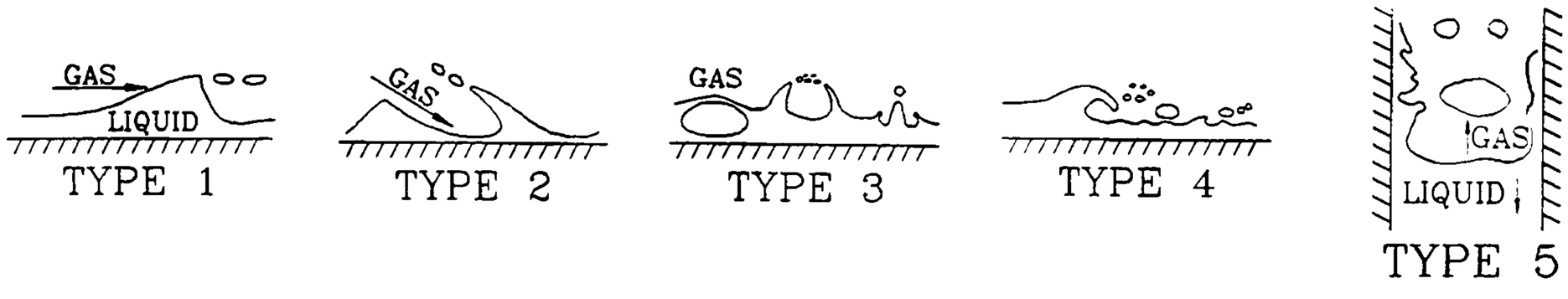

Figure 1.1 *Various mechanisms of entrainment [7]*

The five mechanisms of droplet entrainment can be listed as follows:

1. Shearing of roll wave crests by gas flow
2. Undercutting of the liquid film by gas flow
3. Bursting of gas bubbles
4. Impingement of large drops
5. Disintegration of liquid bulges by gas flow in counter current situations

The latter mechanism is of the greatest importance to the work on interfacial disturbances considered in this thesis.

1.3 SPRAYS

The transformation of bulk liquid into sprays and other physical dispersions of small particles in a gaseous atmosphere is of great importance in many industrial processes as shown in Table 1.1 . Spray devices are generally designated as atomizers or nozzles. The process of atomisation is one in which a liquid jet or sheet is disintegrated by the kinetic energy of the liquid itself, possibly by exposure to high velocity air or gas, in a manner similar to that discussed in the previous section. It is also possible to achieve atomisation as a result of mechanical energy applied externally through a rotating or vibrating device. The design of atomisers used for liquid atomisation depends on the application of the atomised liquid, liquid properties, and operating conditions. In the case of high flow rate of a liquid, rotary atomisers are used most frequently. If very fine atomisation is required, then the atomisers with a low flow rate and high energy consumption are used. Atomisation of very viscous liquids, emulsions and suspensions is realised by means of pneumatic atomisers.

Production or processing	
	Spray drying (dairy products, coffee and tea, soap, etc.)
	Spray cooling
	Spray reactions (absorption, roasting, etc.)
	Atomized suspension technique (effluents, waste liquors, etc.)
	Powdered metals
Treatment	
	Evaporation and aeration
	Cooling (spray ponds, towers, reactors, etc.)
	Humidification and misting
	Air and gas washing and scrubbing
	Industrial washing and cleaning
Coating	
	Surface treatment
	Spray painting (pneumatic, airless, and electrostatic)
	Flame spraying
	Insulation, fibers, and undercoating materials
	Multicomponent resins (urethanes, epoxies, polyesters, etc.)
	Particle coating and encapsulation
Combustion	
	Oil burners (furnaces and heaters, industrial and marine boilers)
	Diesel and gasoline fuel injection
	Gas turbines (aircraft, marine, automotive, etc.)
	Rocket fuel injection
Miscellaneous	
	Dispersion of chemical agents
	Agricultural spraying (insecticides, herbicides, fertilizer solutions, etc.)

Table 1.1 *Spray applications [8]*

Sprays are extremely efficient as means of heat and mass transfer owing to their high surface area to volume ratio. For example for a spray consisting of droplets of 150 micron diameter this ratio is 40 000 (m^{-1}). This fact is widely exploited in power generation equipment not only for fuel injection purposes but also in heat exchangers, direct contact condensers and cooling tower technology (system Heller) [9] - Figure 1.2, and deareators - Figure 1.3.

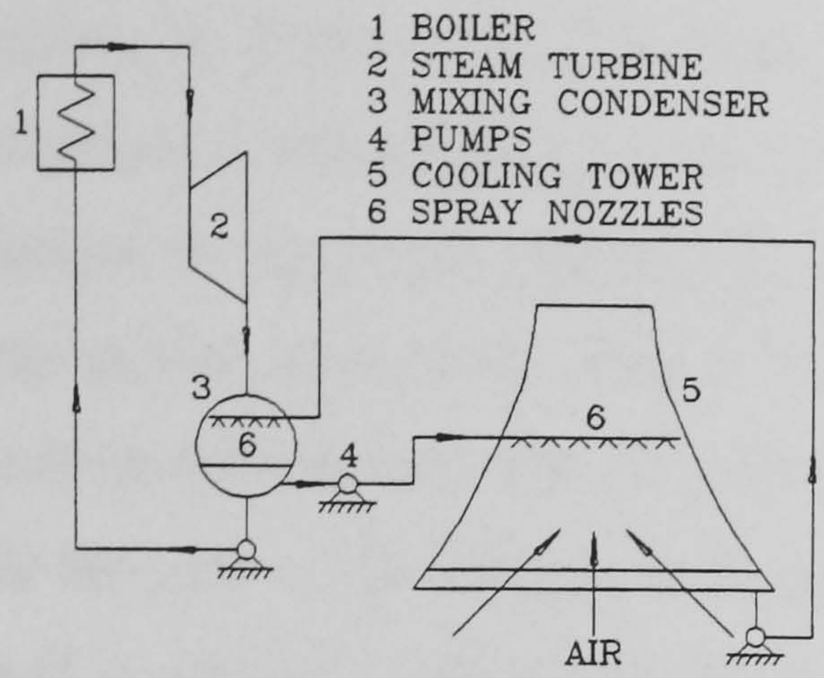

Figure 1.2 System Heller [9]

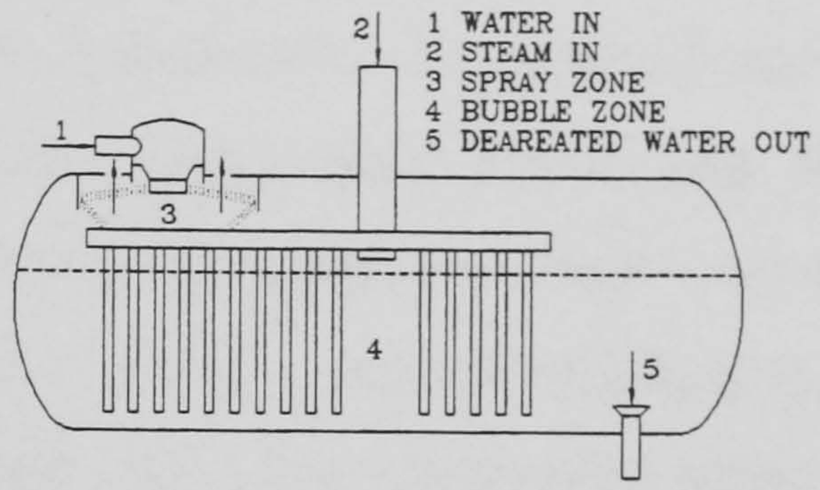

Figure 1.3 Spray type deareator

1.4 RESEARCH CONTEXT AND OBJECTIVES

As previously mentioned, this research on interfacial wave stability and spray heat transfer is applicable to liquid piston heat pumps as reported for example in [10] and [11], which operate on the Stirling cycle principle - see Figure 1.4.

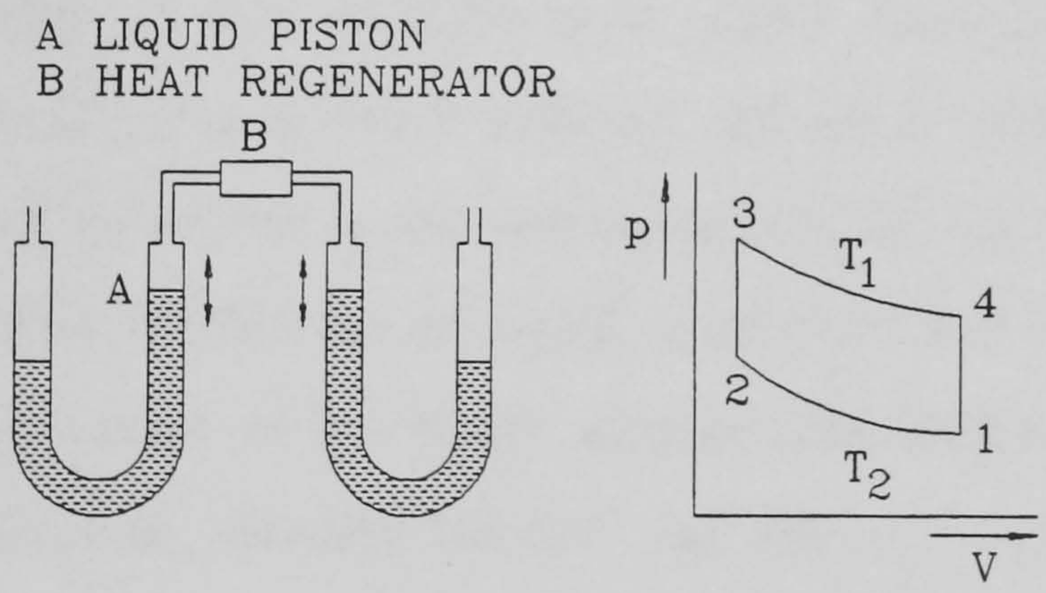

Figure 1.4 Liquid piston heat pump schematics and Stirling cycle

The liquid piston heat pump design considered here is one of a general class of heat actuated heat pumps. Unlike the conventional electric heat pump which converts work input in the form of electricity into heating or cooling output, a heat actuated heat pump utilizes a high temperature heat source for its heat input, which is used to pump heat from a low temperature heat source to an intermediate temperature heat sink, thereby providing either useful heating or cooling. The liquid piston heat pump comprises of a series of

liquid columns, or pistons, contained in U tubes connected by thermal regenerators as shown in Figure 1.4. The liquid pistons oscillate from their equilibrium position thus alternately expanding and compressing the gas contained on either side of the regenerators known as the power regenerator and heat pump regenerator respectively. On one side of the power regenerator, heat is received by the gas from a high temperature heat source and on the opposite side of the power regenerator, heat is rejected to an intermediate sink. In the case of the heat pump regenerator, heat is extracted from a low temperature source and is rejected to an intermediate temperature sink. To achieve the maximum coefficient of performance, isothermal compression and expansion can be approached by means of injecting constant temperature sprays into the gas spaces.

A generalized second order model for simulating the basic thermodynamics and dynamics of the liquid piston heat pump employing some of the above features was developed by Gerstmann and Hules [11]. Their analytical approach, however, neglected potentially important higher order effects. One such possible effect is interfacial instability of the wave system created on the free surface of the liquid pistons which may preclude stable operation at frequencies or stroke amplitudes above certain level.

The main objective of this research is to obtain fundamental knowledge of the processes governing the interfacial wave stability and spray heat transfer. A condition causing the surface wave subjected to the vertical sinusoidal motion to grow unstable is investigated as a function of properties of liquid, frequency and amplitude of the forcing oscillations, as well as geometry of the vessel. Appropriate values of commonly used heat and mass transfer correlations, namely Nusselt and Sherwood numbers, are sought for spray droplets injected at a certain temperature into an enclosed vessel.

Each of the problems has been treated both experimentally and theoretically and agreement between theory and practice was tested. Both analytical and computational models have been developed for the two problems. Chapter 2 of this thesis deals with the interfacial instability and Chapter 3 covers work on the investigation of heat transfer and evaporation in sprays.

LIST OF REFERENCES FOR CHAPTER 1

1. HESTRONI G., *Handbook of Multiphase Systems*, McGraw-Hill Book Company, New York, 1982

2. ONO S. KONDO S., Molecular Theory of Surface Tension in Liquids, *Handbuch der Physik*, edited by S. Flugge, 10:134-280, Springer-Verlag, Berlin, 1960

3. JEFFREYS H., On the Formation of Water Waves by Wind I. and II., *Proceedings of Royal Society of London*, A107:189-206, 1925

4. MILES J. W., On the Generation of Surface Waves by Shear Flows I-IV, *Journal of Fluid Mechanics*, 3:185-204, 1957

5. BENJAMIN B. T., Shearing flow over a Wavy Boundary, *Journal of Fluid Mechanics*, 6:161-205, 1959

6. PHILIPS O. M., On Generation of Waves by Turbulent Wind, *Journal of Fluid Mechanics*, 2:417-445, 1957

7. ISHII M. GROLMES M. A., Inception Criteria for Droplet Entrainment in Two-Phase Concurrent Film Flow, *AIChE Journal*, 21:308-318, 1975

8. LEFEVBRE A. H., Atomization and Sprays, Taylor & Francis, 1989

9. SCEGLAJEV A. V., Parni turbiny, 1. a 2. svazek, SNTL Praha, 1983 (in Czech)

10. READER G. T. CLARKE M. A. TAYLOR D. R., Some Experiences with Fluidyne, *Stirling Engines - Progress Towards Reality*, Mechanical Engineering Publications Limited, 85-92, 1982

11. GERSTMAN J. HULES K., Analytical Study of Liquid Piston Heat Pump Technology, *Internal Report ANL-CT-84-2 Advanced Mechanical Technology Inc.*, Newton, Massachusetts, USA, 1986

CHAPTER 2 : INTERFACIAL INSTABILITY

2.1 FOREWORD

The generation of surface waves by vertically vibrating a horizontal fluid layer has been long known. Michael Faraday opened his *Diary* [1] on 1st July 1831 with the words:

> *"Mercury on a tin plate being vibrated in sunshine gave very beautiful effects of reflection."*

and went on to report similar observations of surface waves on ink, water, alcohol, turpentine, milk, and white of egg covering a horizontal plate subjected to vertical vibrations. Faraday seems to be the first to have noted the important property that the frequency of the waves was half the frequency of the forced vibration of the plate. Later Matthiessen [8] found in similar experiments that the standing waves had the same frequency as the vibration. Lord Rayleigh [9] suggested a qualitative explanation supported by more detailed experiments.

Surface waves induced by vertical motion have more recently received a greater amount of attention, as the principles of wave instabilities are important, for example, for spray technology and ink jet printers. An overview of the published literature on experimental and theoretical studies of interfacial wave instability is given in Section 2.2.

The purpose of this Chapter is to report on investigations of gas - liquid interface behaviour and stability in a vertical cylinder subject to axial sinusoidal oscillations. The general aim of the work is to gain insight into the performance of liquid piston Stirling cycle machines, as discussed in Chapter 1. In Section 2.4 an analytical treatment of the interfacial problem, including a stability analysis, is presented and compared with experimental results from an earlier investigation by the author, which is summarised in Section 2.3. A computational analysis, including surface tension effects is developed in Section 2.5 and overall findings are summarised in Section 2.6.

2.2 LITERATURE OVERVIEW

2.2.1 General

A large number of articles and books dealing with interfacial wave stability have appeared in the specialised literature in the last 30 years. These contributions can be subdivided into three large groups. The first group report on purely experimental works which have yielded data for the second and third groups, dealing with pure mathematical analyses and computational approaches respectively.

2.2.2 Experimental works

Two main types of apparatus have been used by researchers for the generation of precise oscillatory vertical motion for the purposes of investigation of two phase wave instability. Crank - shaft type mechanisms have been used for large amplitude and relatively low frequencies of oscillations [2], [3]. One example of such a device is shown Figure 2.1.

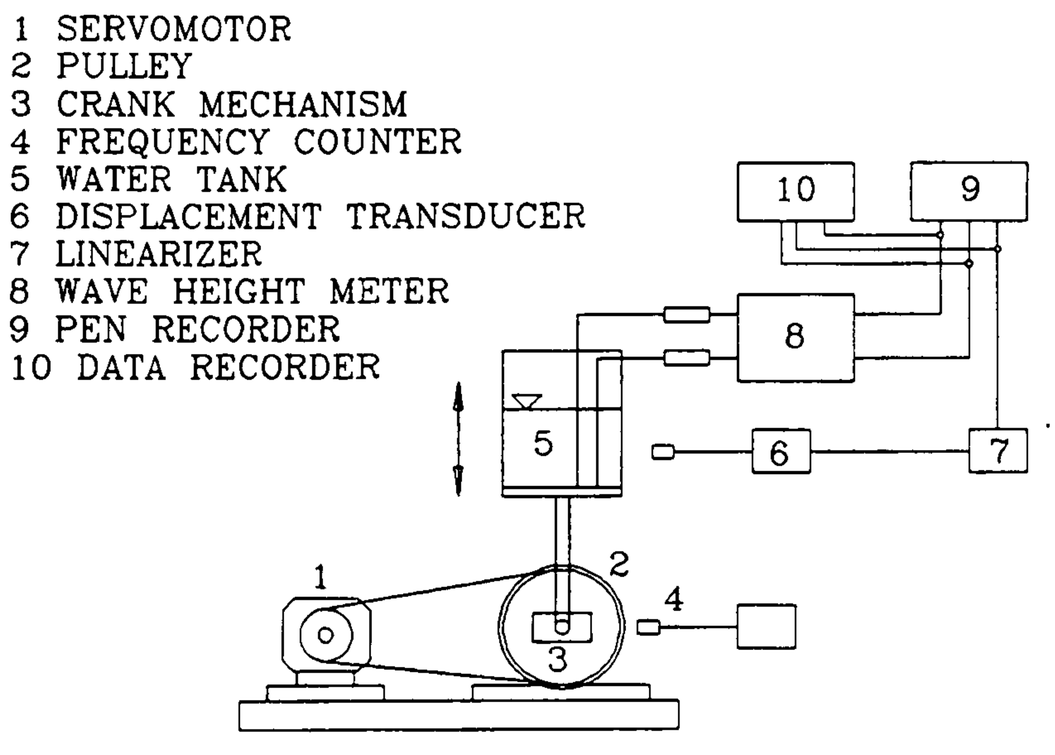

Figure 2.1 Experimental device similar to one used by Funakoshi and Inoue [2]

For small amplitudes and large frequencies most investigators prefer acoustic excitation [4], [5]. Excellent experimental work done by Ciliberto et al [4] on the apparatus shown in Figure 2.2 has been a valuable source of data for many theoretical investigations. They used a novel digital imaging methods in conjunction with time resolved spatial Fourier analysis. These methods allowed to determine linear combinations of the time dependent

amplitudes in modal superposition under certain conditions. They found that the unstable wave oscillations result from the interaction between only two spatial modes.

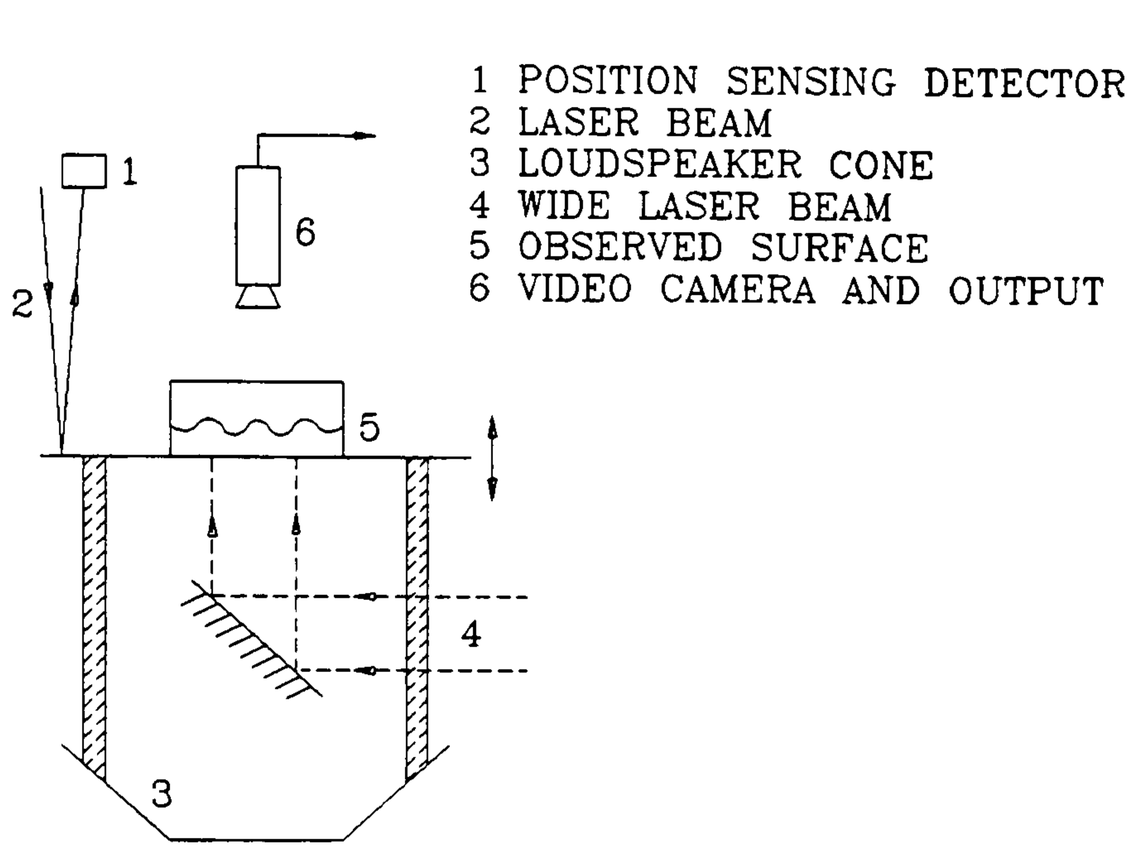

Figure 2.2 *Schematic diagram of the apparatus used by Ciliberto et al [4]*

Various visualisation methods are used, enabling observation of the interface and determination of the oscillatory behaviour, namely mode and frequency of oscillations. Probably the most widely used visualisation technique is so called parallel - light viewing or laser sheet method shown in Figure 2.3 [4], [6], [7]

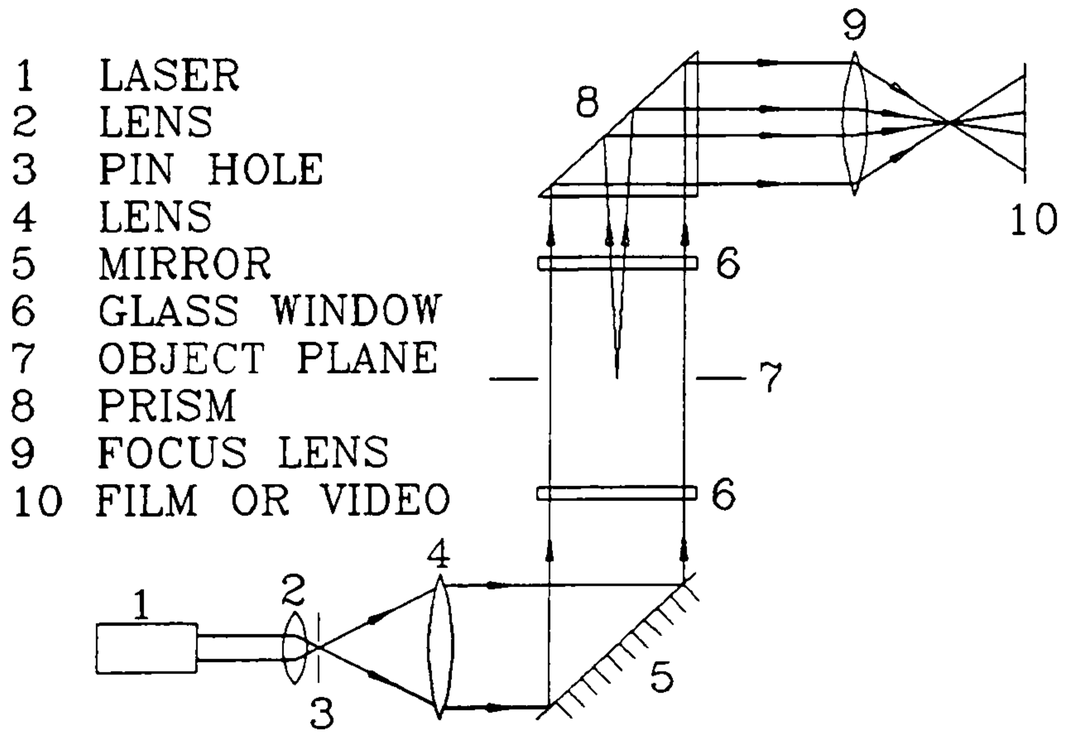

Figure 2.3 *Optical arrangement for parallel-light viewing technique*

2.2.3 Mathematical analyses

Modern analytical approaches to the analysis of interfacial waves follow one of two ways. The first one, due to Miles [10] - [12], expresses the motion of the free surface in terms of the corresponding normal modes and calculated Lagrangian, which includes terms of second and fourth order in the primary mode and second order in the secondary mode. Application of the method of averaging results in a Hamiltonian system being obtained. The second approach, due to Benjamin and Ursell [13], starts with formulation of the governing Euler equations. Application of suitable boundary conditions together with certain simplifications yields a Mathieu equation and its stability behaviour can then be investigated. Table 2.1 gives listing of major published works on the subject distinguishing between the two main approaches.

Classical works	[1] [8] [9]
Approach due to Benjamin & Ursell	[7] [13] [14] [15] [16]
Approach due to Miles	[10] [11] [12] [17] [18] [19] [20] [21] [22] [23] [24] [25] [26] [27]

Table 2.1 *List of major published works on the analytical treatment of interfacial stability*

Miles's approach is often chosen by other authors as it can quite easily demonstrate the shape of the interface. However the mathematics becomes complicated when stability regions are to be determined.

The Benjamin and Ursell method, on the other hand, gives stability regions as a direct solution. The main difficulty lies in the mathematical description of these regions as stability investigation of Mathieu's equation is still under development.

During the later stages of the present work, an article by Kumar and Tuckerman appeared in literature. This article extensively discusses the solution of the two phase problem as well as the mathematical treatment in a way similar to the one developed independently in this work.

2.2.4 Computational fluid dynamics (CFD) and surface flows

CFD is probably the fastest growing field of research in fluid dynamics. The first attempts to apply numerical modelling to surface flows and waves emerged in the mid 1960s together with the appearance of the second generation computers. An excellent overview of these methods is given by Belotserkovskii and Davydoff [28]. Most of the algorithms were developed at the Los Alamos National Laboratories, New Mexico, USA under the leadership of F H Harlow and A Amsden. Table 2.2 summarises the methods developed by their team and gives references to corresponding reports where the methods have been described.

Marker-and-Cell Method (MAC)	[29]
Particle-in-Cell Method (PIC)	[30]
Lagrangian Method for Incompressible Flow (LINC)	[31]
Simplified MAC Method (SMAC)	[32]
Arbitrary Lagrangian-Eulerian Method (ALE)	[33]
Implicit Continuous Fluid Eulerian Method (ICE)	[34]
Arbitrary Lagrangian-Eulerian Method for Fluid Flow at All Speeds (YAQUI)	[35]

Table 2.2 *List of numerical methods developed in Los Alamos National Laboratories, New Mexico, USA*

The marker - and - cell (MAC) method explicitly discretises the time dependent governing equations expressing mass continuity, x-direction momentum, y-direction momentum and utilises a grid of massless Lagrangian particles that are used for representation of fluid position. Mathematical re-arrangement of the governing equations yields a Poisson's equation for pressure. Its solution sometimes causes serious convergence problems, depending on method of solution employed. Despite this drawback,

numerous problems have been solved using this method [36] - [39]. Even though this method is the oldest of the methods listed, it has undergone further developments and it is still widely used nowadays. In the original form as presented in [29] the method, however, does not include the effects of surface tension and volume representation of surface cells is poor. The particle - in - cell method (PIC) [30] is a universal method for numerical tracking of particles and it was developed into the particle - source - in - cell method (PSIC). The Lagrangian method for incompressible flow, or LINC method [31], uses Lagrangian coordinates and allows description of non-overturning surfaces. The simplified marker - and - cell (SMAC) method [32] simplifies problems encountered with boundary condition specifications in the MAC method and the necessity of exact agreement between the momentum equations and Poisson's equation for pressure. In the SMAC method pressure is not calculated over the whole computational domain, but only on the free surface. The arbitrary - Lagrangian - Eulerian method, or ALE method [33], is suitable for problems involving transonic situations. The implicit - continuous - fluid - Eulerian method, or ICE method [34], uses implicit discretisation of governing equations and is suitable for complex problems. The arbitrary Lagrangian - Eulerian method for fluid flow at all speeds, known as YAQUI method [35], is appropriate for high speed problems where shock waves occur and is based on the ICE method. Convergence problems associated with the older iterative schemes for solution of Poisson's equation in the MAC based codes were overcome using new algorithms such as the LU decomposition and the Conjugate gradient method [40].

In the mid 1980s the Volume of Fluid, or VOF, technique was developed [41]. This enabled a better volume representation of surface cells as it solved an extra differential equation for the volume transportation of the fluid.

An enormous amount of work on the development of CFD methods for free surface flows was carried out at Imperial College, London under the leadership of D B Spalding. This team managed to implement a universal method, in which continuity is expressed by a volume rather than mass conservation equation, into the PHOENICS CFD package [42]. Their method is known as the GALA algorithm. Further improvements lead to the incorporation of the Height of Liquid Method [43], similar to VOF technique and the Lagrangian Scalar Equation Method [44].

All of the above analyses, however, omit the important effect of surface tension. Only the recently has the development of a Continuum Surface Force Model (CSF) [45] by the Los Alamos team enabled this phenomenon to be simulated.

Finally there is also a group of researchers who are employing hybrid analytical and CFD approaches to the solution of surface flow problems [46] - [48]. They reduce the governing momentum and continuity equations to a one dimensional form, retaining both viscous and inertial terms, and then numerically solve this equation. Their method, however, has only been applied only to the very narrow area of liquid jet disintegration.

2.3 EXPERIMENTAL INVESTIGATION

2.3.1 General

The experimental investigation of free surface instability described here, involving the design and manufacture of a testing rig, were the subject of the author's final year BEng in Mechanical Engineering project. Consequently only a brief description of the apparatus used and a summary of the main findings is given in the following section. A detailed description of the test rig and the experimental programme together with extensive discussion of the results is given in [49].

2.3.2 Description of experimental apparatus

The apparatus designed enables movement of a column of liquid in a well defined sinusoidal vertical motion. The apparatus is sufficiently flexible to allow for a range of values of the amplitude and the frequency of the angular motion to be generated. A diagram of the experimental apparatus is shown in Figure 2.4.

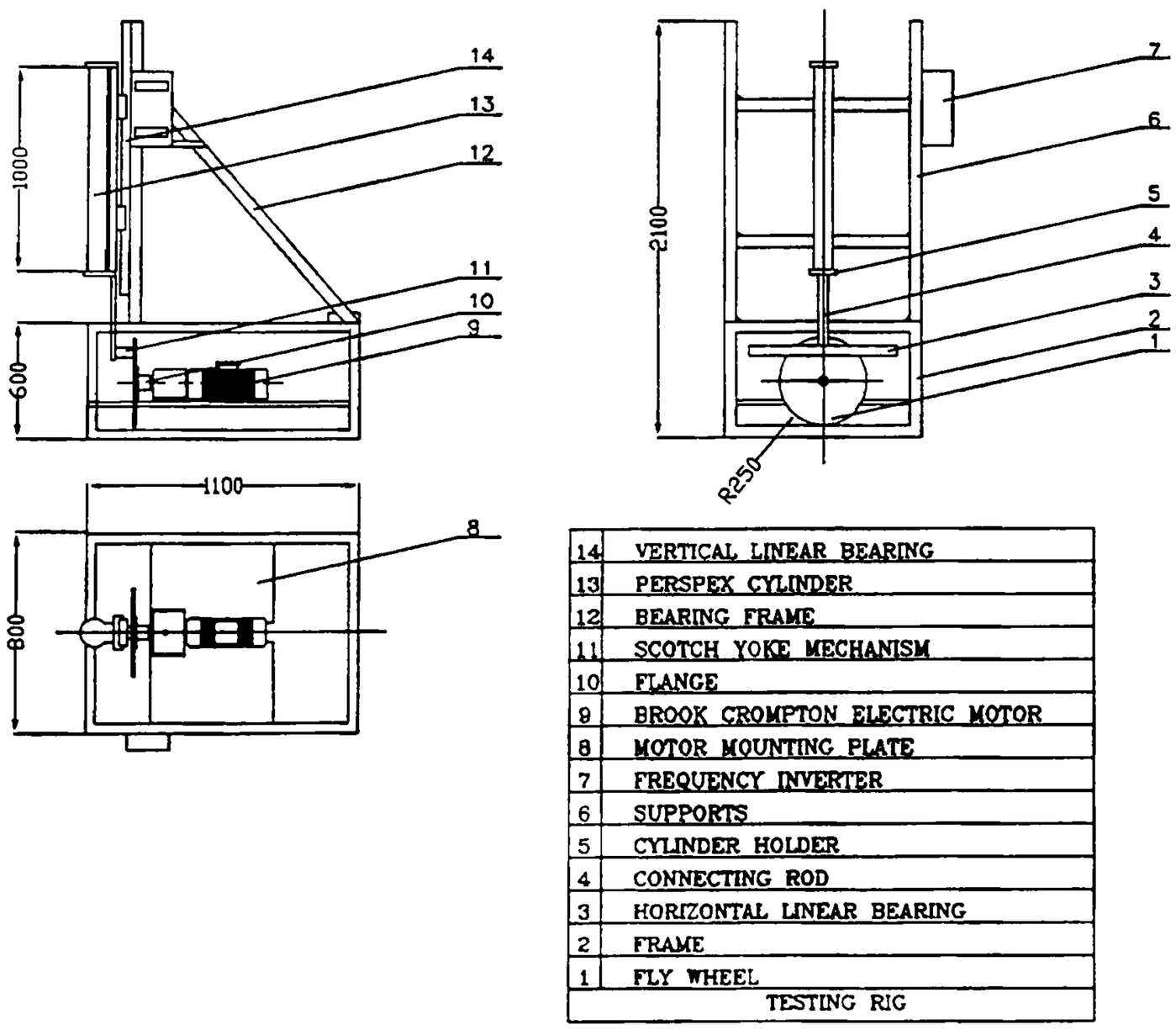

14	VERTICAL LINEAR BEARING
13	PERSPEX CYLINDER
12	BEARING FRAME
11	SCOTCH YOKE MECHANISM
10	FLANGE
9	BROOK CROMPTON ELECTRIC MOTOR
8	MOTOR MOUNTING PLATE
7	FREQUENCY INVERTER
6	SUPPORTS
5	CYLINDER HOLDER
4	CONNECTING ROD
3	HORIZONTAL LINEAR BEARING
2	FRAME
1	FLY WHEEL
TESTING RIG	

Figure 2.4 *A diagram of the experimental apparatus*

The major components are: a rigid support frame, an electric motor fitted with a gearbox, frequency inverter, and a flywheel, a scotch yoke mechanism and linear bearings, and the perspex cylinders and cylinder holder. The acceleration forces acting on the rig are high, thus requiring a robust and rigid construction of the frame. The frame, manufactured from square steel sections, was bolted to the floor, and a protective fence was added to the frame. The motor used is a Brook Crompton 3 phase electric motor, speed controlled with a Panasonic DV-700 frequency inverter. A gearbox is used to deal with the significant starting torque requirements. The assembly was calibrated to obtain the relationship between the frequency of the angular motion and the frequency inverter setting. The test rig design allows frequencies of up to 20 Hz to be achieved.

In order to obtain a well-defined sinusoidal vertical motion a Scotch yoke mechanism is used, as shown diagrammatically in Figure 2.5. A flywheel is used to vary the amplitude of the vertical motion and to improve the dynamic stability of the rig. This flywheel, 500 mm in diameter, is drilled with a set of holes to which the pivot holder of the horizontal linear bearing is attached. This allows for the amplitude of the vertical motion to be varied between 5 mm and 200 mm: in 5 mm steps between 5 and 30 mm and 10 mm steps between 30 and 200 mm.

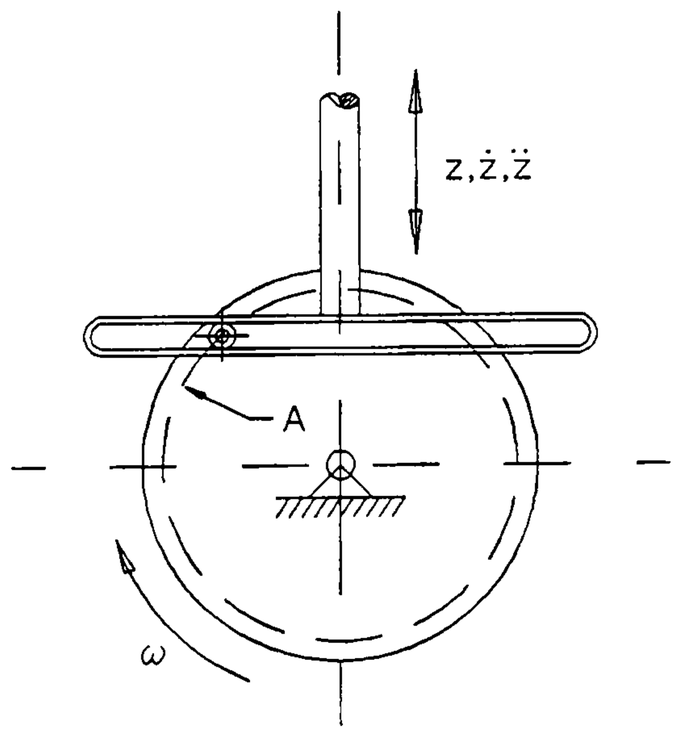

Figure 2.5 A diagram of the Scotch yoke mechanism

The Scotch yoke mechanism consists basically of linear and roller bearings. A pivot, connected to the flywheel is inserted into a roller bearing. The roller bearing is fastened to the sliding member of a horizontal linear bearing. The horizontal roller bearing used

is of a self-aligning type to compensate for inaccuracies or possible vibrations. The other section of the horizontal linear bearing is connected to the cylinder holder via a connecting rod. The test cylinder holder slides on a vertical linear bearing fixed to the frame. Hence, as the flywheel starts spinning a vertical sinusoidal motion of the test cylinder is obtained.

The cylinder holder can accommodate cylinders of up to 80 mm outside diameter and 1000 mm long. Transparent acrylic cylinders were used in the present series of experiments. All cylinders were 1000 mm long with the following internal diameters, D = 8 mm, 16 mm, 24 mm, 45 mm and 69 mm.

2.3.3 Experimental technique and programme

Water, ethanol and glycerol were used as the working liquids for the tests reported in this work. Their properties are given in Appendix A. The perspex cylinder was filled with the working liquid up to the required level, with air at atmospheric condition above the interface. The liquid level was generally set at 500 mm. Its influence was investigated for the cylinders of 24 mm and 69 mm in diameter by comparing the behaviour of the interface for the liquid levels of 250 mm, 500 mm and 750 mm. For each liquid and for given values of the cylinder diameter, the liquid level in the cylinder and the amplitude of the sinusoidal vertical motion, the frequency of the angular motion was gradually increased until a critical frequency was reached. This condition was reasonably well defined and repeatable and was interpreted as the frequency at which significant amounts of liquid were thrown from the two-phase air-liquid interface. No hysteresis effects were observed, as confirmed by gradually decreasing the frequency from above the critical, when the interface became stable at about the same critical frequency. The condition of the interface was also examined using a stroboscopic light set at the appropriate frequency. Video recordings of the interface were made for some test conditions.

2.3.4 Experimental results

In each of the tests conducted to establish the critical frequency of the vertical motion the coherent structure of the interface was lost by the growth of unstable interfacial waves.

Two distinct mechanisms were observed. In the first case, air bubbles penetrated first into the liquid and then the interface became unstable in similar way as illustrated in Chapter 1, Figure 1.1, Type 3. In the second case, liquid drops were ejected into the air as illustrated in Figure 1.1, Type 5.

Figures 2.6, 2.7 and 2.8 present plots of the critical frequency, f_c, of the oscillatory motion versus its amplitude, A, for the three liquids tested and for a liquid height of 500 mm. Each figure presents the data for cylinder diameters of D = 8 mm , 16 mm, 24 mm, 45 mm and 69 mm.

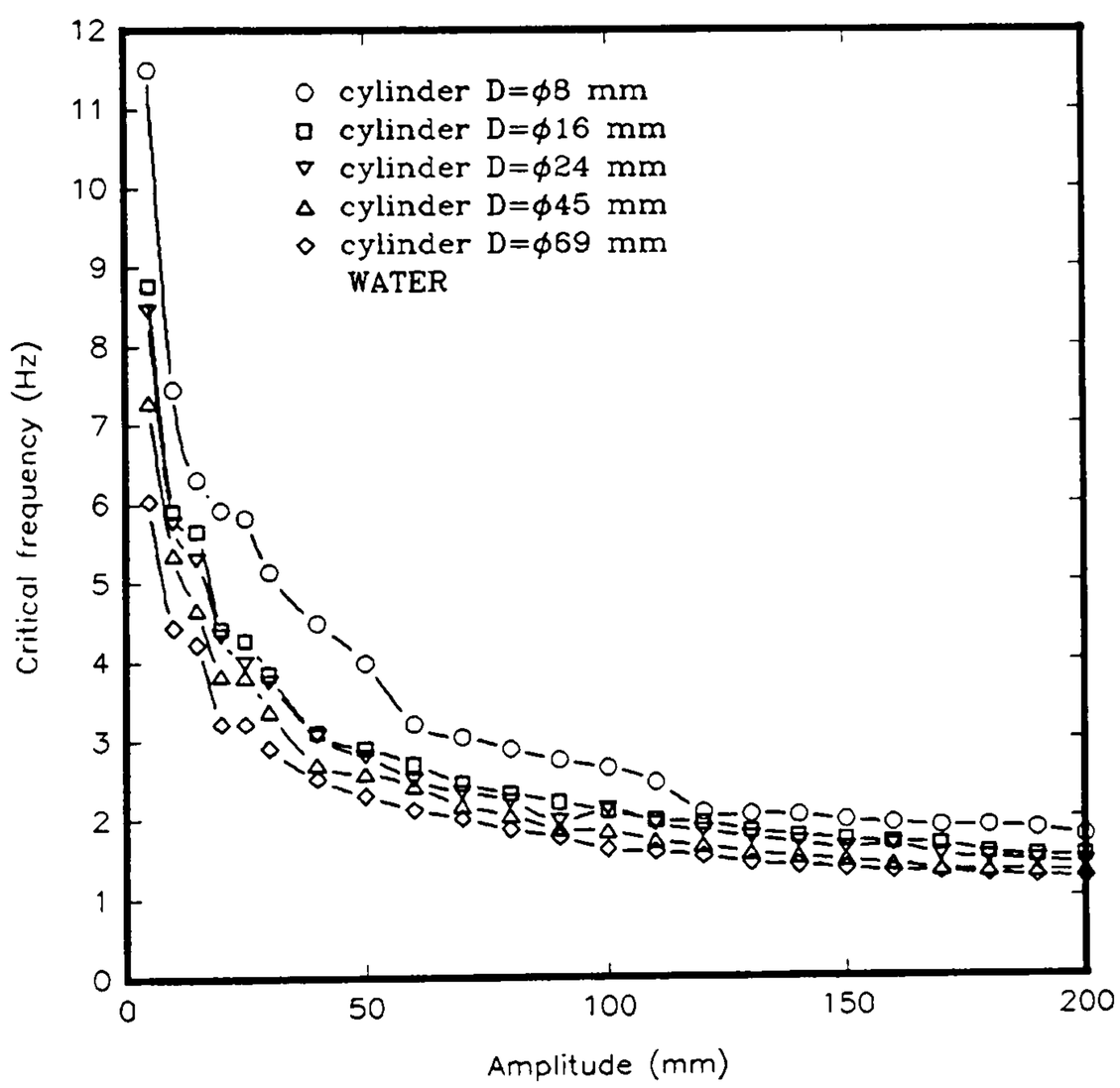

Figure 2.6 *Critical frequency of oscillations versus amplitude - water/air*

For water and air, with D > 8 mm, the critical condition was reached when an instability of Type 3 occurred and air bubbles started to penetrate the interface. However, for D = 8 mm the situation was more complex. Both Type 3 and Type 5 instabilities were observed, with the Type 3 instability being more readily established at lower frequencies.

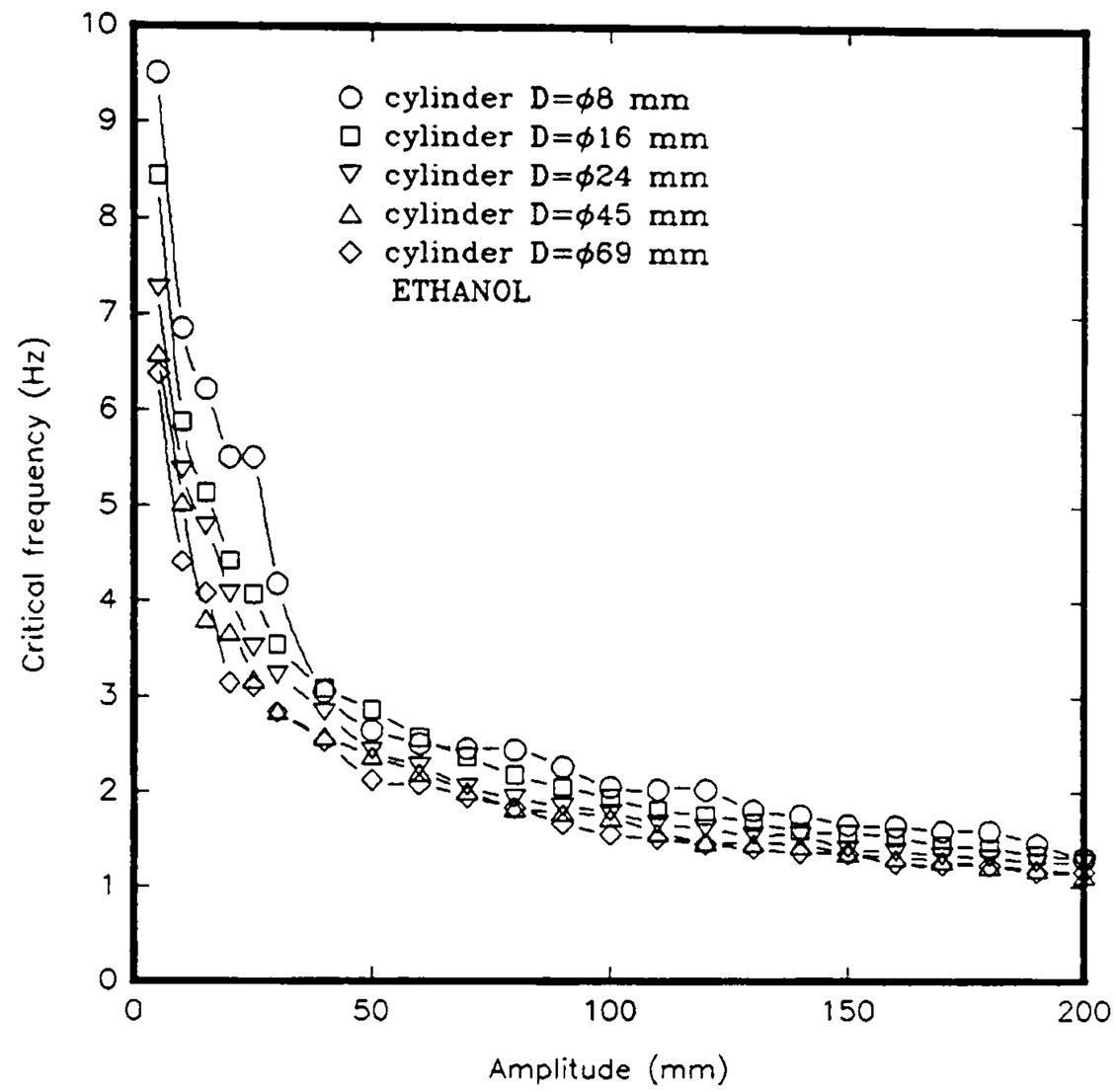

Figure 2.7 *Critical frequency of oscillations versus amplitude - ethanol/air*

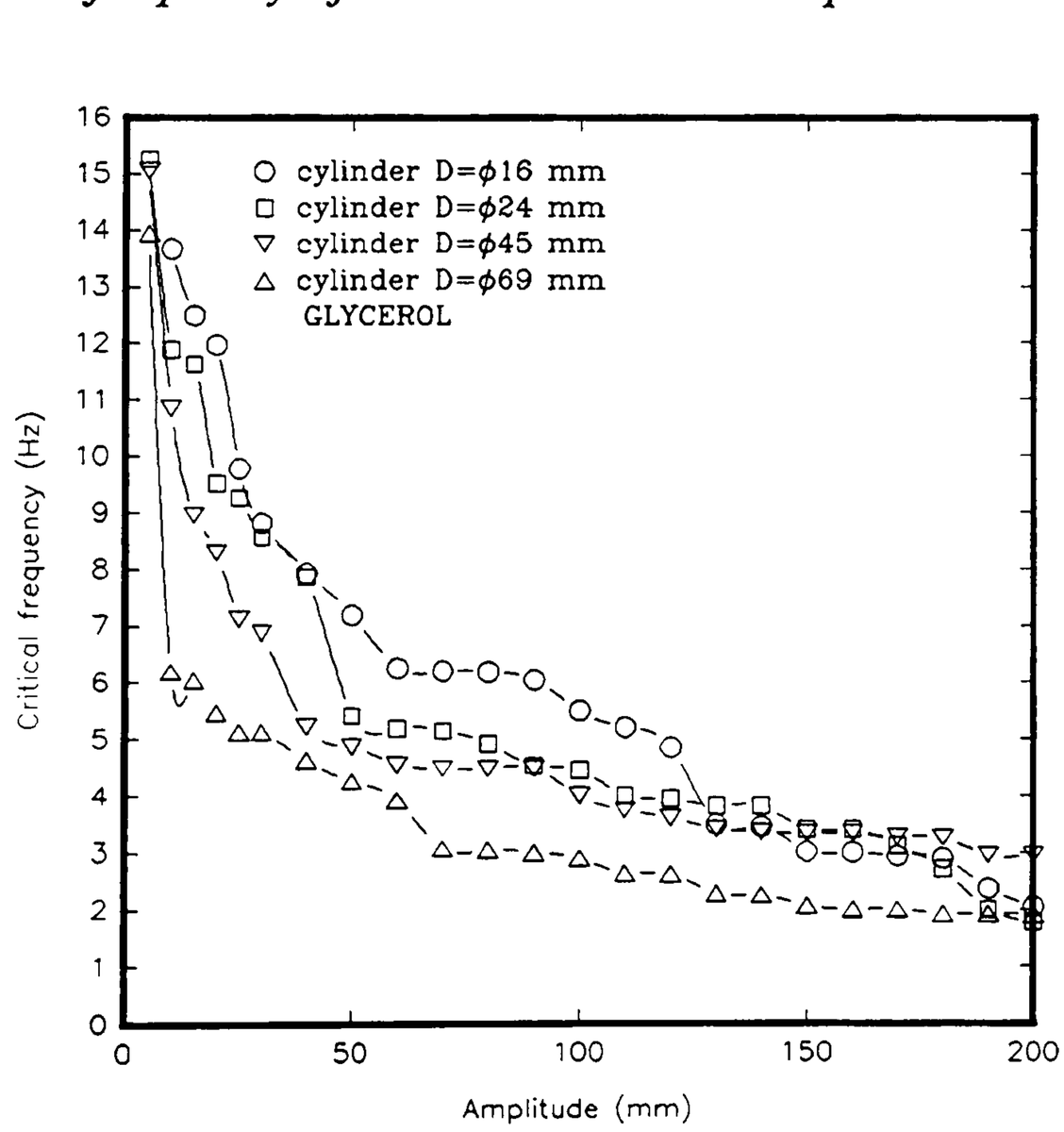

Figure 2.8 *Critical frequency of oscillations versus amplitude - glycerol/air*

In the case of ethanol and air, with D > 8 mm and amplitudes between 5 and 25 mm the interface became unstable due to an instability of Type 5. At higher amplitudes an interfacial instability of Type 3 occurred.

For glycerol and air, the smallest cylinder, D = 8 mm, could not be tested, since the critical frequencies were very high and above the capabilities of the test rig. Therefore, only the larger cylinders with D = 16, 24, 45 and 69 mm were used for glycerol. For amplitudes below 90 mm only Type 5 instability was observed, but for amplitudes above 90 mm both Type 3 and Type 5 instabilities occurred more or less simultaneously.

The influence of the liquid level was investigated for water and air in cylinders of diameter 24 mm and 69 mm, with liquid heights set to be 250 mm, 500 mm and 750 mm. The results indicated that the influence of liquid level is negligible in this range.

Finally, the data shown in Figures 2.6, 2.7 and 2.8 are re-plotted in Figures 2.9, 2.10 and 2.11 as the critical acceleration, defined as $a_c = A(2\pi f_c)^2$, against the amplitude A.

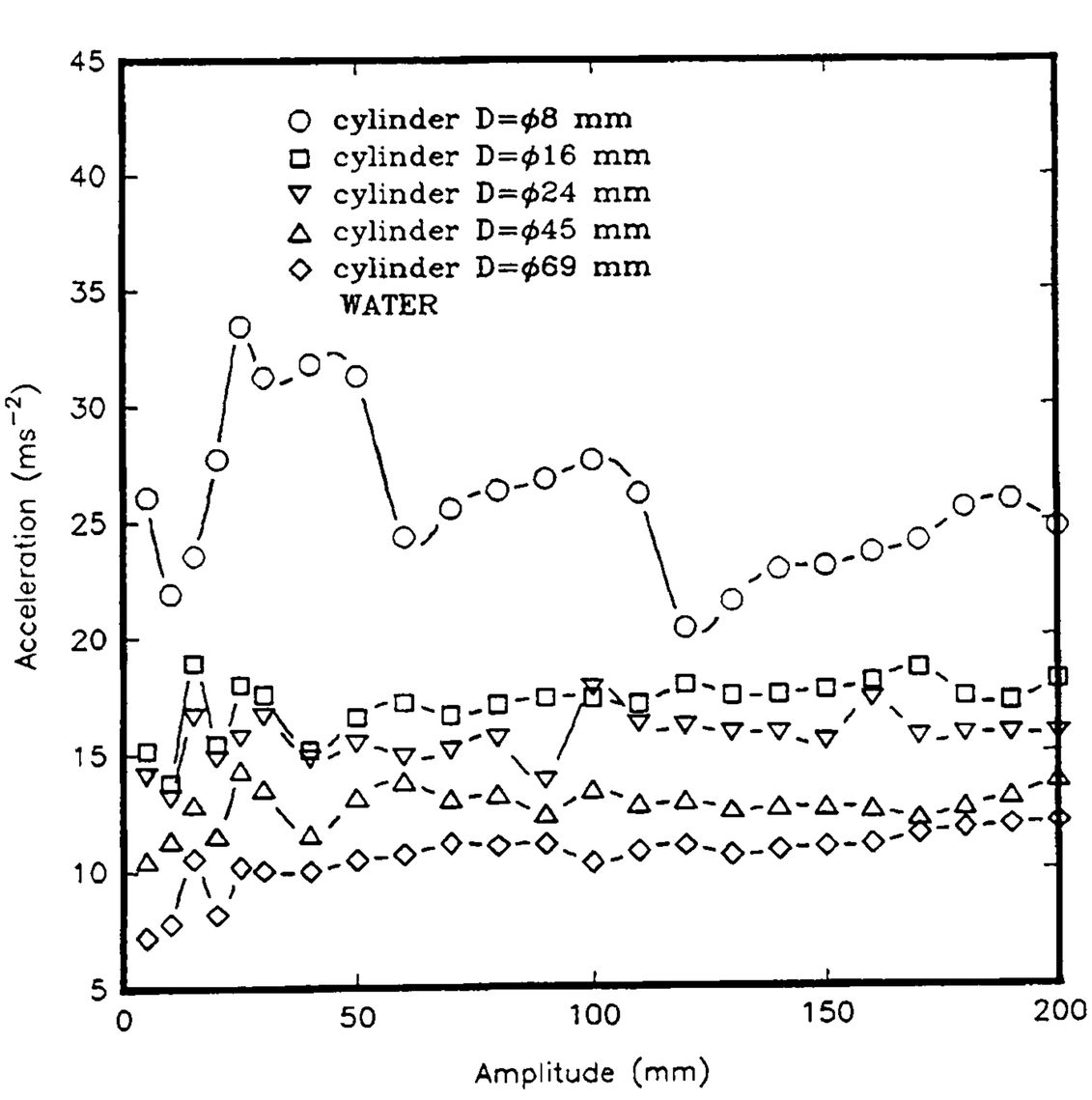

Figure 2.9 *Critical acceleration of oscillations versus amplitude - water/air*

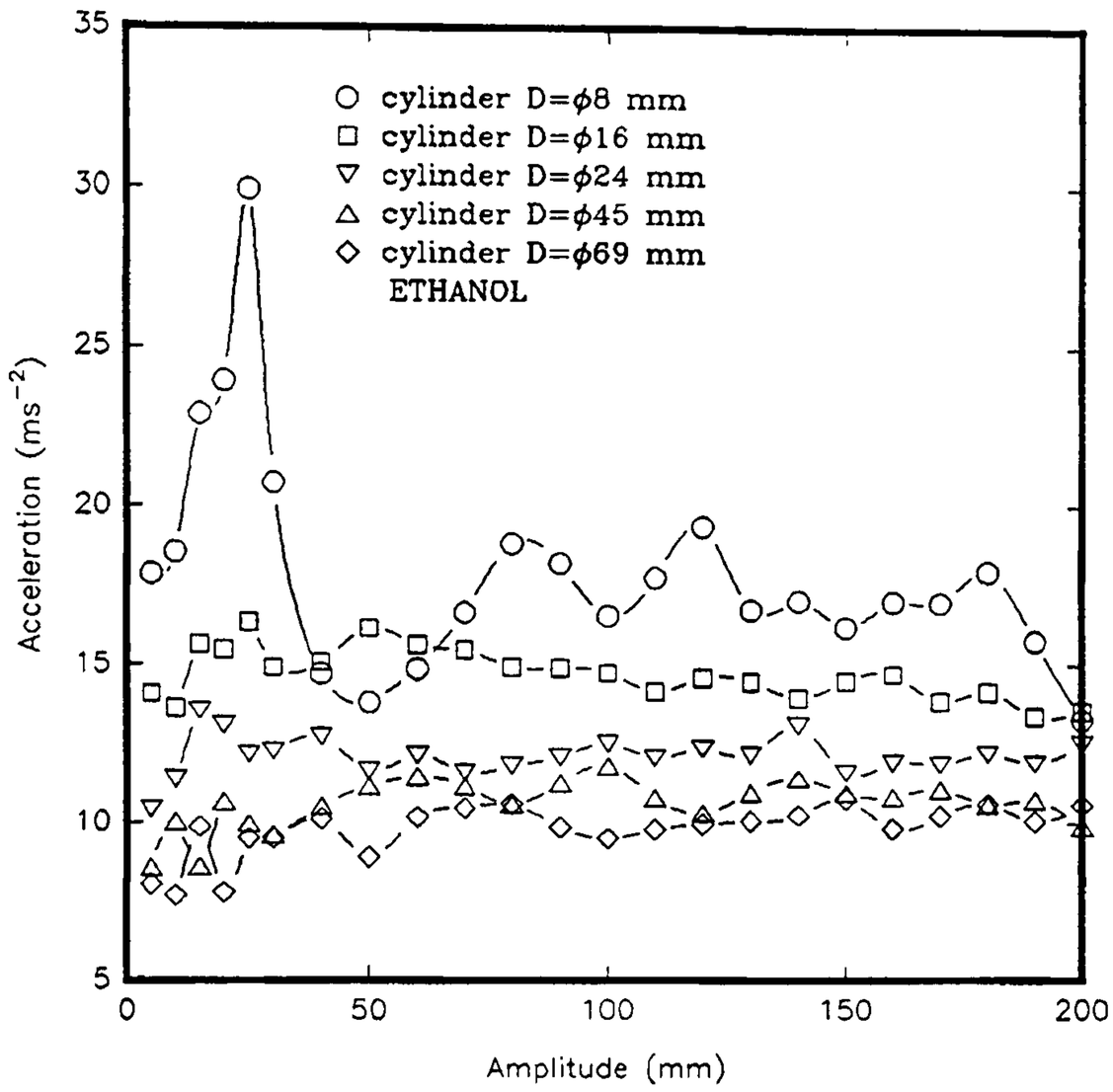

Figure 2.10 *Critical acceleration of oscillation versus amplitude - ethanol/air*

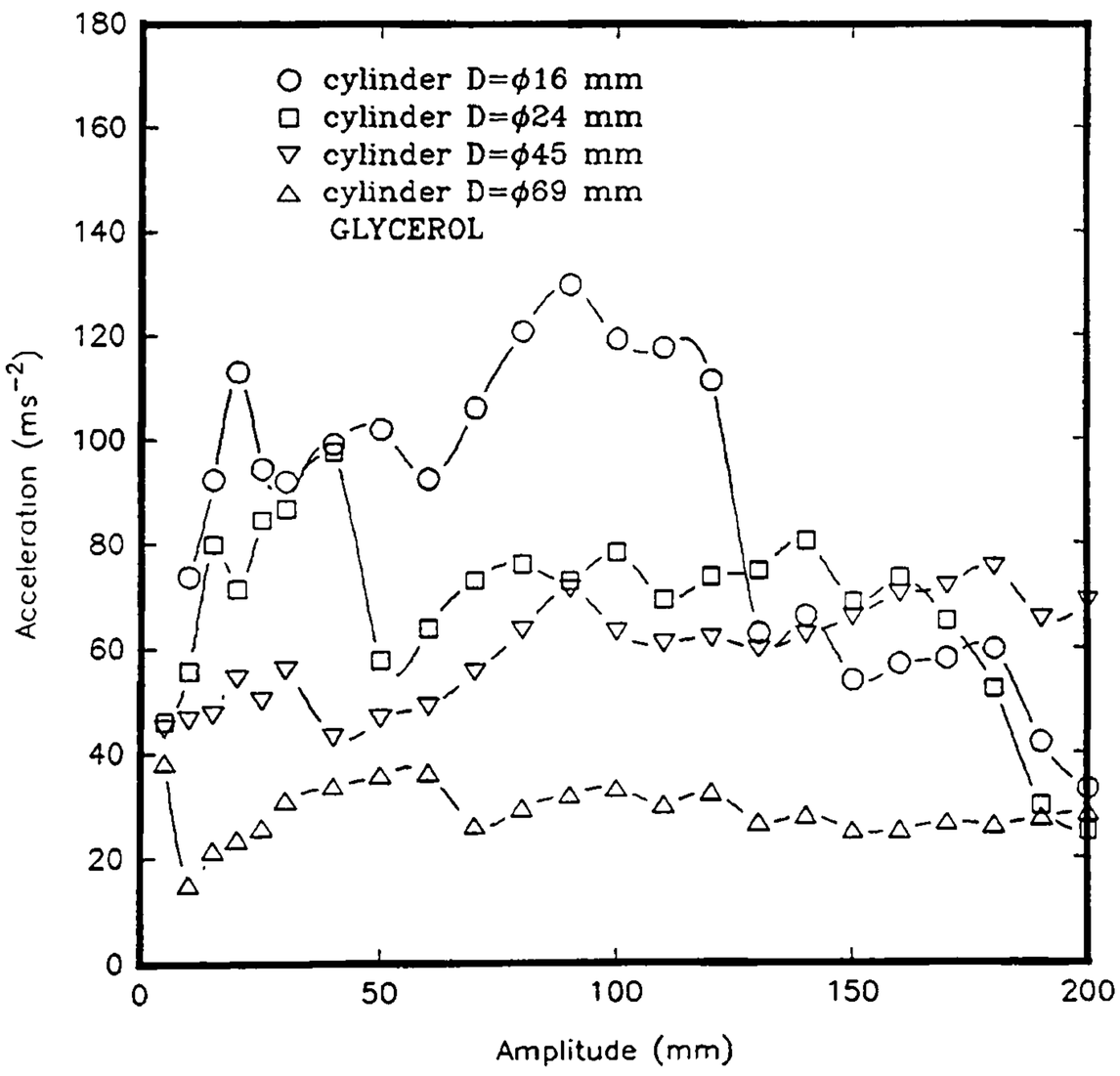

Figure 2.11 *Critical acceleration of oscillations versus amplitude - glycerol/air*

These figures indicate that for water/air and ethanol/air and with amplitudes greater than 50 mm the critical acceleration a_c is approximately constant and hence independent of the amplitude A. The situation is more complex for glycerol/air, when the critical acceleration a_c reaches a constant value only for the two largest diameter cylinders. Figures 2.9 - 2.11 also indicate that the critical acceleration always decreases with increasing cylinder diameter D for the case of water/air and ethanol/air, and generally decreases for the case of glycerol/air.

2.4 MATHEMATICAL ANALYSIS OF THE INTERFACIAL PROBLEM

2.4.1 General

A disturbed liquid surface with surface tension acting on it can be thought of as analogous to a vibrating membrane [50]. Accordingly, the latter problem can be used for mathematical description of the interfacial behaviour. In this work emphasis has been placed on proper formulation of the governing equations, inclusion of the maximum possible number of physical phenomena, correct specification of boundary conditions and the mathematical re-arrangement into a form enabling analytical solution. Figure 2.12 shows the geometry and the corresponding notation that is used throughout the following derivation.

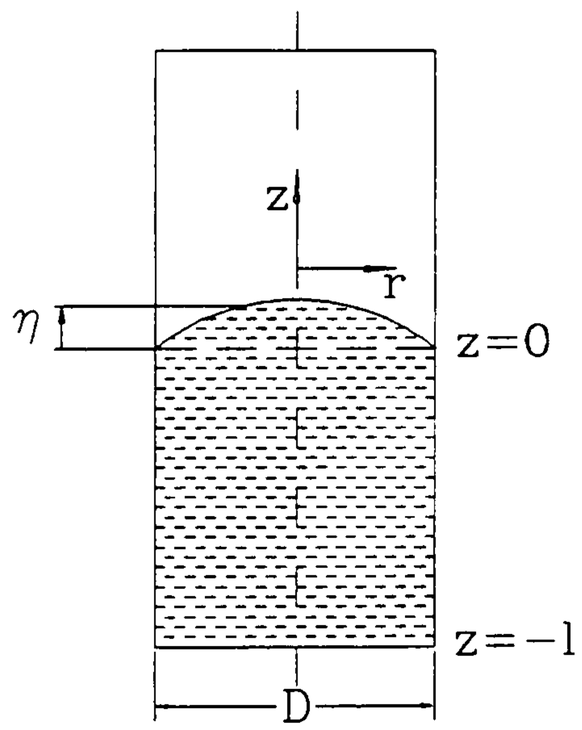

Figure 2.12 Geometry and interfacial wave corresponding notation

As stated in Section 2.2.2, a method similar to that used in previous analyses based on the principles of Benjamin and Ursell [13] (see Table 2.1) has been adopted in this work. This choice was dictated by the main purpose of this investigation which is the determination of the onset of interfacial instability.

2.4.2 Governing equations and boundary conditions

In this section the basic equations are set down in preparation for a mathematical analysis

of the experimental situation described in Section 2.3, and shown in Figure 2.12. The geometry analysed is a vertical cylinder of a certain height and diameter D, respectively radius R. The cylinder contains liquid of height l in its bottom section and air in its top section, and is closed at both ends. The cylinder undergoes regular oscillatory motion along its axis with upward acceleration a, given by:

$$a = A\omega^2\cos(\omega t) \tag{2.1}$$

where A is the amplitude and ω is the angular velocity of the oscillatory motion.

The following equations and conditions must be satisfied for the problem to have physical meaning:

Mass Continuity - which is conservation of mass for the incompressible liquid, written in terms of velocity potential, Ψ, expressed in cylindrical coordinate form, respecting axial symmetry:

$$\frac{\partial^2\Psi}{\partial z^2} + \frac{\partial^2\Psi}{\partial r^2} + \frac{1}{r}\frac{\partial\Psi}{\partial r} = 0 \tag{2.2}$$

Velocity conditions - (i) the z-direction velocity at the gas - liquid interface, at $z = \eta$, can be expressed in two forms that must be equal:

$$\frac{\partial\Psi}{\partial z} = \frac{\partial\eta}{\partial t} \tag{2.3}$$

where $\eta(r,t)$ is a variable representing position of the interface as a function of time t and radial coordinate r.

(ii) zero velocity at the base of the cylinder, i.e. at $z = -l$:

$$\frac{\partial\Psi}{\partial z} = 0 \tag{2.4}$$

Pressure condition - a force balance on the gas - liquid interface [46] - [51], at $z = 0$, including the oscillatory acceleration term, written in terms of the velocity potential:

$$\frac{\partial\Psi}{\partial t} + [g - A\omega^2\cos(\omega t)]\eta - \frac{\sigma}{\rho}\left(\frac{\partial^2\eta}{\partial r^2} + \frac{1}{r}\frac{\partial\eta}{\partial r}\right) = 0 \tag{2.5}$$

where g is the gravitational acceleration, σ is the surface tension and ρ liquid density. It should be noted that the force balance written in this form neglects the effects of viscosity.

The wave shape formed on the gas-liquid interface due to vertical oscillations can be described by the standard wave equation:

$$\frac{\partial^2 \eta}{\partial t^2} = c^2\left(\frac{\partial^2 \eta}{\partial r^2} + \frac{1}{r}\frac{\partial \eta}{\partial r}\right) \tag{2.6}$$

where c is the wave velocity, which, in general is a function of liquid viscosity μ, surface tension σ, the acceleration, a, and the geometry.

2.4.3 Reduction of the governing equations

The preceding section lists all of the governing equations and conditions. The aim of this section is the mathematical re-arrangement and reduction of these equations.

It is assumed that the solution of equation (2.6) can be expressed as a series of orthogonal eigen functions [52]:

$$\eta(r,t) = \sum E_m(t) S_m(r) \tag{2.7}$$

where $E_m(t)$ is only a function of t and $S_m(r)$ is only a function of r. Substitution of equation (2.7) into equation (2.6) and rearrangement, putting the time dependent components into a single variable k_m, yields:

$$\frac{d^2 S_m}{dr^2} + \frac{1}{r}\frac{dS_m}{dr} + k_m^2 S_m = 0 \tag{2.8}$$

A new variable $s = k_m r$ transforms equation (2.8) into a standard Bessel equation

$$\frac{d^2 S_m}{ds^2} + \frac{1}{s}\frac{dS_m}{ds} + S_m = 0 \tag{2.9}$$

whose general solution is given [52] by

$$S_m = C_1 J_o(s) + C_2 Y_o(s) \tag{2.10}$$

where J_o and Y_o are standard Bessel functions.

Since η is small for all values of r, including $r = 0$, C_2 is equal to zero; C_1 is set to 1 and hence:

$$S_m = J_o(s) \tag{2.11}$$

Next it is assumed that there is no displacement on the walls

$$\text{For} \quad r = R \quad \eta = 0 \tag{2.12}$$

and hence

$$J_o(s_{r=R}) = J_o(k_m R) = 0 \tag{2.13}$$

The first four zeros of J_o are $\alpha_1 = k_1 R = 2.4048$; $\alpha_2 = k_2 R = 5.5201$; $\alpha_3 = k_3 R = 8.6537$,

$\alpha_4 = k_4 R = 11.7915$. Each of them corresponds to a different mode of oscillation as shown in Figure 2.13.

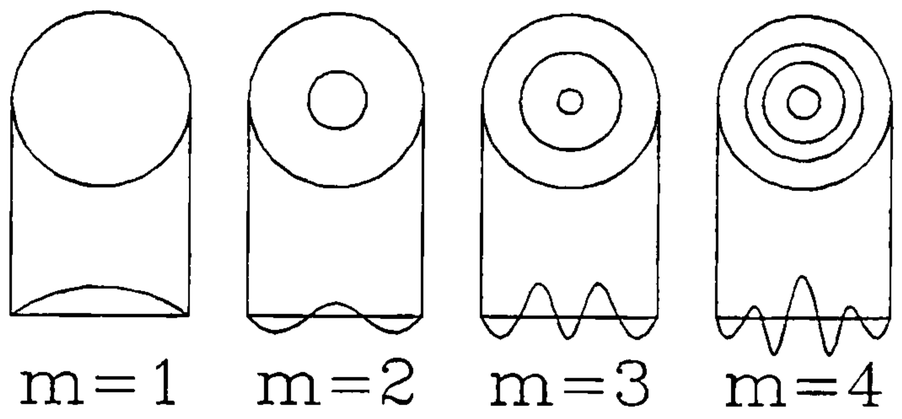

Figure 2.13 Modes of oscillation

Thus η can be expressed as

$$\eta(r,t) = \sum_{m=0}^{m=\infty} E_m(t)\ J_o(k_m\ r) \tag{2.14}$$

where

$$k_m = \frac{\alpha_m}{R} \tag{2.15}$$

The continuity equation (2.2) for the velocity potential Ψ is analogous to equation (2.6), but the wave velocity is constant and equal to imaginary i. Hence, in a similar manner to the solution of equation (2.6), the solution of equation (2.2) is given as

$$\Psi(r,z) = \sum_{m=0}^{m=\infty} Z_m(z)\, J_o(k_m\, r) \tag{2.16}$$

Substitution of equation (2.16) into equation (2.2) gives for Z_m, that is only function of z

$$\frac{d^2 Z_m}{dz^2} - k_m^2 Z_m = 0 \tag{2.17}$$

Using the velocity boundary conditions, given by equations (2.3) and (2.4), together with equation (2.14), the velocity potential Ψ can be expressed as

$$\Psi = \sum_{m=0}^{m=\infty} \frac{dE_m}{dt} \frac{\cosh[k_m(l+z)]}{k_m \sinh[k_m\, l]}\, J_o(k_m\, r) \tag{2.18}$$

The velocity potential in this form includes the function of time $E_m(t)$, which is determined from the pressure or force balance condition on the interface as given by equation (2.5). Substitution of equation (2.18) into equation (2.5) gives

$$\sum_{m=0}^{m=\infty} \frac{d^2 E_m}{dt^2} + E_m k_m \tanh(k_m\, l)\left[\frac{\sigma}{\rho} k_m^2 + g - A\omega^2 \cos(\omega t)\right] = 0 \tag{2.19}$$

When only a single mode of oscillation is considered, equation (2.19) can be rearranged as

$$\frac{d^2 E}{du^2} + [p - 2q\, \cos(2u)]E = 0 \tag{2.20}$$

where

$$u = \frac{\omega t}{2} \tag{2.21}$$

$$p = \frac{4}{\omega^2}\, k_m\, \tanh(k_m l)\left[\frac{\sigma}{\rho} k_m^2 + g\right] \tag{2.22}$$

$$q = 2A\, k_m\, \tanh(k_m l) \tag{2.23}$$

Equation (2.20) for E as a function of u, with parameters p and q is known as Mathieu's equation. It should be noted that in this form the parameter p depends on the frequency of the angular motion and the parameter q depends on the amplitude of the angular motion.

2.4.4 Mathieu equation and its stability analysis

Mathieu's equation has been investigated by many authors [50], [53] - [56]. A basic method for investigating the stability of equation (2.20) was suggested by Ince [53], [54]. The solution is assumed to be in the form of a Fourier series yielding after substitution to equation (2.20), an infinite set of equations. Solution of this set of equations becomes progressively more difficult for higher sets, i. e. increasing values p and q, and subsequent research has concentrated on the development of a universal method.

An extensive mathematical analysis made by Kumar and Tuckerman [16], published after this work has been completed, gives the stability regions for high values of p and q. A similar approach has been independently adopted in the present work. The derivation of the stability regions is rather tedious and details are given in Appendix B. The stability diagram in the p-q domain resulting from this derivation is shown in Figure 2.14. The symbols a and b on Figure 2.14 correspond to the roots of the continued fractions derived in Appendix B.

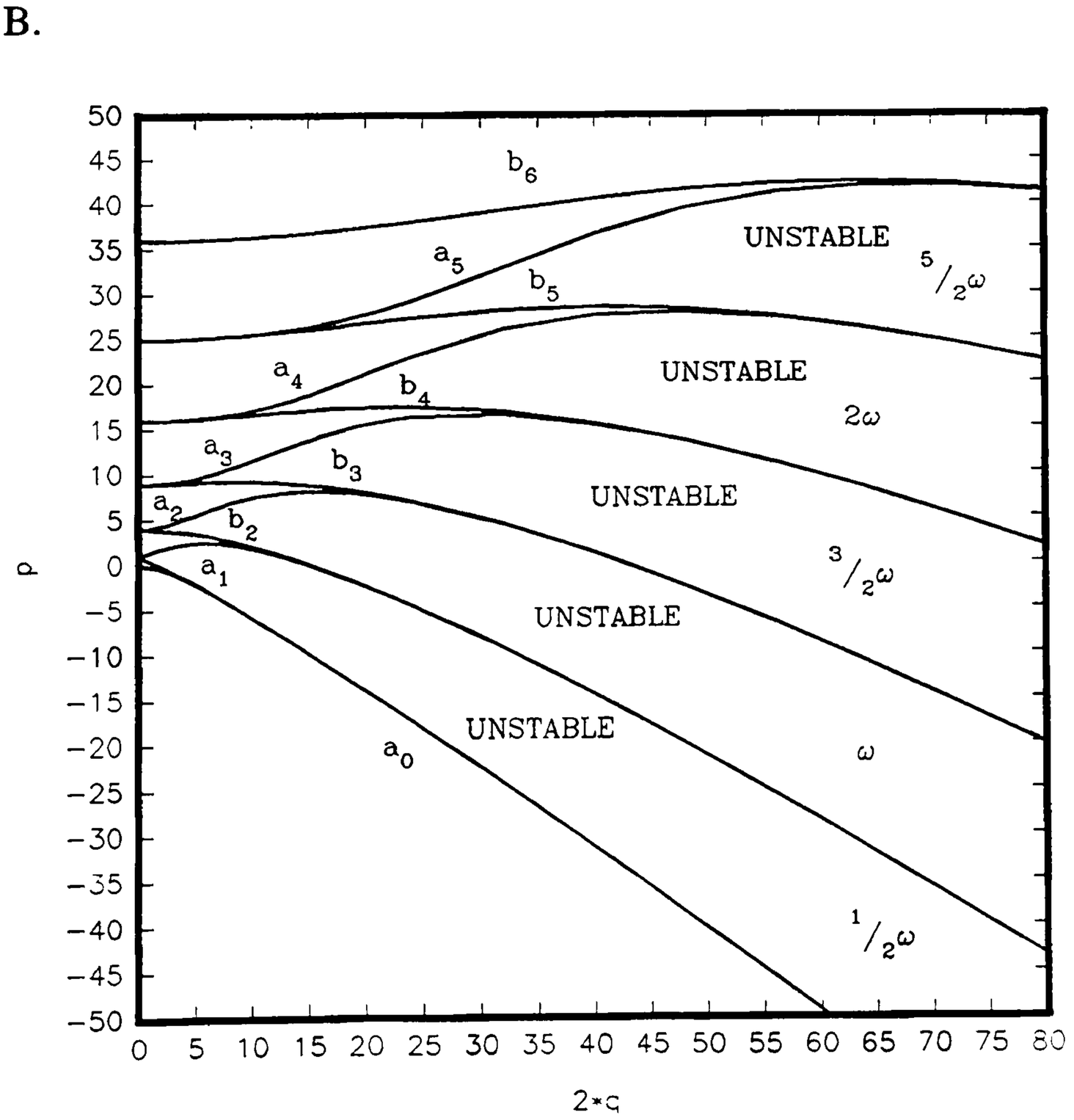

Figure 2.14 Stability regions of the p-q domain

The curves of marginal stability shown in Figure 2.14 correspond to solutions for E with periods equal to either odd or even multiples of ½ω, i.e. multiples of the frequency of the forced oscillation or multiples of half that frequency. The unstable solutions also oscillate with these periods, whereas their amplitudes increase exponentially [16], [51].

2.4.5 Results and discussion

The experimental data sets presented in Section 2.3 show critical values of amplitude A and frequency f of the oscillatory motion. Amplitude A is represented by 2q and frequency f by p in the stability analysis of equation (2.20). Provided that the mode of oscillation, k_m, of the interface is known it is possible to transform the experimental data into p - q domain of the stability diagram such as Figure 2.14. This provides a comparison of the experimental and analytical data and enables frequency of the standing waves on the interface to be determined.

In practice higher order modes are damped by viscosity or dissipative contact effects at the edge of the liquid surface and an appreciable disturbance of the free surface is observed only when one of the lower-order modes is unstable. The effect of mode overlapping is rare for stable interface oscillations, but it occurs on the stability boundary [4], [16]. The experimental data from [49] have been re-plotted in the p - q domain assuming that the first mode of oscillation, k_1, is established. This assumption is also verified by observations of experimental video recordings of the interface. The results of the comparison are shown in Figure 2.15 for water, 2.16 for ethanol and 2.17 for glycerol.

The experiments [49] show that instability occurred independently of the height of the water column. The column heights, l, investigated were 250 mm, 500 mm and 750 mm and cylinder diameters were 8, 16, 24 and 69 mm. $\tanh(k_m.l) = \tanh(\alpha_1/R.l)$ is for any combination of height of liquid column and cylinder diameter equal to 1. This means that the values of p and q did not change for the given heights and agree well with the experimental findings.

Figures 2.15-2.17 show that the experimental data are generally on the boundary between the stable and unstable regions or inside the unstable regions, thus indicating the

onset of interfacial instability.

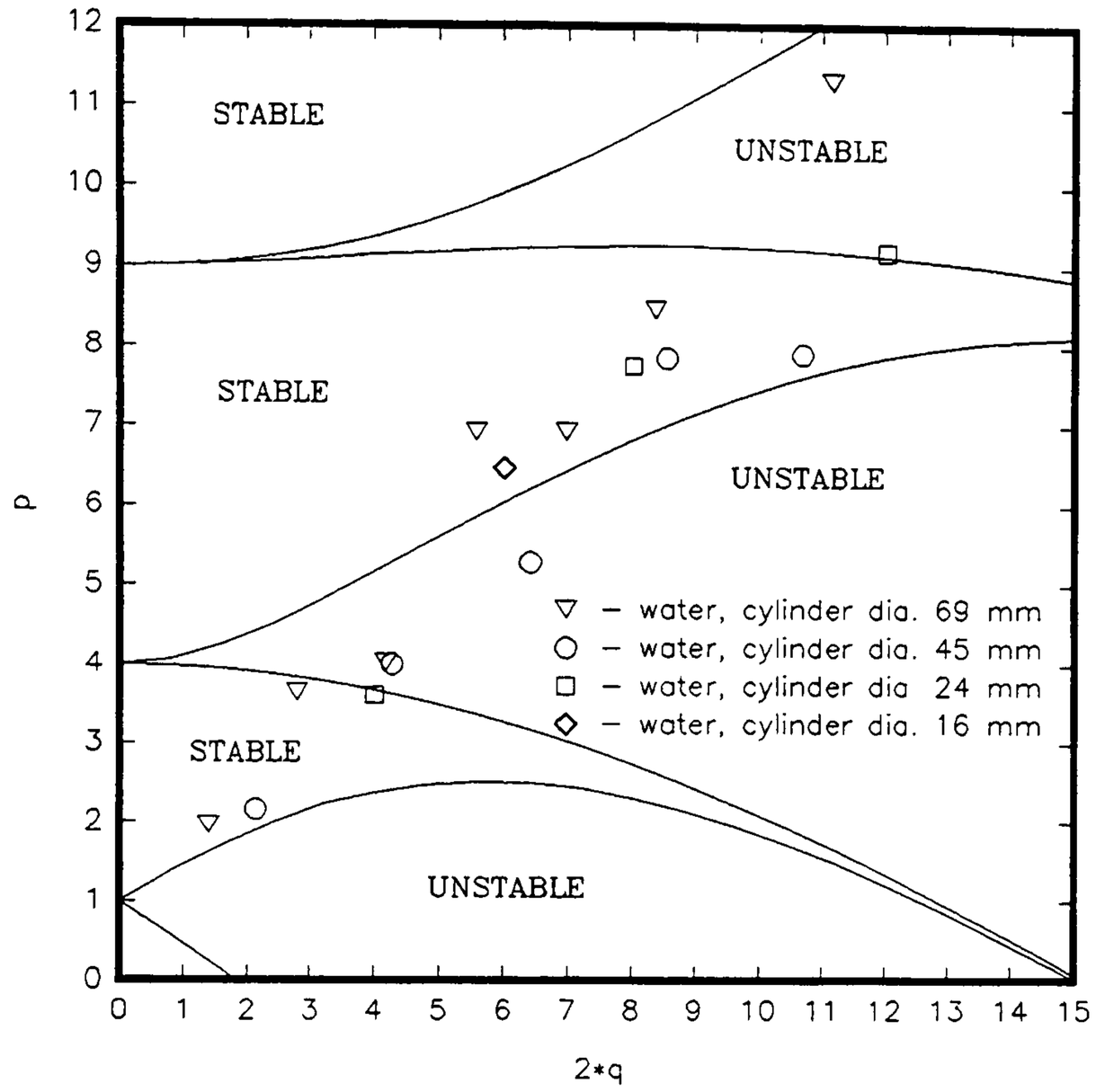

Figure 2.15 *Experimental results for water in p-q domain stability diagram*

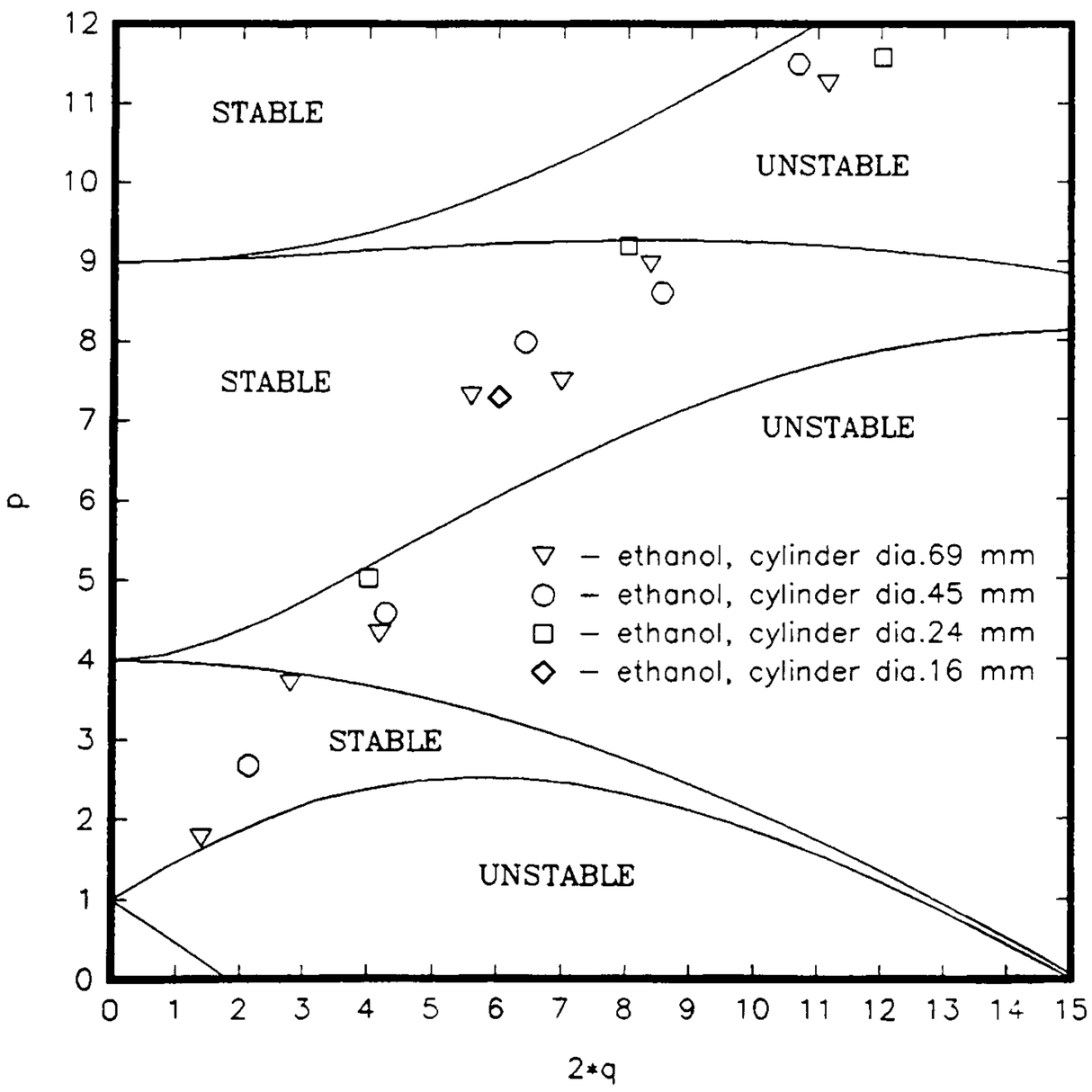

Figure 2.16 *Experimental results for ethanol in p-q domain stability diagram*

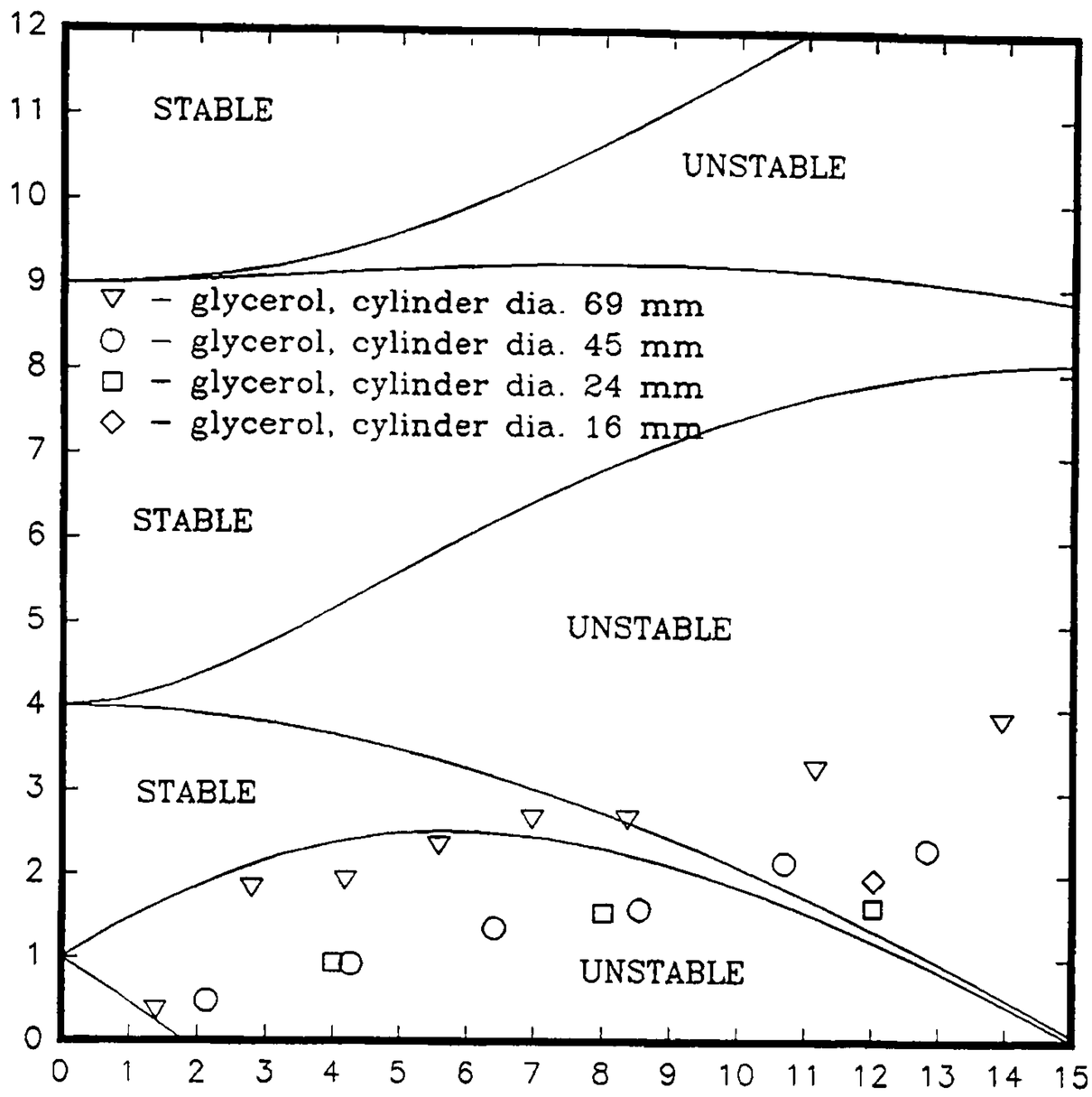

Figure 2.17 Experimental results for glycerol in p-q domain stability diagram

Experimental data have also been transformed to p - q domain for higher modes of oscillation. It was found that this transformation caused the results to fall into the stable p - q regions. This fact provides further proof of the correct choice for the mode of oscillation, k_m.

Figures 2.15 and 2.16, for water and ethanol respectively, which have similar viscosities and surface tensions indicate that the frequency of the waves generated on the interface is very sensitive to the amplitude, A, of the forcing vertical motion. Figure 2.17, however, shows that for glycerol, which is approximately 800 times more viscous than water and ethanol, this sensitivity is much smaller. This finding agrees well with the published literature [4], [13], [16].

Figures 2.15 - 2.17 also indicate that for larger amplitudes, the results for the first mode of oscillation fall deep into the unstable regions. In such cases mode overlapping is believed to occur [13].

2.5 COMPUTATIONAL ANALYSIS OF THE INTERFACIAL PROBLEM

2.5.1 General

A number of methods available for CFD simulation are listed in the literature overview in Section 2.2.3. Probably the most widely used method for the simulation of problems concerning time-dependent, viscous flow of an incompressible fluid in several space dimensions is the MAC method [29]. The simplified MAC (SMAC) method [32] has at least as great a range of applicability as MAC, but is significantly simpler to use, as problems associated with the Poisson's equation for pressure are eliminated. The SMAC method has been chosen for the present analysis. It has been extended to incorporate a method similar to the Volume of Fluid (VOF) method [41] together with Continuum Surface Force (CSF) Model [45], [57] thus enabling the modelling of surface tension effects.

This algorithm has been applied to the vertical motion induced interfacial wave problem considered in this Chapter. The following sections describe the SMAC computational method, the incorporation of surface tension effects and the results of the numerical experiments.

2.5.2 Governing equations

The basic equations describing two-dimensional, time dependent flow of a constant viscosity, incompressible fluid are:

$$D \equiv \frac{1}{r^{\alpha}}\frac{\partial r^{\alpha} u}{\partial r} + \frac{\partial v}{\partial z} = 0 \qquad (2.24)$$

$$\frac{\partial u}{\partial t} + \frac{1}{r^{\alpha}}\frac{\partial r^{\alpha} u^2}{\partial r} + \frac{\partial uv}{\partial z} = -\frac{\partial \Phi}{\partial r} + g_r + \nu\frac{\partial}{\partial z}\left(\frac{\partial u}{\partial z} - \frac{\partial v}{\partial r}\right) + F_{br} \qquad (2.25)$$

$$\frac{\partial v}{\partial t} + \frac{1}{r^{\alpha}}\frac{\partial r^{\alpha} uv}{\partial r} + \frac{\partial v^2}{\partial z} = -\frac{\partial \Phi}{\partial z} + g_z - \frac{\nu}{r^{\alpha}}\frac{\partial}{\partial r}\left[r^{\alpha}\left(\frac{\partial u}{\partial z} - \frac{\partial v}{\partial r}\right)\right] + F_{bz} \qquad (2.26)$$

Equation (2.24) represents continuity and equations (2.25) and (2.26) describe conservation of momentum in the r and z direction respectively. When working in

cartesian coordinates, the exponent $\alpha = 0$, and when in cylindrical coordinates $\alpha = 1$. For the case of a vertically vibrating system analysed here, horizontal component of acceleration, $g_r = 0$ in equation (2.25) and vertical component of acceleration, g_z in equation (2.26) is a function of time as in equation (2.5). That is

$$g_z = -g - A\omega^2\cos(\omega t) \tag{2.27}$$

F_{br} and F_{bz} represent forces that will be used for modelling of surface tension and their significance will be discussed later. The equation for vorticity, Ω is

$$\Omega = \frac{\partial u}{\partial z} - \frac{\partial v}{\partial r} \tag{2.28}$$

Vorticity is independent of the pressure, so that any field of pressure inserted into the equations (2.25) and (2.26) will ensure that the resulting velocity field carries the consistent vorticity. An arbitrary pressure field will not, however, ensure satisfaction of the continuity equation, but if the velocity field is altered by the addition of the gradient of an appropriate potential function, the resulting field will carry the same vorticity, satisfy continuity and accordingly will be uniquely determined.

This is the essence of the computational procedure that is carried out in finite difference form. Equations (2.24) (2.25) (2.26) and (2.28) are written in finite difference form in Appendix C together with other differencing definitions. The true pressure normalised to unity density, Φ, is replaced by arbitrary pressure field, θ, and accordingly the new-time velocities are marked with tildes. The notation associated with a typical SMAC finite difference cell is shown in Figure 2.18

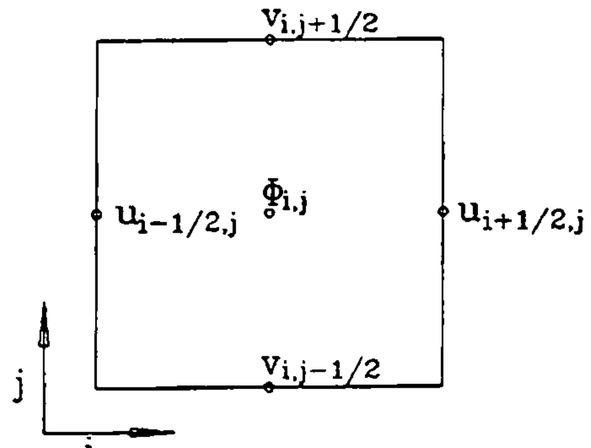

Figure 2.18 SMAC finite difference cell and location of the cell variables

The time - dependent finite difference equations, listed in Appendix C, are written in explicit form. The cell centred momentum convection terms are written in the so called

ZIP form [32], which, although continuing to ensure momentum conservation for the interior of the domain, as in MAC, also allows SMAC to conserve momentum in the immediate vicinity of a rigid wall.

The finite difference forms of the r-direction and z-direction momentum conservation equations (Appendix C, equations (C.2) and (C.3)) can be combined to obtain a transport expression for $\Omega_{i+1/2,j+1/2}$, which is independent of the pressure, θ, field. Accordingly the explicit calculation of the tilde velocities ensures that the vorticity at every mesh corner point is consistent, independent of the choice of θ.

2.5.3 Boundary conditions

Consider a liquid bounded in part by rigid boundaries and in part by a free surface. The various types of finite difference cells required for this situation are illustrated in Figure 2.19.

First, consider indexing appropriate to the full cell, $F_{i,j}$, adjacent to the left boundary. A detail of the situation is shown in the right hand part of Figure 2.19. Two types of boundary may be considered.

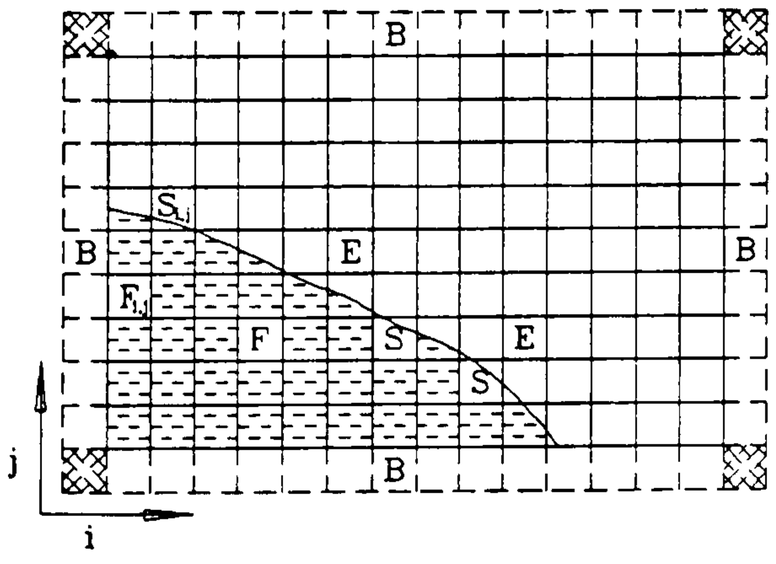

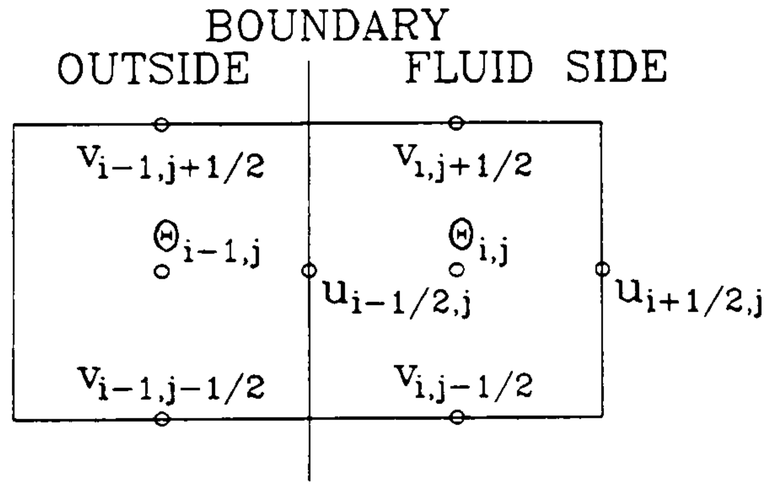

Figure 2.19 *SMAC computational mesh containing full (F) cells, free surface (S) cells, empty cells (E) and boundary cells (B); variable positions at a SMAC left wall*

A free - slip boundary represents an axial centerline or a plane of symmetry or a nonadhering surface that exerts no drag upon the fluid. The normal velocity component

vanishes at a free - slip boundary and there is no normal gradient in either tangential velocity or pressure. In finite difference form, these free - slip boundary conditions are written as follows:

$$v_{i-1,j+1/2} = v_{i,j+1/2} \tag{2.29}$$

$$v_{i-1,j-1/2} = v_{i,j-1/2} \tag{2.30}$$

$$\theta_{i-1,j} = \theta_{i,j} \tag{2.31}$$

$$u_{i-1/2,j} = 0 \tag{2.32}$$

A no-slip boundary corresponds to a rigid wall that exerts a drag upon the fluid. In this case the tangential velocity is forced to go to zero at the wall. The boundary conditions for a no - slip boundary are as follows:

$$u_{i-1/2,j} = 0 \tag{2.33}$$

$$v_{i-1,j+1/2} = -v_{i,j+1/2} \tag{2.34}$$

$$v_{i-1,j-1/2} = -v_{i,j-1/2} \tag{2.35}$$

$$\theta_{i-1,j} = \theta_{i,j} \tag{2.36}$$

Second, consider indexing appropriate to the free surface cells, $S_{i,j}$, in Figure 2.19 which has a full cell below and an empty one above. The tangential stress condition is at the free surface:

$$\frac{\partial u}{\partial z} + \frac{\partial v}{\partial r} = 0 \tag{2.37}$$

so that $u_{i+1/2,j+1}$ is determined by the equation:

$$u_{i+1/2,j+1} = u_{i+1/2,j} - \frac{\delta z}{\delta r}(v_{i+1,j+1/2} - v_{i,j+1/2}) \tag{2.38}$$

This ensures that the tangential viscous momentum flux vanishes when calculated by the

r-direction momentum conservation equation written in finite difference form (Appendix C, equation (C.2)) for $u_{i+1/2,j}$. In addition, the normal stress condition is:

$$\Phi_{i,j} = \Phi_{i,j}\ (applied) + \frac{2\nu}{\delta z}(v_{i,j+1/2} - v_{i,j-1/2}) + surface\ tension\ stress \qquad (2.39)$$

$\Phi_{i,j}$(applied) is specified according to the requirements of the problem, while the viscous stress and surface tension stress terms ensures that there is otherwise no net flux of normal momentum through the surface.

2.5.4 Steps in calculation

In the SMAC computational method used in this work all cells are allocated an initial flag indicating whether they are an empty, a full or a surface cell. During computation, because the fluid is not stationary, a cell may change from empty (E) to surface (S) and then to full (F), or the reverse. It is therefore necessary to check during each cycle to see if the cell flags need adjusting. First, a sweep is made through cells to ascertain which contain fluid and which cells do not. Second, all surface (S) cells that no longer contain fluid become empty (E) cells, and velocities are zeroed on any faces of such cells that are adjacent to other empty (E) cells. Third, a check is made on the full (F) cells. If a full cell (F) has any empty (E) neighbours, it becomes a surface cell (S). Finally, the surface cells (S) with no empty (E) neighbours become full cells (F).

In the first phase of computation, the r-direction and z-direction momentum equations are used to calculate $\tilde{u}$ and $\tilde{v}$ throughout the mesh. For the full cells, $\theta_{i,j} = 0$. No values for $\theta_{i,j}$ need be specified for cells outside the rigid walls, the normal velocity at each wall position is simply set to zero. In every surface cell, the value of $\theta_{i,j}$ is given by equation (2.39). Tilde velocities are not, however, calculated for the empty-cell faces of the surface cells. They are determined later in the cycle in such a way as to satisfy the continuity equation for each surface cell. As a result of this phase the vorticity has been correctly implanted into the new velocity field, which may, however, be everywhere incorrect because it does not satisfy continuity.

The function of the second phase is to convert the tilde velocity field into a final velocity field for the cycle, that satisfies continuity for every cell. This must occur in such

a way as to preserve the vorticity deposited in the field in the first phase. Accordingly, the change in every velocity must be given by the gradient of a potential function Ψ:

$$u_{i+1/2,j}^{n+1} = \tilde{u}_{i+1/2,j}^{n+1} - \frac{\delta\psi}{\delta r} = \tilde{u}_{i+1/2,j}^{n+1} - \frac{1}{\delta r}(\psi_{i+1,j} - \psi_{i,j}) \tag{2.40}$$

$$v_{i,j+1/2}^{n+1} = \tilde{v}_{i,j+1/2}^{n+1} - \frac{\delta\psi}{\delta z} = \tilde{v}_{i,j+1/2}^{n+1} - \frac{1}{\delta z}(\psi_{i,j+1} - \psi_{i,j}) \tag{2.41}$$

Substitution of (2.40) and (2.41) into the finite difference expression of the continuity equation (Appendix C, equation (C.1)) yields:

$$\begin{aligned} D_{ij}^{n+1} = \tilde{D}_{i,j} &- \frac{1}{r_i^{\alpha}\delta r^2}[r_{i+1/2}^{\alpha}(\psi_{i+1,j}-\psi_{i,j}) - r_{i-1/2}^{\alpha}(\psi_{i,j}-\psi_{i-1,j})] \\ &- \frac{1}{\delta z^2}(\psi_{i,j+1}+\psi_{i,j-1}-2\psi_{i,j}) = 0 \end{aligned} \tag{2.42}$$

which together with appropriate boundary conditions serves to determine uniquely the value of $\Psi_{i,j}$ for every cell. For the boundary condition near a rigid wall (see Figure 2.19):

$$\psi_{i-1,j} = \psi_{i,j} \tag{2.43}$$

which ensures that the normal velocity at the wall will still vanish after transformation. For free surface cells $\Psi_{i,j} = 0$.

The final stage is the calculation of new velocities by substitution of Ψ values into equations (2.40) and (2.41) for every position except the empty-cell faces of the surface cells, which are now chosen in such a way as to make $D^{n+1}{}_{i,j} = 0$ for each of those cells. For surface cells with two empty sides, the tangential stress condition is also invoked. Appendix D gives details of all possible surface cell fluid configurations and lists the equations for surface cell velocities.

2.5.5 Marker particles

In addition to the mesh of Eulerian cells, the SMAC algorithm employs a set of massless marker particles, which enable visual representation of the fluid, but whose essential purpose is to define the position of the free surface so that the configuration of surface cells can be sensed and also to determine amount of fluid in the surface cells for calculation of surface tension effects as discussed later. The marker particles do not enter

into the calculation, but are embedded in the fluid and are carried along by it. The marker particles are moved with a weighted average of the four nearest u velocities and of the four nearest v velocities in the manner described in Appendix E.

2.5.6 Incorporation of surface tension

The influence of surface tension effects has been indicated in previous sections in equations (2.25) (2.26) and (2.39). This section deals in detail with the incorporation of surface tension phenomena in these equations.

The exact surface stress boundary conditions at a free surface are given below. Pressure boundary condition given by [58]

$$p = p_v + p(applied) + 2\mu\frac{\partial v}{\partial z} + \sigma\kappa \qquad (2.44)$$

for the normal direction, where p_v is the vapour pressure on the phase interface, σ is the surface tension coefficient and κ is the local free surface curvature. Neglecting p_v the equation (2.44) reduces to equation (2.39) in finite difference form, known as Laplace's formula [58]. Stress balance in the tangential direction is [58] given by

$$\mu\left(\frac{\partial u}{\partial z}+\frac{\partial v}{\partial r}\right) = \frac{\partial \sigma}{\partial s} \qquad (2.45)$$

Assuming a constant surface tension coefficient this equation reduces to (2.37).

In the present analysis the surface tension pressure in equation (2.44) is treated as a volume force using the Continuum Surface Force (CSF) model [45], [57], [59] as

$$\vec{F}_{sv}(\vec{x}) = \sigma\ \kappa(\vec{x})\ \nabla F(\vec{x}) \qquad (2.46)$$

and appears as a body force contribution in equations (2.25) and (2.26). The Volume Of Fluid (VOF) function, F, as specified by [41], averaged over a cell, represents the fractional volume of the cell occupied by fluid. In particular, a unit value of F would correspond to a cell full of liquid, while a zero value would indicate that the cell contained no liquid. Cells with F values between zero and one must then contain a free surface. Hirt and Nichols [41] devised an algorithm for accurate solution of a differential equation for the transport of F. The method provides an economical way to track the surfaces, but the surface shape resolution is rather poor and requires a complicated reconstruction algorithm

to obtain the surface orientation from the F function.

The method used in this work to obtain value of F splits surface cells into a subgrid as shown in Figure 2.20.

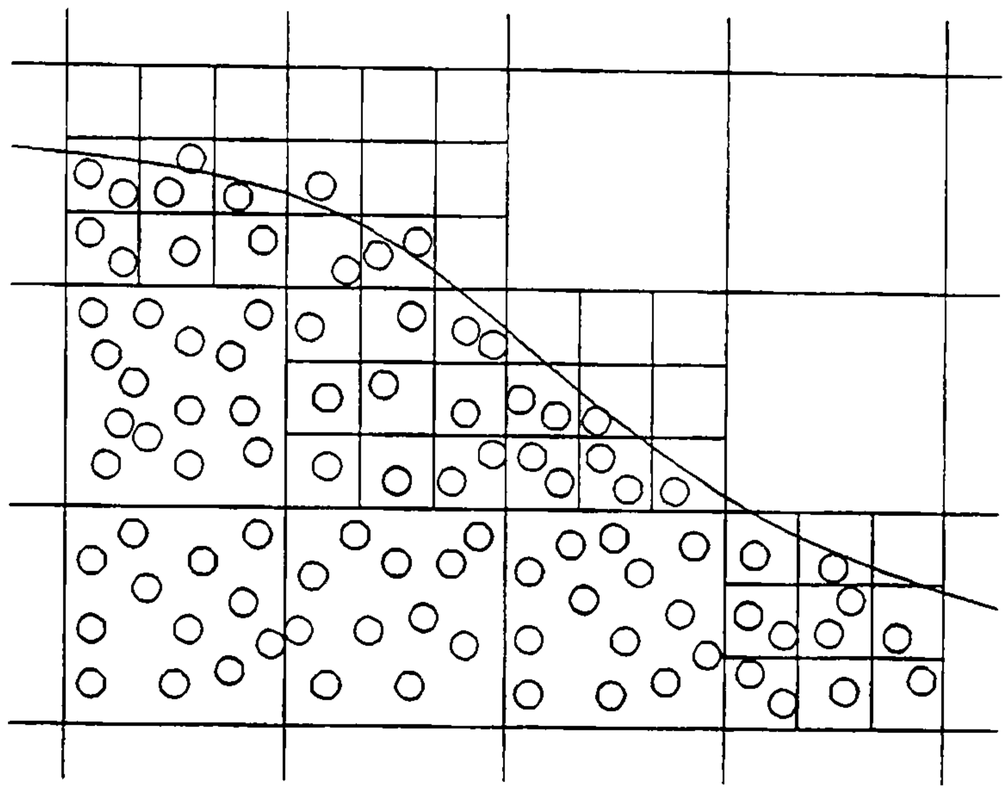

Figure 2.20 *Subgrid of the surface cells*

All particles are checked for whether or not they belong to surface cells. Once it is established that a particle lies in a surface cell, the volume of the particular subgrid cell, corresponding to the particle position is added to the 'full volume' value of i,j cell. If there is more than one particle in the subgrid cell the addition of the subgrid volume occurs only once. After all particles have been checked the 'full volume' value of each surface cell is divided by the total volume of the cell, thus giving the value of $F_{i,j}$.

The curvature, κ, of a surface follows from the expression:

$$\kappa = -(\nabla.\hat{n}) = \frac{1}{|\vec{n}|}.\left[\left(\frac{\vec{n}}{|\vec{n}|}.\nabla\right)|\vec{n}| - (\nabla.\vec{n})\right] \qquad (2.47)$$

where the unit normal $\hat{n}$

$$\hat{n} = \frac{\vec{n}}{|\vec{n}|} \qquad (2.48)$$

is derived from a normal vector $\vec{n}$,

$$\vec{n} = \nabla F \qquad (2.49)$$

A general derivation of equation (2.47) in three dimensions can be found in the paper by Brackbill, Kothe and Zemach [59], and a similar derivation for a two dimensional case is included in Appendix F. The curvature in equation (2.47) is rewritten in terms of $\vec{n}$ and

$|\vec{n}|$ to ensure that the principal contributions to the finite difference approximation for κ come directly from the position of the interfacial surface.

The volume force F_{sv} given by equation (2.46) and appearing in equations (2.25) and (2.26) is located at computational cell centres. Equation (2.46) shows that the curvature, κ, must also be located at cell centres. The CSF model for surface tension applied in the present analysis places the normal vector at the vertices, taking the cell centred normal as the average of vertex normals, and the curvature, κ, at cell centres as shown in Figure 2.21.

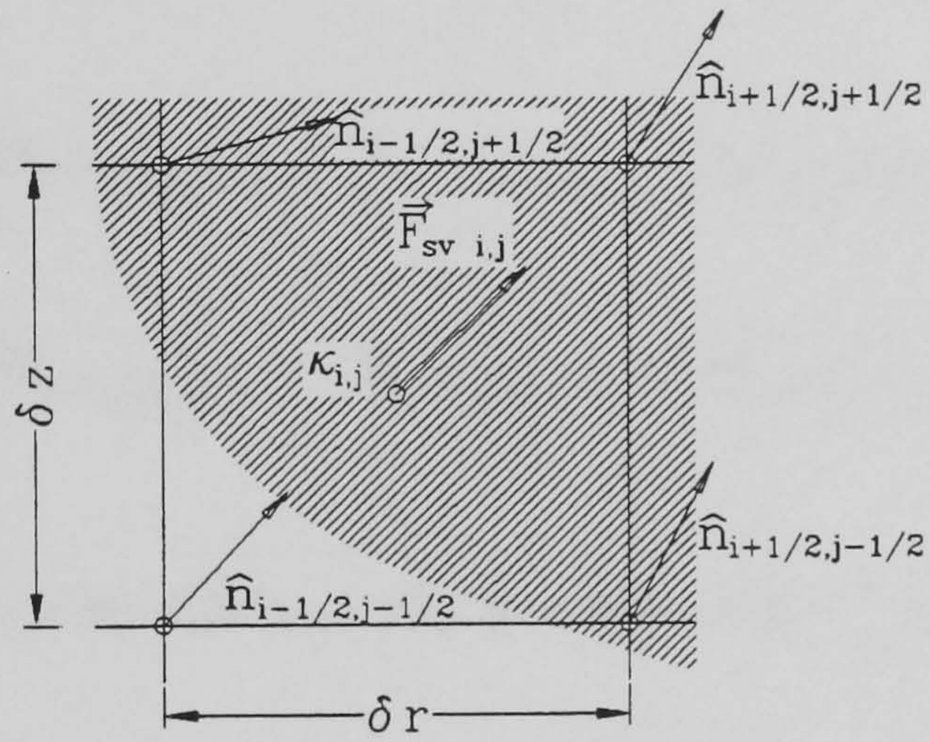

Figure 2.21 *Placement of free surface force, $\bar{F}_{sv}$, curvature, κ, and unit normals, $\hat{n}$, in the CSF model*

Using equation (2.49), $\vec{n}_{i+1/2,j+1/2}$ is expressed in finite difference form for uniform grid as:

$$\vec{n}_{i+1/2,j+1/2} = \left[\frac{F_{i+1,j+1}-F_{i,j+1}+F_{i+1,j}-F_{i,j}}{2\delta r}\right]\hat{i} + \left[\frac{F_{i+1,j+1}-F_{i+1,j}+F_{i,j+1}-F_{i,j}}{2\delta z}\right]\hat{j} \quad \textbf{(2.50)}$$

The curvature follows from an indirect differentiation of the unit normal, $\hat{n}$, as given by the two terms on the right hand side of equation (2.47), the first term, the directional derivative of $|\vec{n}|$ along the cell centred unit normal, $\hat{n}_{i,j}$, is given by:

$$\left(\frac{\vec{n}_{i,j}}{|\vec{n}_{i,j}|}.\nabla\right)|\vec{n}| = \left(\frac{n_r}{|\vec{n}|}\right)_{i,j}\left(\frac{\partial|\vec{n}|}{\partial r}\right)_{i,j} + \left(\frac{n_z}{|\vec{n}|}\right)_{i,j}\left(\frac{\partial|\vec{n}|}{\partial z}\right)_{i,j} \quad \textbf{(2.51)}$$

$$= \left(\frac{n_r}{|\vec{n}|}\right)^2_{i,j}\left(\frac{\partial n_r}{\partial r}\right)_{i,j} + \left(\frac{n_r.n_z}{|\vec{n}|^2}\right)_{i,j}\left(\frac{\partial n_r}{\partial z}+\frac{\partial n_z}{\partial r}\right)_{i,j} + \left(\frac{n_z}{|\vec{n}|}\right)^2_{i,j}\left(\frac{\partial n_z}{\partial z}\right)_{i,j}$$

where

$$|\vec{n}| = \sqrt{n_r^2 + n_z^2} \tag{2.52}$$

The derivatives of the $\vec{n}$ components follow from a knowledge of $\vec{n}$ at the vertices, and are:

$$\left(\frac{\partial n_r}{\partial r}\right)_{ij} = \frac{1}{2\delta r}[n_{r\ i+1/2j+1/2} + n_{r\ i+1/2j-1/2} - n_{r\ i-1/2j+1/2} - n_{r\ i-1/2j-1/2}] \tag{2.53}$$

$$\left(\frac{\partial n_z}{\partial z}\right)_{ij} = \frac{1}{2\delta z}[n_{z\ i+1/2j+1/2} + n_{z\ i-1/2j+1/2} - n_{z\ i+1/2j-1/2} - n_{z\ i-1/2j-1/2}] \tag{2.54}$$

$$\left(\frac{\partial n_r}{\partial z}\right)_{ij} = \frac{1}{2\delta z}[n_{r\ i+1/2j+1/2} + n_{r\ i-1/2j+1/2} - n_{r\ i+1/2j-1/2} - n_{r\ i-1/2j-1/2}] \tag{2.55}$$

$$\left(\frac{\partial n_z}{\partial r}\right)_{ij} = \frac{1}{2\delta r}[n_{z\ i+1/2j+1/2} + n_{z\ i+1/2j-1/2} - n_{z\ i-1/2j+1/2} - n_{z\ j-1/2j-1/2}] \tag{2.56}$$

The cell centred normal will be taken as the average of the vertex normals, as mentioned above:

$$\vec{n}_{ij} = \frac{1}{4}(\vec{n}_{i+1/2,j+1/2} + \vec{n}_{i+1/2,j-1/2} + \vec{n}_{i-1/2,j+1/2} + \vec{n}_{i-1/2,j-1/2}) \tag{2.57}$$

The second term of the right hand side in equation (2.47), the divergence of $\vec{n}$, is computed as:

$$(\nabla.\vec{n})_{ij} = \frac{1}{r_i^\alpha}\frac{\delta}{\delta r}(r^\alpha n_r)_{ij} + \left(\frac{\delta n_z}{\delta z}\right)_{ij} \tag{2.58}$$

where

$$\frac{1}{r_i^\alpha}\frac{\delta}{\delta r}(r^\alpha n_r)_{ij} = \frac{1}{2\delta r\ r_i^\alpha}[r_{i+1/2}^\alpha(n_{r\ i+1/2j+1/2} + n_{r\ i+1/2j-1/2}) - r_{i-1/2}^\alpha(n_{r\ i-1/2j+1/2} + n_{r\ i-1/2j-1/2})] \tag{2.59}$$

Equations (2.53) - (2.57) are substituted into equation (2.51) for the directional derivative of $|\vec{n}|$, and equation (2.59) is substituted into equation (2.58) for the divergence of $\vec{n}$. Thus the surface curvature, given by equation (2.47) can be evaluated. Equation (2.49) modifies the Continuum Surface Force Model given by equation (2.46) to:

$$\vec{F}_{sv}(\vec{x}) = \sigma \kappa \vec{n} \qquad (2.60)$$

Components of $\bar{F}_{sv}$ in the r and z directions are obtained evaluating $\hat{i}$ and $\hat{j}$ coefficients of equation (2.50) for vertex normals and then taking their average, as in equation (2.57), to get a cell centred value. Thus:

$$F_{sv\,r} = |\vec{F}_{sv\,r}(\vec{x}_r)| = \sigma \kappa \vec{n}_r \qquad F_{sv\,z} = |\vec{F}_{sv\,z}(\vec{x}_r)| = \sigma \kappa \vec{n}_z \qquad (2.61)$$

The surface tension forces, F_b, appearing in equations (2.25) and (2.26) are normalized by dividing by density, so that

$$F_{b\,r} = \frac{F_{sv\,r}}{\rho} \quad , \quad F_{b\,z} = \frac{F_{sv\,z}}{\rho} \qquad (2.62)$$

are the source terms representing the effects of surface tension in the computational procedure, which are additional to the accelerations g_r and g_z for each cell.

2.5.7 Overview of the computational cycle

The above described procedure has been implemented into a computer program, written in the FORTRAN-77 language. The program calculates time dependent fluid velocities and distributes massless marker particles accordingly whose positions are stored in output files for subsequent import into a scientific plotting package enabling flow visualisation. The finite difference mesh employs uniform δr and δz sizes. A constant timestep δt is used.

The flow diagram of the main computational cycle is shown in Figure 2.22 and the function of each of the blocks is described in the following paragraphs.

READ INPUT DATA - user specified data read by the program to provide the following initial settings: size of the computational mesh, values of δr, δz and timestep δt; overall timespan of the calculation; specification of co-ordinate system - the program can solve problems both in cartesian and cylindrical co-ordinates; the location of the initial disturbance of the free surface and its magnitude are given; details of the domain boundary conditions are provided - either no - or free-slip, the axis of symmetry for problems in cylindrical co-ordinates, is located on the left vertical line of the computational domain; the following properties of the fluid are set: density, kinematic viscosity and surface tension coefficient; next the iteration convergence condition, ϵ, and the over relaxation

parameter α, whose purpose will be described later, are read; finally the number of marker particles per cell and their initial distribution are specified.

INITIALIZE CELL FLAGS, gives each cell a flag indicating that it is either a boundary wall cell, a full cell, a surface cell or an empty cell. It is based on the information given in the **READ INPUT DATA BLOCK**.

REFLAGGING is a procedure which can be performed either before or after each time cycle. It gives appropriate flags to the mesh cells based on the newly calculated particle positions.

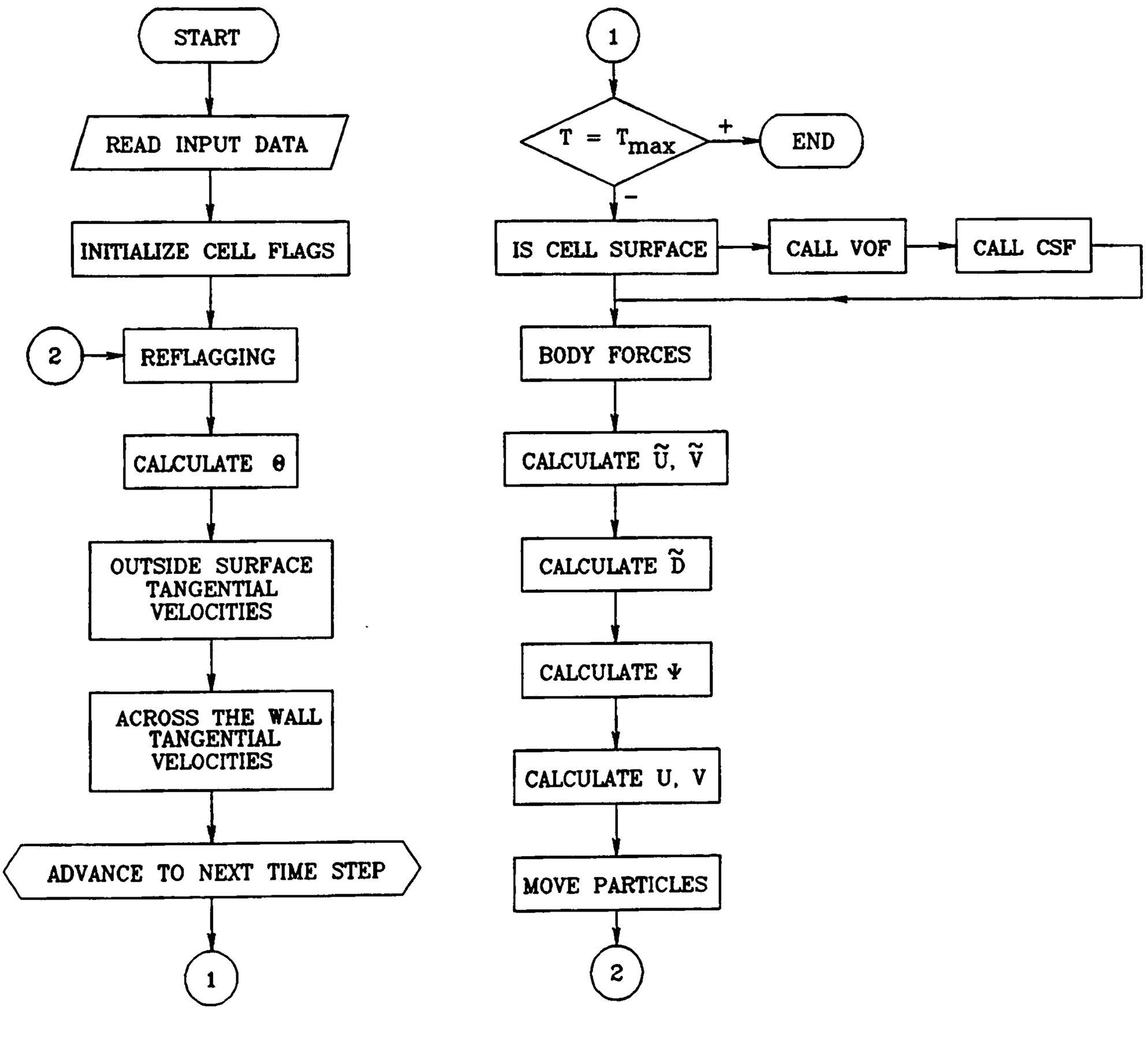

Figure 2.22 Flow diagram of the computational cycle

θ CALCULATION, calculates the pseudopressure θ, as given by equation (2.39) for surface cells. Surface tension stress, however, is not included here, because the CSF model expresses the surface force as a volume force, which is added to the acceleration

terms for each surface cell. For full cells θ is simply set to 0.

OUTSIDE SURFACE TANGENTIAL VELOCITIES determines the values of the tangential velocities in the cells just outside surface cells, that must satisfy the tangential stress condition given by equation (2.37).

ACROSS THE WALL TANGENTIAL VELOCITIES sets the velocities for cells just outside the computational domain appropriate for no- or free- slip conditions, as discussed in Section 2.5.3.

ADVANCE TO NEXT TIME STEP monitors the time marching loop and stops the computation if the maximum time span, or number or time steps, is exceeded. All cells are then checked and the subroutines **VOF**, which determines the value of the F function and **CSF** for the calculation of volume force sources due to surface tension, as discussed in Section 2.5.6, are called for the surface cells.

BODY FORCES, this block determines the body forces acting on each cell including gravity, acceleration due to the forced vibration caused by the Scotch yoke mechanism and the volume force due to surface tension.

CALCULATE $\tilde{u}$ $\tilde{v}$ computes the tilde velocities using the finite difference expressions as given in Appendix C, equations (C.2) and (C.3), and the forces given by previous step.

CALCULATE D calculates the value of D using the expression given in Appendix C, equation (C.1), for the values of $\tilde{u}$ and $\tilde{v}$. This is needed in the following steps for the calculation of corrected velocities.

CALCULATE Ψ, is performed for full cells only. First, Ψ in every surface cell is put equal to 0. Second, the Ψ calculation for full cells is performed through an iterative process. The last field of Ψ's from the previous cycle is used as the first guess for the current cycle. Across the wall values of Ψ are taken according to equation (2.43) to ensure an unchanged normal velocity at the wall. The iteration proceeds from left to right by rows. The equation, resulting from equation (2.42), for the new value of Ψ is:

$$\psi_{i,j}^{n+1} = \frac{(1+\alpha)}{\left(\frac{2}{\delta r^2}+\frac{2}{\delta z^2}\right)}\left[-\tilde{D}_{i,j}+\frac{r_{i+1/2}\psi_{i+1,j}^{n}+r_{i-1/2}\psi_{i-1,j}^{n+1}}{r_i \delta r^2}+\frac{\psi_{i,j+1}^{n}+\psi_{i,j-1}^{n+1}}{\delta z^2}\right] - \alpha\psi_{i,j}^{n} \quad \textbf{(2.63)}$$

where α is an over-relaxation parameter ranging between 0 and 1. The iteration is

considered to have converged when

$$\left| \frac{|\psi_{ij}^{n+1}| - |\psi_{ij}^{n}|}{|\psi_{ij}^{n+1}| + |\psi_{ij}^{n}|} \right| < \epsilon \qquad (2.64)$$

where ϵ is the iteration convergence condition given as an user input. The sweeps through the mesh are repeated until equation (2.64) is satisfied for all cells.

CALCULATE u, v determines the final u and v velocities from equations (2.40) and (2.41).

MOVE PARTICLES this block moves cell particles using new velocity weighing scheme described in Appendix E.

The program then returns control to the reflagging block and the whole process repeats.

2.5.8 Results and discussion

The numerical method described in the above sections has been applied to investigate the behaviour of interfacial surface waves induced by vertical sinusoidal motion. A number of numerical experiments were carried out to investigate the influence of liquid properties, the nature of the forcing oscillations and the initial disturbance on the interfacial surface.

All numerical experiments were run on a two dimensional 25 x 30 uniform cylindrical coordinate mesh of 0.00138 m grid size in both the r and z directions, corresponding to the size of the 69 mm diameter cylinder used in the experimental work described in Section 2.3. The mesh shown in Figure 2.23 represents only half of the cylinder as the problem is axially symmetrical. The axis of symmetry is located on the left hand boundary of the computational mesh. All boundaries were chosen to be of free-slip type, thus exerting no drag upon the fluid.

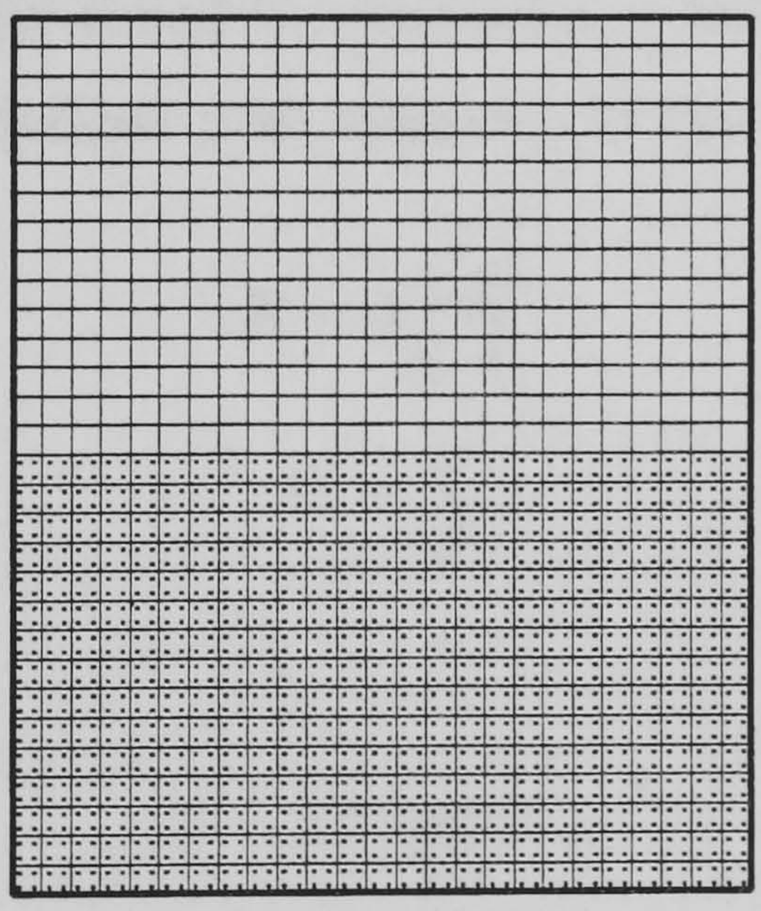

Figure 2.23 *Computational mesh used for the numerical experiments*

Four marker particles per cell, initially uniformly distributed, were used throughout the range of the covered numerical work. Figure 2.23 shows initial distribution of the liquid inside the computational domain. Equations (2.22) and (2.23) indicate that the influence of liquid height on the behaviour of the interfacial wave is expressed via the $\tanh(k_m l)$ term. If only the first and second modes of oscillation are assumed to occur on the interface, then the $\tanh(k_m l)$ values are 0.894 and 0.997 respectively. These values are close enough to 1, and therefore the effects of the liquid base, represented by the lowest

part of the computational domain, on the numerical result may be neglected. The typical timestep used was 0.0001 seconds. Tests were also run with halved timestep and halved mesh size and no significant changes in the results obtained were found. The iteration parameter ϵ used as a convergence criterion defined, by equation (2.64), was set to 2.10^{-4} for all problems investigated.

The calculations were started by applying a pressure pulse in the form of a sinusoidal wave on the surface cells for the first time cycle. In the surface cells, the pseudopressure is equal to the true pressure. The term representing the pulse which is added to the surface pressure Φ, denoted in equation (2.39) by Φ(applied) is:

$$\Phi(applied) = \frac{B\ \cos(XCr)}{\delta t} \tag{2.65}$$

where X is a parameter chosen to be 1 for a half sinusoidal wave, 2 for a full sinusoidal wave, and so on. Only the two cases of X equal to 1 and X equal to 2 were investigated in the present work. Parameters B and C, obtained as a result of linear analysis [29] [51] for a rectangular vessel, are defined with reference to Figure 2.24 as follows:

$$B = h\sqrt{\frac{gl}{\xi}} \tag{2.66}$$

$$C = \frac{\pi}{R} \tag{2.67}$$

where

$$\xi = Cl\ \tanh(Cl) \tag{2.68}$$

Equations (2.66)-(2.68), even though derived for a rectangular geometry, provided a good means of commencing the calculations. The influence of the magnitude of this initial disturbance, specified in terms of the wave amplitude h, on the stability of the interface was also a subject of this investigation.

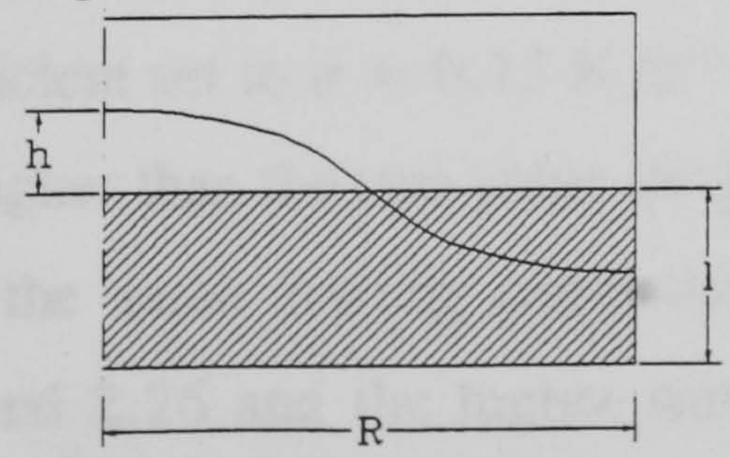

Figure 2.24 *Pressure pulse wave applied on the free surface*

The numerical experiments were performed for water and glycerol. These two liquids have significantly different viscosity, as shown in Appendix A. The analytical work presented in Section 2.4 neglects the effects of viscosity but shows the influence of surface tension on the oscillation of free surface waves. The analysis of Kumar and Tuckerman in [16], based on a non-linear analysis of the problem, describes the influence of viscosity on the frequency of the interfacial wave oscillations. The present numerical analysis allows both surface tension and viscosity effects to be included and thus enables a comparison between the computational and analytical results, and the findings will be discussed later. Three groups of numerical tests were therefore run. The first group was a set of computations where surface tension phenomena were not taken into account. In the second group the true surface tension values of the two liquids were considered and the CSF model was employed to simulate the related phenomenon. Finally a third group of tests was run assuming a higher value of surface tension. The amplitude of the forcing oscillations from the Scotch yoke mechanism was set to be 70 mm for most of the tests. This value was chosen because it is approximately in the middle of the range of amplitudes used in the experimental work. However, some tests were also run for an amplitude of the forcing oscillations equal to 30 mm.

Figure 2.25 shows a time sequence of the interfacial position for glycerol but neglecting surface tension. The surface has been initially disturbed by a half sinusoidal pulse, where h in equation (2.66) was chosen to be 20 mm, the amplitude and the frequency of the forcing oscillations were 70 mm and 3 Hz respectively. It can be seen that the wave created on the interface did not become unstable in this particular case. The results for the same conditions but including the surface tension phenomenon are shown in Figure 2.26. The surface tension coefficient of glycerol was taken as $\sigma = 0.030$ N m^{-1}. Very little difference can be observed between the marker particle positions in Figures 2.25 and 2.26. To investigate fully the significance of surface tension, a set of experiments with the surface tension coefficient set to $\sigma = 0.15$ N m^{-1} was also run. This value of the surface tension is five times higher than the true value for glycerol. Figure 2.27 shows the time sequence obtained for the same forcing oscillation conditions as for the cases considered in Figures 2.25 and 2.26 and the higher surface tension coefficient. Local ripple occurrences, caused by different curvature of the interface, can be seen.

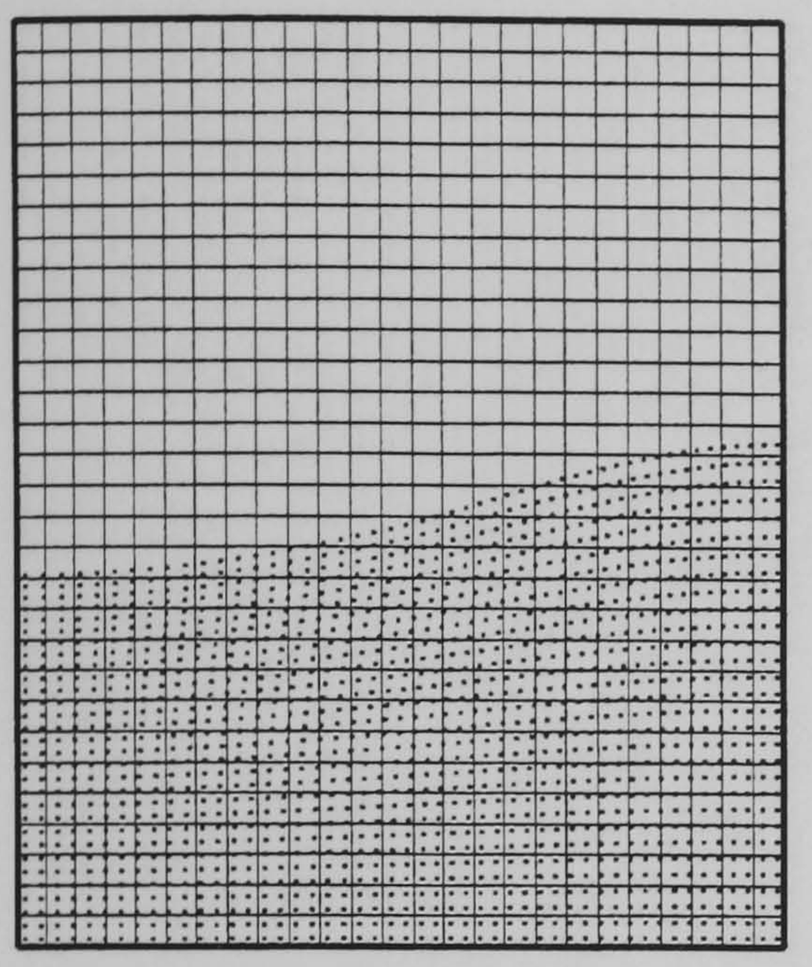

t = 0.005 s

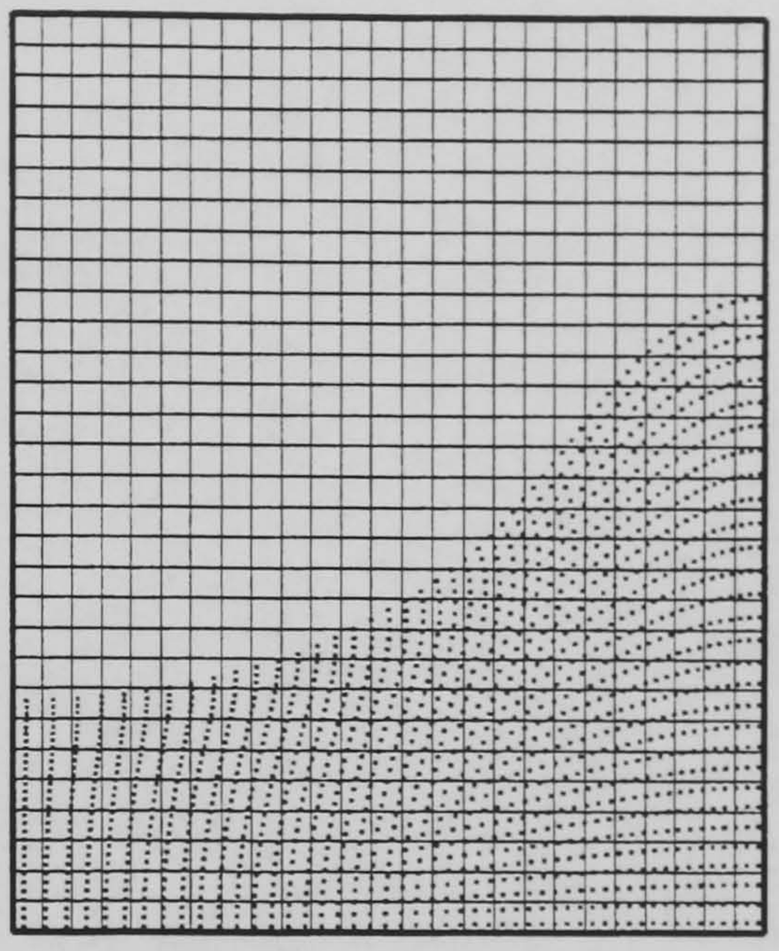

t = 0.03 s

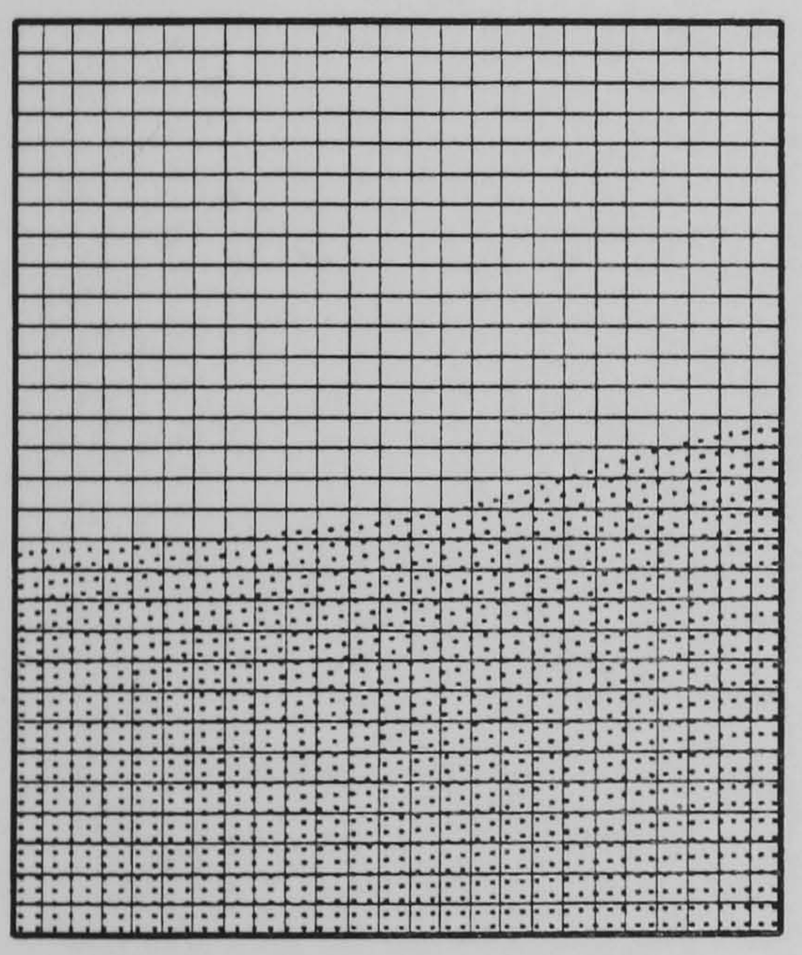

t = 0.06 s

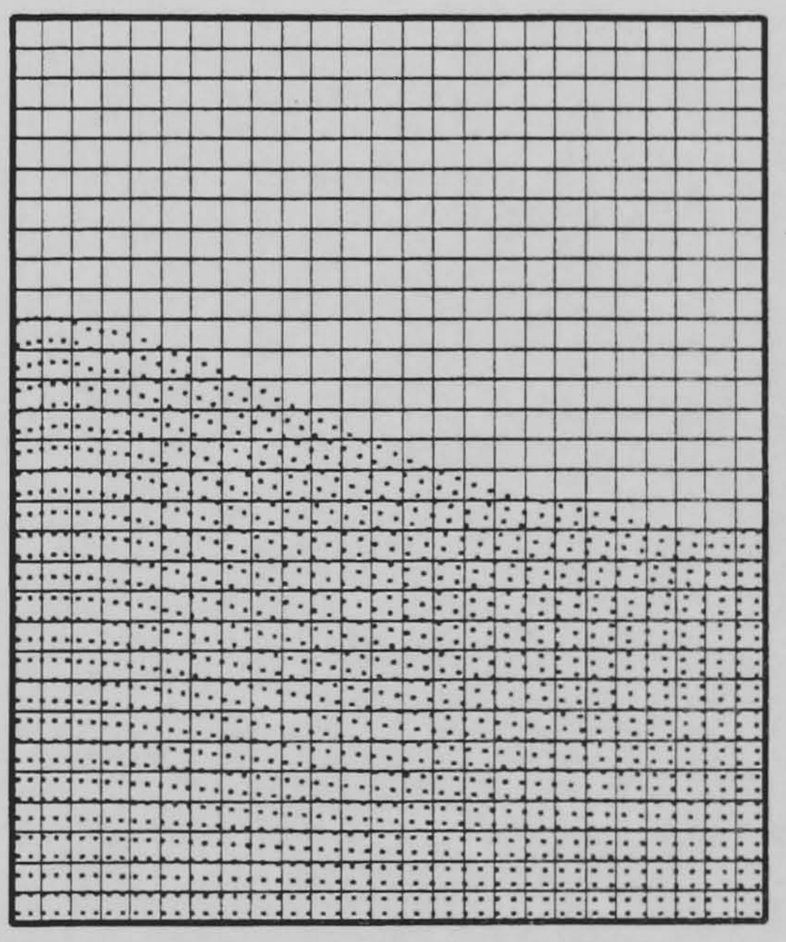

t = 0.09 s

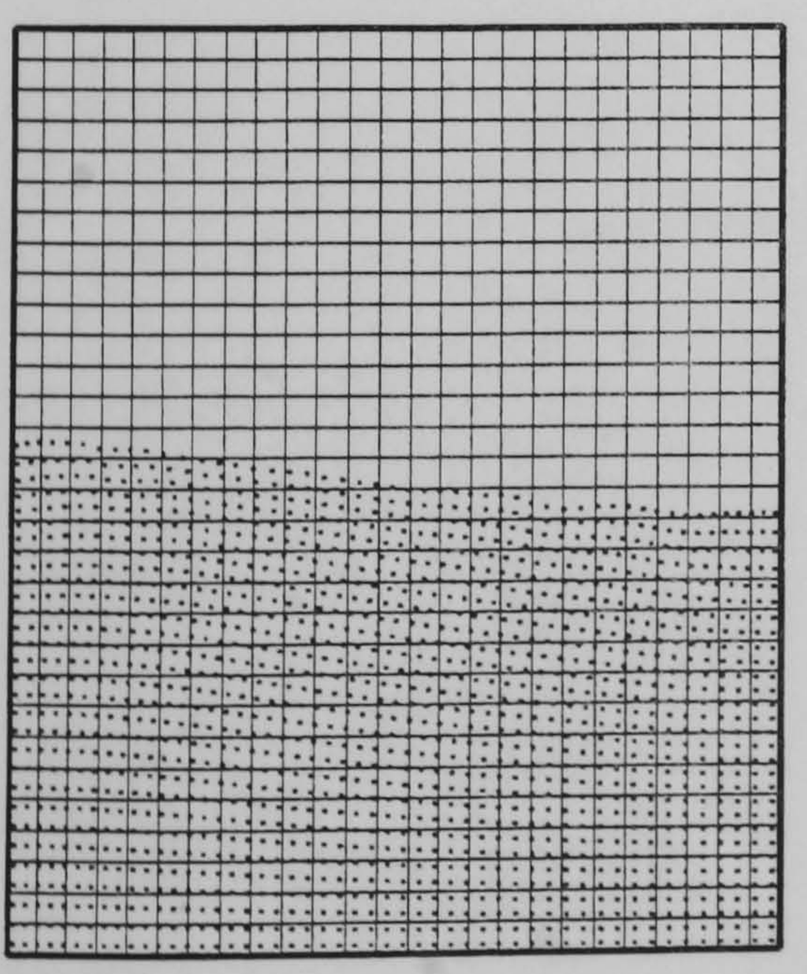

t = 0.12 s

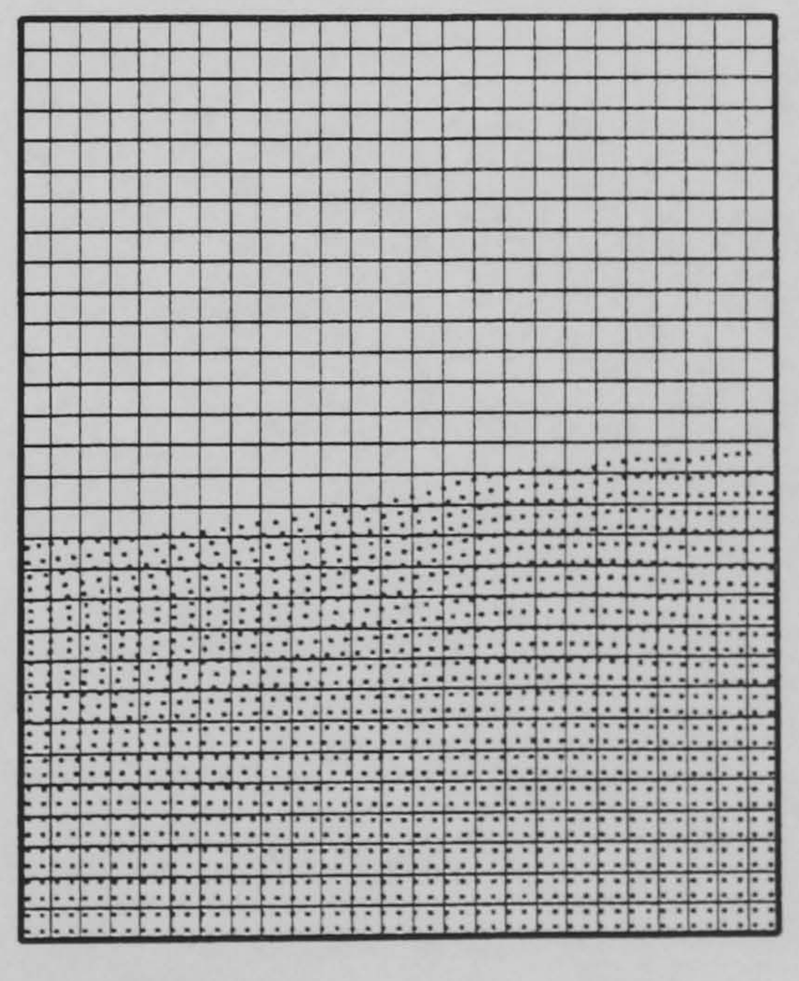

t = 0.15 s

Figure 2.25 *Glycerol, surface tension neglected, initial pulse amplitude h = 20 mm Forcing oscillation amplitude A = 70 mm, frequency 3 Hz*

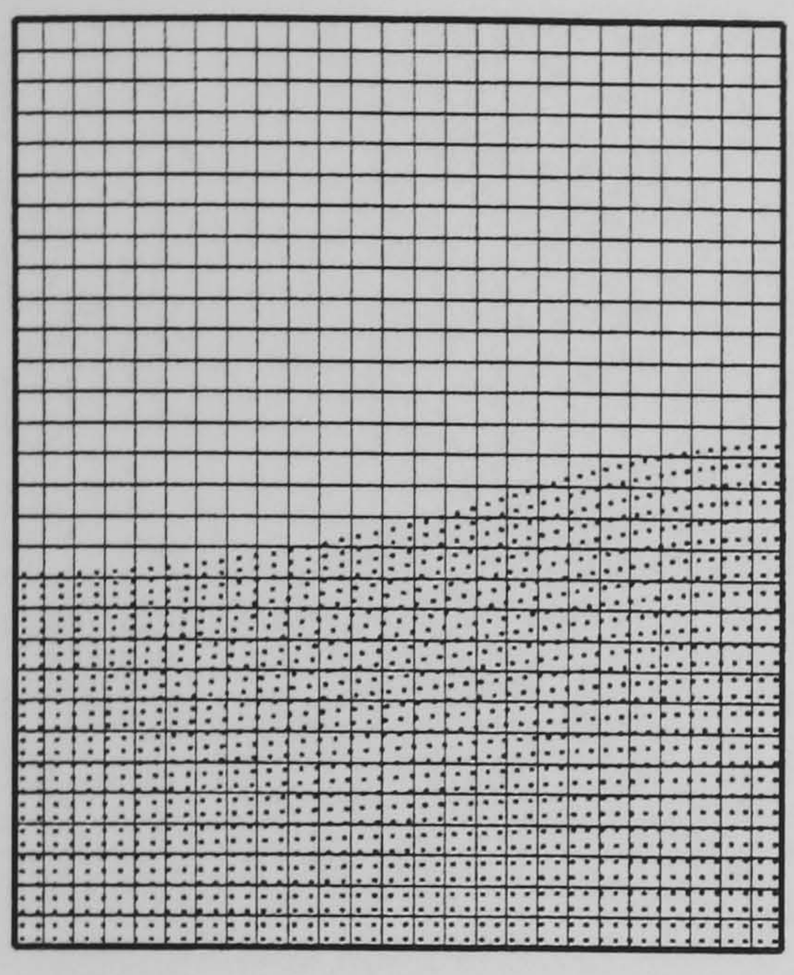

t = 0.005 s

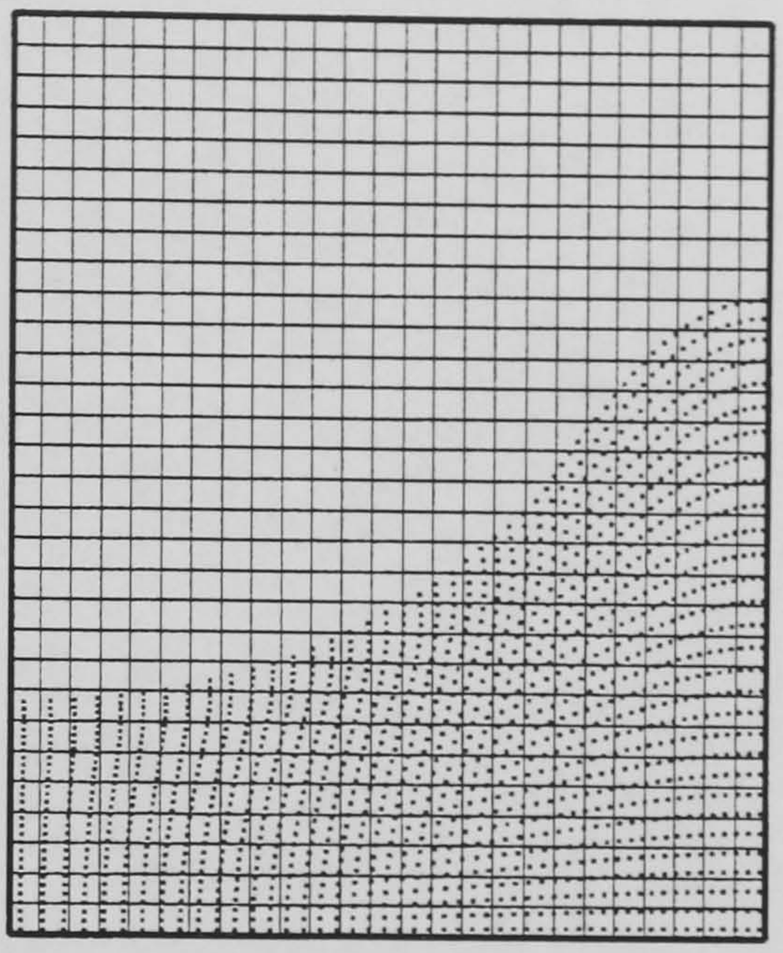

t = 0.03 s

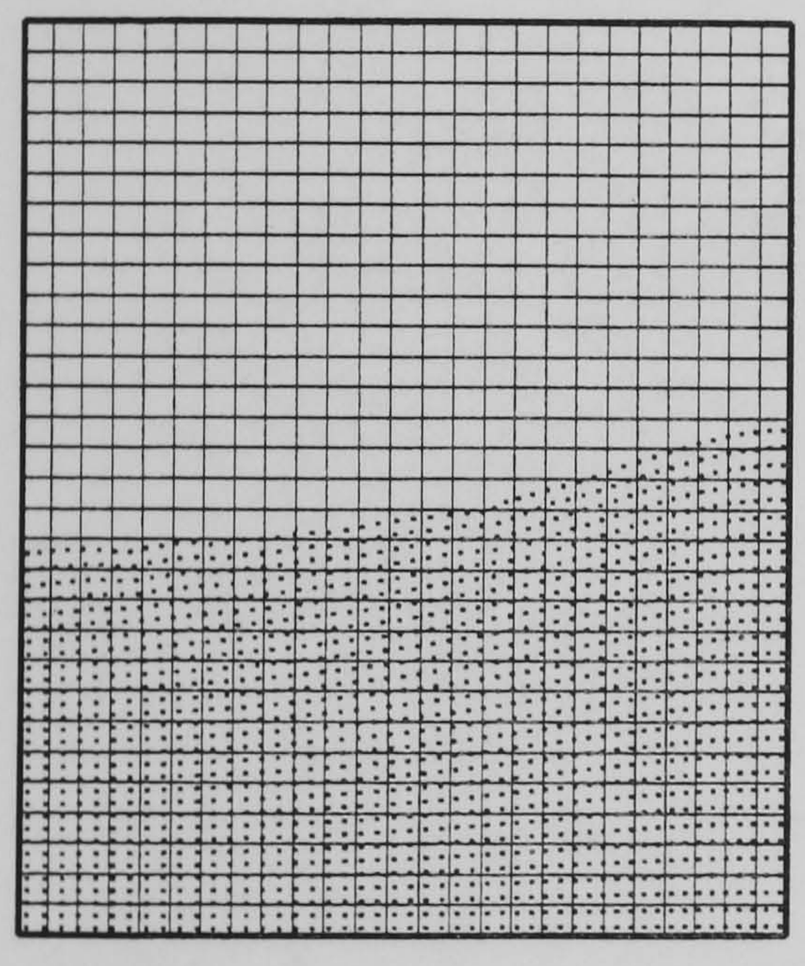

t = 0.06 s

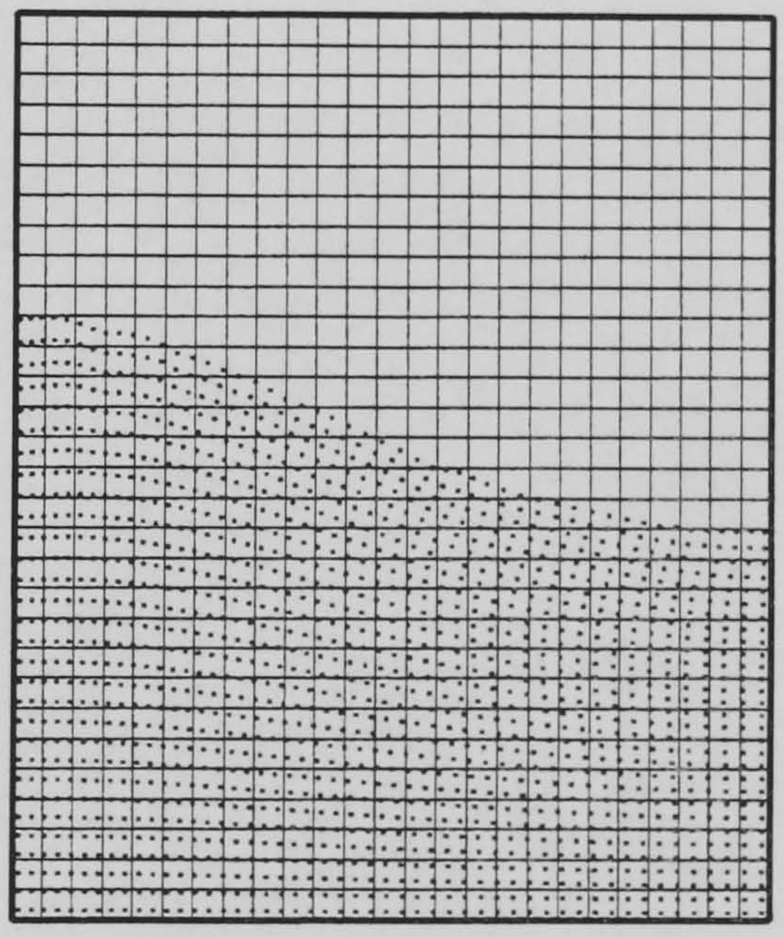

t = 0.09 s

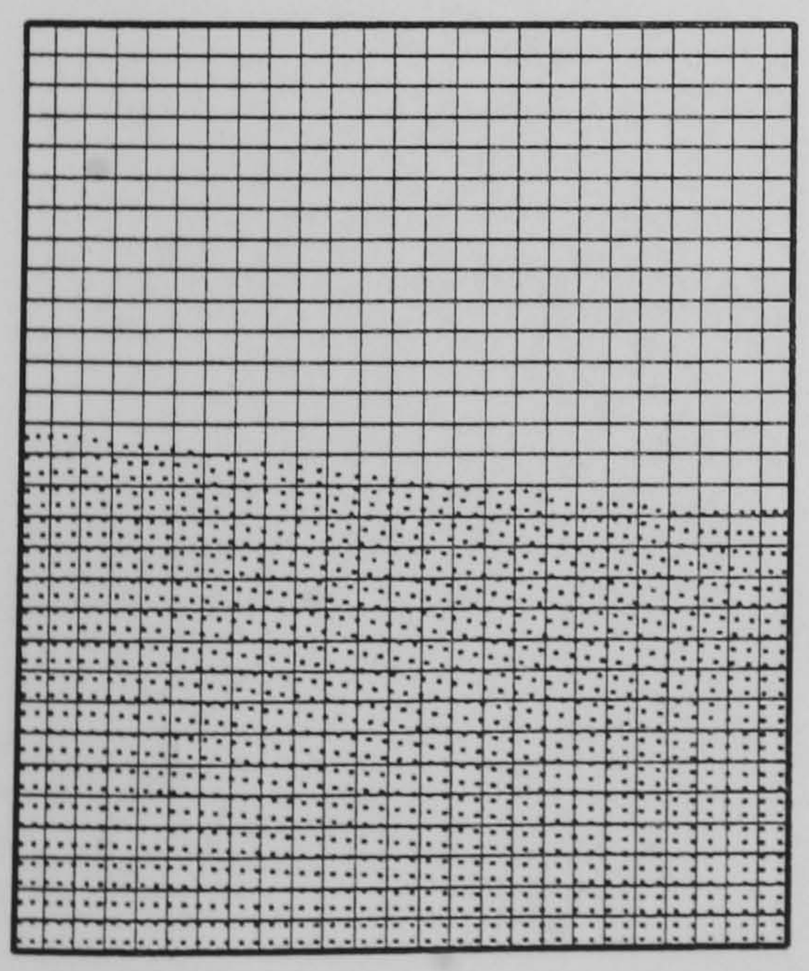

t = 0.12 s

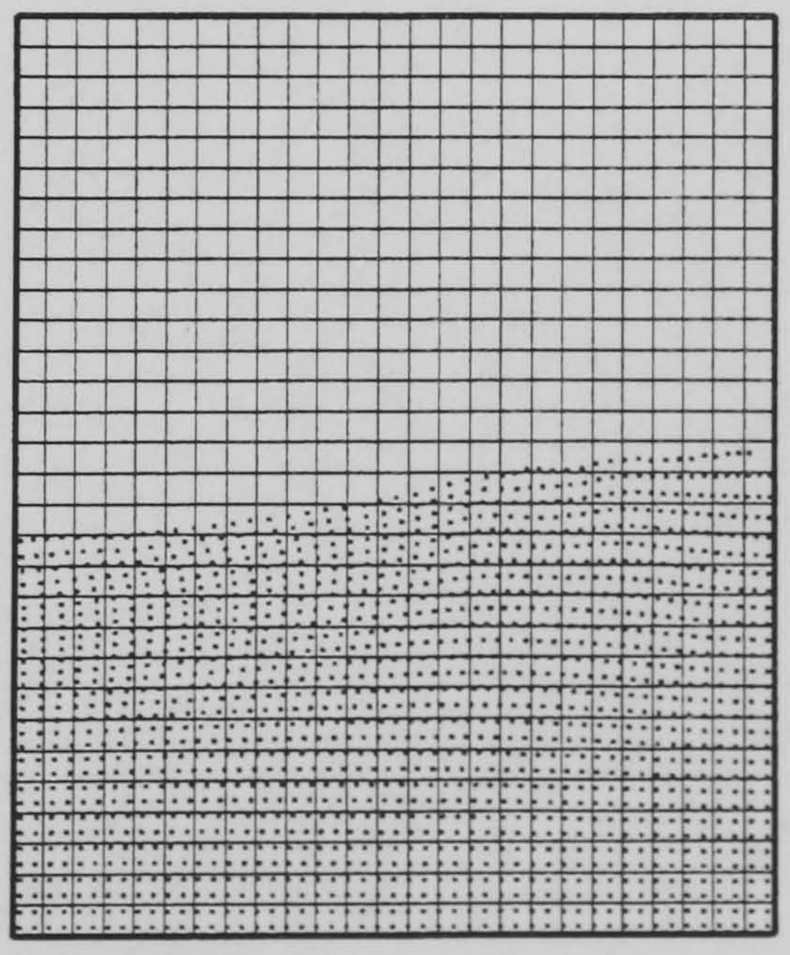

t = 0.15 s

Figure 2.26 *Glycerol, surface tension coefficient $\sigma = 0.030\ Nm^{-1}$, $h = 20$ mm*
Forcing oscillation amplitude $A = 70$ mm, frequency 3 Hz

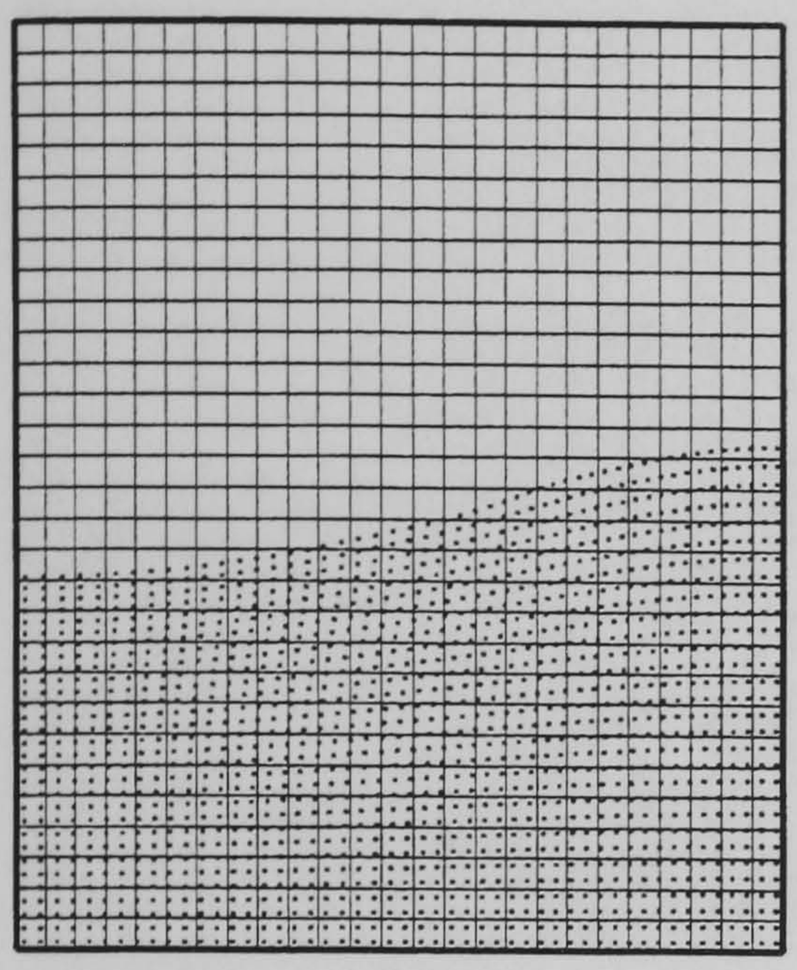

t = 0.005 s

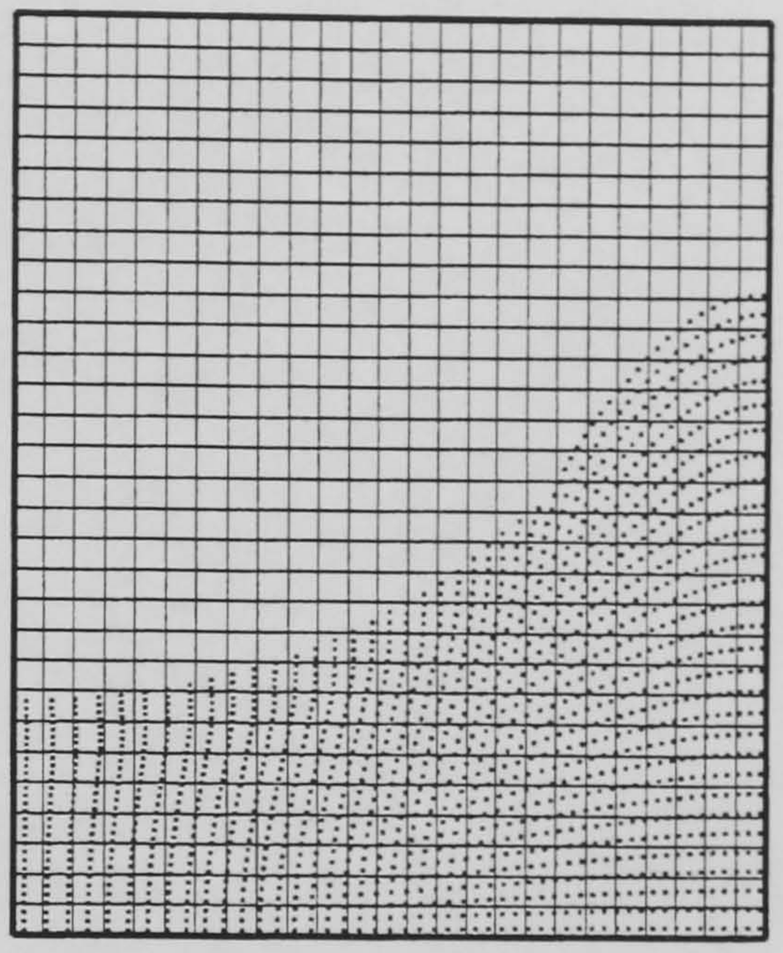

t = 0.03 s

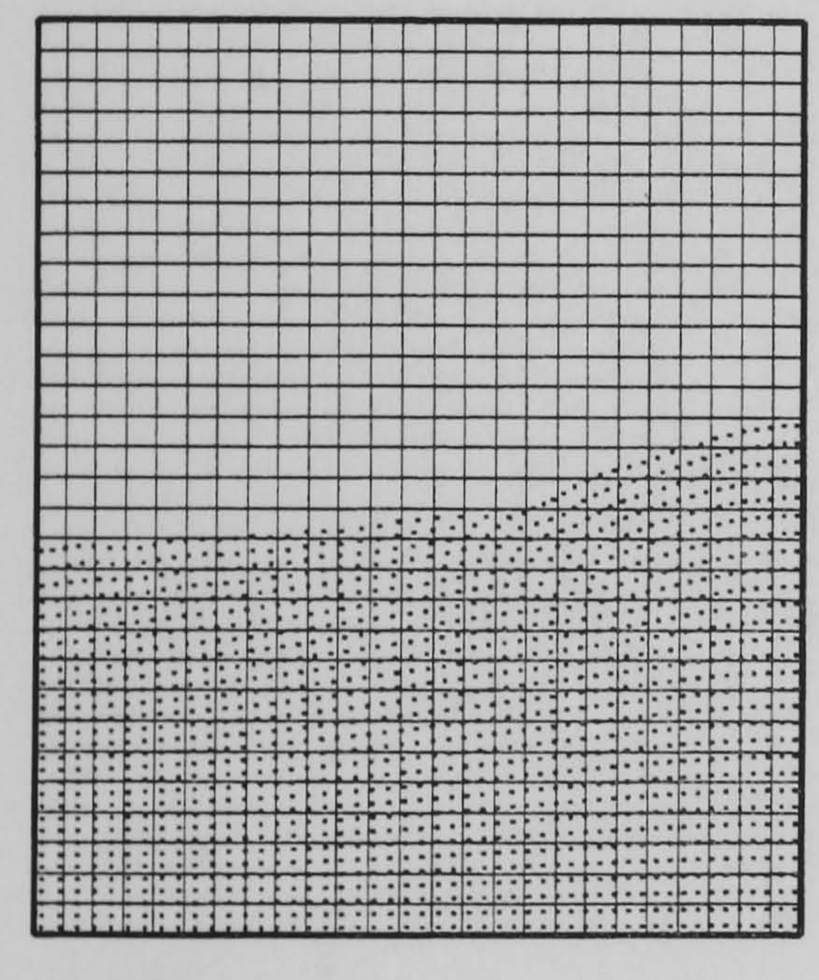

t = 0.06 s

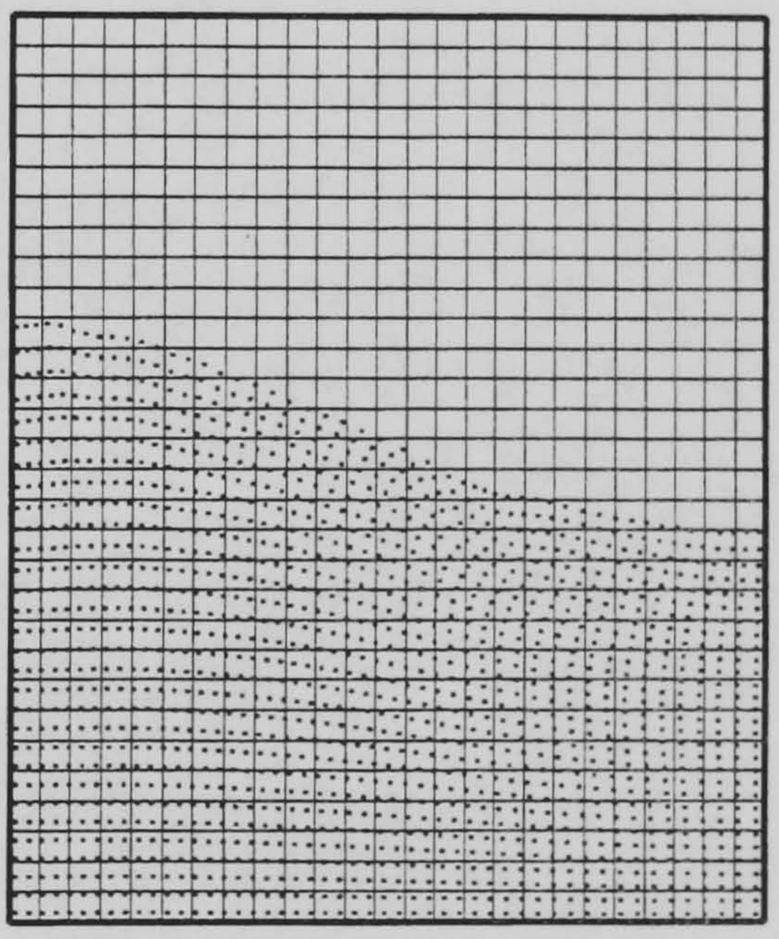

t = 0.09 s

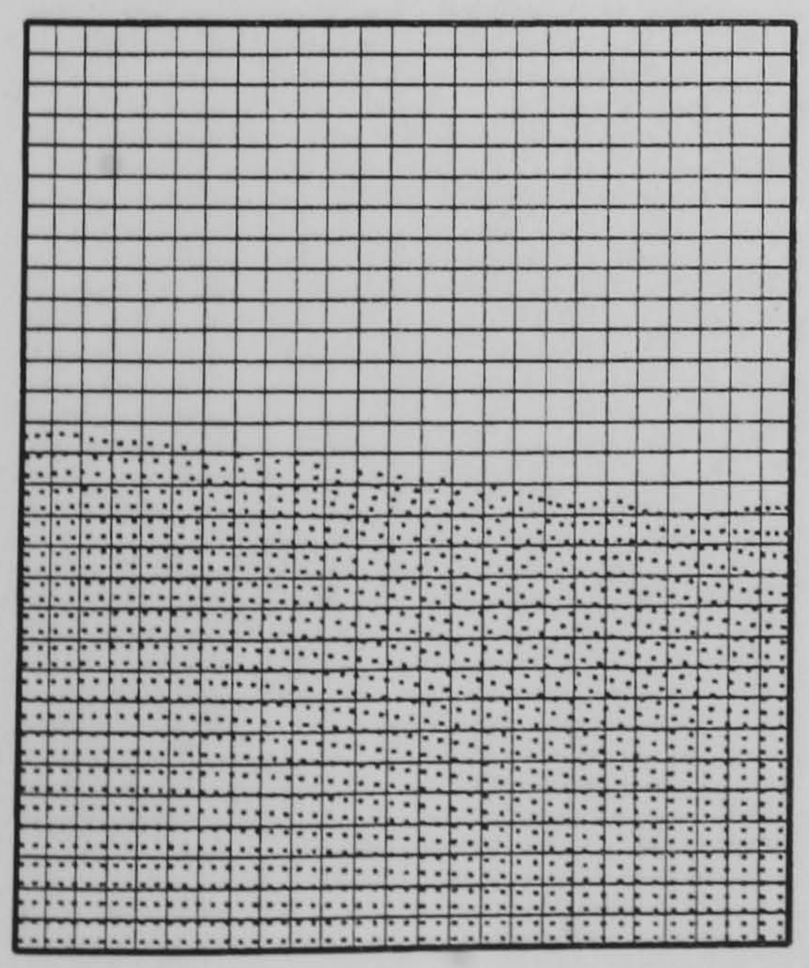

t = 0.12 s

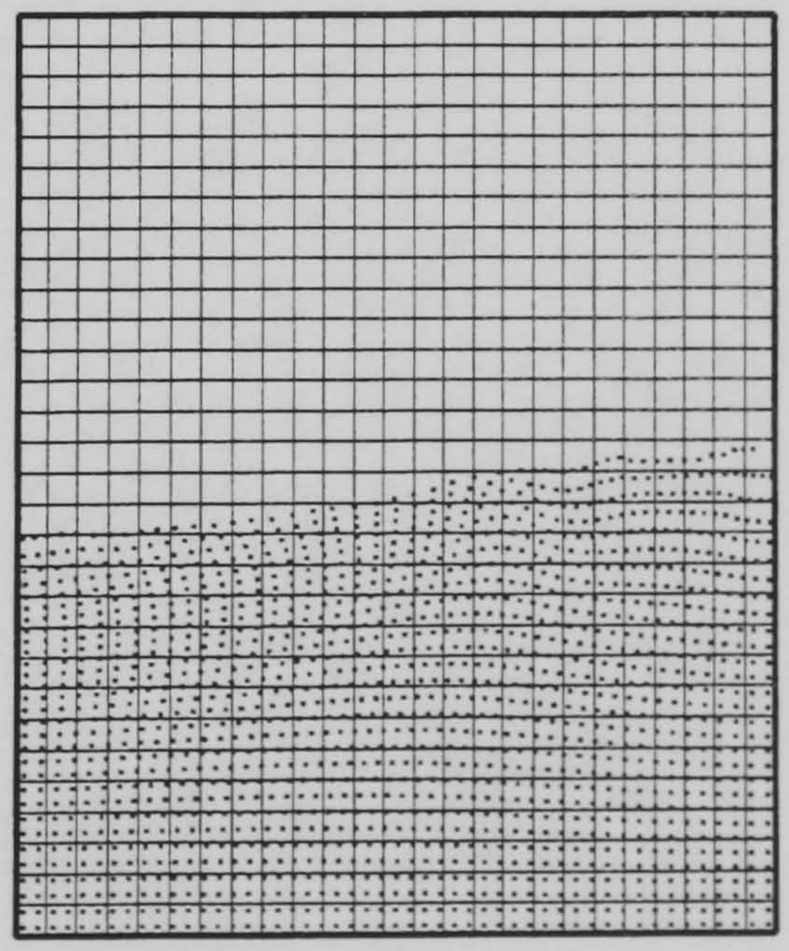

t = 0.15 s

Figure 2.27 *Glycerol, high surface tension coefficient $\sigma = 0.15\ Nm^{-1}$, initial pulse amplitude h = 20 mm. Forcing oscillation amplitude A = 70 mm, frequency 3 Hz*

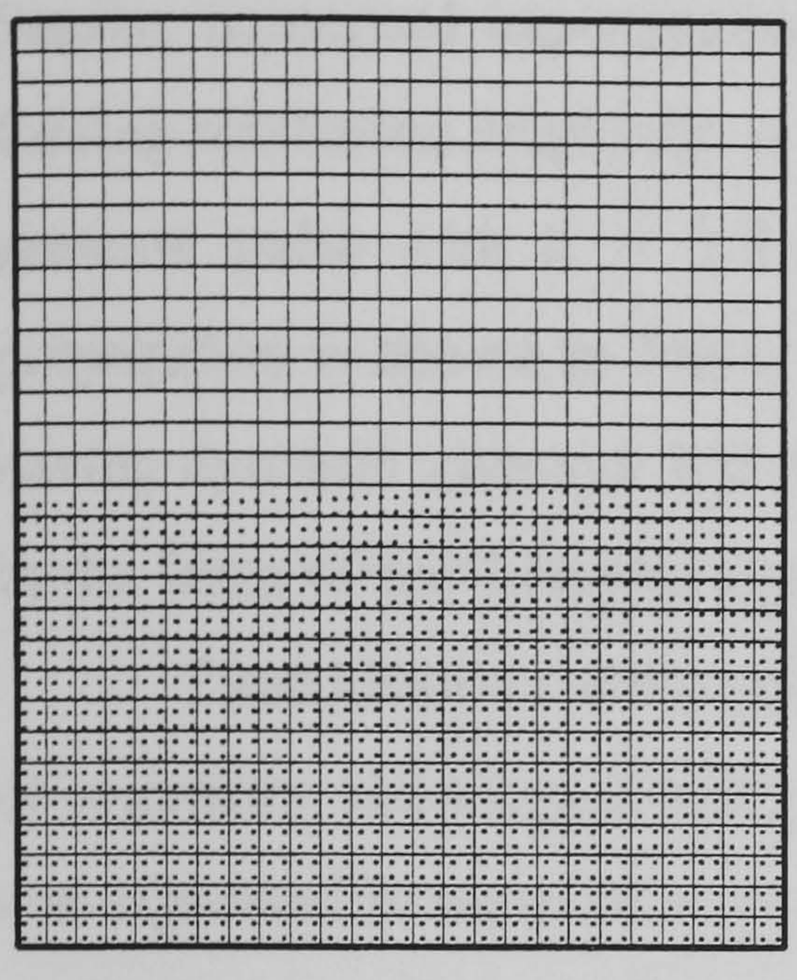

t = 0.005 s

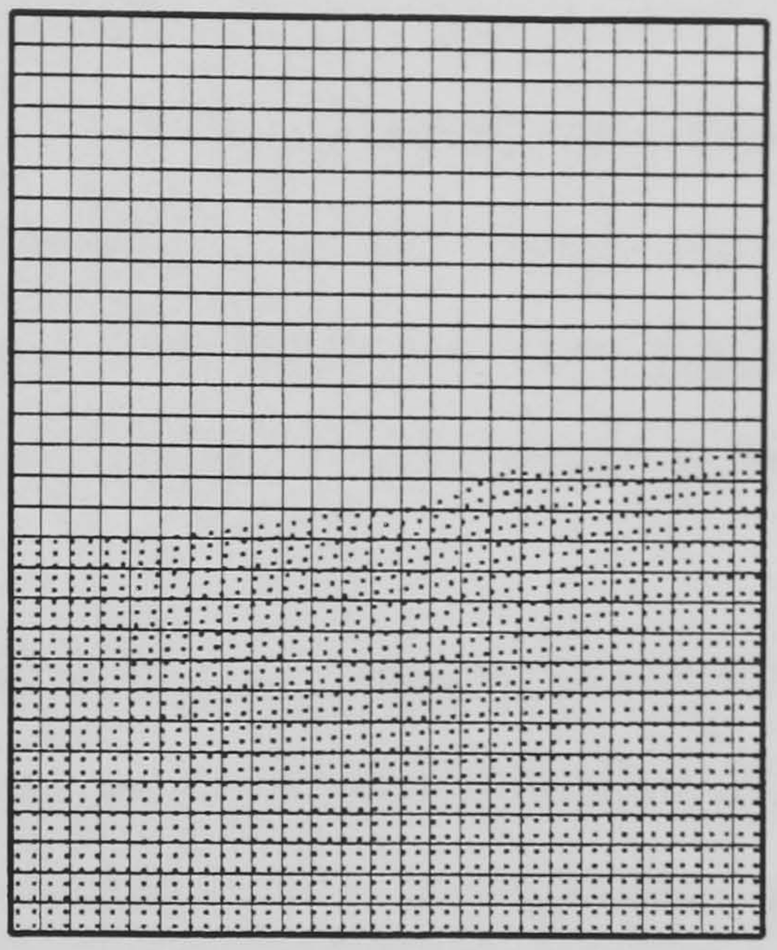

t = 0.03 s

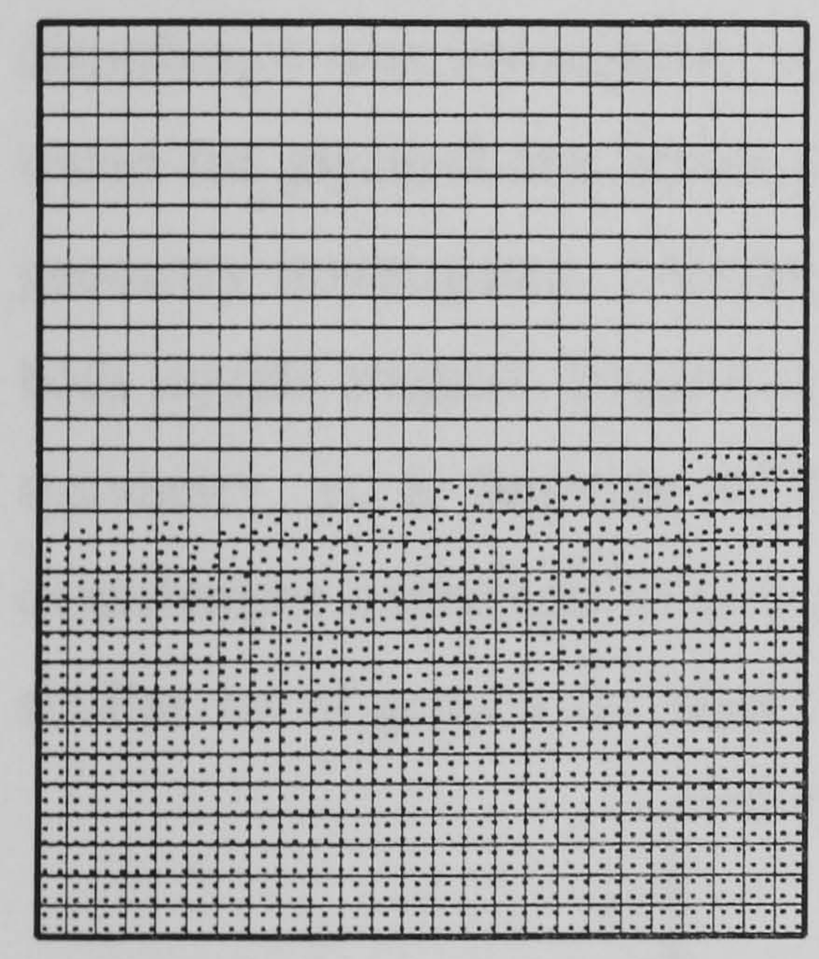

t = 0.06 s

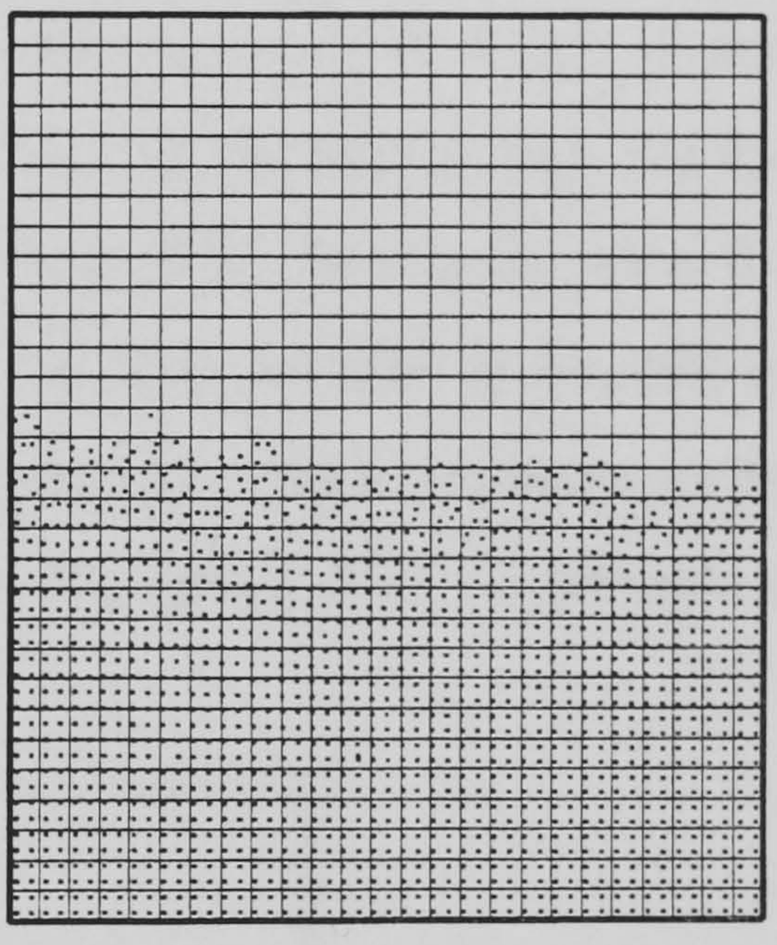

t = 0.09 s

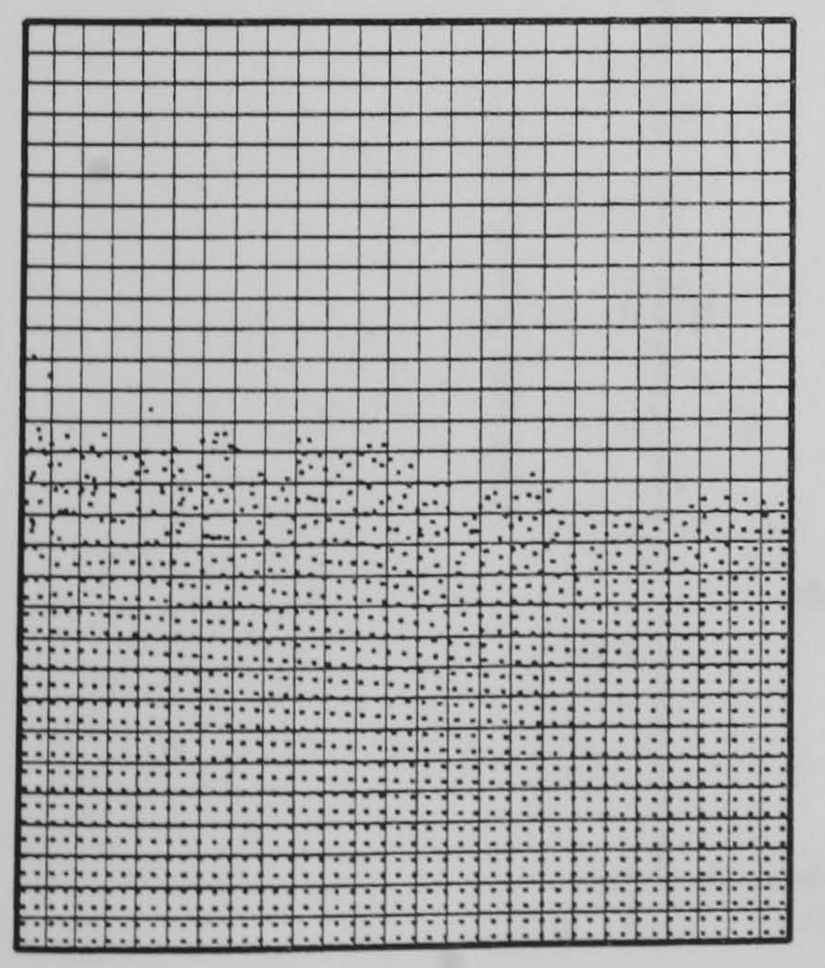

t = 0.12 s

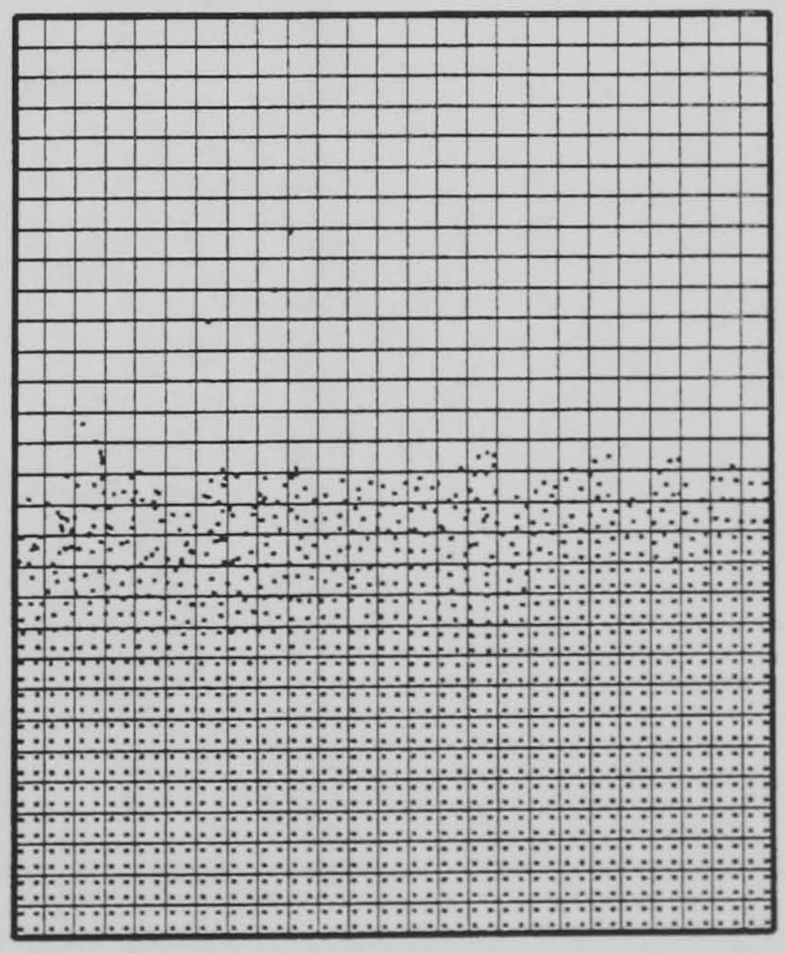

t = 0.15 s

Figure 2.28 *Water, surface tension neglected, initial pulse amplitude h = 2.5 mm*
Forcing oscillation amplitude A = 70 mm, frequency 2 Hz

Similar numerical experiments were run for water neglecting surface tension, with a forcing oscillation amplitude A = 70 mm and a frequency f = 2 Hz. An initial sinusoidal pressure pulse with h = 2.5 mm was used. The time sequence of the surface wave propagation is shown in Figure 2.28. The damping effect of viscosity is low now, water having dynamic viscosity 830 times lower than glycerol, and higher modes of oscillation in the form of local ripples can be observed.

Time histories of the predicted interfacial wave displacements, measured at the axis of symmetry and taken directly from graphs similar to those shows in Figures 2.25-2.28, and expressed in terms of mesh units are discussed next. The accuracy of the displacement readings is to about 25 % of the mesh grid size. The influence of initial pressure pulse disturbance was investigated for values of h = 5, 10, 20, 30 mm and h = 1, 2.5, 5 mm tested for glycerol and water respectively. It was found that surface tension has, for the geometry investigated, only negligible effect on the behaviour of the interfacial wave for both liquids studied. Figures 2.29 - 2.32 show plots of wave displacement at the axis of symmetry as a function of time for glycerol with different initial pressure pulse disturbances expressed in terms of initial wave amplitude, h. Figures 2.33 - 2.35 show a similar set of graphs for water.

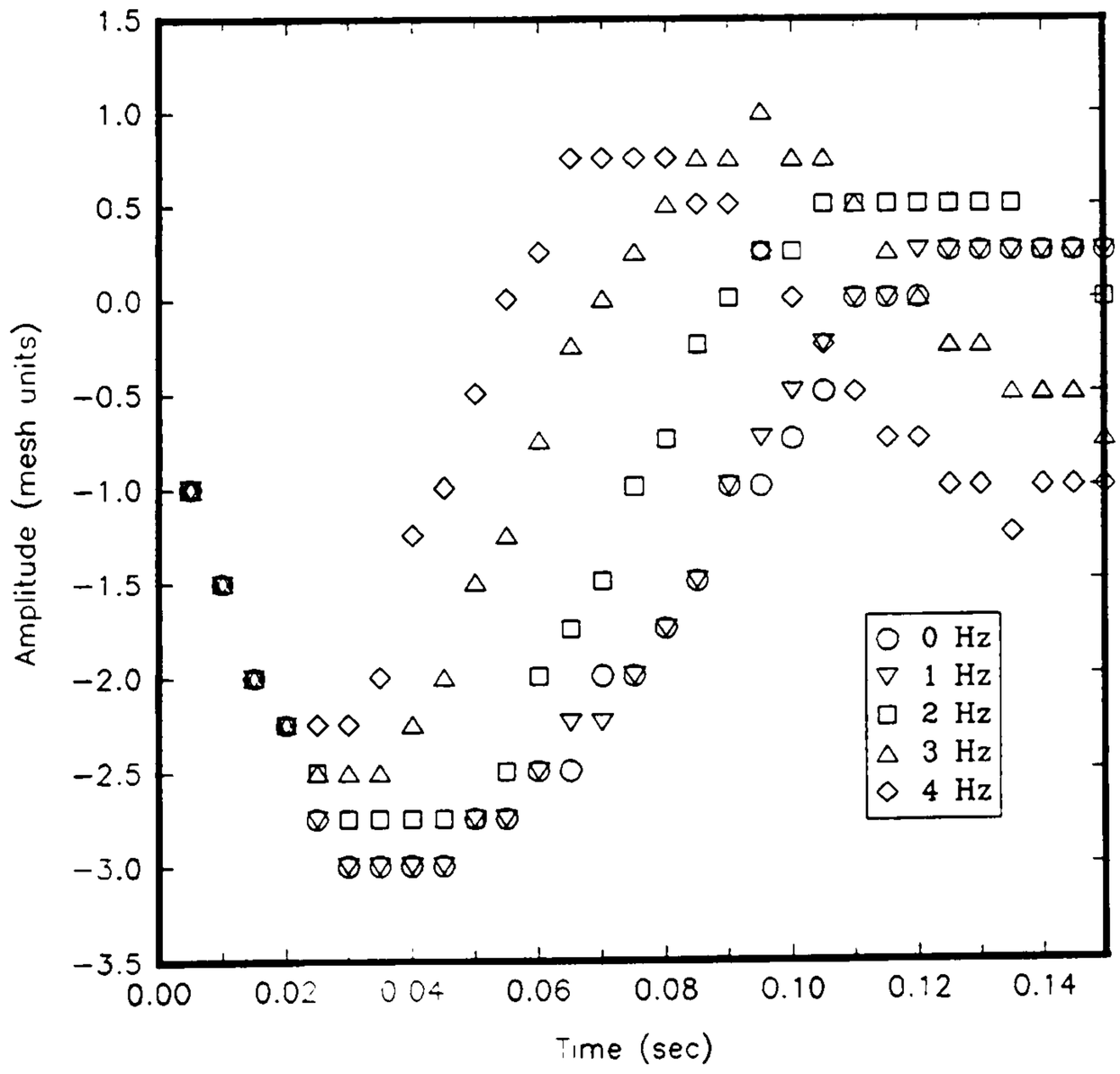

Figure 2.29 *Wave displacement measured on the axis of symmetry with forcing oscillation frequency as a parameter, glycerol, initial wave amplitude h = 5 mm, surface tension neglected, forcing oscillation amplitude A = 70 mm*

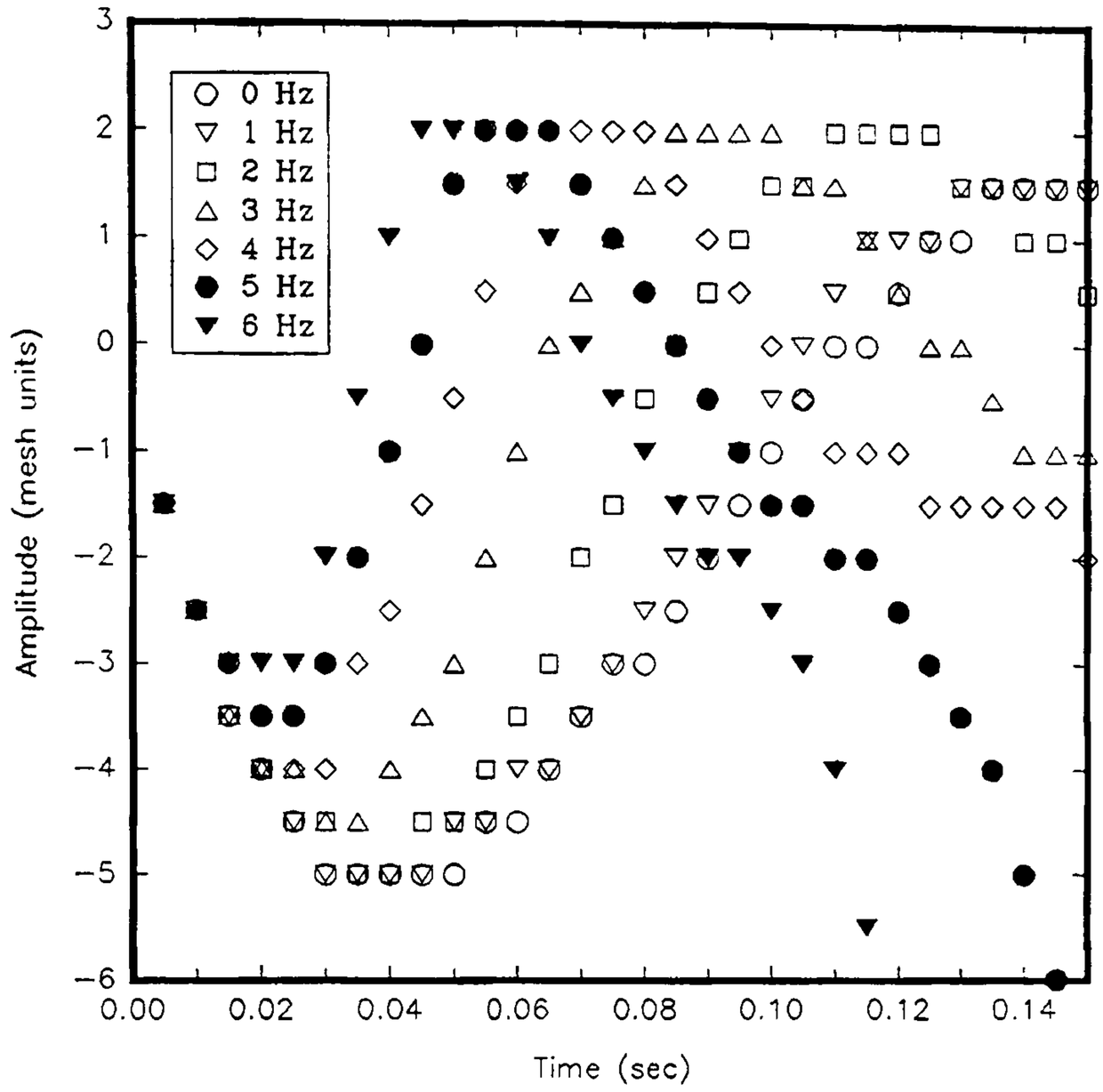

Figure 2.30 *Wave displacement measured on the axis of symmetry with oscillation frequency as a parameter, glycerol, initial wave amplitude h = 10 mm, surface tension neglected, forcing oscillation amplitude A = 70 mm*

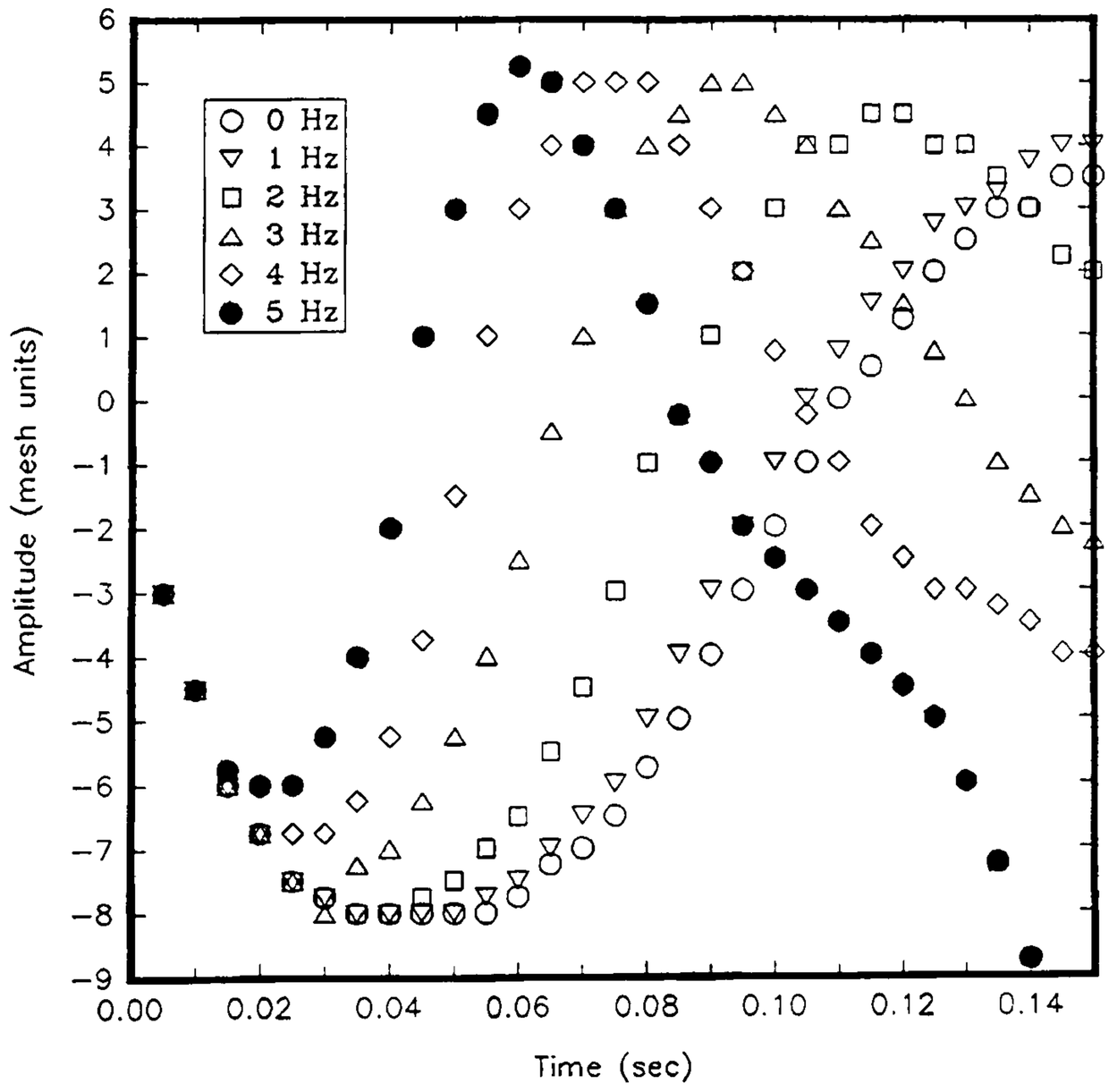

Figure 2.31 *Wave displacement measured on the axis of symmetry with oscillation frequency as a parameter, glycerol, initial wave amplitude h= 20 mm, surface tension neglected, forcing oscillation amplitude A = 70 mm*

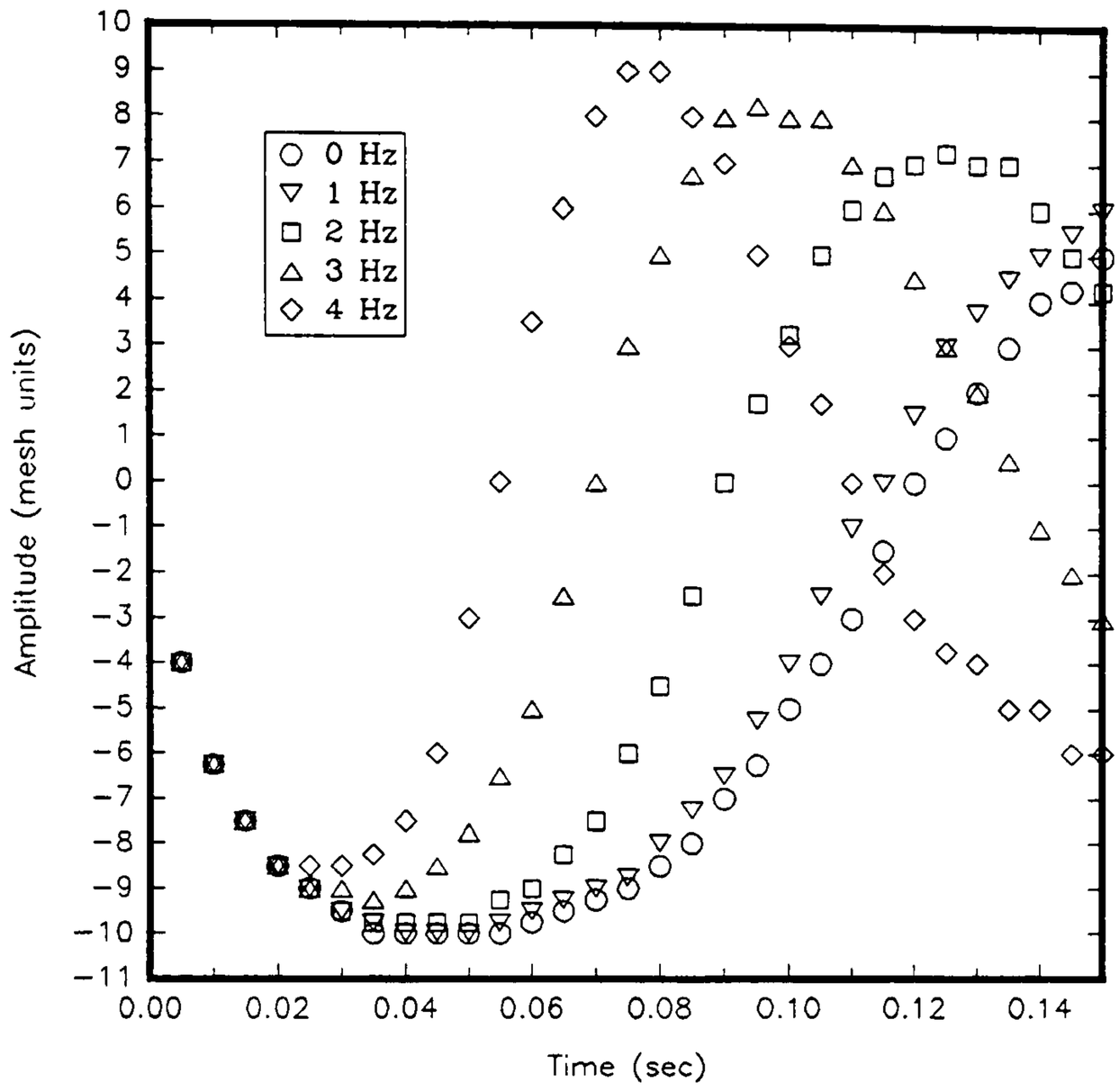

Figure 2.32 *Wave displacement measured on the axis of symmetry with forcing oscillation frequency as a parameter, glycerol, initial wave amplitude h = 30 mm, surface tension neglected, forcing oscillation amplitude A = 70 mm*

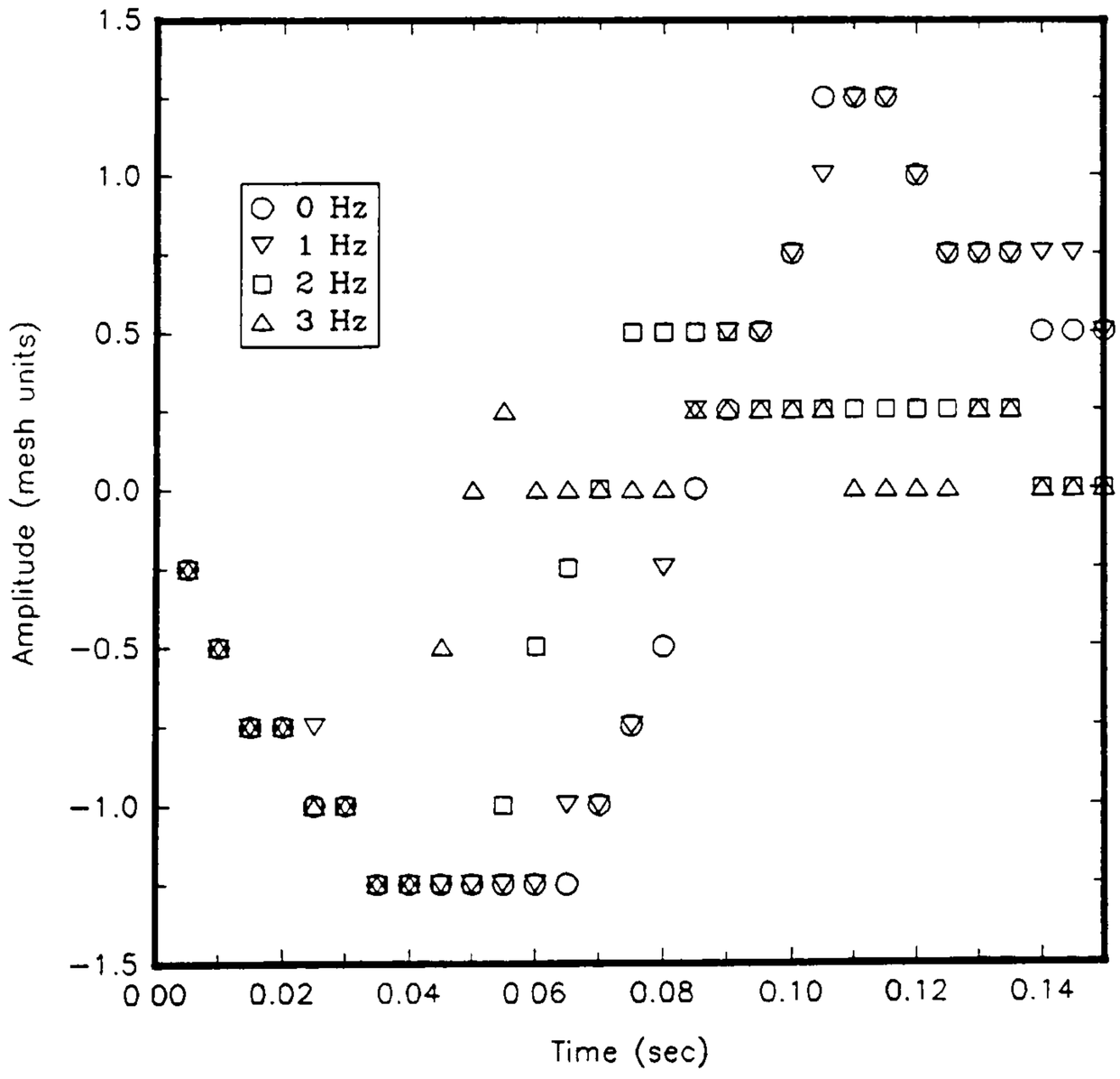

Figure 2.33 *Wave displacement measured on the axis of symmetry with forcing oscillation frequency as a parameter, water, initial wave amplitude h = 1 mm, surface tension neglected, forcing oscillation amplitude A = 70 mm*

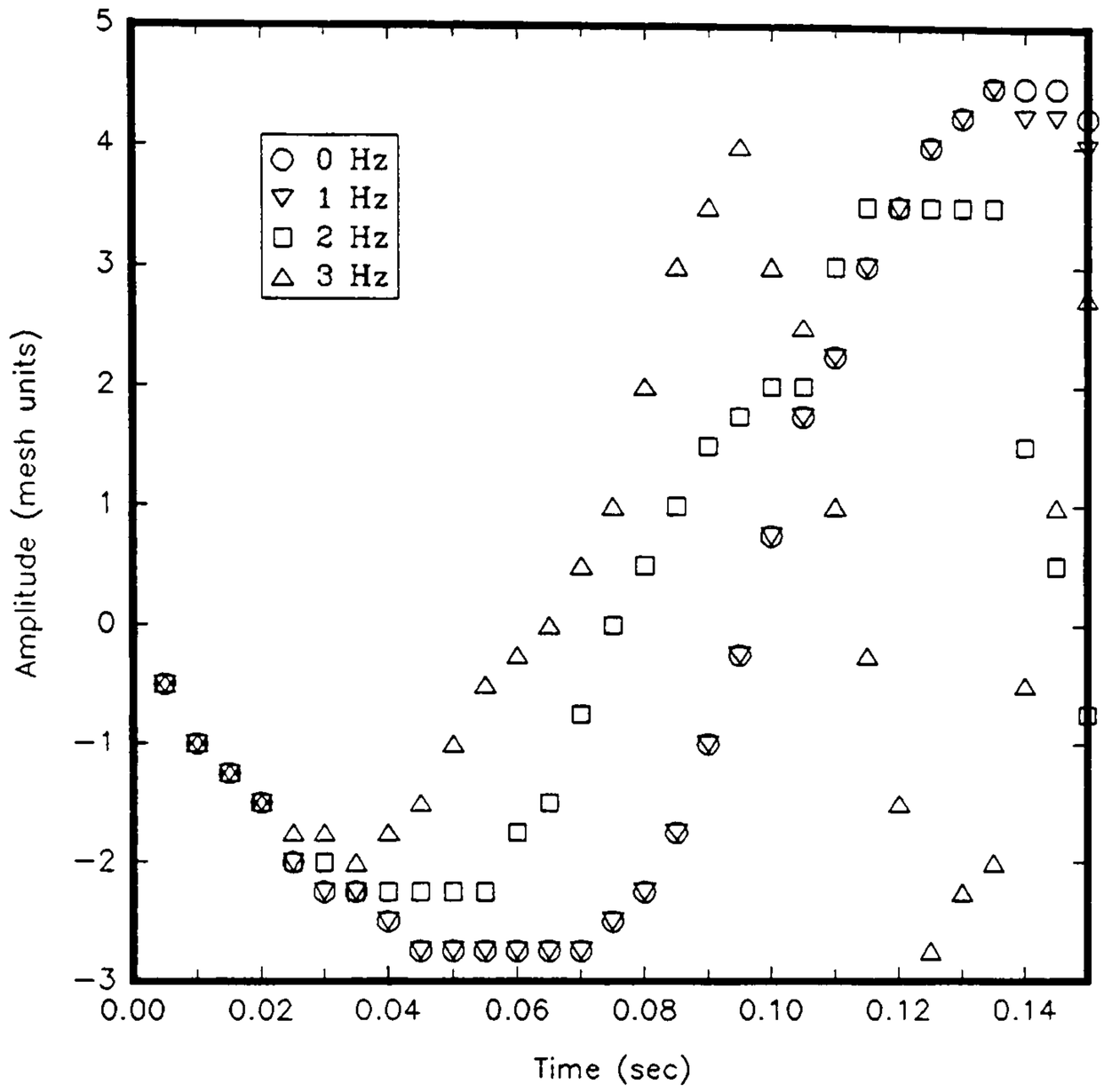

Figure 2.34 *Wave displacement measured on the axis of symmetry with forcing oscillation frequency as a parameter, water, initial wave amplitude h = 2.5 mm, surface tension neglected, forcing oscillation amplitude A = 70 mm*

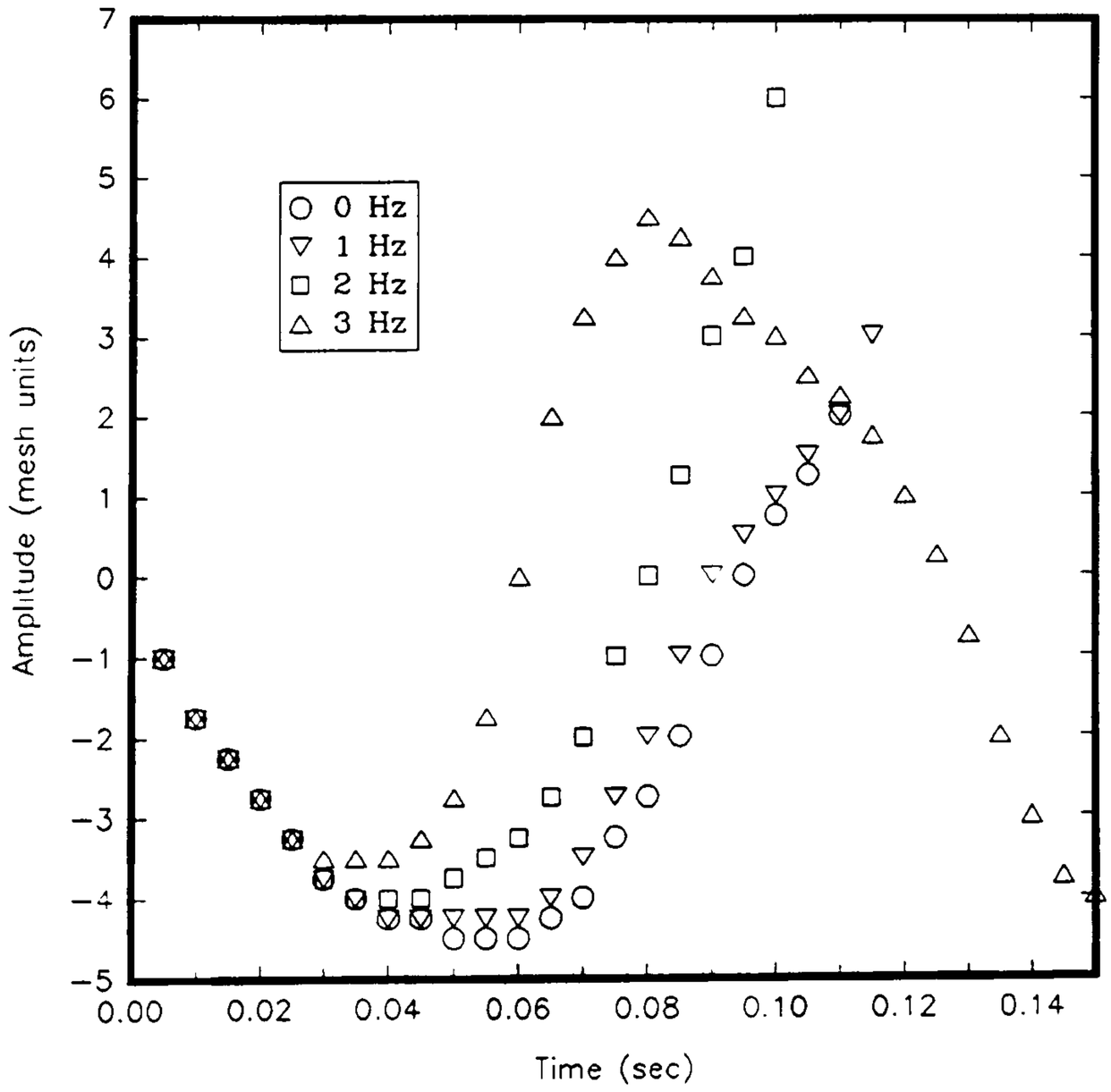

Figure 2.35 *Wave displacement measured on the axis of symmetry with forcing oscillation frequency as a parameter, water, initial wave amplitude h = 5 mm, surface tension neglected, forcing oscillation amplitude A = 70 mm*

The experimental results shown in Figures 2.6 - 2.8 indicate that the critical frequency causing the interfacial wave to grow unstable is, for 70 mm amplitude of forcing oscillations, 2 Hz for water and 4 Hz for glycerol. In the numerical computations exponential wave growth is first observed for glycerol in Figure 2.30, for a forcing oscillation frequency of 5 Hz with an initial disturbance of h = 10 mm. Figures 2.31 and 2.32, for higher values of h, do not seem to indicate that the wave grows unstable for lower forcing frequencies. Figures 2.33 - 2.35 show the results for water with amplitudes of the initial pulse of h = 1, 2.5, 5 mm respectively. Figure 2.33 indicates that for h = 1 mm the wave does not grow unstable for the range of frequencies investigated. For an initial amplitude of the pulse h= 2.5 mm, shown in Figure 2.34, growth of oscillations with time occurs for frequencies higher or equal to 2 Hz. This is in good agreement with the experimental findings. Figure 2.35 indicates that the interfacial wave has already grown unstable for a forcing frequency of 1 Hz. Analytical solution of the problem was based on assumption of small oscillations of the interfacial wave. The numerical solution indicates that the stability of the interface is dependent not only on the forcing oscillations but also on the initial disturbance applied to the surface.

Equation (2.20) can be re-written, assuming that all points on the interface undergo identical oscillations as:

$$\frac{d^2\eta}{dt^2} + \omega_o^2 \left[1 - \frac{k_m A \omega^2 \cos(\omega t)}{\omega_o^2}\right]\eta = 0 \qquad (2.69)$$

where

$$\omega_o^2 = \frac{\sigma}{\rho} k_m^3 + g k_m \qquad (2.70)$$

and ω_o is the angular velocity of oscillations of the interface under no forcing vibrations. The corresponding period of the interfacial wave oscillations can be easily determined from equation (2.70). The half period of the interfacial oscillations can also be estimated from Figures 2.29 - 2.35. These findings are summarized in Figures 2.36 and 2.37 for water and glycerol respectively.

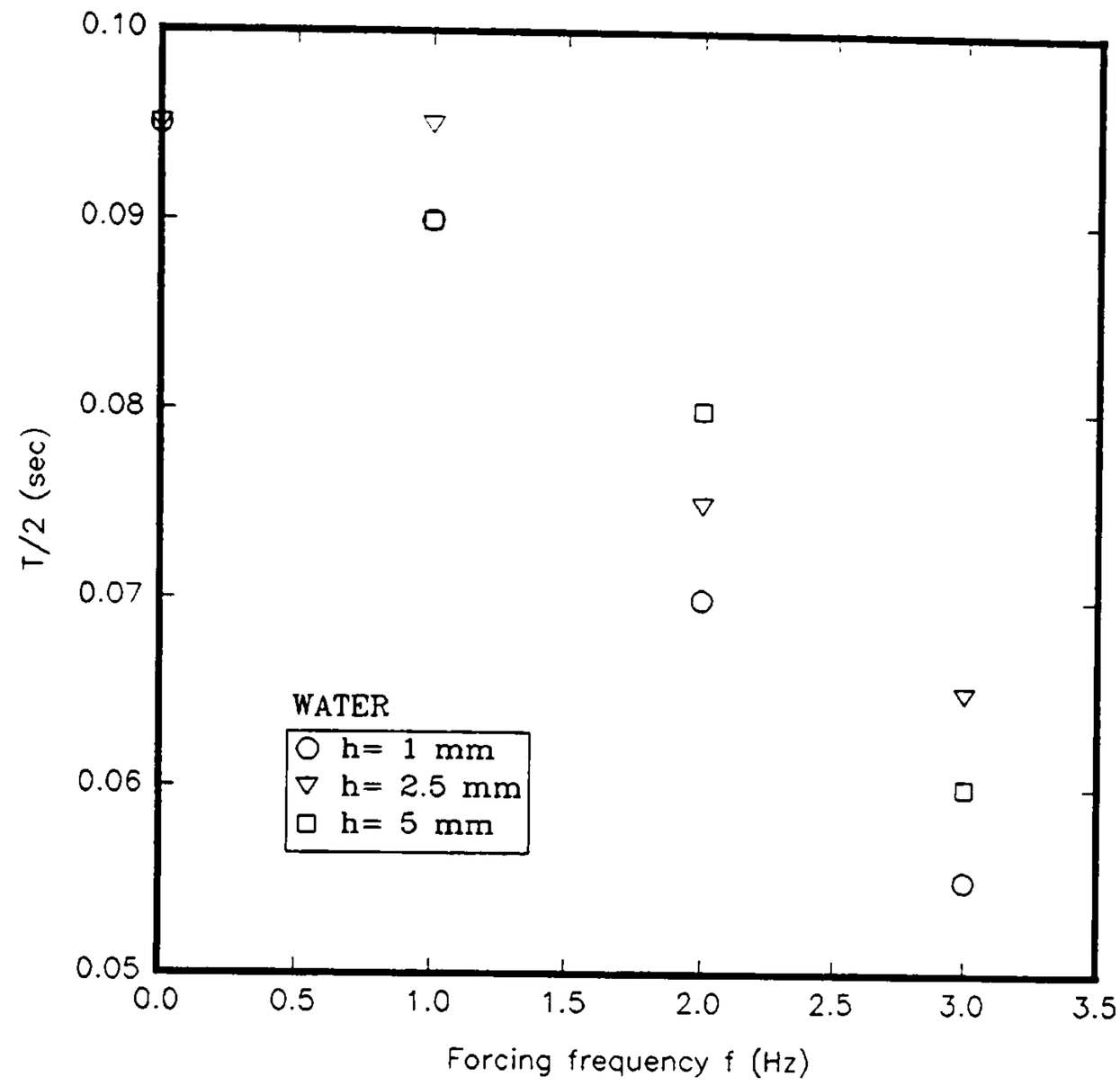

Figure 2.36 *Half period of oscillation of the interfacial wave, water, amplitude of forcing oscillations A = 70 mm*

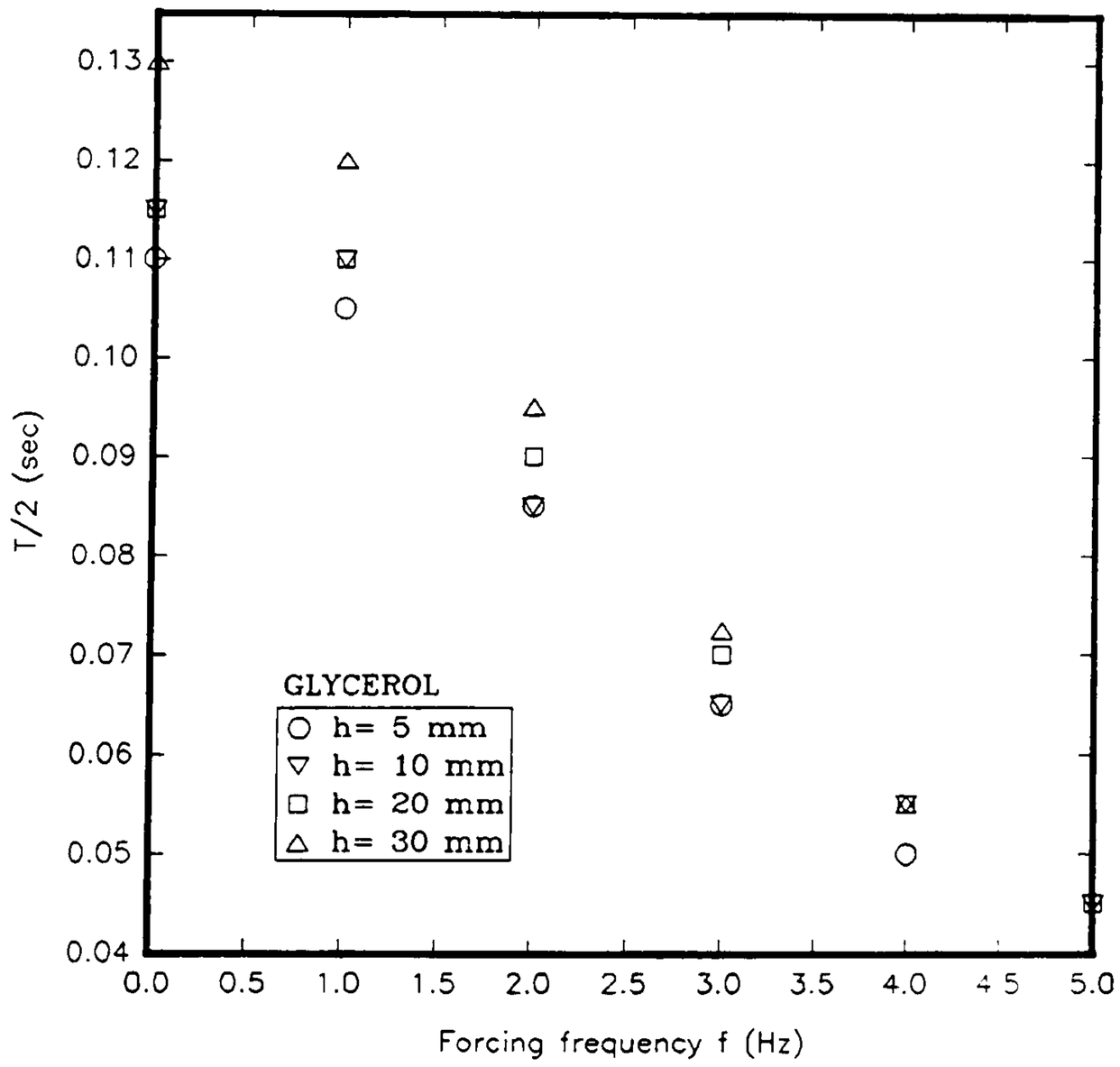

Figure 2.37 *Half period of oscillation of the interfacial wave, glycerol, amplitude of forcing oscillations A = 70 mm*

It can be seen that the magnitude of the initial pulse disturbance has little influence on the half period of oscillation of the interfacial wave. Equation (2.70) gives an expression for the angular velocity of oscillations of the interfacial wave under no forcing vibrations. The corresponding analytically derived half periods are compared with those obtained numerically in Table 2.3. Only the first mode of oscillation is assumed to occur, therefore for the given 69 mm diameter cylinder $k_m = 69.7\ m^{-1}$.

	ANALYTICAL RESULT		CFD RESULT
	ω_o^2 (rad^2/s^2)	$T_o/2$ (s)	$T_o/2$ (s)
WATER	710	0.118	0.095
GLYCEROL	690	0.119	0.118*

* averaged value for investigated range of h

Table 2.3 *Comparison of half period values obtained by mathematical analysis and by numerical computation*

As mentioned earlier, and shown for example in Figure 2.28, higher modes of oscillation can occur on a liquid surface. This fact is mathematically expressed by the summation over the range of modes of oscillation in equation (2.19). However, the Floquet theorem analysis of the governing Mathieu equation presented in Appendix B assumes only a single mode of oscillation. Nevertheless it may be assumed that the value of k_m increases due to the presence of the higher modes and therefore the period and also the half period of oscillation of the interfacial wave decrease correspondingly. This may provide an explanation of the slight difference between the analytical and CFD results for water. It is also demonstrated in Figure 2.34 by steeper decrease of interfacial displacement at times above 0.07 seconds for the case of no forcing vibrations. Good agreement between the analytical and computational results is found for glycerol where a single mode of oscillation is maintained throughout most of the investigated timespan.

Kumar and Tuckerman [16] derived an expression for the angular velocity of interfacial wave oscillations incorporating the effect of liquid viscosity. In their analysis they derived a damping coefficient, γ, which is based on the rate of dissipation of the total

mechanical energy due to viscosity. The expression obtained for the coefficient γ is:

$$\gamma = 2k_m^2 \frac{\mu}{\rho} = 2k_m^2 \nu \tag{2.71}$$

The corrected angular velocity of oscillations incorporating the effect of viscosity is given by:

$$\omega_D^2 = \omega_o^2 - \gamma^2 \tag{2.72}$$

where ω_D is the angular velocity of the damped oscillations. Expression (2.72) implies that the period of oscillation of the free surface wave increases with increasing liquid viscosity. This change is insignificant for water. For glycerol, however, the square of angular velocity of the damped oscillations $\omega_D^2 = 650.8$ rad^2/s^2 and the corresponding half period is 0.123 s. This value is still within the range of half periods shown in Figure 2.37 for no forcing vibrations and there is only a 3 % difference between the period of damped and non-viscous wave oscillations.

To investigate the influence of mode of oscillation, numerical experiments were run for a half sinusoidal initial pressure pulse disturbance. It was found that the wave created on the interface adopted similar oscillatory behaviour to that found in the case when a full sinusoidal initial disturbance was applied on the surface. The corresponding time history of the wave displacement is shown in Figure 2.38.

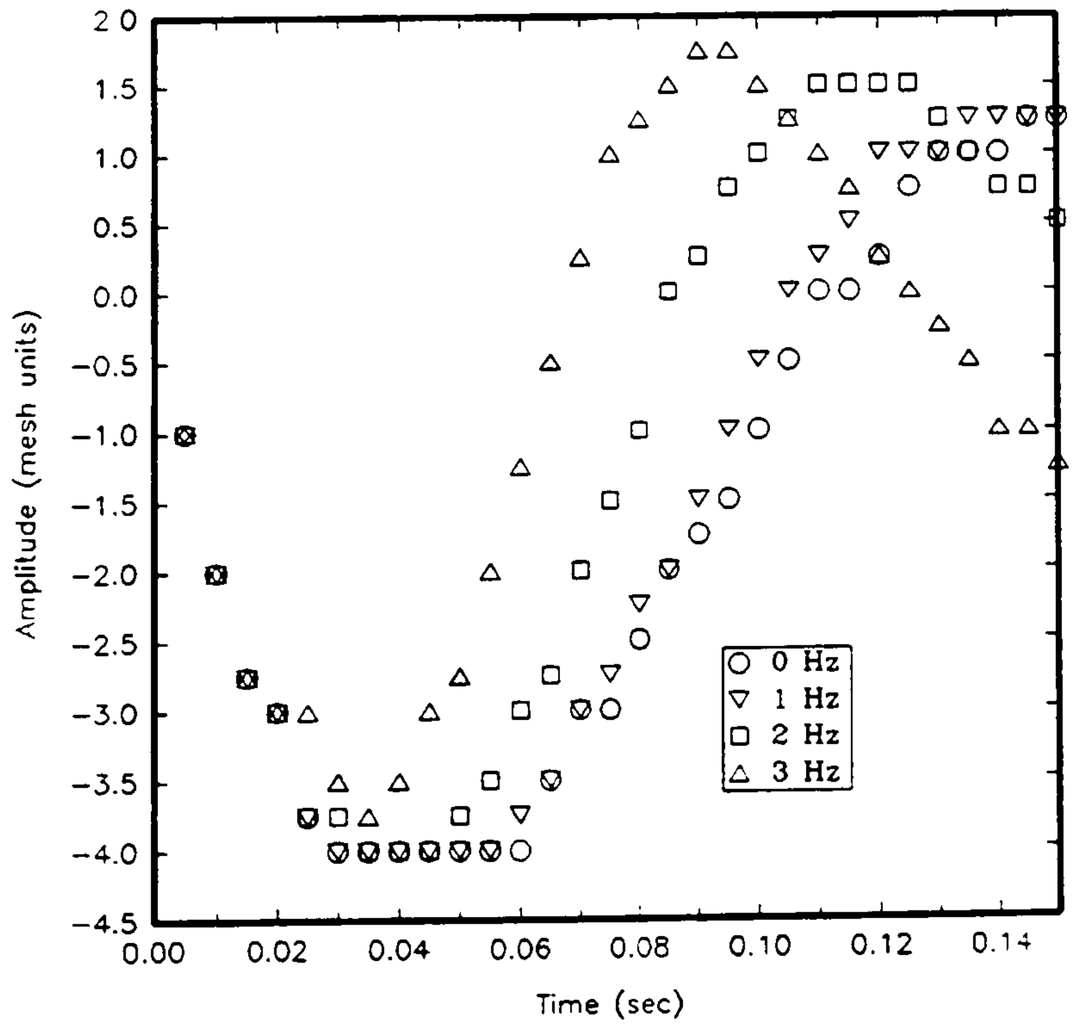

Figure 2.38 *Wave displacement measured on the axis of symmetry with forcing oscillation frequency as a parameter, glycerol, half sinusoidal initial pressure pulse, h = 20 mm, surface tension neglected, forcing oscillation amplitude A = 70 mm*

Compared to Figure 2.31 the period of wave oscillation remains unchanged thus confirming the use of only the first mode of oscillation in the above discussion.

Numerical experiments were also run to investigate the effect of the forcing vibration amplitude, including tests for the amplitude A = 30 mm. Experimental data presented in Figure 2.8 show that at this amplitude the critical frequency for the interfacial wave to grow unstable is 5 Hz. The numerically predicted time history of the wave displacement is shown in Figure 2.39.

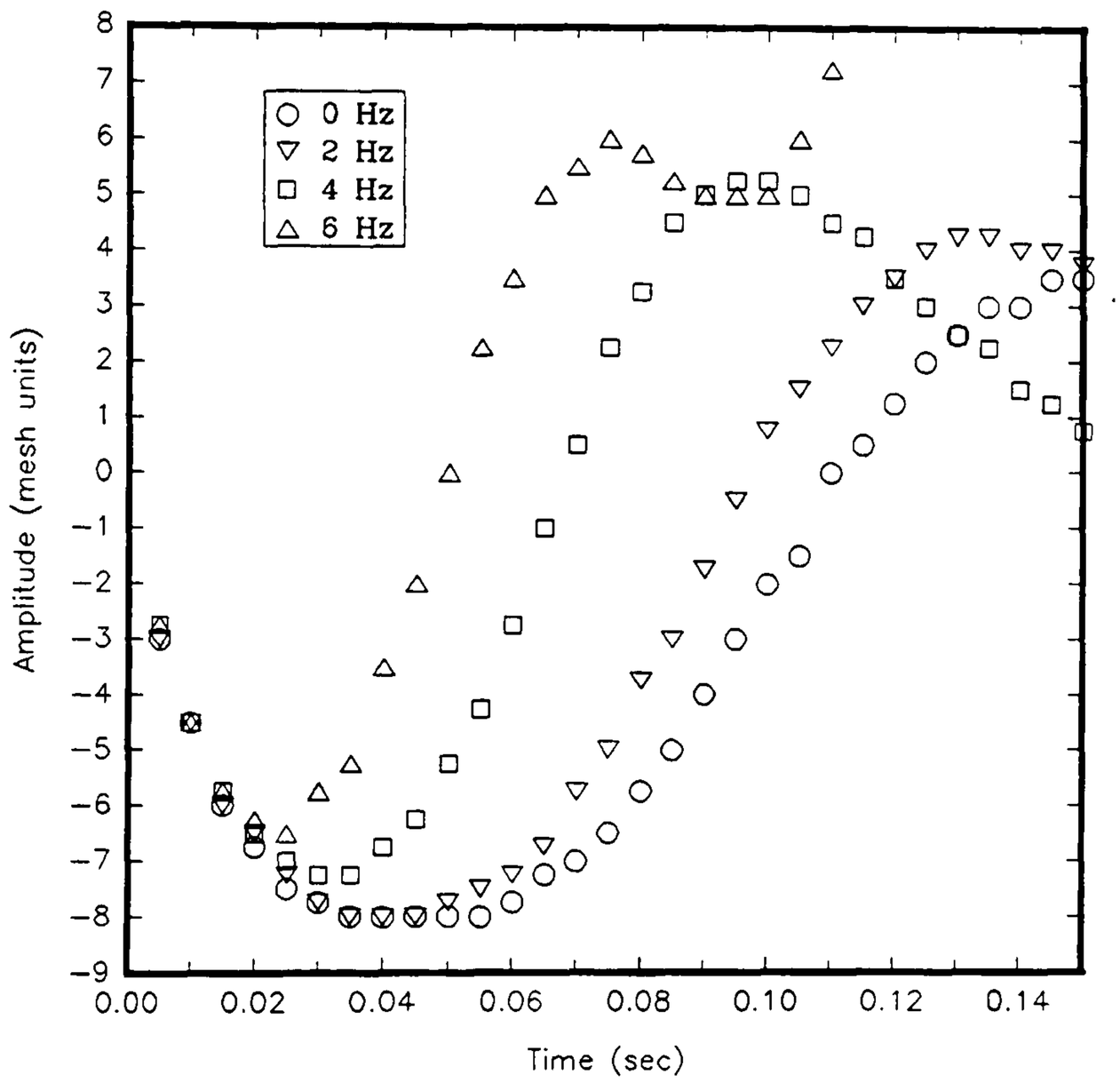

Figure 2.39 *Wave displacement measured on the axis of symmetry with forcing oscillation frequency as a parameter, glycerol, amplitude of forcing oscillations A = 30 mm, initial wave amplitude h = 20 mm, surface tension neglected*

It can be observed that for this particular case the wave created on the interface is clearly unstable for a forcing oscillation frequency of 6 Hz, although it is still stable for 4 Hz. It may be deduced that the point at which the sudden instability occurs lies within the range of these two values, which is in good agreement with the experimental findings. The ratios of the wave oscillation frequency and the forcing frequency, calculated using the half periods taken from the graph shown in Figure 2.39, are approximately 2, 3/2 and 3/2 for 4, 5, and 6 Hz excitation frequencies respectively.

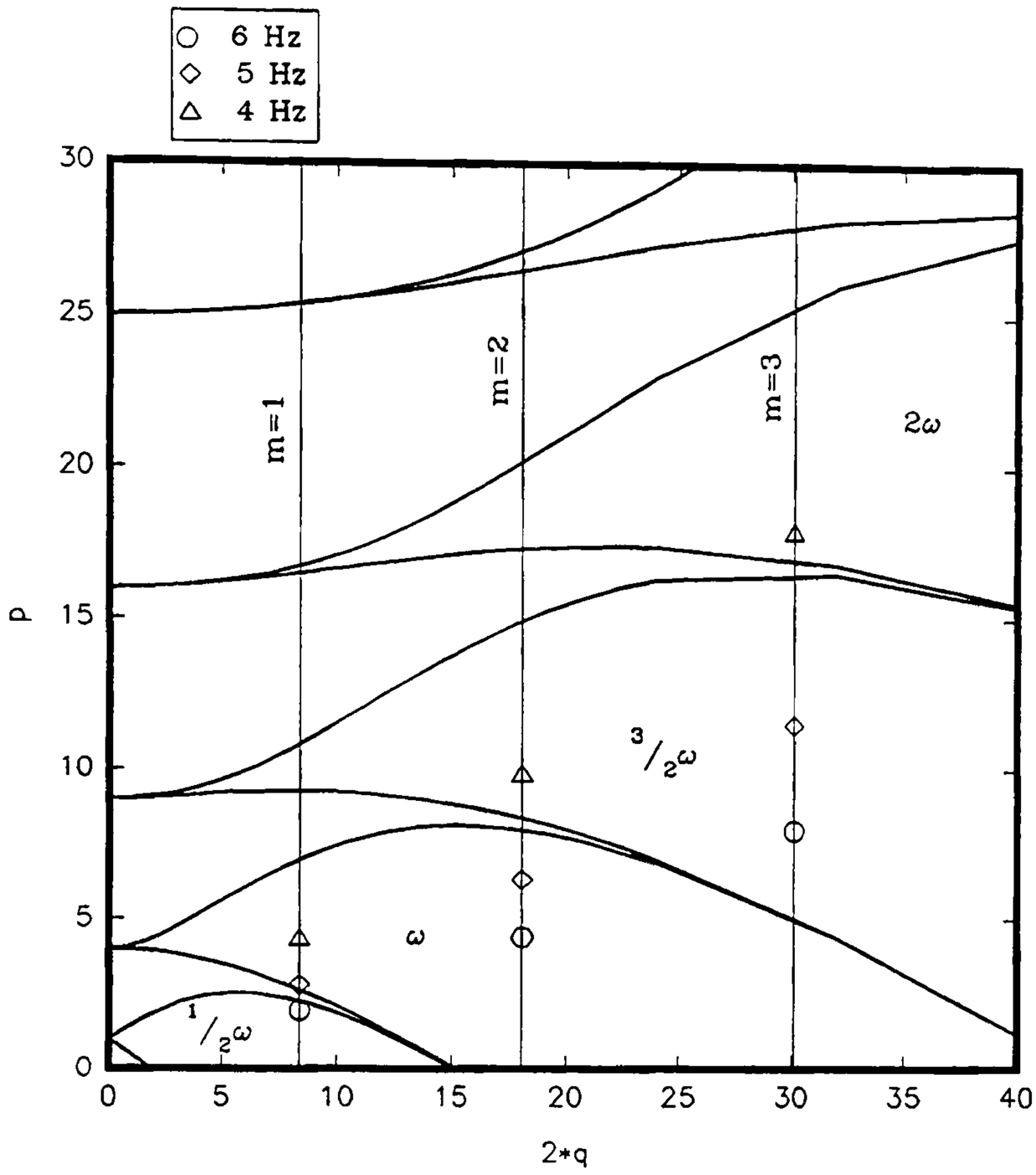

Figure 2.40 *Stability diagram with plotted points corresponding to forcing oscillations of 30 mm amplitude and frequencies of 4, 5 and 6 Hz and the first three modes of oscillation*

The points corresponding to those frequencies and the first three modes of oscillation are plotted in the p - q stability diagram shown in Figure 2.40. The results for the first and second mode of oscillation indicate lower frequency ratios. The results for the third mode of oscillation, however, demonstrate a very good agreement with both numerical and experimental findings. Figure 2.40 shows that for the third mode of oscillation the point representing 4 Hz forcing frequency lies close enough to the 2ω stability boundary and it may be assumed stable, as the present stability analysis does not incorporate damping effects of viscosity. The points representing 5 and 6 Hz forcing vibrations are clearly inside the $3/2\omega$ unstable region. This situation corresponds to the results for the forcing frequency to the wave oscillation frequency ratios obtained numerically. It also agrees well with the findings published by Ciliberto et al [4], suggesting that mode overlapping occurs on the stability boundary.

When comparing the periods of oscillation of the interfacial waves for forcing

vibration amplitudes of 30 and 70 mm, see Figures 2.39 and 2.31, it may be observed that at any given forcing frequency the oscillation period is shorter for the case of A = 70 mm. This is emphasised particularly for the higher forcing frequencies. Analytical stability investigation supports this finding of the numerical investigation. If lines of constant p are drawn on the stability diagram and followed for an increasing value of 2.q, there is a certain point when stability boundary is crossed into a region where the angular velocity of the free surface wave oscillations is higher, for example from $3/2\omega$ to 2ω. The corresponding period of oscillation therefore decreases.

Figures 2.29 - 2.35, 2.38 and 2.39 indicate that frequency of oscillation of the interfacial wave increases with increasing forcing frequency. This finding is supported by the mathematical analysis which suggests that the frequency of oscillations of the interfacial wave is determined uniquely by the frequency of the forcing vibrations. The wave can oscillate with angular velocities equal to multiples of half of the angular velocity of the forcing vibrations as illustrated for example in Figure 2.40. Assuming a wave to be unstable and oscillating with a frequency determined by one of the unstable regions then for a particular amplitude of forcing oscillations, given by a fixed value of q, the value of p, which is inversely proportional to square of forcing oscillation frequency, decreases with the increasing forcing oscillations. As stated above, the wave is assumed to be oscillating with an angular frequency equal to multiples of $\omega/2$. Therefore as the forcing frequency is increased, the frequency of the interfacial wave must therefore also increase for the situations occurring within a single unstable region.

2.6 CONCLUSIONS

2.6.1 Summary of major findings

An experimental and theoretical investigation has been undertaken to examine the behaviour of a gas liquid interface in a vertical cylindrical vessel subjected to a sinusoidal vertical motion. Water, glycerol and ethanol were the liquids considered.

Experimental results indicate that there is a certain frequency of the forcing oscillations at which significant amounts of liquid are thrown from the interface and the interface thus loses its coherent structure. This critical frequency is related to a critical acceleration, which is generally independent of the amplitude of the angular motion and decreases with increasing cylinder diameter.

Mathematical analysis, based on stability investigation of the Mathieu equation, even though it neglects the effects of viscosity, agrees reasonably well with the experimental findings. The analysis suggests that only the first mode of oscillation occurs on the liquid interface. Higher modes are damped by viscosity. Experimental results replotted in the p - q domain, where p is inversely proportional to square of frequency of the forcing oscillations and q is directly proportional to the amplitude, fall, for the first mode of oscillations, either on the curves of marginal stability or inside the unstable regions. It was also found that the height of the liquid column did not have any effect on the interfacial wave stability as for the heights investigated in the present work because the term tanh (k_m.l), used as a multiplier, expressing this effect is equal to one.

A computational analysis, based on a simplified MAC (SMAC) method incorporating Continuum Surface Force (CSF) model for surface tension modelling, was performed for water and glycerol. It was found that the surface tension has very little effect on the period and amplitude of oscillation of the interfacial wave. However small local ripples caused by surface tension effects do occur. The computations and subsequent analysis for both water and glycerol, indicate that higher modes of oscillation are established on the stability boundary.

It was found that the magnitude of the initial sinusoidal pressure disturbance imposed on the interface does not have any significant effect on the period of oscillation

of the interfacial wave, it, however, influences its amplitude. Stability of the interfacial wave was found to be dependent on the initial pressure pulse disturbance. Exponential growth of the interfacial wave was observed in some cases. The period of wave oscillation determined computationally for a cylinder without forcing oscillations agrees well with the analytical findings. The agreement is particularly good for high viscosity liquids like glycerol.

Numerical experiments were run for a half sinusoidal initial pressure disturbance on the surface to investigate the influence on the mode of oscillation. It was found that the wave created on the interface established oscillatory behaviour similar to that found in the case of a full sinusoidal disturbance, thus confirming that only a single dominant mode of oscillation occurs.

The influence of the forcing oscillation amplitude was also investigated. The computational findings suggest that for higher values of the forcing oscillation amplitude and a particular frequency, the oscillation period becomes shorter. This fact agrees well with the analytical result. The computations have also shown that with increasing forcing vibration frequency the frequency of oscillations of the interfacial wave also increases. This statement is supported by the mathematical analysis.

2.6.2 Suggestions for further work

The problem of interfacial wave instability has been thoroughly studied as shown in the preceding sections. There are, however, certain areas that could be investigated in greater detail.

A visualisation technique, similar to that shown in Figure 2.3, should be used to observe the behaviour of the interface. The mode of oscillation of the interfacial wave could be determined from such observations. This would also enable comparisons to be made with the interfacial wave shapes predicted by the computational scheme.

The mathematical analysis could be extended to incorporate the effects of viscosity as suggested by Kumar and Tuckerman [16].

The computational technique described in Section 2.5 can be greatly improved. A method giving a better representation of the volume of fluid, VOF, function can be

incorporated. The computational analysis also neglects the effect of wetting angle at the wall which becomes significant mainly for geometries with small dimensions. Furthermore the computational method currently assumes a uniform temperature throughout the liquid. This assumption may be correct for the present work, but is not valid in general terms. Incorporating solution of the temperature field into the calculations would, however, necessitate inclusion of the energy equation into the computational scheme. Also, for the sake of completeness, the effect of vapour pressure at the interface between the liquid and gas phases should be considered.

LIST OF REFERENCES FOR CHAPTER 2

1. FARADAY M., On a Peculiar Class of Acoustical Figures and on Certain Forms Assumed by Groups of Particles Upon Vibrating Elastic Surfaces, *Philos. Trans. R. Soc. London*, 121:299-340, 1831

2. FUNAKOSHI M. INOUE S., Surface Waves Due to Resonant Horizontal Oscillation, *Journal of Fluid Mechanics*, 192:219-247, 1988

3. WU J. KEOLIAN R. RUDNICK J., Observation of Non-Propagating Hydrodynamic Solition, *Phys. Rev. Letter*, 52:1421-1424, 1984

4. CILIBERTO S. GOLLUB J. P., Chaotic Mode Competition in Parametrically Forced Surface Waves, *Journal of Fluid Mechanics*, 158:381-398, 1985

5. EZERSKII A. B. KOROTIN P. I. RABINOVICH M. I., Random Self-Modulation of Two-Dimensional Structures on a Liquid Surface During Parametric Excitation, *JETP Letters*, 41:157-160 No. 4, 1985

6. WHALLEY P. B. HEWITT G. F. TERRY J. W., Photographic Studies of Two-Phase Flow Using a Parallel Light Technique, *Report AERE-R9389, UKAEA, Harwell*, 1979

7. FAUVE S. KUMAR K. LAROCHE C. BEYSENS D. GARRABOS Y., Parametric Instability of a Liquid-Vapor Interface Close to the Critical Point, *Physical Review Letters*, 68:3160-3163 No. 21, 1992

8. MATTHIESSEN L., Ueber der Transversalschwingungen Tonender Tropfbarer und Elastischer Flussigkeiten, *Ann. Phys. Chem.*, 141:375-393 No. 2, 1870

9. RAYLEIGH LORD, On the Crispations of Fluid Resting Upon a Vibrating Support, *Phil. Mag.*, 16:50-58, 1883

10. MILES J., Surface Wave Damping in Closed Basins, *Proceedings of Royal Soc. London*, A297:459-475, 1967

11. MILES J., Nonlinear Surface Waves in Closed Basins, *Journal of Fluid Mechanics*, 75:419-448, 1976

12. MILES J., Nonlinear Faraday Resonance, *Journal of Fluid Mechanics*, 146:285-302, 1984

13. BENJAMIN T. B. URSELL F., The Stability of the Plane Free Surface of a Liquid in Vertical Periodic Motion, *Proc. R. Soc. London*, A225:505-515, 1954

14. KEOLIAN R. TURKEVICH L. A. PUTTERMAN S. J. RUDNICK I., *Phys. Rev. Lett.*, 47:1133, 1981

15. GUTHART G. S. YAO-TSU WU T., Observation of a Standing Tank Cross Wave Parametrically Excited, *Proc. R. Soc. London*, 434:435-440, 1991

16. KUMAR K. TUCKERMAN L. S., Parametric Instability of the Interface Between Two Fluids, *Journal of Fluid Mechanics*, 279:49-68, 1994

17. MILES J., Parametrically Excited Solitary Waves, *Journal of Fluid Mechanics*, 148:451-460, 1984

18. LARRAZA A. PUTTERMAN S., Theory of Non-Propagating Surface Wave Solitons, *Journal of Fluid Mechanics*, 148:443-449, 1984

19. TUFILLARO N. B. RAMSHANKAR R. GOLLUB J. P., Order-Disorder Transition in Capillary Ripples, *Physical Review Letters*, 62:422-425 No. 4, 1989

20. WEI R. WANG B. MAO Y. ZHENG X. MIAO G., Further Investigation of Non-Propagating Solitions and Their Transition to Chaos, *J. Acoust. Soc. Am.*, 88(1):469-472, 1990

21. FUNAKOSHI M. INOUE S., Bifurcations of Limit Cycles in Surface Waves Due to Resonant Forcing, *Fluid Dynamics Research*, 5:255-271, 1990

22. KAMBE T. UMEKI M., Nonlinear Dynamics of Two-Mode Interactions in Parametric Excitation of Surface Waves, *Journal of Fluid Mechanics*, 212:373-393, 1990

23. MILES J. HENDERSON D., Parametrically Forced Surface Waves, *Annu. Rev. Fluid Mech.*, 22:143-165, 1990

24. UMEKI M., Faraday Resonance in Rectangular Geometry, *Journal of Fluid Mechanics*, 227:161-192, 1991

25. FUNAKOSHI M. INOUE S., Stable Periodic Orbits of Equations for Resonantly Forced Water Waves, *Journal of the Physical Society of Japan*, 61:341-3412 No. 9, 1992

26. XUE-NONG CHEN & RONG-JUE WEI, Dynamic Behaviour of a Non-Propagating Solition Under a Periodically Modulating Oscillation, *Journal of Fluid Mechanics*, 259:291-303, 1994

27. FRIEDEL H. LAEDKE E. W. SPATSCHEK K. H., Bifurcations and Nonlinear Dynamics of Surface Waves in Faraday Resonance, *Journal of Fluid Mechanics*, 284:341-358, 1995, 1995

28. BELOTSERKOVSKII O. M. DAVYDOFF J. M., Metod Krupnykh Czastic v Gazovoi Mechanike, *Glavnaia Redakcia Matematitcheskoi Literaturi*, Moscow, 1982 (Метод Крупных Частиц в Газовой Мєханике - in Russian)

29. WELCH J. E. HARLOW F. H. SHANNON J. P. DALY B. J., The MAC Method - A Computing Technique for Solving Viscous, Incompressible, Transient Fluid-flow Problems Involving Free Surfaces, *Los Alamos Scientific Laboratory Report LA-3425*, 1965

30. AMSDEN A. A., Particle-In-Cell Method for Calculation of the Dynamics of Compressible Fluid, *Los Alamos Scientific Laboratory Report LA-3466*, 1966

31. HIRT C. W. COOK J. L. BUTLER T. D., A Lagrangian Method for Calculating the Dynamics of an Incompressible Fluid with Free Surface, *Los Alamos Scientific Laboratory Report*, 1969

32. AMSDEN A. A. HARLOW F. H., The SMAC Method: A numerical Technique for Calculating Incompressible Fluid Flows, *Los Alamos Scientific Laboratory Report LA-4370*, 1970

33. HIRT C. W., *Proceedings of the Second International Conference on Numerical Methods in fluid Dynamics*, Berkeley, 1970

34. HARLOW F. H. AMSDEN A. A., A Numerical Fluid Dynamics Calculation Method for All Flow Speeds, *Journal of computational Physics*, 8:197-213 No. 2, 1971

35. AMSDEN A. HIRT C. W., YAQUI: Arbitrary Lagrangian-Eulerian Computer Program for Fluid flow at All Speeds, *Los Alamos Scientifc Laboratory report LA-5100*, 1973

36. HARLOW F. H. WELCH E. J., Numerical Calculation of Time-Dependent Viscous Incompressible Flow of Fluid with Free Surface, *The Physics of Fluids*, 8:2182-2189, 1965

37. DALY B. J., Numerical Study of Two Fluid Rayleigh Taylor Instability, *The Physics of Fluids*, 10:297-307, 1967

38. HARLOW F. H. SHANNON J. P., The Splash of a Liquid Drop, *Journal of Applied Physics*, 38:3855-3866, 1967

39. HARLOW F. H. WELCH J. E., Numerical Study of Large Amplitude Free-Surface Motions, *Physics of Fluids*, 9:842-851, 1966

40. PRESS W. H. TEUKOLSKY S. A. VETTERLING W. T. FLANNERY B. P., Numerical Recipes in FORTRAN - The Art of Scientific Computing, *Cambridge University Press*, 1992

41. HIRT C. W. NICHOLS B. D., Volume of Fluid (VOF) Method for the Dynamics of Free Boundaries, *Journal of Computational Physics*, 39:201, 1981

42. CHAM DEVELOPMENT TEAM, The PHOENICS Reference Manual, Report TR200, *Cham Ltd.*, 1990

43. LIU JUN, PhD Thesis, *Imperial College*, London, 1988

44. LIU JUN SPALDING D. B., Numerical Simulation of Flows with Moving Interfaces, *PhysicoChemical Hydrodynamics*, 10:625-637 No. 5/6, 1988

45. BRACKBILL J. U. KOTHE D. B. ZEMACH C., A Continuum Method for Modelling Surface Tension, *Los Alamos National Laboratory Report LA-87545*, 1990

46. SHKOOHI F. ELROD H. G., Numerical Investigation of the Disintegration of Liquid Jets, *Journal of Computational Physics*, 71:324-342, 1987

47. SHKOOHI F. ELROD H. G., Algorithms for Eulerian Treatment of Jet Backup Induced by Surface Tension, *Journal of Computational Physics*, 89:483-487, 1990

48. SELLENS R. W., A Numerical Model of the Capillary Instability, *ICLASS-91, Paper No. 11*, Gaithersburg, MD, USA, July 1991

49. VALHA J., Investigation of Two-Phase Interface Stability, BEng Honours in Mechanical Engineering Report, Faculty of Engineering, Science and Mathematics, School of Mechanical and Manufacturing Engineering, *Middlesex University*, London, 1993

50. GULKIN S. STOKER J. J., Stability of Columns and Strings under Periodically Varying forces, *Quarterly of Applied Mathematics*, 1:215-236, 1943

51. DRAZIN P. REID W., Hydrodynamic Stability, Cambridge Monographs on Mechanics and Applied Mathematics, *Cambridge University Press*, 1981

52. REKTORYS et. al., Survey of Applicable Mathematics, *Iliffe Books Ltd.*, London, 1969

53. INCE E. L., Researches into the Characteristic Numbers of the Mathieu's Equation, *Proceedings of the Royal Society of Edinburgh*, 46:20-29, 46:316-322, 1925

54. INCE E. L., Researches into the Characteristic Numbers of the Mathieu's Equation, *Proceedings of Royal Society of Edinburgh*, 47:294-301, 1927

55. McLACHLAN N. W., Application of Mathieu's Equation to Stability of Non-Linear Oscillator, *Mathematical Gazette*, 35:105-107, 1951

56. BLANCH G., Asymptotic Expansions for the Odd Periodic Mathieu's Functions, *Transactions of the American Mathematical Society*, 97(2):357-366, 1960

57. KOTHE D. B. MJOLSNESS R. C. TORREY M. D., Ripple : A Computer Program for Incompressible Flows with Free Surfaces, *Los Alamos National Laboratory Report LA-12007-MS*, 1991

58. LANDAU L. D. LIFSHITZ E. M., Fluid Mechanics, Pergamon Press, New York, 1959

59. BRACKBILL J. U. KOTHE D. B. ZEMACH C., A Continuum Method for Modelling Surface Tension, *Journal of Computational Physics*, 100:335-354, 1992

CHAPTER 3 : TRANSIENT HEAT TRANSFER BETWEEN LIQUID SPRAYS AND SURROUNDING GAS

3.1 FOREWORD

Sprays provide an efficient means of heat transfer and are utilised in many important heat and power production devices, such as the liquid piston heat pump (LPHP), discussed in Chapter 1.

The experimental and theoretical studies described in this chapter were undertaken to gain a better understanding of the spray droplet heat transfer and evaporation processes which occur when a hot liquid is injected into a closed vessel containing a gas at a lower temperature. In pursuit of this aim the following objectives were set:

1. To prepare a detailed literature survey [1] to identify: (i) the latest techniques and procedures for predicting heat transfer characteristics between liquid sprays and gases, (ii) the available measurement techniques and (iii) those areas where relevant data are lacking and ways of rectifying this situation.
2. To construct an experimental rig based around a constant volume spray chamber. The liquid will be injected into the chamber through one or more nozzles, using a cylinder and piston arrangement. It will be possible to set the total volume and the rate of injection of the liquid. The temperature of the injected liquid will be controlled. The volume of gas in the spray chamber will be adjustable. Several nozzle designs and configurations will be investigated.
3. To conduct a programme of experimental work to determine: (i) heat transfer rates between liquid droplet sprays and the surrounding gas, (ii) energies of droplet production and (iii) the most efficient method of obtaining good gas-droplet heat transfer.

The experimental programme includes the following parameters as independent variables:

- nozzle design (manufacturers' data for droplet sizes and distributions will be used)
- nozzle configurations
- flowrate of the injected liquid (water)
- total amount of injected liquid (water)
- temperature of the injected liquid

- choice of gas in the spray chamber
- initial gas pressure in the spray chamber
- the initial proportion of gas/liquid in the spray chamber

The dependent parameters measured in the experiments are as follows:

- pressure changes in the gas space of the spray chamber
- pressure drop across the nozzles

4. To analyse the experimental data to determine appropriate dimensionless relationships.

A technical report [2] covers the requirements given in the above points 2 - 4. Section 3.2 of this Chapter gives literature overview of the articles and books published on the spray heat and mass transfer phenomena. Section 3.3 describes an experimental apparatus designed by the author and presents the typical experimental results obtained. An analysis of the spray heat and mass transfer problem is given in Sections 3.4 and 3.5. Overall findings are summarised in Section 3.6.

3.2 LITERATURE OVERVIEW

3.2.1 General

This section covers literature that has been published on spray heat transfer.

First, fundamentals of droplet generation and listing of available spray nozzles are given. The review was used to choose the most suitable nozzles for the present experimental work. This is followed by overview of the experimental work, concentrating on non-combustible media, experimental methods available to researchers and implications to present work. Finally the third part deals with analytical approaches to the problem including computational fluid dynamics (CFD) modelling of sprays.

Literature survey identified a large number of reports, journals, books and other documents. However, most of the literature deals either with relatively well-defined theoretical cases, such as heat transfer to a single rigid spherical droplet, or with specific applications, such as heat transfer processes in mixing condensers. Very few publications consider simultaneous experimental and theoretical analyses.

3.2.2 Spray nozzles

The atomiser system suitable for the earlier mentioned industrial application must satisfy the following criteria:

(i) Production of droplets of required size

(ii) Minimum energy consumption

(iii) Uniform mixing, i. e. uniform distribution in the spray chamber. Consideration should be given to atomiser positioning and configuration.

(iv) Low cost

(v) Reliability and durability

(vi) Flexibility - i. e. the ability to change dropsize independently of flowrate

(vii) Atomiser dimensions as small as possible

List of available atomisers classified by the energy source [3] [4], shown in Figure 3.1, provides a wide range for selection of the correct atomising device. On the left hand side of Figure 3.1 are the traditional atomisers most commonly found in industry. Broadly classified these are pressure jet nozzles where the energy is supplied by pumping the liquid under pressure through a small orifice; twin fluid where pressure energy is supplied to a second atomising fluid; and rotary atomisers where energy is supplied to the liquid by feeding onto a rotating wheel or disc. On the lower right-hand side are the more exotic types, such as the ultrasonic and electrostatic atomisers which use energy from mechanical vibration, shock waves or electrical energy. In general, these are only suitable for low liquid flowrates and are less widely used. Figure 3.1 also shows that there are overlaps in the classification since many atomisers use energy from several sources. The three most likely atomisers for the present applications are rotary atomisers, 2 fluid and pressure nozzles. Rotary atomisers produce only 180° hollow cone pattern as a result of liquid ligament break-up on rotating disc due to centrifugal force. This is not ideal for good distribution of droplets in the spray chamber. Also, because of wide spray pattern, there would be a significant number of droplets striking the walls. Commercial rotary atomisers, moreover, are not designed to operate under rapidly varying outside pressure, since this may put a large fatigue stress on the rotary disc. The motor, gearbox and transmission that power the rotary disc require regular maintainance and their cost is high. Due to the above reasons it was decided not to the use this type of atomisers in the present work. In 2-fluid nozzles (also called pneumatic, air assist or air blast nozzles) atomisation is achieved by contacting the liquid with a high velocity atomising gas stream. Liquid break-up occurs due to the high shearing forces present. 2-fluid nozzles are very good at
producing fine sprays, however, they are regarded [3] [4] as being far more energy input consuming than pressure or rotary atomisers and, moreover, there has to be a continuous supply of pressurised gas. It was therefore decided to use pressure nozzles.

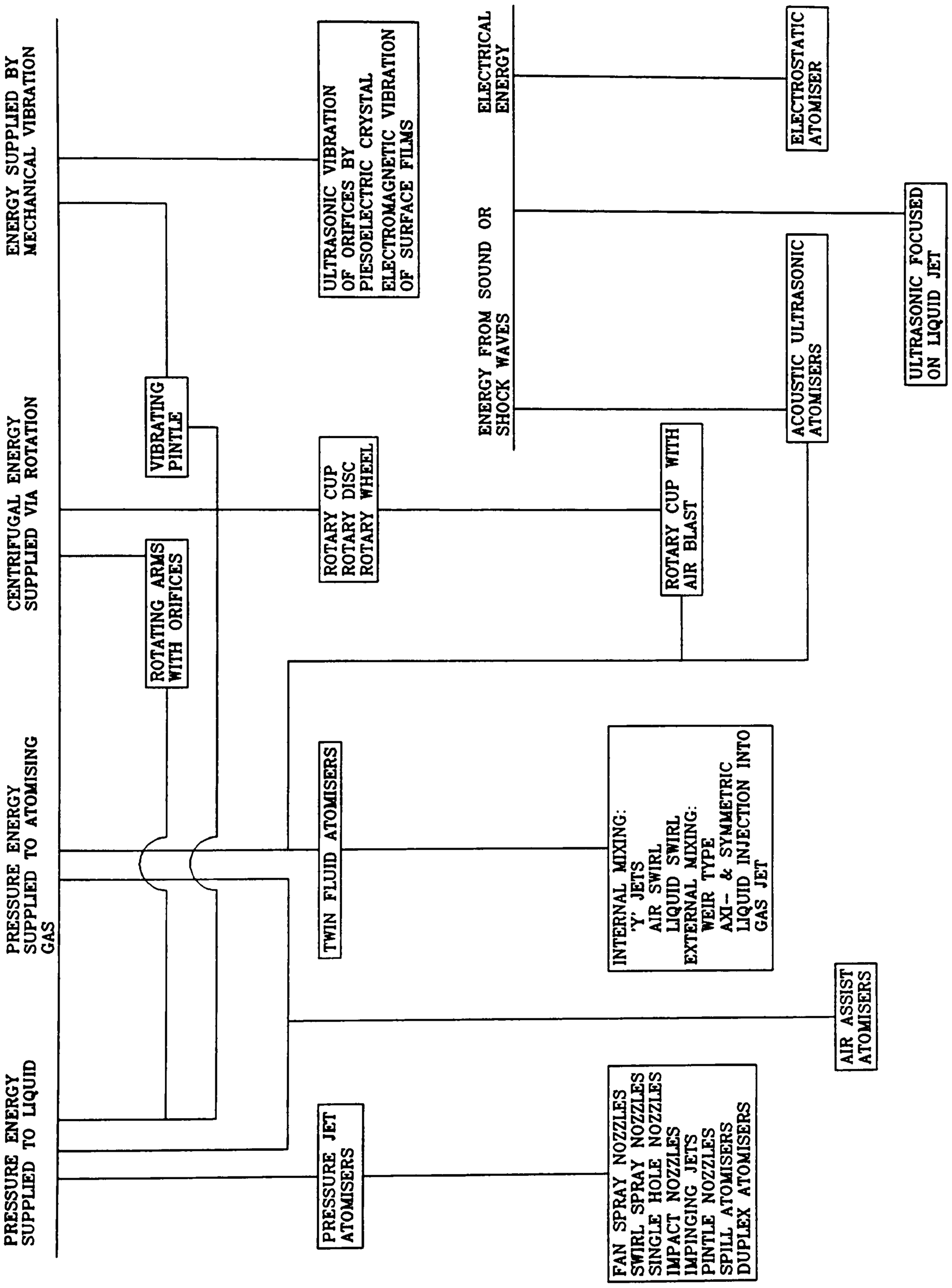

Figure 3.1 *Atomisers classified by energy source*

3.2.3 Pressure nozzles

In pressure nozzles, the liquid to be atomised is forced under pressure through a small orifice. Atomisation is achieved by utilising the energy supplied to the liquid. There are four main types:

(i) Pressure swirl nozzles

(ii) Plain orifice nozzles

(iii) Fan jet nozzles

(iv) Impact and impingement nozzles

In pressure swirl nozzles, also known as simplex, a conical sheet of liquid is produced by imparting a high degree of rotation by introducing the liquid into a swirl chamber through tangential inlets, inserts or grooves. The conical sheet thus formed is subsequently broken-up into droplets as it leaves the nozzle. There are two basic types of simplex nozzles. In one design the spray is comprised of drops that are distributed fairly uniformly throughout its volume, this is generally described as a solid-cone spray. The other nozzle type produces a hollow-cone spray, in which most of the drops are concentrated at the outer edge of conical spray pattern. Figure 3.2 shows a pressure nozzle, in which the swirl produced by the tangential inlets, is sufficient to cause the formation of a central air-core and produces a characteristic hollow-cone spray pattern.

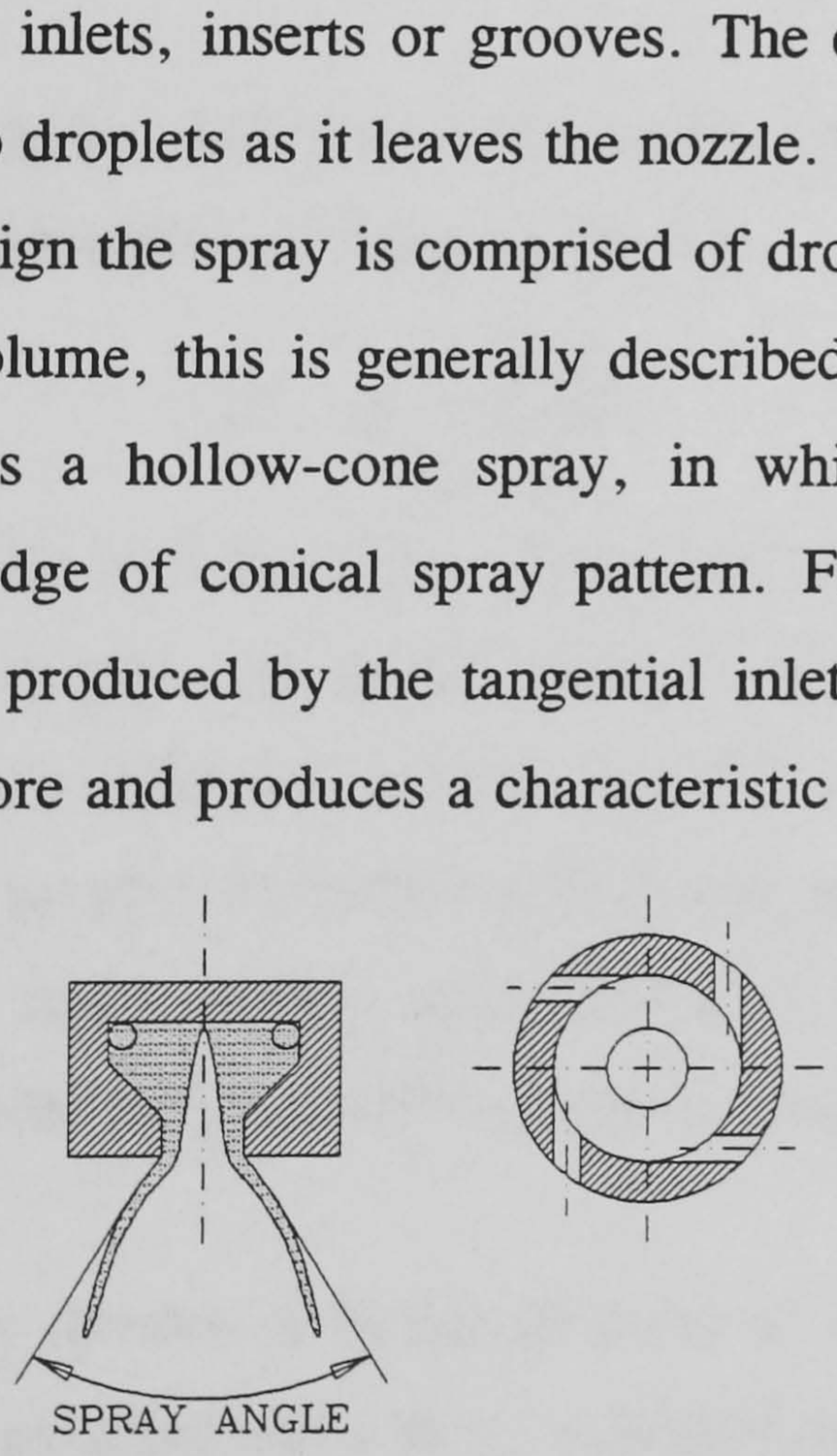

Figure 3.2 *Schematic view of a hollow cone simplex swirl atomiser*

The cone angle of the spray is determined by the ratio of the axial to tangential components of velocity as the liquid exits through the orifice. A solid (or full) cone spray pattern can be produced with pressure swirl nozzles by introducing a second jet of liquid axially into the swirl chamber so that no air core is formed. The development of the spray

passes through several stages as the liquid injection pressure is increased from zero as shown in Figure 3.3.

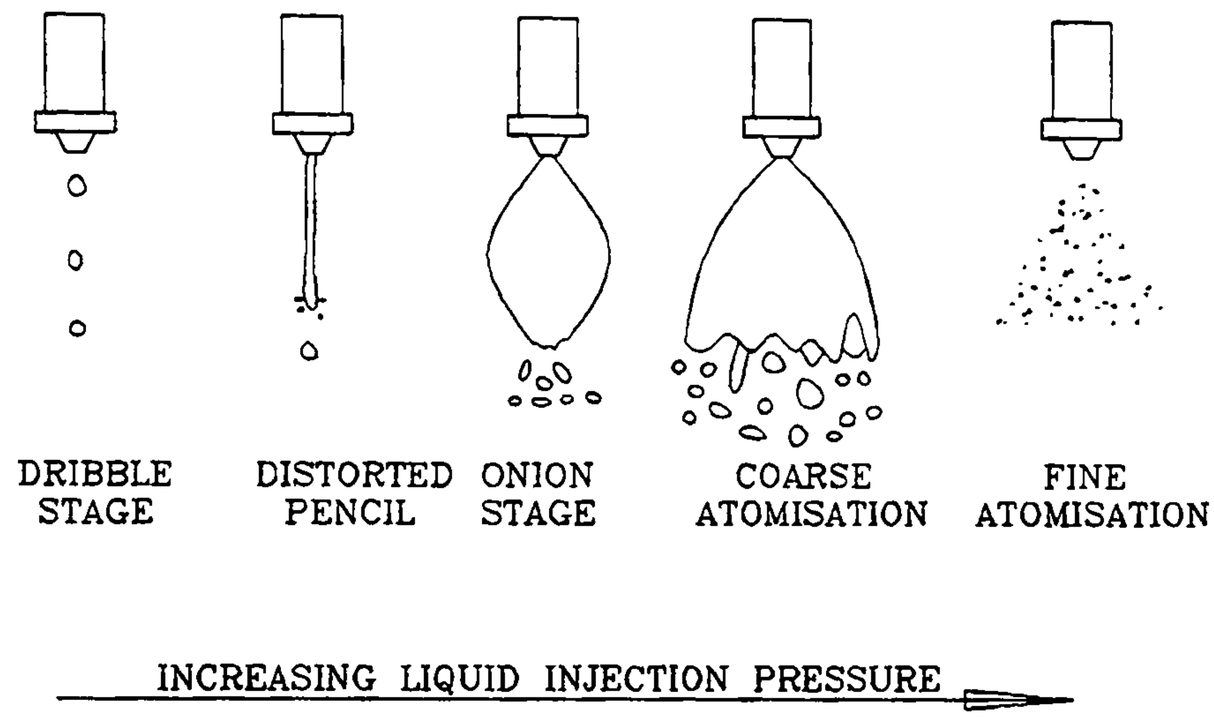

Figure 3.3 *Stages in spray development with increase in liquid injection pressure*

A major drawback of the simplex atomiser is that its flow rate varies as the square root of the injection pressure differential according to [5] [6]:

$$Q = K\sqrt{\frac{2\,\Delta p}{\rho_L}} \qquad (3.1)$$

where K is the nozzle constant, ρ_L is the liquid density and Δp is the nozzle pressure drop

In basic plain orifice nozzles, the liquid is forced at high pressure through a simple plain orifice. This produces a solid jet of liquid which is subsequently broken up into droplets. Since in this case, no sheet is formed and droplet formation is directly from the solid jet, the attainment of small droplet sizes requires a small orifice size and high pressures. The sprays produced by plain-orifice atomisers have a cone angle that usually lies between 5° and 15°.

In fan jet nozzles two streams of liquid are made to impinge behind an orifice by specially designed approach passages and a sheet is formed in a plane perpendicular to the plane or the streams. A flat sheet is produces as the liquid spreads through the orifice limited only by the side walls. At low pressures this sheet remains thick and atomisation proceeds from instabilities of the thick rims of the sheet. At higher pressures wave instabilities occur in the sheet leading to ligaments and droplets. Fan jets are not suitable for producing fine dropsizes and tend to produce larger dropsizes than swirl simplex nozzles at the same pressure.

Impact and impingement nozzles are devices where droplets are generated by impacting a velocity liquid stream on a suitable surface. In general these devices produce larger dropsizes than pressure swirl nozzles. Their main advantage, however, is that they are less liable to clogging.

The above paragraphs indicate that a nozzle type best suited for the present application is full cone pressure swirl nozzle system. Table 3.1 lists main manufacturers of these nozzles and their company coding names.

Spraying Systems	Quick Jet & UniJet Systems General Purpose Nozzles
Lurmark	Full cone nozzles FN, GN, TN series
Delavan	Full cone nozzles BL, BP, WL series
PNR	Full cone nozzle CAY 1870

Table 3.1 Commercially available full cone pressure swirl nozzles

3.2.4 Experimental approach

Experimental investigations of sprays are approached by researchers in three general ways.

First there is a large group of researchers dealing with fundamental of sprays, their characterisation, distribution & sizing of droplets and velocity measurements. The methods used range from a simple collector as shown in Figure 3.4.

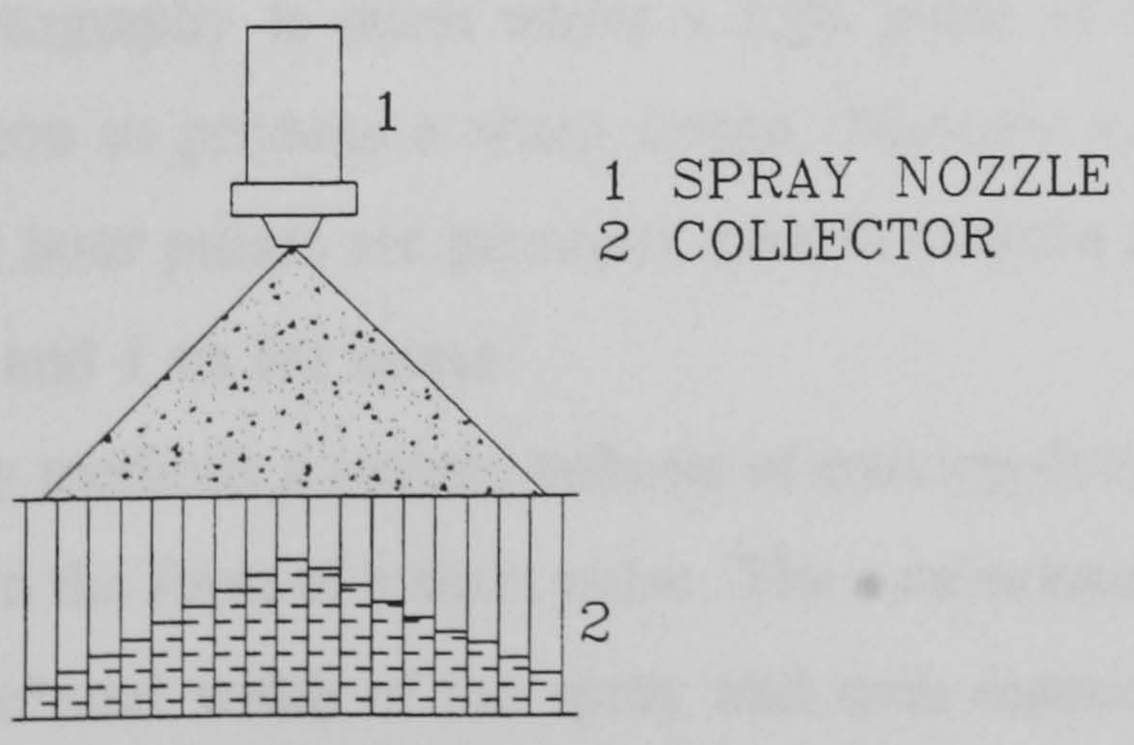

Figure 3.4 Collector for measurement of radial distribution of liquid jet density

Further refinement of drop sizing is based on the following:

- drop collection on slides or in cells, where drops are deposited on a flat surface with suitable structure, such a surface is usually a plate covered with a suitable filter paper, or layer of magnesium oxide or soot.
- drop freezing methods, where drops are sprayed into an airtight cooled container and are sorted by sieving after freezing
- substitute liquid methods that are based on replacing the actual liquid with another one which, after atomisation solidifies immediately and drops are then again sorted by sieving
- gravitational classification methods based on the analysis of differential penetration of drops during their fall in a stationary environment
- drop evaporation methods, where captured drops are heated and rate of droplet mass loss is measured
- contact electrode methods, where two sharp needles with a gap between them are placed in a spray. They are connected to a voltage source and a pulse counter. Each short circuit, caused by a droplet falling between the electrodes, is registered by the counter
- charged wire methods, whose principle of measurements is based on the fact that a drop colliding with a wire connected to a voltage source removes an amount of charge depending on the drop size.

Finally there are optical drop sizing methods, that have been improved during the past 20 years. These techniques include photography, cinematography, videobased systems, shadowgraphy and holography.

High speed photography is taken under a light pulse of sufficient intensity and sufficiently short duration to produce a sharp image. Mercury vapour lamps, electrical sparks, flash lights, and laser pulses are generally used to create a light source of duration of 1 μs for flashlights, and 1 ns for lasers.

With holography methods a sample volume of moving drops is illuminated with a coherent beam of light in the form of a short pulse. The measurement volume is a cylinder with length equal to the total width of the spray and with diameter equal to that of the laser beam. As the duration of the laser pulse is extremely short - 20 ns - the drops

contained within the measurement volume are effectively frozen. The resulting hologram provides a completed three dimensional image of the spray in which drops as small as 15 μm are clearly visible.

The most widely used analysing instruments include Malvern Particle Analyzer and Phase Doppler Particle Analyser.

The Laser Diffraction Analyser, shown in Figure 3.5, utilises the fact that a spray drop will cause laser light to scatter through an angle dependent on diameter of the drop.

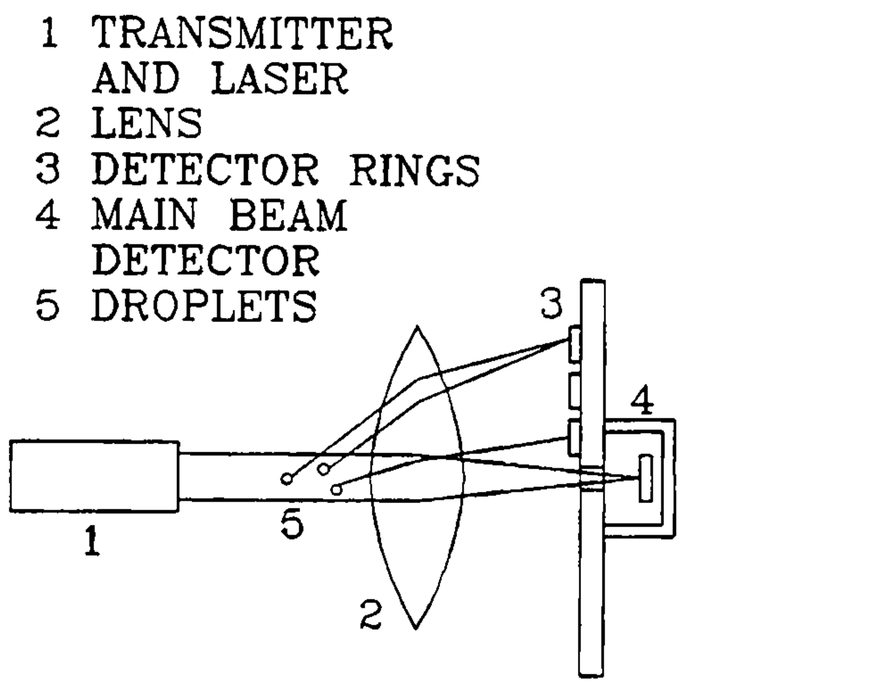

Figure 3.5 Laser Diffraction Analyser

The scattered light intensity is measured using a series of semicircular photo-diodes. The Phase Doppler Particle Analyser (PDPA), shown in Figure 3.6, is a device that focuses on a small portion of the total spray pattern.

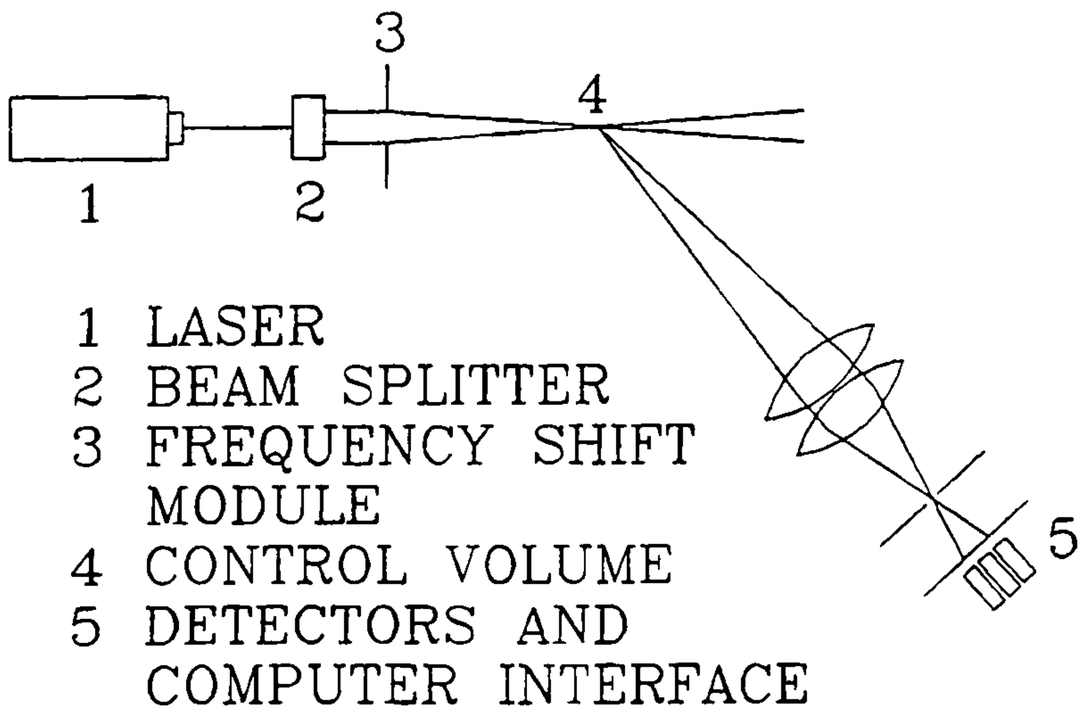

Figure 3.6 Phase Doppler Particle Analyser

The PDPA uses a low power laser light that is split into two beams by utilizing a beam splitter and a frequency shift module. The two laser beams intersect again into a single beam at the sample volume location. When a drop passes through the intersection region of the two laser beams, an interference fringe pattern is formed by scattered light. Since the drop is moving, the scattered interference pattern sweeps past the receiver aperture at the Doppler shift frequency, which is proportional to the drop velocity. The spatial frequency of the fringe pattern is inversely proportional to the drop diameter. Signal processing is based on software analysis of digitized Doppler bursts. Size range of the instrument is 5 μm to 10 mm, maximum measured velocities can be about 200 ms^{-1}, maximum concentration up to 1000 drops/mm^3, measuring volume is usually about 0.5 x 0.3 x 0.3 mm, and measuring distance is up to 600 mm. The commonly used lasers are either 25 mW He-Ne or a 2 W argon-ion laser. Histograms of drop size and velocity distributions are displayed in real time. Data acquisition and transfer to computer memory require, in most commercially available devices, 20 μs per drop.

Table 3.2 lists a selection of works that were published on the above techniques.

Collector method for measurements of radial distribution in sprays	[7]
Drop collection method	[8]
Drop freezing	[9]
Gravitational classification	[10]
Contact electrode method	[11]
Photography, Cinematography, Holography	[12] [13] [14] [15] [16]
Malvern Particle Sizing	[17]
Phase Doppler Particle Analysis	[12] [18] [19]

Table 3.2 *Selection of works published on spray analysis*

The second group of researchers aims their activities at the investigation of processes occurring on a single spray droplet. Subject of interest are measurements of heat and mass transfer and single droplet penetration in various ambient conditions.

A paper fundamental for spray research, by Ranz and Marshall [20], describes the investigation of factors influencing the rate of evaporation of pure liquid drops, and the rate of evaporation of water drops containing dissolved and suspended solids. Similar, but more sophisticated equipment was used by Yuen and Chew [21], who were generating a single droplet using a syringe-like arrangement. The droplet was exposed to a stream of air of a given temperature. The flow rate from the syringe to the droplet was maintained such as to compensate for the droplet evaporation, so as to keep diameter of the droplet constant. From the evaporation rate data they were able to determine, using one dimensional analysis, correlations for heat mass transfer and drag coefficients.

Investigations of the vaporisation of a single alcohol droplet in air with various degrees of humidity were reported by Law et al. in [23]. The experiment involved recording the magnified image of the vaporizing droplet by a video camera, from which the signal was displayed on a TV monitor, stored on tape for future playback and digitized and sent to a micro-computer for real-time analysis and printout.

Aworonin in [24] investigated evaporation rates of freely falling liquid nitrogen droplets in air by filming a droplet's fall and comparing recorded droplet sizes frame by frame.

Evaporation rates of pure hydrocarbon and trichlorotrifluoroethane drops in high temperature, moderate pressure environment were experimentally investigated by Harfield & Farrell [25]. They used a video recorder connected to a digital frame analyser for determination of evaporation rates and changes of droplet shapes.

The last, and probably the most relevant to the present work, is the group of experiments in which sprays are used as means of heating or cooling and processes occurring in the bulk are investigated. General discussion on the qualitative advantages and disadvantages, together with applications to industry, is given in references [26] [27] [28]. Lekic and Ford [29] carried out experiments with steam-water system, using three different full cone nozzles at different pressure drops. Figure 3.7 shows the apparatus used in their investigation.

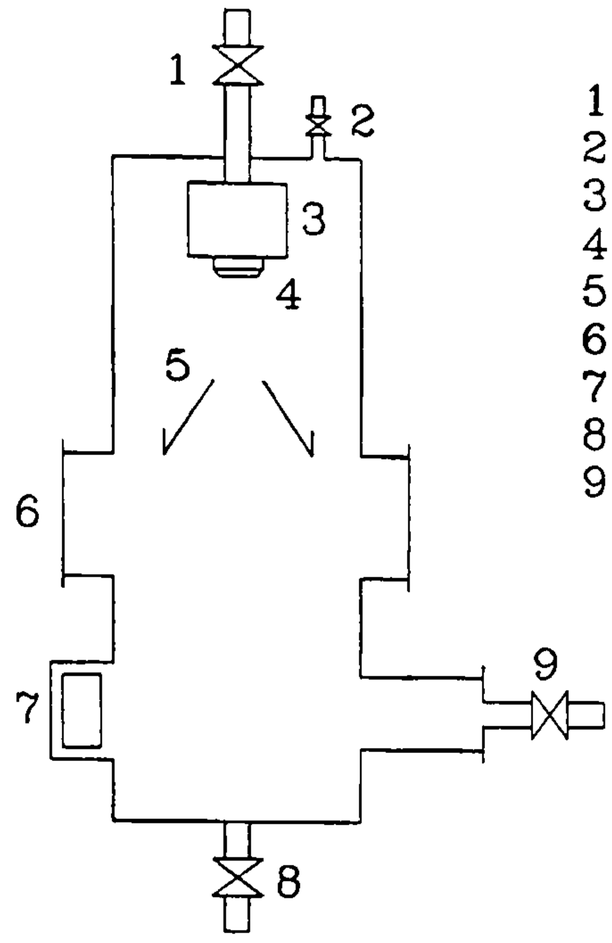

1 WATER VALVE
2 VENTING VALVE
3 EXTENSION TUBE
4 NOZZLE
5 SPLITTER
6 WINDOW
7 SIGHT GLASS
8 OUTLET VALVE
9 STEAM INLET VALVE

Figure 3.7 *Schematic diagram of the apparatus as used by Lekic and Ford [29]*

To measure the heat transfer rates at different distances from the nozzle, three extension tubes of different lengths were made. These tubes were placed between the top flange of the apparatus and the nozzle. To determine the heat transfer rates, the temperatures of condensate at the outlet were measured.

Experimental investigation of heat transfer rates from high pressure glycerin sprays produced by fan-jet pressure nozzles is reported in reference [30]. Heated glycerin was sprayed into the atmosphere and the average cup mixing temperature of the spray was measured in order to obtain an indication of the heat transferred from the sprayed liquid. A similar set of experiments was also carried out for for water. It was found that with water, evaporation appears to account for up to 80 % of the heat transferred but it was not important for glycerin, the reason for it are different vapour pressures of the two fluids.

Russian authors Buglayev, Vasilyev and Strebkov experimentally analysed various aspects of cooling of gas flows by the injection of water [31]. They stressed the need for experimental data on cooling and heating of air using sprays having droplets of 50 to 200 μm in diameter.

Kabaldin and Ivanistov [32] analysed operation of sprayers with respect to their heat-and-energy characteristics. Their study discusses the main technological and construction parameters of spray atomisers. The results have been processed by regression method and mathematical relationships were obtained which can be used for the calculation

and comparative estimation of operating sprayers.

Results of experiments performed on a droplet heat exchanger are given in reference [33]. The experimental rig used in this analysis is shown in Figure 3.8. A compressor and

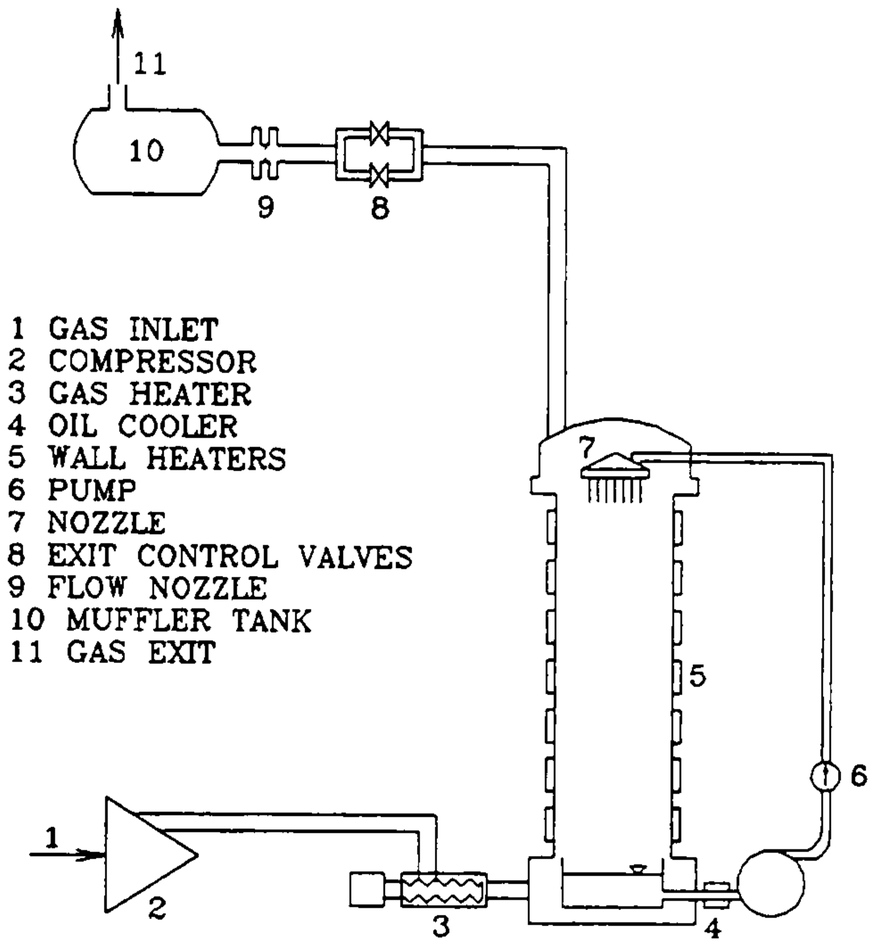

Figure 3.8 *Laboratory droplet heat exchanger system [33]*

a gas heater supplied hot air that was circulated in 3 m long and 20 cm diameter column, that was heated on the walls to maintain adiabatic state. All gas, drop, column and heater temperatures were monitored using a computer. Gas and liquid flow rates were set and maintained at desired levels also via computer. Droplet shower was formed by pumping silicon oil through 150 plain orifice nozzles fitted with an acoustic vibrator. Heat transfer in the test was always from air to droplets with inlet air temperature at approximately 120°C and inlet droplet temperature at 18°C. All tests were conducted to determine the net heat transferred from air to droplets during their passage through the column. The total heat transfer rate was determined from the measured liquid and gas mass flowrates, the known heat capacities and the average temperature change of the fluid from top to bottom of the heat exchanger.

Experimental study of evaporation from superheated water droplets in low pressure system is given in reference [34]. This was the only reference found dealing with momentary boiling, or flashing evaporation that happens after injection to low pressure environment.

References [8] [35] [36] investigate spray heat and mass transfer processes of industrial atomising units under practical conditions, testing safety systems of nuclear power plants. Reference [37] deals with optimised design of industrial spray heat exchangers, based on experimental data taken from literature.

Analysis of the experimental results yields fundamental relationship used in spray heat transfer theory - correlations for drag coefficient on the droplets, Nusselt number for heat transfer, and Sherwood number for mass transfer. B_H - the heat transfer number - represents the driving force for the evaporation process, the ratio of the available enthalpy in the surrounding gas and the heat required to evaporate the liquid drop. B_M - the mass transfer number - is the mass transfer equivalent of B_H. Reynolds number, Re, in basic form is related to a diameter of spray droplet and it compares the effect of inertia and viscous forces. Prandtl number, Pr, compares momentum and heat diffusivity and its mass transfer equivalent, the Schmidt number, Sc, compares momentum and mass diffusivity. These are shown in Table 3.3. Expression 1. for drag coefficient in Table 3.3, known as the Stokes' law, holds only for flows that are entirely dominated by viscous forces, i. e. for low Reynolds number, Re. Drag coefficient equations 2. and 3. approach Stoke's law, but can be used up to $Re = 1000$. The effect of evaporation on a droplet drag may be due to two factors: (i) the effect of mass transfer on drag, known as the "blowing effect", and (ii) the temperature and concentration gradient near the drop surface due to evaporation. This effect has been incorporated in equation 5., but it is valid only for $Re < 200$. Correlation 6. is widely used for intense mass transfer. Equation 7. uses Re^*, that is based on drop cluster diameter, rather than on droplet diameter. This relationship takes into account proximity of other droplets and it is valid for $Re < 10000$.

Ranz & Marshall's formula for Nusselt number, given by equation 8., and similar expressions 10. & 11., though widely used, is based upon quasi-steady, constant radius, porous wetted sphere experiments. Those experiments did no account for transient heating/cooling, regressing interface and internal circulation of droplets. Experiments were carried out for extremely cold liquids - liquid nitrogen - and yielded equation 9., similar to expressions 8., 10., 11. . Correlation 12. comes from theoretical analysis based on energy balances. Equations 5., 13. & 16. are the most general expressions available. They account for blowing effect, evaporation and also internal circulation.

DRAG COEFFICIENT

1. $C_D = \frac{24}{Re}$ [38] [39]

2. $C_D = \frac{24}{Re}(1 + 0.15\ Re)^{0.687}$ [42]

3. $C_D = \frac{24}{Re}(1 + \frac{1}{6}\ Re^{2/3})$ [3]

5. $C_D = \frac{23}{Sc^{0.14}Re}(1 + 0.276\ Sc^{0.33}Re^{0.5})(1 + B_M)^{-1}$ [21] [23]

6. $C_D = \frac{C_D}{1 + B_M}$ [3]

7. $C_D = 0.271\ Re^{*0.21}$ [40] [41]

NUSSELT NUMBER

8. $Nu = 2 + 0.6\ Re^{0.5}Pr^{0.33}$ [20]

9. $Nu = 2 + 0.75\ Re^{0.5}Pr^{1/3}$ [24]

10. $Nu = 2\ (1 + 0.276\ Re^{0.5}Pr^{0.33})$ [3]

11. $Nu = 2 + \frac{0.55\ Re^{0.5}Pr^{1/3}}{\left(1 + \frac{1.232}{Re\ Pr^{4/3}}\right)^{0.5}}$ [42]

12. $Nu = 2\ \frac{\ln\ (1+B_H)}{B_H}$ [3]

13. $Nu = 1.275\ (1 + B_H)^{-0.678}Re^{0.438}Pr^{0.619}$ [38]

14. $Nu = 3.74\times10^{-10}\ Re^{2.1}We^{-0.5}K^{0.25}M^{1.75}G^{-0.7}$ [31]

SHERWOOD NUMBER

15. $Sh = 2 + 0.55\ Re^{1/2}Sc^{1/3}$ [28]

16. $Sh = 1.224\ (1 + B_M)^{-0.568}Re^{0.385}Sc^{0.492}$ [38]

where

heat transfer number	$B_H = \frac{h_{bl} - h_s}{L}$
mass transfer number	$B_M = \frac{Y_{FS} - Y_{F\infty}}{1 - Y_{FS}}$
modified heat transfer number	$K = \frac{L}{c_{pg}} (T_g - T_s)$
density ratio	$M = \frac{\rho_L}{\rho_g}$
Prandtl number	$Pr = \frac{c_p \mu}{k}$
Reynolds number	$Re = \frac{\rho \lvert U_G - U_D \rvert D}{\mu}$
Schmidt number	$Sc = \frac{\mu}{\rho D_{ab}}$
Weber number	$We = \frac{\rho U^2 D}{\sigma}$
Nusselt number	$Nu = \frac{hD}{k}$
Sherwood number	$Sh = \frac{k_c D}{D_{ab}}$

Table 3.3 *List of most commonly used formulae for drag coefficient, Nusselt number and Sherwood number*

Expression 14. for Nusselt number is the only one found that incorporates effect of surface tension on heat transfer. It should, however, be noted that it does not contain the Prandtl number and thus is of limited validity. Sherwood number is mass transfer equivalent of Nusselt number - due to similarity between Fourier's law for heat transfer and Fick's law for mass transfer [39]. Generally the same expressions are valid for Sherwood number as for Nusselt number, but Prandtl number, Pr, is substituted by Schmidt number Sc.

3.2.5 Analytical works on spray heat transfer

Analytical works on sprays use experimental results - i. e. correlations similar to those given in Table 3.3, together with fundamental physical laws describing the trajectories of the droplet particles, the gas flow patterns and heat and mass transfer processes between the liquid and gas phases. Many analytical works have been dedicated to the description of spray combustion phenomena in relation to diesel engines and will be discussed only briefly here. In the following review the main emphasis has been placed on the available literature concerning spray heat transfer of non-combustible media.

The equation governing the droplet motion is [43] [44]:

$$m_D \frac{d\vec{u}_D}{dt} = \frac{1}{2} C_D \rho A |\vec{U}_G - \vec{U}_D| (\vec{U}_G - \vec{U}_D) + m_D \vec{g} \tag{3.2}$$

the droplet mass m_D is, for an evaporating droplet, a function of time given by [39] [3]:

$$\frac{dm_D}{dt} = \pi D \rho_D D_{ab} Sh (Y_{FS} - Y_{F\infty}) \tag{3.3}$$

A heat balance for the droplet can be written as follows [44]:

$$m_D c_p \frac{dT_D}{dt} = \dot{q} + h_{fg} \left(\frac{dm_D}{dt} \right) = Nu \pi k D (T_G - T_D) + h_{fg} \left(\frac{dm_D}{dt} \right) \tag{3.4}$$

The gas phase is governed by similar set of equations to (2.24) - (2.26), that can be re-written for a general variable Φ, allow compressibility to be taken into account and can be written as [45] [46]:

$$\frac{\delta(\rho\Phi)}{\delta t} + \frac{\delta}{\delta x}(\rho u \Phi) + \frac{\delta}{\delta y}(\rho v \Phi) = \frac{\delta}{\delta x}\left(\Gamma \frac{\delta \Phi}{\delta x}\right) + \frac{\delta}{\delta y}\left(\Gamma \frac{\delta \Phi}{\delta y}\right) + S_\Phi + S_\Phi^D \tag{3.5}$$

The extra source term S_Φ^D represents the net efflux of Φ into the gas phase due to the interaction between the gas and the droplets.

Empirical correlations may be used to predict mean spray droplet sizes [3]. These correlations are frequently expressed in terms of the Sauter mean diameter d_{32}, which can be interpreted as the diameter of a droplet having the same volume to surface area ratio as the whole spray and which is usually considered the most appropriate for mass and heat transfer calculations:

$$d_{32} = \frac{\sum_{i-1}^{n} d_i^3 \, \Delta N}{\sum_{i-1}^{N} d_i^2 \, \Delta N} \tag{3.6}$$

where ΔN is the number of droplets in the size group represented by the diameter range $d_i - \Delta d_i$ to $d_i + \Delta d_i$.

In addition, the following assumptions are usually made in theoretical analyses:

(i) For small droplets (< 500 μm), the assumption of rigid, spherical drops outside the drop formation region can be made [6].

(ii) The initial droplet velocity is the same for all the drops.

(iii) The heat and momentum transfer at the nozzle inlet is ignored.

Analyses of the processes occurring between the two phases, in general, adopt one of the following two approaches: (i) zero and one dimensional analysis and (ii) computational fluid dynamics. Both approaches require a numerical solution due to the mutual coupling of the governing equations. Each area of practical application presents different problems to the construction of an appropriate spray model. Table 3.4 summarises the possible situations. Reference [44] describes a single droplet theory to simulate the behaviour of sprays in open chamber diesel engines. The model presented includes the motion induced by the spray in otherwise still air. Reference [47] presents a study of transient effects and variable properties for single droplet evaporation into an infinite stagnant gas. It was found that the effects of temporal storage of mass, species, energy, and radial pressure variations in the vapour phase prove to be negligible, the early transient behaviour being solely due to sensible heat effects within the droplet and related variations in the vapour side driving forces. Chen and Trezek [48] [49] introduced a spray energy release (SER) model for the purpose of predicting the thermal performance of single spray units as well as multiple spray units, suitable for open atmosphere spray cooling systems. Reference [29] presents a theoretical analysis and a comparison it with experiment for vapour condensation on a spray of subcooled liquid droplets. The analysis incorporates drop size distribution, motion of drops and their effect on heat transfer rate. Average spray temperature results for a given length of spray were obtained. It was found that drop size was the most important parameter influencing the heat transfer.

Application	Independent variables	Structure	Configuration
Prevaporating systems; Afterburners; Lean combustors; Rocket engines	z	steady evaporation	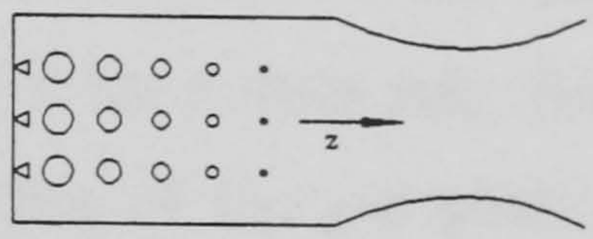
Gas Turbine combustors; Furnaces; mixing condensers	x,y,z	steady evaporation combustion	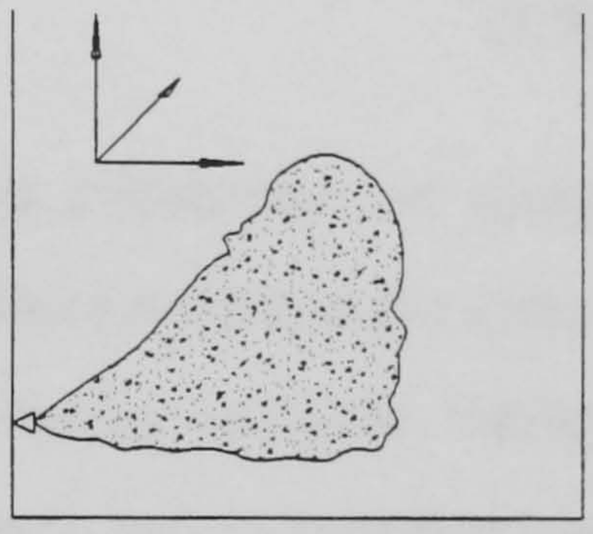
Diesel engines; Spray regenerators	t,x,y,z	transient evaporation combustion	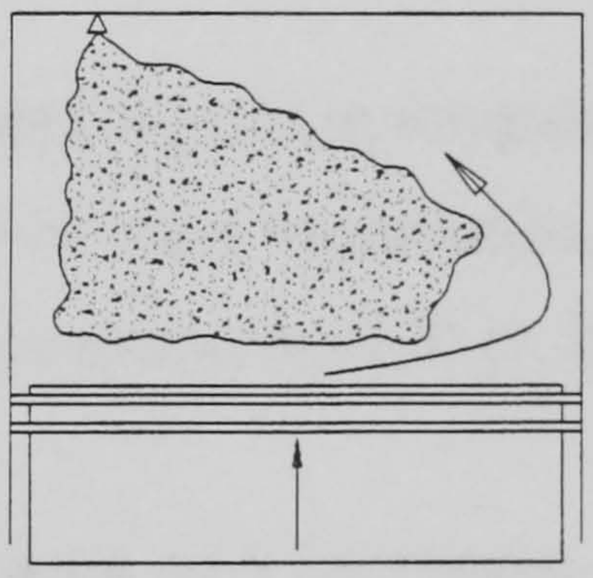

Table 3.4 Spray systems and modelling classification

Studies of the heat transfer rate to a spray droplet, under conditions of a loss of coolant accident in a light water reactor, is reported in references [50] [51]. Two models for calculation of droplet temperature are described. The first, the complete mixing droplet model assumes a droplet to be at a uniform temperature. The heat balance of a droplet is given as:

$$\frac{\rho_d \, c_{pD}}{3} \, \frac{d}{dt}\left(\frac{D^3}{8} T_D\right) = \frac{D^2}{4} \, \dot{q} \qquad (3.7)$$

where the initial droplet temperature must be specified. The second, the rigid droplet

model, considers heat is transferred by conduction only in a droplet, governed by:

$$\rho_D \, c_{pD} \, \frac{\delta T_D}{\delta t} = k \, \frac{1}{r^2} \, \frac{\delta}{\delta r}\left(k \, r^2 \, \frac{\delta T_D}{\delta r} \right) \tag{3.8}$$

and subject to appropriate initial and boundary conditions. The authors stress, that the distance a spray droplet falls in the vertical direction is a function of the droplet size, the droplet initial velocity, the spray angle and the physical properties of the gas phase. Furthermore, it was found that the spray heat transfer efficiency, defined as:

$$\eta = \frac{T_D - T_{D0}}{T_\infty - T_{D0}} \tag{3.9}$$

expressed as a function of fall time of a droplet is inadequate for evaluating the spray effectiveness for heat removal in a vessel of finite volume. It was also found that the spray heat transfer efficiency is nearly independent of spray angle. A similar analysis, taking into account droplet internal circulation, reached similar conclusions and is presented in reference [52]. Yet another similar study, described in reference [53], considers a single multicomponent droplet.

A fourth-order Runge-Kutta technique was used in references [54] [55] to compute the variations of droplet size, temperature, vapour pressure, rate of mass vaporisation, heat transfer and heat flux with time by integrating a set of equations similar to (3.2) (3.3) and (3.4).

A full CFD treatment of a gas-particle, or spray, system based on a Lagrangian-Eulerian equation coupling, as given by equations (3.2)-(3.5), was first proposed by Migdal and Agosta [56]. This work was completed by Crowe et. al [57] whose method is known as the Particle-Source-In Cell (PSI Cell) model. The PSI Cell calculations start by solving the gas flow field assuming no droplets are present. Using this flow field, the droplet trajectories together with the droplet size and temperature histories along the trajectories are calculated. The mass, momentum and energy source terms for each Eulerian cell throughout the flow field are then determined. The gas flow field is then solved again, incorporating these source terms. The new gas flow field is used to establish new droplet trajectories and temperature histories, which constitute the effect of the gas phase on the droplets. The calculation of the new source terms and their incorporation into the gas flow field equations constitutes the effect of the droplet cloud on the gas phase,

thereby completing the cycle of mutual interaction or "two-way" coupling. The method has been successfully used in simulations of spray cooling systems [58] [59] [60] [61]. The method, though widely used, is computationally expensive and there are convergence problems reported, due to the disturbing effect of S_Φ^D term in the Eulerian phase. The method also can not predict transient development of the gas phase behaviour and it neglects the volume occupied by particles in the computational cells in comparison with the volume of the gas.

A transient numerical technique, based on the ICED-ALE method - see Chapter 2, was developed by Dukowicz [62]. It also incorporates the effect of particle volume inside the computational cells. Further developments of this algorithm resulted in the production of the CONCHAS-SPRAY computer code [63] for modelling diesel fuel injection systems. This code incorporates a simple length scaling turbulence model and its primary stability criterion is that the fluid can not traverse more than one spatial increment per time cycle. Its three dimensional variant is the KIVA code [64], which incorporates a sophisticated turbulence model.

In general, it can be concluded that all CFD models suitable for spray modelling are very complex and computationally time consuming.

3.3 EXPERIMENTAL WORK

3.3.1 General

This section describes in detail the experimental apparatus constructed by the author, the experimental programme and the technique employed, and presents the main experimental findings and the conclusions derived from them.

The testing rig was designed to deliver a spray, through one or multiple nozzles, into a constant volume spray chamber. The delivery system is a syringe-like arrangement, comprising a piston and cylinder, enabling injection of water at a predetermined temperature and flowrate. A sophisticated data acquisition and control system is employed, that enables transient measurements of pressure and temperature both upstream of the nozzle and inside the spray chamber. Single readings of initial and final temperature in three different positions inside the spray chamber are recorded manually. Bulk heat transfer rates between the droplets and the gas phase are determined from the spray chamber pressure variation. A schematic of the complete experimental setup is shown in Figure 3.9.

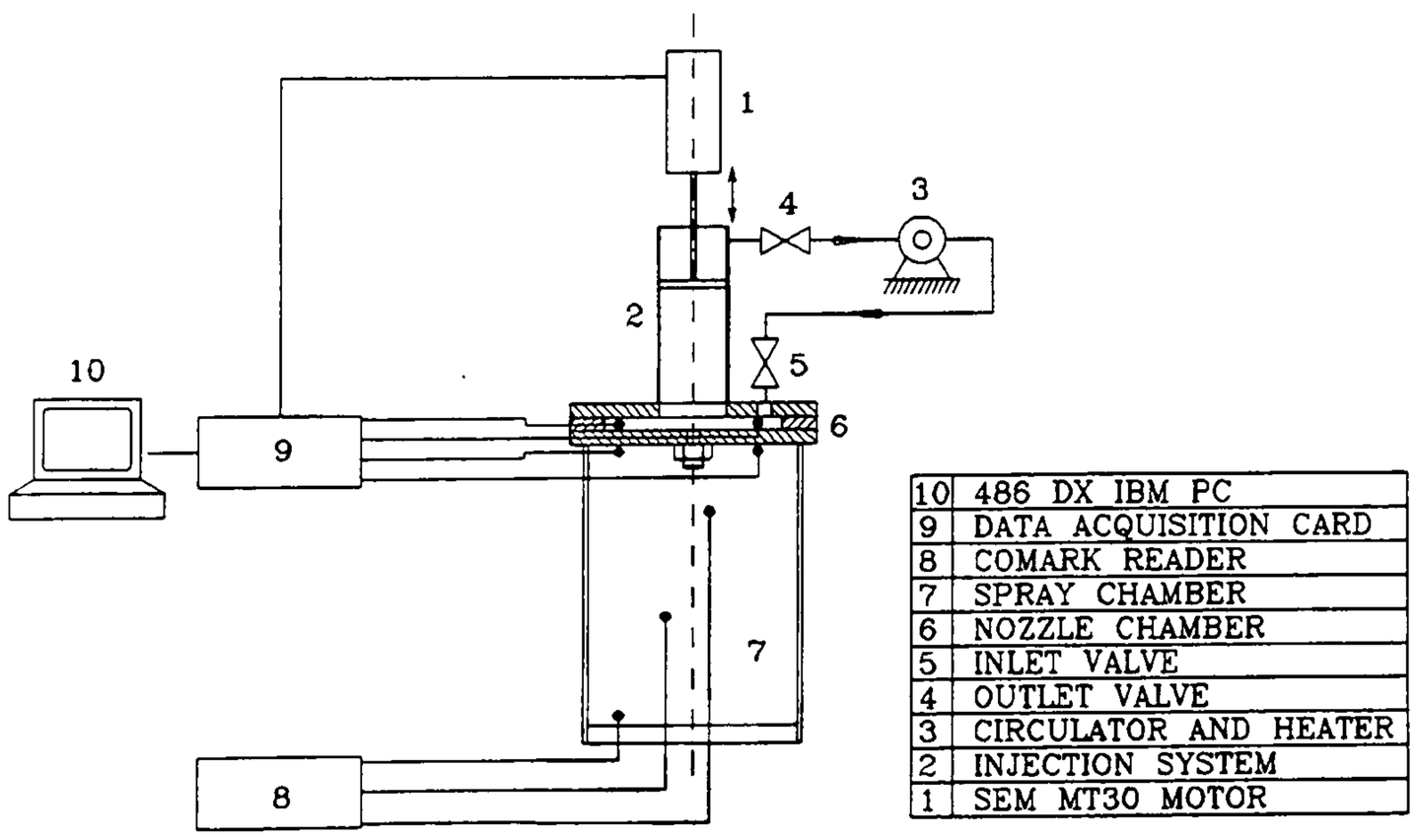

Figure 3.9 *Schematic of the experimental setup used in the present analysis*

The performance of various nozzle types, nozzle configurations and initial conditions were investigated in the experimental programme.

3.3.2 Testing rig

A schematic of the testing rig is shown in Figure 3.10.

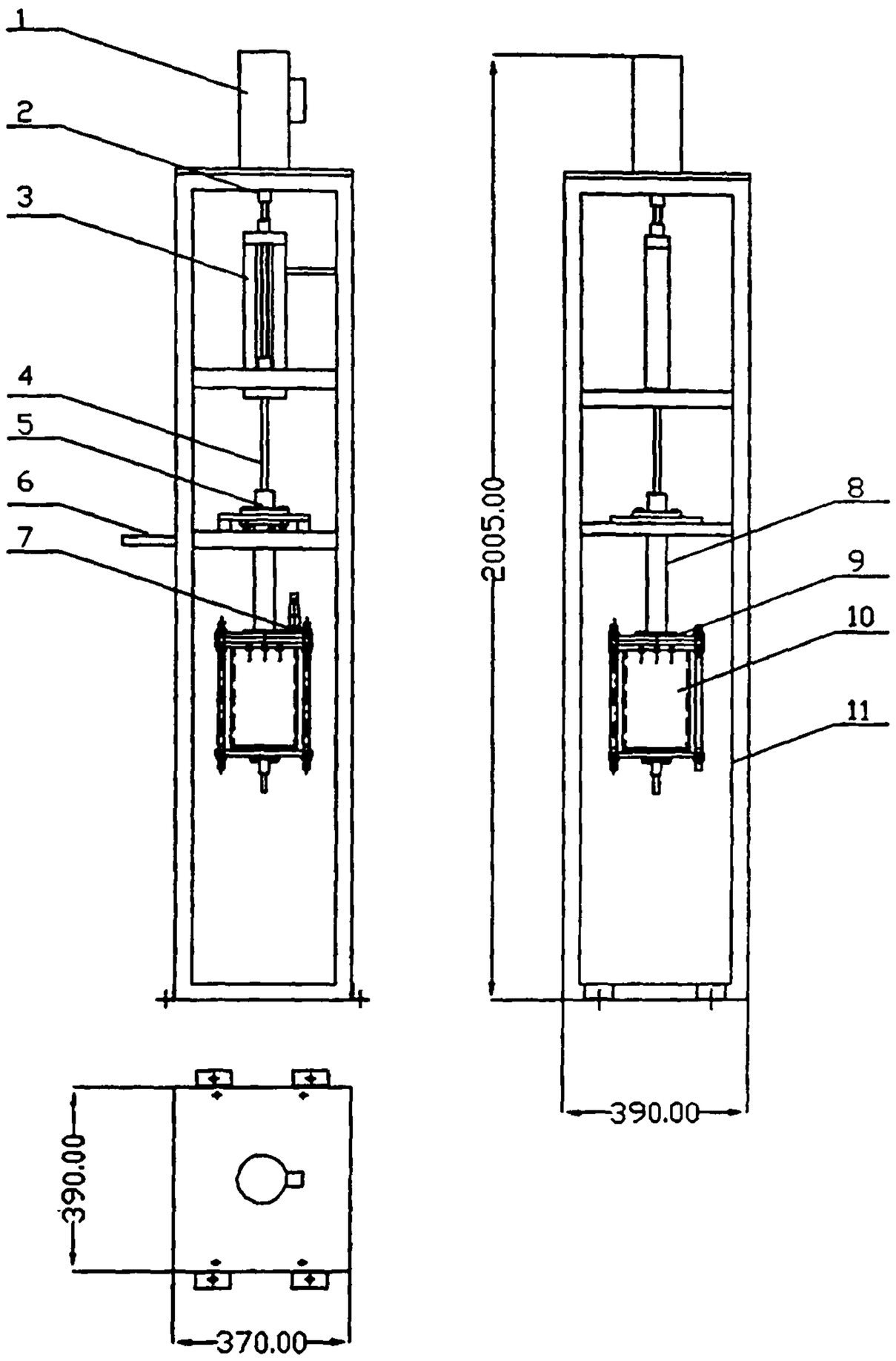

11	FRAME
10	SPRAY CHAMBER AND NOZZLES
9	NOZZLE CHAMBER
8	INJECTION CYLINDER & PISTON
7	WATER INLET VALVE
6	WATER OUTLET VALVE
5	BRASS BEARING
4	CONNECTING ROD
3	BALLSCREW ASSEMBLY
2	FLEXIBLE COUPLING
1	SEM DCDPM30 ELECTRIC MOTOR
	TESTING RIG

Figure 3.10 *Schematic of the testing rig*

The major components are:

- rigid support frame
- spray chamber assembly
- nozzle chamber
- injection cylinder and piston arrangement
- ballscrew drive assembly
- circulator and heater bath

Frame

A rigid frame, having the dimensions shown in Figure 3.10, supports most parts of the experimental rig. The forces exerted on the rig due to injection pressure of the sprayed liquid are high, requiring a robust and rigid construction of the frame. The support frame was manufactured from 45 mm x 35 mm square steel sections and was securely bolted to the floor.

Spray chamber

A diagram of the spray chamber is shown in Figure 3.11. The spray chamber is constructed from a clear acrylic (perspex) tube, 121 mm internal diameter, 6 mm wall thickness and 190 mm long. It is able to withstand maximum internal pressure of about 4 bar. Aluminium cover plates were fitted to both ends of the chamber which were provided with an internal PVC layer to minimise heat leakage.

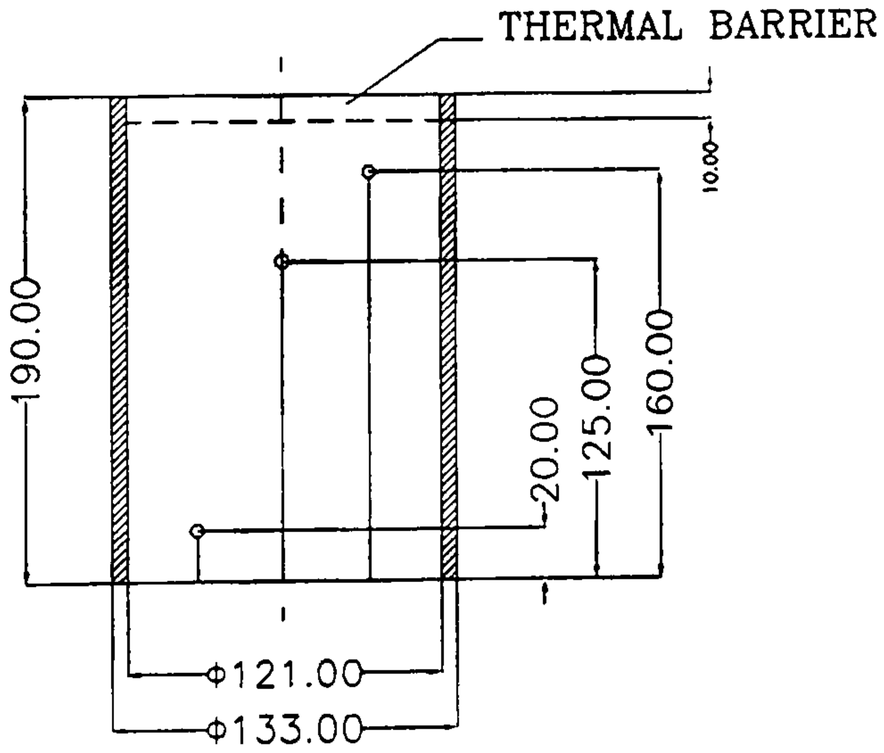

Figure 3.11 Diagram of the spray chamber

The spray nozzles are screwed into the top cover of the chamber. The position of the bottom cover is designed to be adjustable. This feature was not, however, used as the chamber volume was set by filling it with a certain amount of water. The bottom cover plate accommodates a valve to allow the chamber to be drained. To secure airtighteness, O-rings were placed between the perspex cylinder and top and bottom cover plates. The whole spray chamber assembly was clamped together using four tie-bolts.

Nozzle chamber

The nozzle chamber is bolted to the top cover of the spray chamber, accommodating the spray nozzles, and enables water under predetermined pressure and temperature to be uniformly supplied to the nozzles. The chamber is constructed from thick aluminium plates, to withstand the injection pressure without distortion, and is sealed by O-rings. A 1/2'' PN16 inlet ball valve is fitted in the top of the chamber to allow water at the required temperature to be circulated from the heater bath prior to injection. The top plate of the nozzle chamber also houses a pressure transducer and a thermocouple to measure the conditions of the injected water.

Injection cylinder and piston arrangement

The injection cylinder and piston assembly form a syringe like system that can deliver up to 0.28 litre of water into the nozzle chamber at a given flowrate. It is able to withstand the very high pressures that can build up during an experimental run. The cylinder is made of stainless steel tube of 41 mm internal diameter, 0.5 mm wall thickness and 224 mm length. Attachment to the nozzle chamber is via a flange and 4 M8 bolts, with an O-ring in between. The upper end of the cylinder is fitted with a DNO 1/4'' stainless steel outlet ball valve, that is opened during water circulation prior to injection. Thermal insulation is wrapped around the cylinder to prevent heat loss.

The piston, also made of stainless steel, is 40.5 mm in diameter and 20 mm long. It has two circumferential grooves accommodating rubber seals to prevent leakage. Piston motion is actuated using an electric motor and ballscrew assembly. Connection between the piston and the ballscrew assembly is via a connecting rod having a M12 thread.

The injection cylinder is attached to the frame at its upper flange and also acts as a support for the spray chamber below. This design ensures that there are no excessive forces due to the high injection pressures exerted on the fragile spray chamber.

The cylinder and piston system was tested and it proved to be leak proof even when pressures higher than 10 bar built up in the injection chamber.

Ballscrew assembly

The ballscrew assembly is driven by an SEM MT30R4-58 DC electric permanent magnet servomotor with a maximum power output of 0.5 kW and maximum speed of 2500 RPM. It well suited the power requirements of the injection system and proved to be easily

controllable.

The ball screw is connected to the servomotor via a standard FENNER LN70 flexible coupling. The ballscrew, type SFT 1205, has a characteristic diameter of 15 mm, a pitch of 5 mm and a length of 300 mm. The female part of the ballscrew is bolted into the ballscrew holder. The bottom part of the screw has cylindrical ending, that is fitted into a ball bearing thus enabling smooth running. The ball bearing and its holder are firmly fitted onto the rigid frame.

When the ballscrew starts spinning, the female part, together with the ballscrew holder and the connecting rod moved downwards (or upwards). This action causes the required displacement of the liquid injection piston.

Circulator and Heater bath

The circulator and heater bath, HAAKE/FISONS type DC1, is an essential part of the test rig. The bath has a digital controller enabling the bath temperature to be set to the required level and a digital display showing the instantaneous bath temperature. The circulator has inlet and outlet ports that are connected to the inlet and outlet valves of the testing rig via 5 mm internal diameter plastic hoses. The bath has an internal volume of 3 litre and the circulator is able to pump 15 l/min. The injection water is allowed to circulate through injection cylinder for about a minute prior to injection to ensure its uniform temperature.

3.3.3 Nozzles

Solid cone, 90° spray angle, pressure swirl nozzles manufactured by Delavan and Spraying Systems were used in the experimental work.

The nozzles were fitted on the top cover of the spray chamber, pointing downwards, in one or more positions shown in Figure 3.12.

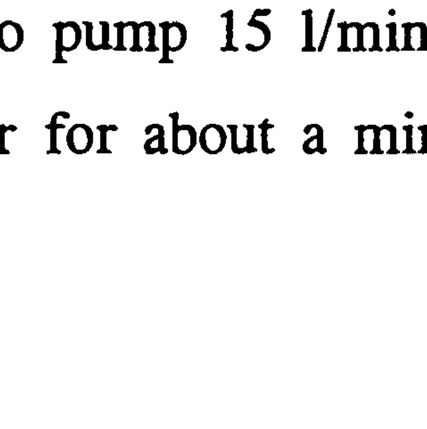

Figure 3.12 Nozzle positions

The following nozzle configurations were used:

- 1 central nozzle
- 1 side nozzle on the 60 mm circle
- 2 side nozzles equally-spaced on the 60 mm circle
- 4 side nozzles equally-spaced on the 60 mm circle

The manufacturer's data on operating pressure, spray angle and Sauter mean droplet diameter for two different flowrates of water at 80°C, are listed in Table 3.5 for each type of nozzle.

Nozzle reference	Water flowrate 35 litre/hour			Water flowrate 70 litre/hour		
	Operating pressure	Spray angle	SMD	Operating pressure	Spray angle	SMD
	bar	degree	micron	bar	degree	micron
DELAVAN						
BP 8-60	2.55	60	220.9	10.2	50	159.4
BP 10-90	1.63	90	216.0	6.55	80	150.6
BP 12-90	1.14	85	255.3	4.55	85	168.4
BP 14-90	0.83	80	296.9	3.31	90	185.2
BP 16-90	0.64	75	337.5	2.55	90	204.5
BP 18-90	0.50	65	396.5	2.0	90	224.3
SPRAYING SYSTEMS						
LN 8	3.8	86	160	15	90	130
LN10	2.95	82	180	10	85	160

Table 3.5 *Manufacturer's data on spray nozzles used in experimental programme*

3.3.4 Sensors

Two types of sensors are incorporated in the testing rig. These are thermocouples and pressure transducers.

Pressure transducers

The nozzle injection and the spray chamber pressures are measured using 0-7 bar silicon diaphragm pressure transducers, Druck type PDCR 810, which employ a strain gauge as the pressure sensing element. Both transducers have a recommended working range of up to 7 bar, but it is possible to reach double of this value without loss of accuracy. The maximum output voltage from the transducers of 100 mV, achieved with 10 V excitation, had to be scaled down to 30 mV to be compatible with the requirements of the National Instruments 5B38 signal conditioning module. Two units had to be designed to scale down the excitation voltage to the required values as shown in Figure 3.13.

Thermocouples

The following mineral insulated thermocouples are used:

(i) Thermocouple type T (copper - constantan), stainless steel sheath of 1.5 mm in diameter, used to measure the temperature of water prior to injection.

(ii) Thermocouple type T (copper - constantan), stainless steel sheath of 1.5 mm in diameter, used to measure temperature at the top of the spraying chamber.

(iii) A further three type T thermocouples are used for measuring the initial and final gas temperature distribution inside the spray chamber. Their positions are shown in Figure 3.11.

Only the outputs from thermocouples (i) and (ii) are monitored using the National Instruments data acquisition hardware and software.

3.3.5 Data acquisition and control system

A block diagram of the system is shown in Figure 3.13. The system enables both data acquisition and control of the test rig. At the heart of the measurement and control system of the experimental apparatus is a National Instruments Lab PC+ multifunction input/output board which is installed in a IBM compatible 486 DX/33 MHz/8 Mb RAM microcomputer. This board performs analogue - to - digital conversion of the inputs from the pressure transducers and thermocouples, and digital - to - analogue conversion of the voltage output to control the servomotor speed, both with 12 bit resolution.

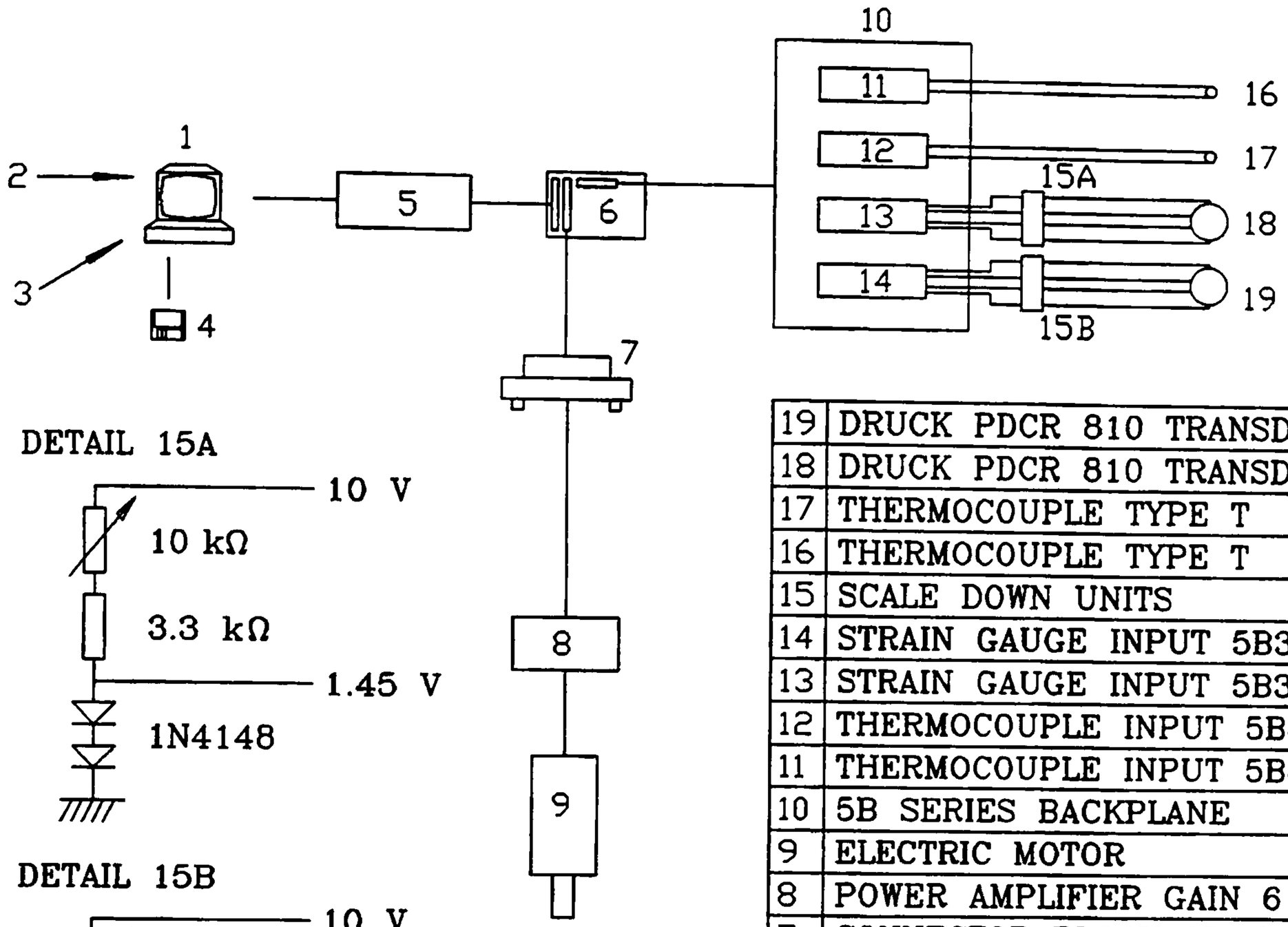

19	DRUCK PDCR 810 TRANSDUCER
18	DRUCK PDCR 810 TRANSDUCER
17	THERMOCOUPLE TYPE T
16	THERMOCOUPLE TYPE T
15	SCALE DOWN UNITS
14	STRAIN GAUGE INPUT 5B38
13	STRAIN GAUGE INPUT 5B38
12	THERMOCOUPLE INPUT 5B47
11	THERMOCOUPLE INPUT 5B47
10	5B SERIES BACKPLANE
9	ELECTRIC MOTOR
8	POWER AMPLIFIER GAIN 6
7	CONNECTOR BLOCK CB-50
6	CABLE ADAPTER SC-2053
5	Lab-PC+ DAQ BOARD
4	DATA STORAGE DISK
3	SIGMAPLOT SOFTWARE
2	LabVIEW SOFTWARE
1	IBM 486 33 MHz/8 Mb RAM

Figure 3.13 *Block diagram of the data acquisition and control system.*

The analogue inputs from the pressure transducers and thermocouples are connected to the Lab PC+ data acquisition board via individual analogue signal conditioning modules which provide isolation, noise resistance and amplification. The signal conditioning modules plug into an externally mounted National Instruments 5B series backplane. The following signal conditioning modules are used:

(i) 5B47 Linearised Thermocouple Input Module providing signal conditioning, amplification and cold junction compensation for the type T thermocouples. The output range of the 5B47 unit is 0 to ∓5 V and the bandwidth is 4 Hz. The unit has built in linearisation capability for the type T thermocouples, therefore no additional manipulation of data is necessary.

(ii) 5B38 Strain Gauge Input Module providing excitation, signal conditioning and the amplification for the Druck pressure transducers. The maximum input range to the unit is 30 mV, therefore two scale down units, shown in Figure 3.13, were used to reduce the excitation voltages for the pressure transducers measuring the liquid injection pressure and pressure inside the spray chamber to 1.45 V and 4 V respectively, thus obtaining output voltages acceptable for the signal conditioning module. The output from the 5B38 unit is ∓5 V and the bandwidth is 10 kHz. Thus the unit is fast enough to monitor any pressure changes occurring inside the injection cylinder and inside the spray chamber.

The data acquisition board is adjusted to operate with four differential inputs, thus all available inputs are used by the four sensors discussed above.

The 5B backplane is connected to the Lab PC+ card via a SC2051 National Instruments Cable Adapter. This adapter also accommodates a CB-50 Pin Connector, that is used as a voltage output terminal for the servomotor control. The Lab PC+ board has two output channels configured to generate voltages within range of ∓5 V. An external power amplifier, type RCA R1189-4, with gain set to 6, was employed to boost up the card output voltage to the level required to power the electric servomotor.

3.3.6 Data acquisition and control software

The Lab PC+ board is controlled via LabView for Windows, together with NI-DAQ driver software, by National Instruments. The program and interface is created in LabView environment using graphical programming language 'G', and designed such that maximum control and flexibility over the experimental programme is achieved. The interface panel is shown in Figure 3.14.

The **device**, **channels** and **output channel** windows specify the hardware of the data acquisition and control system. Channels 0, 1, 2, 3 of the Lab PC+ board (**device** 1) are scanned using a timed, buffered and continuous data acquisition technique to obtain data from the thermocouples and pressure transducers.

The system uses a buffer size of 15 000 samples and the chosen scan rate is 40 Hz

per channel for all experiments. The **scan backlog** is continuously monitored and shows amount of data acquired minus the amount of data read from the data acquisition buffer. If the **scan backlog** increases the data are not being read fast enough and the **number of scans to read at a time** value must be increased.

The nozzle **configuration** determines the time span of the experiment. The typical flowrate per nozzle was 20 g/s and the time span for a one nozzle configuration was 15 seconds, for a two nozzle configuration 7.5 seconds and for a four nozzle configuration 3.5 seconds. This time span is monitored by the Oki 82C53 counter/timer mounted on the Lab PC+ board. It is displayed in **total time** window on the control panel.

The program itself has three sequences:

(i) Read Sequence - reads the reference timer value.

(ii) Control and Data Acquisition Sequence - controls the experiment, performs data acquisition and actual time recording into the file specified in the **file path** window.

(iii) Modification Sequence - the acquired values are read from the file, compensated for initial inaccuracies of the pressure transducers, converted to pressure (bar) and temperature (°C) units and stored in the file, overwriting the old, unconverted, values. The results are then displayed on the four graph windows.

The data can be easily imported into any common spreadsheet or, as in this work, into a plotting package. Additional details and a full description of the program is given in Appendix G.

3.3.7 Experimental technique and programme

Water was used as the working liquid for all the tests reported in this work. Each test was conducted for a given type and configuration of nozzles. The initial proportion of gas and water in the spray chamber was set by partially filling the chamber with water. Hence the height of the sprace occupied by the gas could be varied from 190 mm to 76 mm (four water levels were tested).

Front Panel

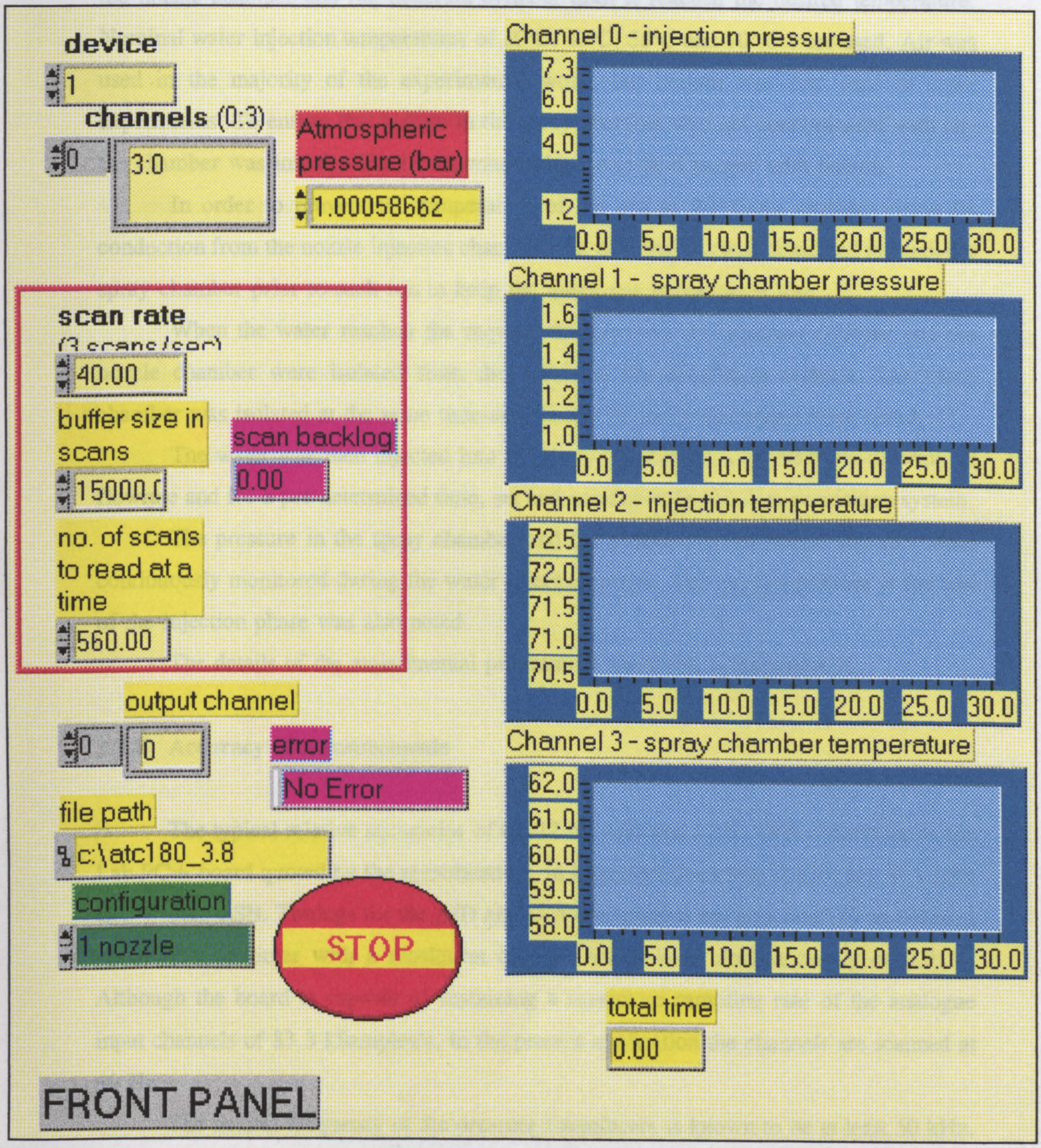

Figure 3.14 *Front panel of the user interface*

The water to be injected was circulated through an external temperature controlled bath, the nozzle chamber and the injection cylinder until it reached the desired temperature. Nominal water injection temperatures of 20°C, 40°C, 55°C and 70° C were used. Air was used in the majority of the experimental work, but helium was also used in some experiments. To ensure that helium in the spray chamber was not contaminated with air, the chamber was initially filled with water which was then purged with helium.

In order to prevent the temperature of the gas in the spray chamber rising by conduction from the nozzle injection chamber, the working gas was circulated through the spray chamber prior to each run to keep the initial gas temperature low.

When the water reached the required temperature the injection cylinder and the nozzle chamber were isolated from the bath and the circulation stopped. The spray chamber was isolated at the same time and the initial gas temperatures were noted.

The water was then injected into the spray chamber at a constant pre-determined flowrate and for a pre-determined time, set and controlled by the data acquisition system.

The pressure in the spray chamber and the pressure in the nozzle chamber were continuously monitored during the water injection phase. The gas temperature at the end of the injection phase was also noted.

The details of the experimental programme are given in Appendix H.

3.3.8 Accuracy of measurements

The typical relative accuracies of the 12 bit A/D and 12 bit D/A convertors on the Lab PC+ board quoted by the manufacturer, in least significant bits (LSB), are $\mp$ 1 LSB and $\mp$ 0.25 LSB. Timings for the A/D and D/A conversions are generated by an onboard 16 bit counter/timer with a resolution of 1 μs and a base clock accuracy of 0.01%. Although the board is capable of sustaining a maximum sampling rate of the analogue input channels of 83.3 kSamples/s, in the present application the channels are scanned at 40 Hz.

The natural frequency of the pressure transducers is known to be at least 50 kHz. Assuming that the frequency response is linear up to 20% of this frequency, would allow the transducers to be used to monitor rapid pressure rises ($>$ 25 μs). The technical

specification provided by the transducer manufacturer gives the combined non-linearity, hysteresis and repeatability as ∓0.1% best straight line. The transducers are temperature compensated to give a total error band of ∓0.5% of full-scale over the range 0°C to 50°C, although higher temperatures in the permissible operating range, which extends up to 80°C, have been utilised in the experiments.

Type T mineral insulated thermocouples, stainless steel sheath diameter 1.5 mm, are used to measure the water injection temperature and the temperature in the upper part of the spray chamber. The standard tolerance for this thermocouple type is ∓1°C up to 100°C.

The specified accuracy of the signal conditioning modules is ∓0.05%. The bandwidth of the full bridge strain gauge modules used for the pressure transducers is 10 kHz. The thermocouple modules, which also provide cold junction compensation, have a bandwidth of only 4 Hz.

3.3.9 Experimental results and discussion

As discussed above, experiments were conducted for one central nozzle, one perimeter nozzle and two and four symmetrically spaced side nozzle configurations. Five different Delavan nozzle sizes and two different Spraying Systems nozzle sizes were covered. Furthermore, the effects of the initial gas pressure, p_o, the initial volume of the spray chamber, the type of gas present, air or helium, the initial temperature difference between the injected liquid and the gas and the effects of nozzle flowrate were also considered. The experimental results are presented in the form of dimensionless pressure in the chamber, defined as the ratio p/p_o, against the injection time. It should be pointed out that the temperature of the injected liquid varied somewhat over the duration of the experiment, as shown in Figure 3.15, and hence the best estimates of temperature are quoted. Furthermore, even though the initial pressure, p_o, was nominally atmospheric in the majority of tests, it, once again, varied from experiment to experiment. However, all the figures presented give important results in that they show accurately the rapid initial rise of pressure in the spray chamber, which is closely related to the initial rapid rate of heat transfer between droplet sprays and the surrounding gas. Figure 3.15 shows the influence of the injected liquid temperature on the variation of spray chamber pressure with time with all other parameters held constant. The table in Figure 3.15 gives the initial gas temperature distribution inside the spray chamber measured using the Comark thermocouple reading device. T_1 is measured at the top, T_2 at mid - height and T_3 at the bottom of the spray chamber. Figure 3.11 gives the exact positions of the thermocouples.

In general the pressure rise in the spray chamber is due to three mechanisms:

(i) increase in the temperature of the contained gas,

(ii) increase in the steam partial pressure by evaporation from the injected liquid,

(iii) decrease in the volume of the gas due to the accumulation of the injected liquid in the spray chamber.

This is well demonstrated in Figure 3.15 where the initial rapid pressure rise is predominantly due to mechanisms (i) and (ii), as the gas is heated to approach the liquid injection temperature and liquid is evaporated from the droplets.

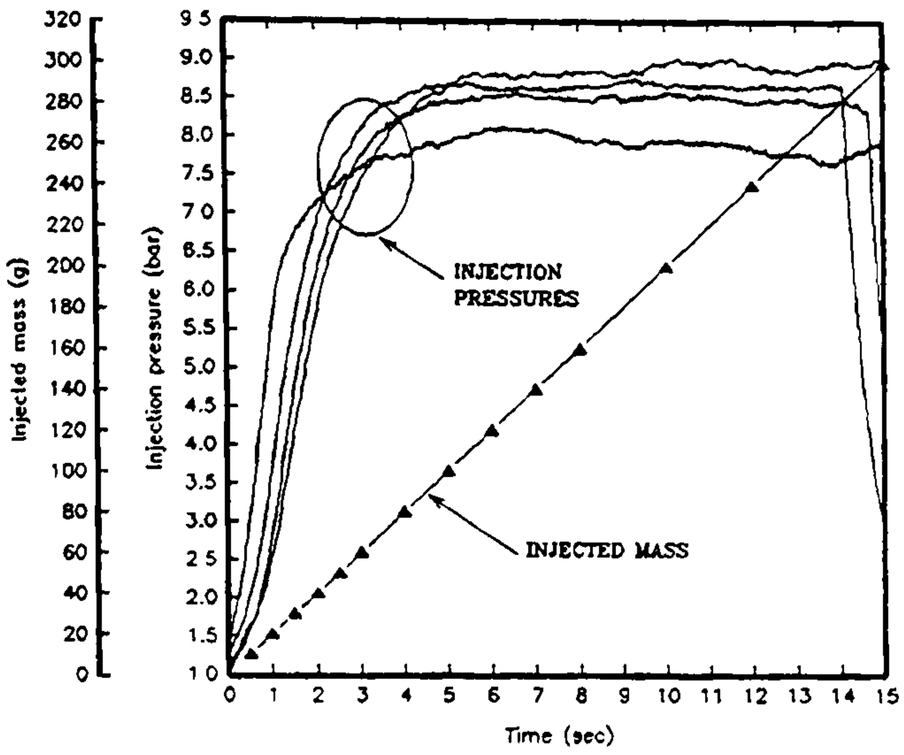

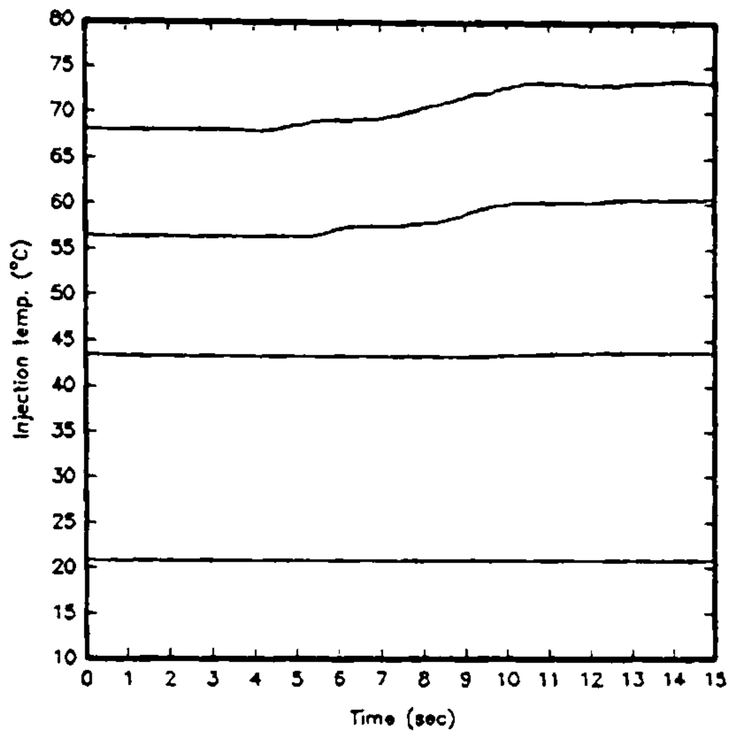

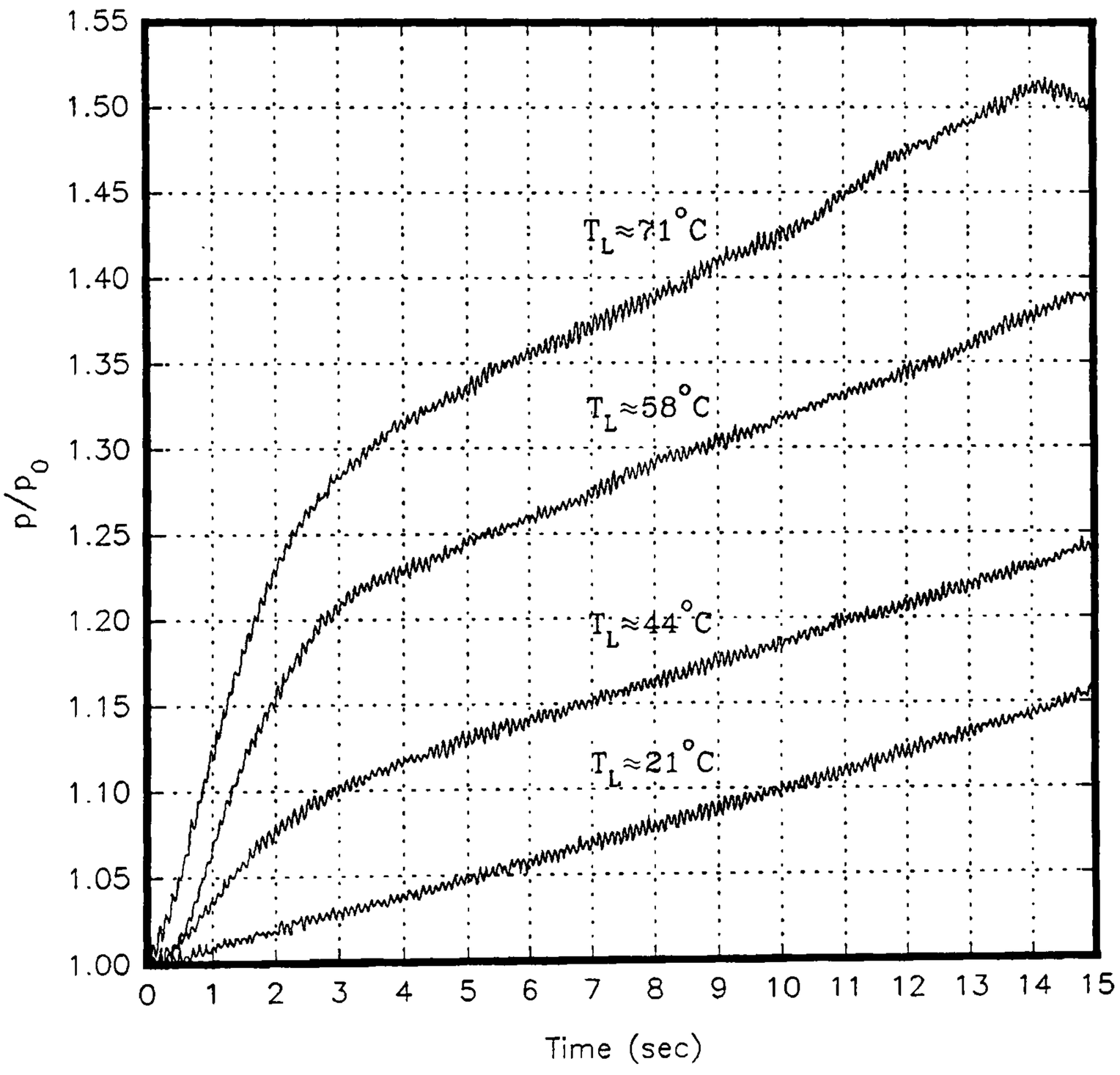

INJECTION TEMP. (°C)	21	44	58	71
T_1 (°C)	19.1	29.9	29.7	35.1
T_2 (°C)	19.0	29.4	28.8	33.1
T_3 (°C)	19.1	30.3	29.5	33.7

Figure 3.15 *Influence of injected liquid temperature for 1 central BP10-90 nozzle in air, water injection flowrate 20 g/s, p_o= 1.0004 bar.*

As the injection period proceeds the pressure - time curves assume a lower positive slope consistent with mechanism (iii). As expected, Figure 3.15 shows that an increase in the difference between the temperature of the liquid and the initial gas temperature results in a greater overall pressure rise in the chamber and a faster initial rate of pressure increase.

The top left graph of Figure 3.15 shows the apparatus injection pressure - time characteristics. All experiments presented in this work had more or less the same injection characteristics and they will not, therefore, be discussed again. The time required for the nozzle operating pressure to build-up to the level corresponding to the manufacturer's data was normally 2 - 3 seconds. Preliminary experiments involving the collection of injected liquid for short injection times showed that the required injection flowrate was maintained during this initial period, this is well demonstrated on the graph. Also, tests with water at ambient temperature, so that the pressure rise in the spray chamber was only due to mechanism (iii) above, showed a linear rise of the spray chamber pressure, thus providing further confirmation that the injection flowrate remained constant throughout the injection period.

Figure 3.16 shows the influence of thermophysical properties of the surrounding gas, either helium or air, on the variation of pressure with time. Even though the injection temperature of the water was lower in the test with helium, and thus the overall pressure rise was lower, it can be seen, that the rate of pressure rise during the first second is faster for helium than for air due to its higher thermal conductivity.

Figure 3.17 shows the influence of the initial pressure in the chamber with air as the working gas. It shows that the rise in the dimensionless pressure, p/p_o, is faster for a lower initial pressure, p_o. However, the rise in the absolute pressure, p, is faster for the higher initial pressure p_o. The absolute pressure change for fifteen seconds injection duration for the lower initial pressure is 0.52 bar, compared to 0.74 bar for the higher initial pressure. This agrees with the findings for a droplet of 70 μm diameter given by Chin and Lefevbre [3].

Figure 3.18 shows the influence of the installation position of a single nozzle by comparing the pressure rise characteristics for one central nozzle and one nozzle of the same design installed at one of the perimeter positions shown in Figure 3.12.

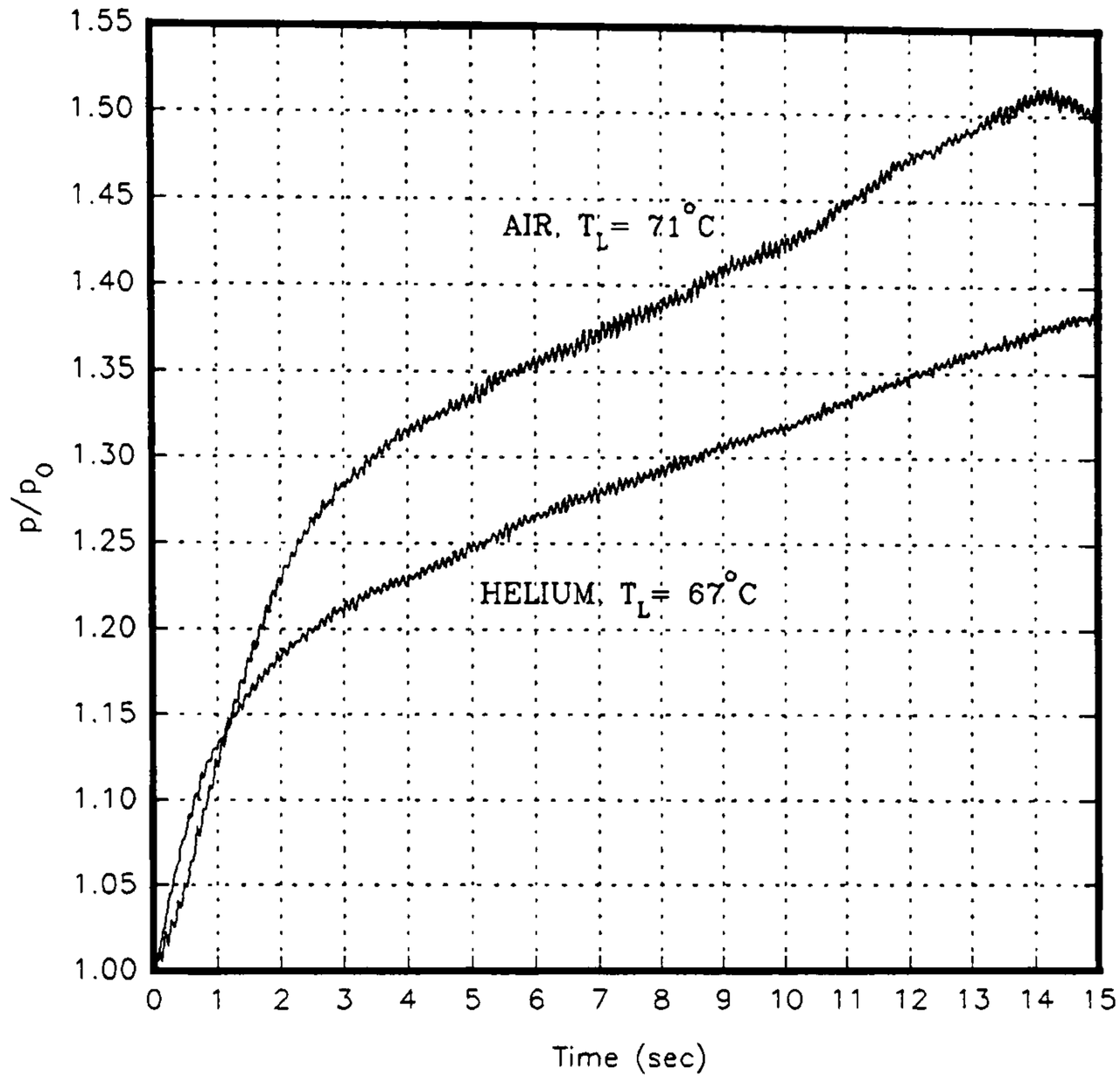

Figure 3.16 *Influence of the surrounding gas with 1 central BP10-90 nozzle, water flowrate 20 g/s.*

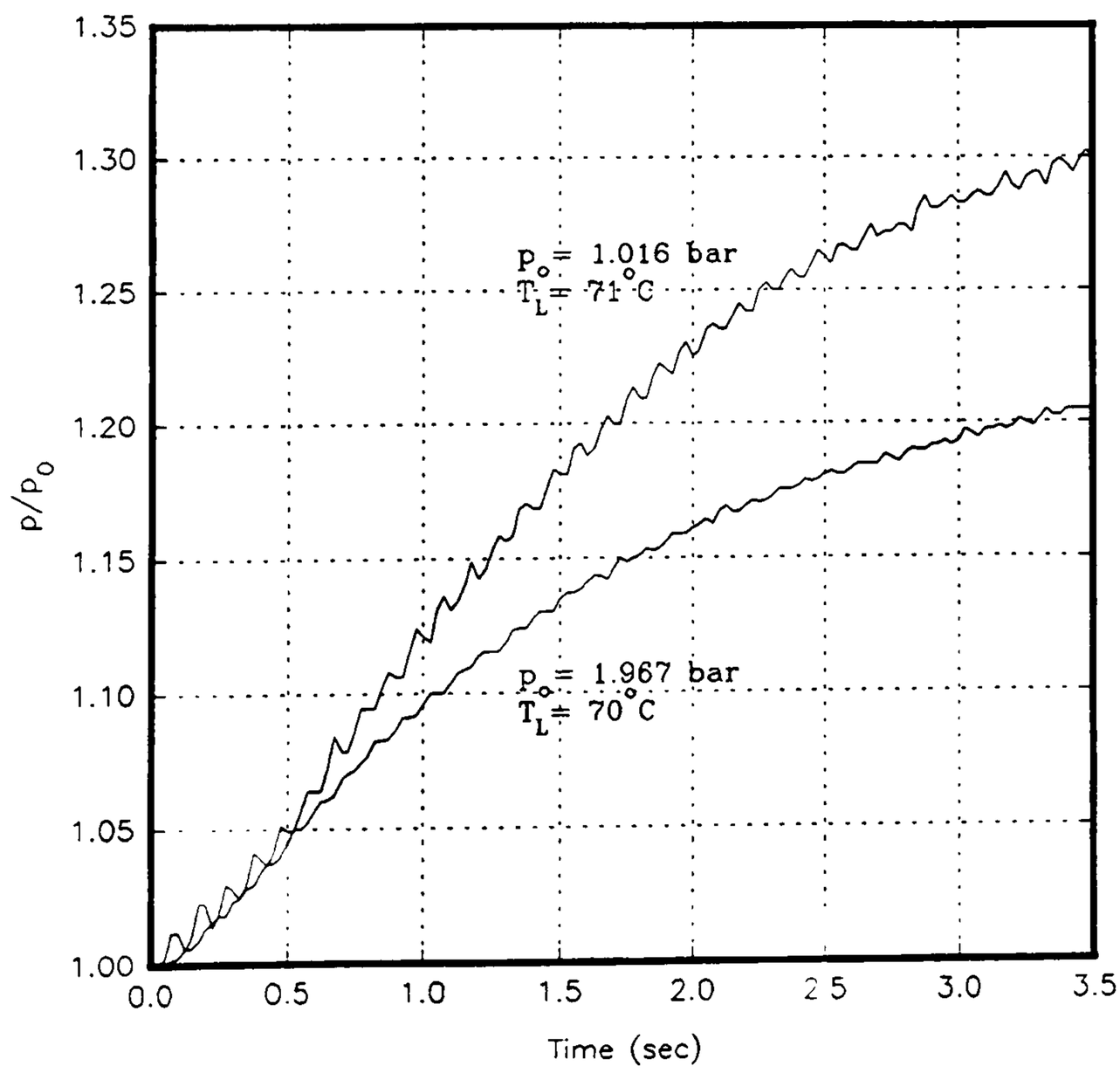

Figure 3.17 *Influence of the initial pressure level with 1 central BP10-90 nozzle in air. Water flowrate 20 g/s.*

The same test conditions apply to both cases. The figure indicates that the pressure rise is somewhat greater for the central nozzle. This is due to the larger volume of the zone in which the spray droplets are in contact with the surrounding gas. This contact zone is defined by the volume inside the spray cone, which is bounded by the free surface of the accumulated liquid at the bottom of the chamber and the walls of the spray chamber. Furthermore a larger proportion of the spray is also lost by the formation of a liquid film on the chamber wall in the case of non - central nozzle.

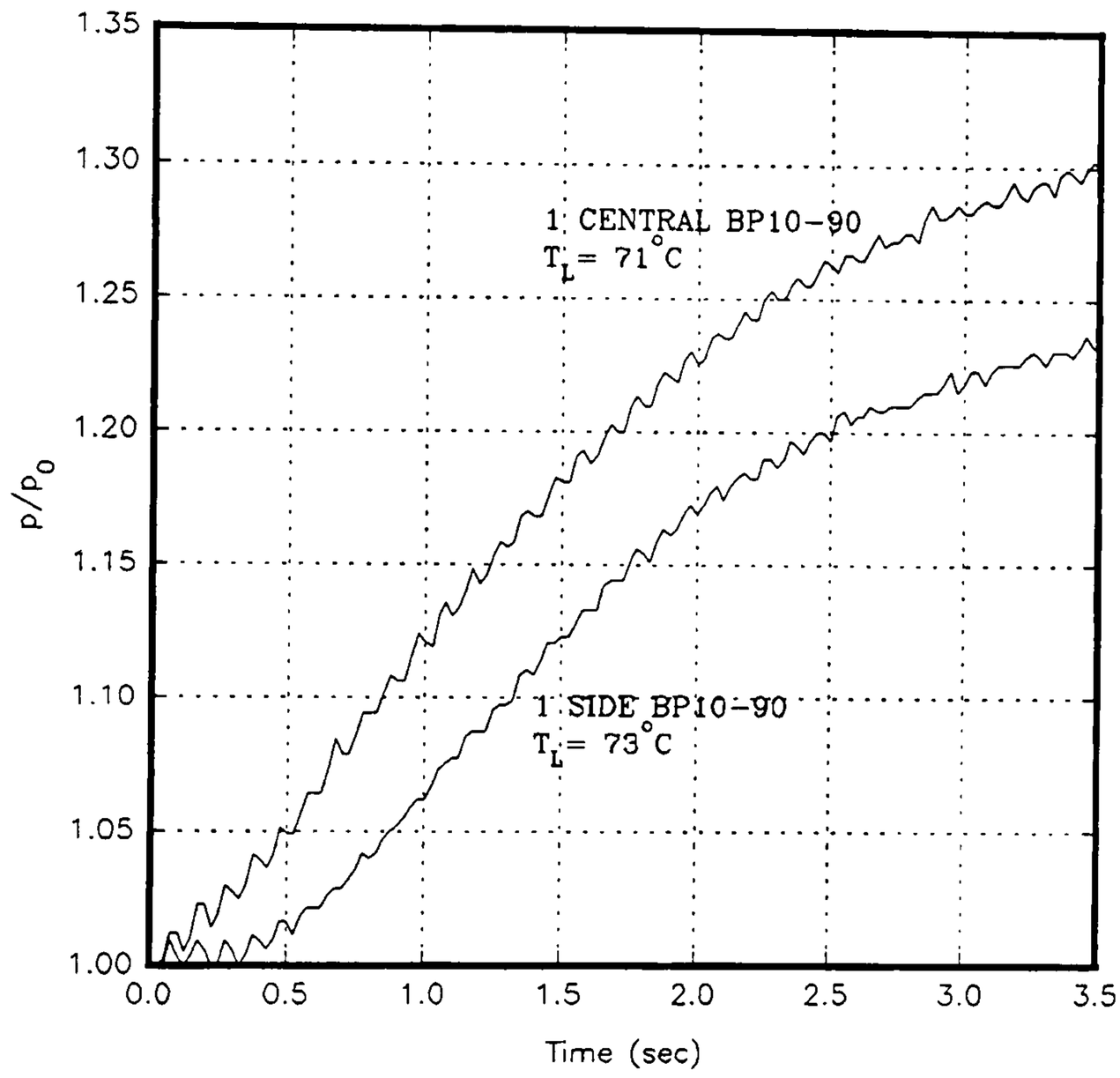

Figure 3.18 *Influence of BP10-90 nozzle position in the spray chamber*

Figure 3.19 shows the influence of the orifice size of a single nozzle on the variation of the spray chamber pressure with time with all other parameters held constant. This figure includes test results for five different sizes of Delavan 90° solid cone nozzles. Manufacturer's data on these nozzles, including Sauter mean diameter are given in Table 3.5. The results indicate that the pressure rise depends only weakly on the size of the nozzle. Furthermore, there is no observable systematic influence of the nozzle size on the pressure rise in the chamber. For example, nozzles BP10-90 and BP12-90 indicate better heat transfer mechanism than nozzles BP14-90, BP16-90 and BP18-90, but nozzle BP12-90 gives better performance than nozzle BP10-90, and nozzle BP18-90

gives better performance than nozzles BP14-90 and BP16-90. Hence the effect of the Sauter mean diameter of the spray droplets, which covered the range 150 - 224 μm according to the manufacturer, appears to be small in the range investigated.

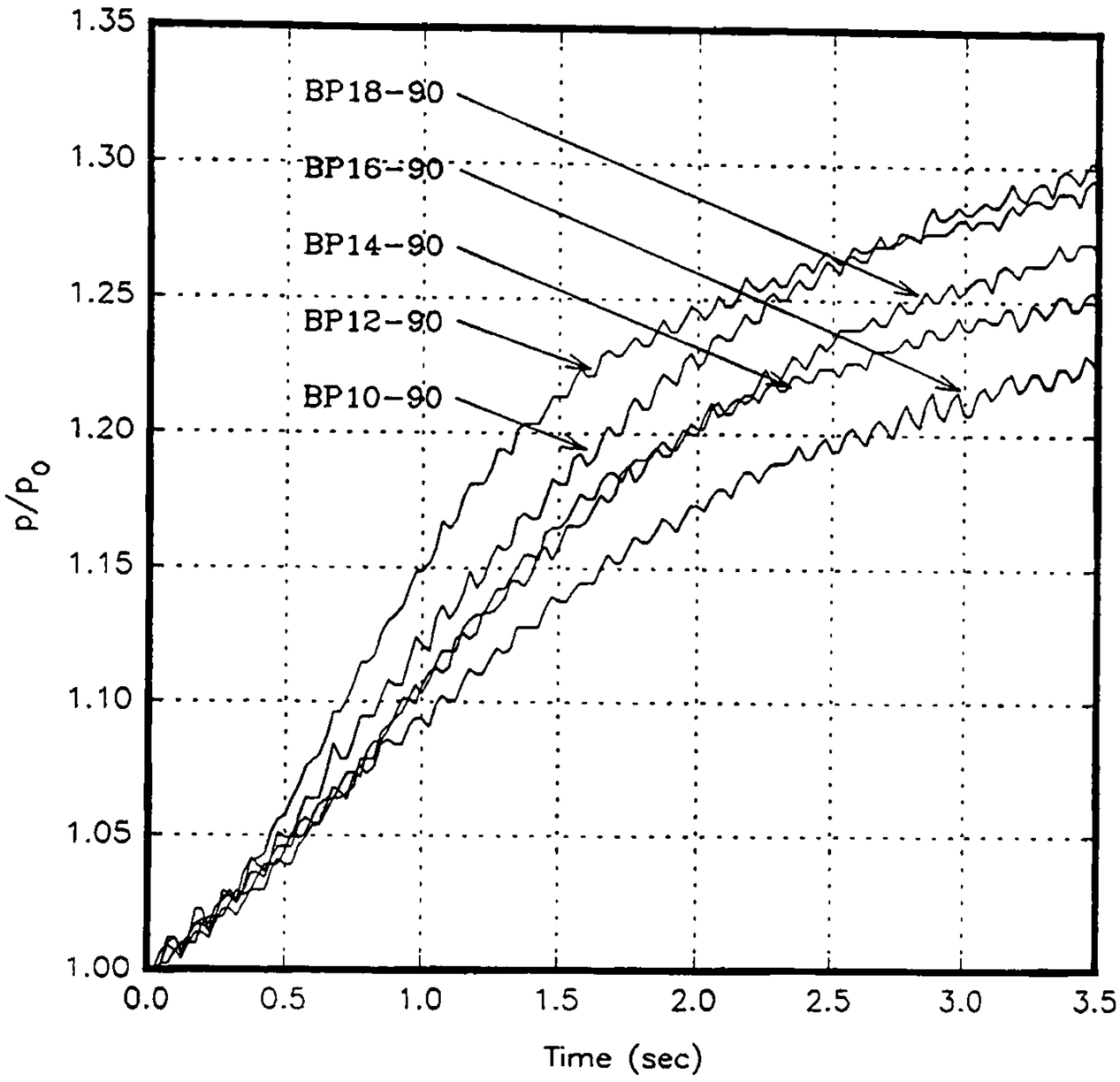

Figure 3.19 *Comparison of nozzle performance, water flowrate 20 g/s.*

Figure 3.20 shows the influence of the number of identical BP14-90 nozzles on the variation of spray chamber pressure with time. The figure compares the performance of one central nozzle, two side nozzles and four side nozzles. In each case the water flowrate is 20 g/s per nozzle (20 g/s for the single nozzle, 40 g/s for two nozzles and 80 g/s for four nozzles). Not surprisingly the figure indicates that the total flowrate of the injected liquid has a primary influence on the overall rates of heat transfer and evaporation and thus on the pressure rise in the chamber.

Finally, Figure 3.21 compares the performance of one central BP18-90 nozzle with a liquid flowrate of 20 g/s and one central BP10-90 nozzle with a liquid flowrate of 10 g/s, with all other parameters constant. These two cases were chosen, because, as indicated in Table 3.5, the nominal Sauter mean drop diameters quoted by the manufacturer are similar (224 micron and 216 micron respectively). This figure once

again confirms the above statement that the flowrate of the injected liquid is of primary importance in controlling the pressure rise in the spray chamber.

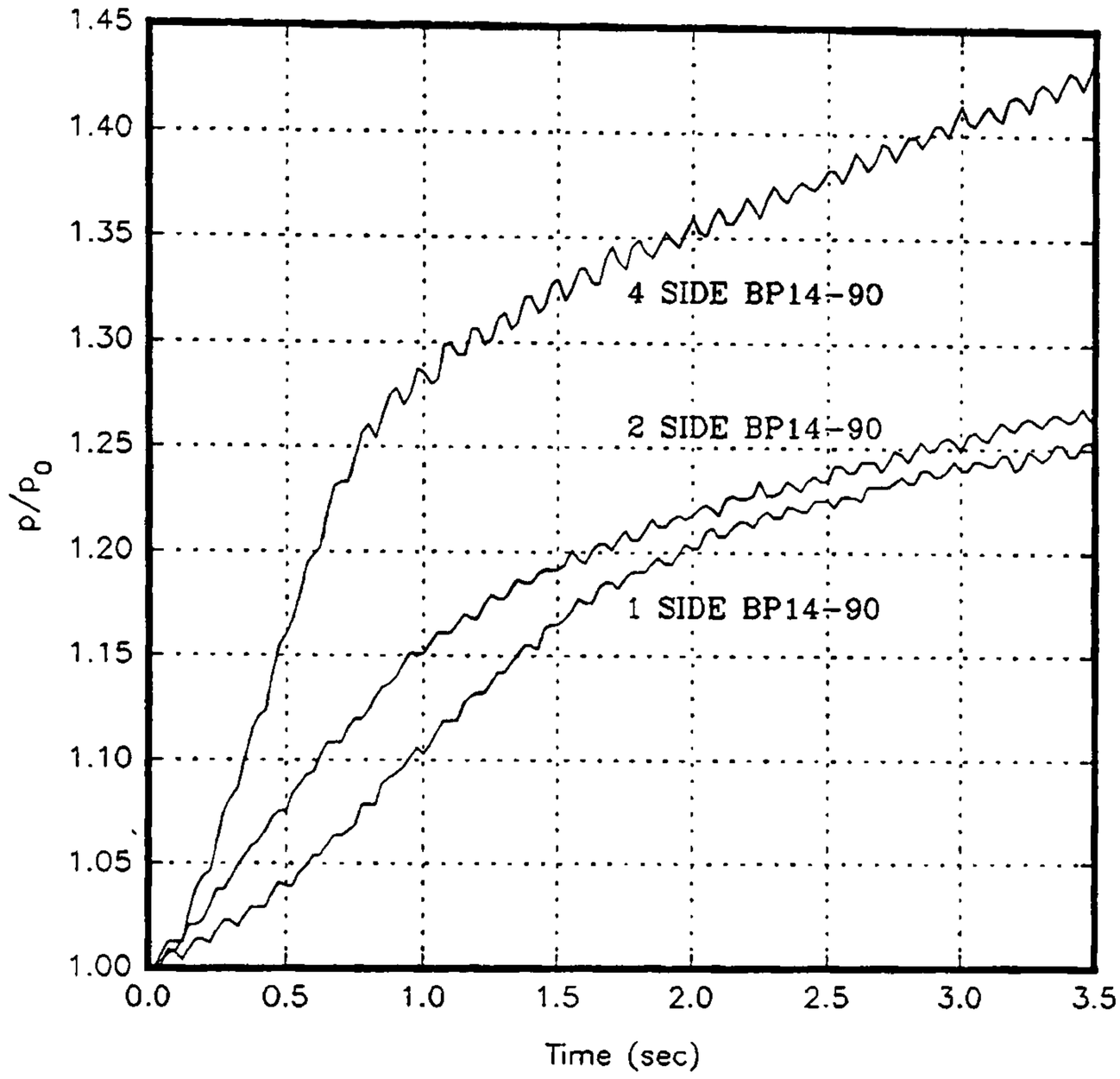

Figure 3.20 *Influence of number of BP14-90 nozzles in air (water flowrate 20 g/s per nozzle)*

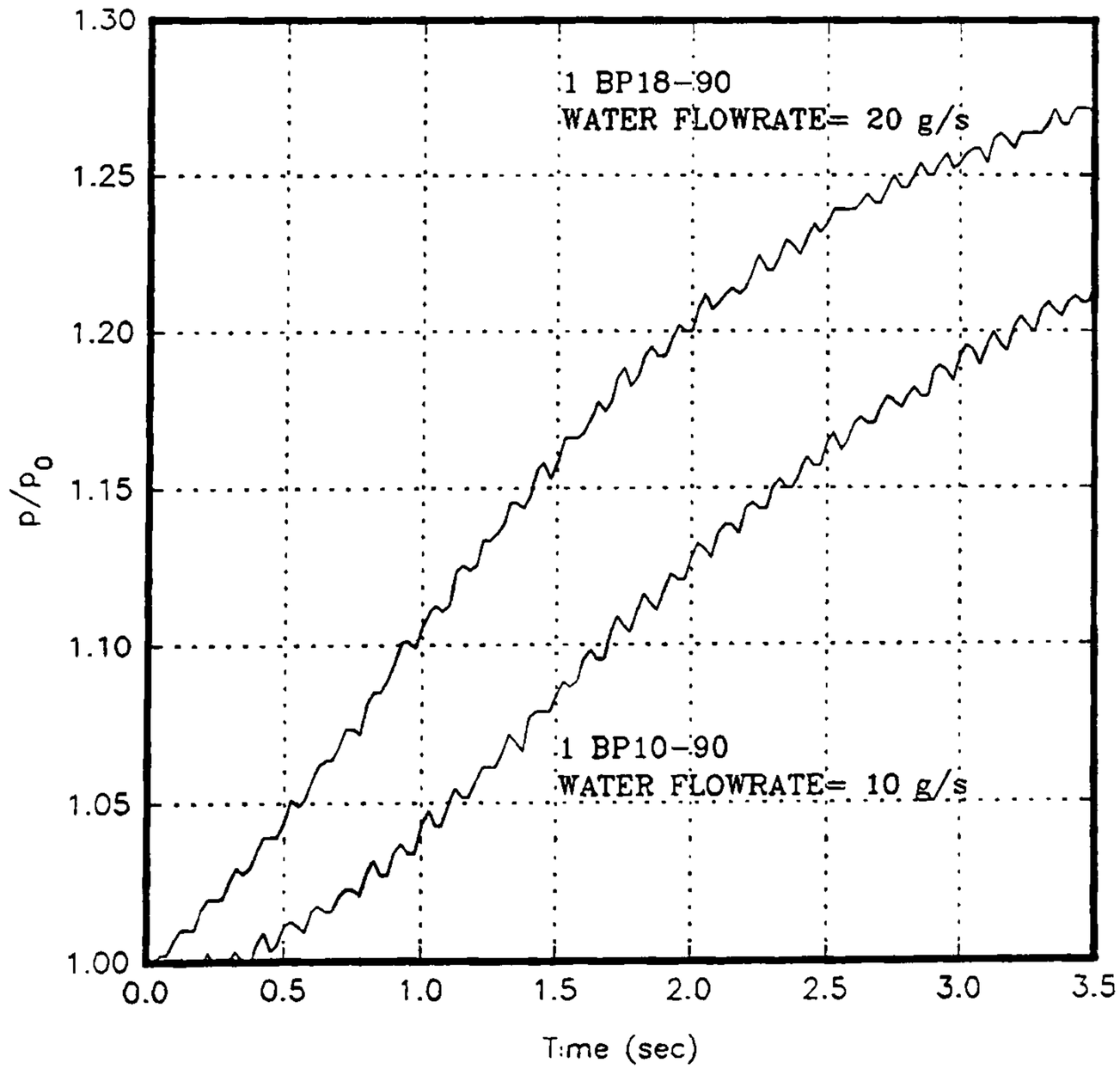

Figure 3.21 *Influence of water flowrate with 1 central nozzle in air and SMD approximately equal for both*

A similar series of experiments was run with Spraying Systems LN8 and LN10 nozzles - see Appendix H - and the same general conclusions may be drawn from the results obtained. However one important difference observed was that the pressure drop across the Spraying Systems LN series of nozzles is higher for the same flowrate than that of Delavan nozzles, and therefore the energy required to produce the spray was higher.

To summarise, it may be stated that the experimental results obtained for different sizes of nozzles indicate that the heat transfer characteristics are, to a first approximation, independent of the size of the nozzles, in the range investigated in this work. For all practical purposes the heat transfer characteristics between spray droplets and gases depend primarily on the mass flowrate of the injected liquid. Since the energy required for the production of spray droplets increases with the pressure drop across the nozzles, and since the size of the nozzles does not markedly influence the heat transfer rates, the most efficient way of producing high heat transfer rates between spray droplets and gases is to use larger nozzles. From the selection of nozzles tested, the Delavan BP18-90, therefore, seems to be the most suitable one for the intended industrial application.

3.4 BULK ANALYSIS

3.4.1 General

This section presents an analysis of the transient pressure rise in a closed gas - filled chamber due to the injection of hot liquid spray droplets. The analysis involves a bulk treatment of the process based on the assumption of ideal gas behaviour together with an energy balance between the liquid and gas phases. It considers the spray chamber as a single control volume. A nondimensional equation for the transient pressure change in the spray chamber is obtained. This equation includes a dimensionless group, which isolates the three parameters which primarily influence the heat transfer characteristics between the spray droplets and the gas: the typical droplet size, the typical droplet velocity and the typical droplet heat transfer coefficient.

The analysis considers that, as shown in Figure 3.22 for the case of one central nozzle, the spray chamber consists of three zones: (i) the liquid zone, formed by the water accumulating at the bottom of the spray chamber, whose volume increases with time, (ii) the transfer zone, formed by the solid cone of the injected droplets and bounded by the walls of the cylindrical chamber and the surface of the liquid zone, and (iii) the still zone, which is the volume of the chamber above the transfer zone (and the liquid zone). It is assumed that the heat and mass transfer processes are confined to the transfer zone, and that the still zone and the transfer zones are separated by an imaginary partition, which allows the equality of pressures between the two zones, but does not allow heat or mass transfer between the two zones.

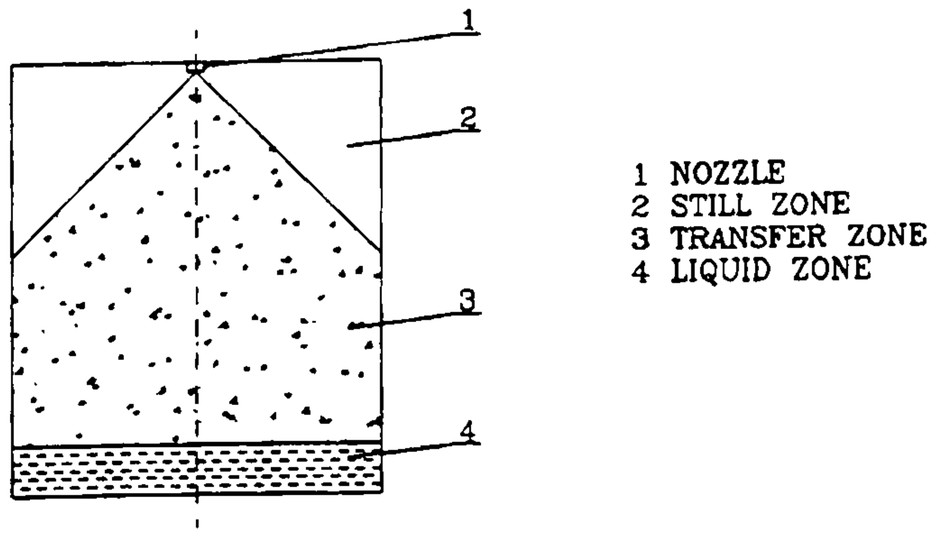

Figure 3.22 Zone classification of the spray chamber

Details of zone geometries for different nozzle configurations are given in Appendix I.

3.4.2 Governing equations

If we assume that both the gas and the vapour obey the ideal gas law, the total pressure in the transfer zone, p_T is given by

$$p_T = p_{GT} + p_{VT} \tag{3.10}$$

where

$$p_{GT}V_T = R_G M_{GT} T_{GT} \tag{3.11}$$

$$p_{VT}V_T = R_V M_{VT} T_{VT} \tag{3.12}$$

where p_{GT} and p_{VT} are the partial pressures of the gas and the water vapour in the transfer zone, V_T is the volume of the transfer zone, R is the gas constant, M_T is the mass of the constituent in the transfer zone, T_T is temperature of the constituent in the transfer zone, and the additional subscripts G and V refer to the gas and the vapour constituents respectively.

Similarly the total pressure in the still zone, p_s is given by

$$p_s = p_{GS} + p_{VS} \tag{3.13}$$

where

$$p_{GS}V_S = R_G M_{GS} T_{GS} \tag{3.14}$$

$$p_{VS}V_S = R_V M_{VS} T_{VS} \tag{3.15}$$

where p_{GS} and p_{VS} are the partial pressures of the gas and the vapour phase in the still zone, V_S is the volume of the still zone, M_S is the mass of the phase in the still zone, T_S is the constituent temperature in the transfer zone, and the additional subscripts G and V refer to the gas and the vapour phase respectively.

It is assumed that the temperature in the still zone is uniform and constant and equal to the initial temperature in the spray chamber, T_{S0}. It is further assumed that, due to the vigorous mixing in the transfer zone, the water vapour and gas are in thermal

equilibrium and the mixture temperature is uniform and equal to T_T

$$T_T = T_{GT} = T_{VT} \tag{3.16}$$

and that, the partial gas pressure in the spray chamber, p_G is uniform

$$p_G = p_{GT} = p_{GS} \tag{3.17}$$

and hence that from equations (3.11) and (3.14)

$$p_G\,(V_T+V_S) = R_G(M_{GT}T_T+M_{GS}T_{S0}) \tag{3.18}$$

The heat and mass transfer between a representative droplet and the surrounding gas can be represented by equation similar to equation (3.4) as

$$m_D c_{pD}\frac{dT_D}{dt} = hS_D(T_T-T_D) + h_{fg}\frac{dm_D}{dt} \tag{3.19}$$

where m_D is the mass of the droplet, T_D is the droplet temperature, S_D is the droplet surface area, t is time, c_{pD} is the specific heat of the droplet, h is the droplet-gas heat transfer coefficient and h_{fg} is the specific enthalpy of evaporation. Equation (3.19) shows that the droplet loses its internal energy by sensible cooling (first term) and by evaporation (second term); the vapour will be diffusing from the droplet at droplet surface temperature T_D.

The mixture of gas and vapour surrounding each droplet is heated by the sensible heat convected from the surface of the droplet and by the sensible heat convected by the diffusing vapour, q_S

$$m_m c_{vm}\frac{dT_T}{dt} = hS_D(T_D-T_T) + q_S \tag{3.20}$$

where m_m is the mass of the gas/vapour mixture associated with each droplet and c_{vm} is its specific heat. The mass transfer term in equation (3.19) can be calculated, for example, by equation (3.3). However, there are two major problems. First, the appropriate value of the mass transfer coefficient is difficult to determine and second, it is difficult to calculate the sensible heat transferred from the diffusing vapour, q_S. Hence

a different method has been developed in this work. It is based on three major assumptions.

First, since $m_D c_{Pd}$ is generally much greater than $m_m c_{vm}$, dT_D/dt is generally much smaller than dT_T/dt, and it is assumed that the droplet temperature, T_D, is uniform and constant. Second, it is assumed that the evaporation is not responsible for the heating of the mixture associated with each droplet, nor for the increase in the heat capacity of the mixture. In other words, q_S is assumed equal to zero and only the gas is assumed to be in contact with the droplet. Third, the evaporation process leads to an increase of the vapour partial pressure in the transfer zone, p_{VT}, which is assumed equal to the saturation pressure at the transfer zone temperature. Hence equation (3.20) simplifies to

$$m_G c_{vG} \frac{dT_T}{dt} = hS_D(T_D - T_S) \tag{3.21}$$

where m_G is the mass of gas associated with each droplet and c_{Vg} is its specific heat.

3.4.3 Reduction of the governing equations

The mass of gas associated with each droplet is calculated next. The number of droplets produced per second, n is given by

$$n = \frac{\dot{m}_L}{m_D} \tag{3.22}$$

where $\dot{m}_L$ is the mass flowrate of the injected spray liquid. The average number of droplets present in the transfer zone, N_D is

$$N_D = n\, t_D \tag{3.23}$$

where t_D is the average droplet residence time in the transfer zone, given as

$$t_D = \frac{l_T}{U_D} \tag{3.24}$$

where l_T is the length of a typical droplet trajectory in the transfer zone, shown in Figure 3.22, and U_D is the typical droplet velocity calculated on the basis of pressure drop across

the nozzle using equation (3.1). Neglecting the volume occupied by each water droplet, we can then calculate m_G as

$$m_G = \rho_G \frac{V_T}{N_D} \tag{3.25}$$

Substituting equations (3.22) to (3.25) into equation (3.21) we obtain

$$\frac{\rho_G \rho_L c_{vG}}{3\dot{m}_L} \frac{aU_D}{h} \frac{V_T}{l_T} \frac{dT_T}{dt} = T_D - T_T \tag{3.26}$$

where a is the typical droplet radius.

It is assumed that all thermophysical properties with the exception of ρ_G are independent of pressure and temperature and hence constant. The gas density is obtained from the ideal gas law relationship as

$$\rho_G = \rho_{G0} \frac{p_G}{p_{G0}} \frac{T_{T0}}{T_T} \tag{3.27}$$

where the additional subscript 0 refers to the initial condition in the spray chamber. Substituting equation (3.27) into equation (3.26) the following dimensionless equation is obtained

$$P_G T_0 K_1 K_2 K_3 \frac{dT}{dt^*} = T(1-T) \tag{3.28}$$

where

$$P_G = \frac{p_G}{p_{G0}} \tag{3.29}$$

$$T = \frac{T_T}{T_D} \tag{3.30}$$

$$T_0 = \frac{T_{T0}}{T_D} \tag{3.31}$$

$$t^* = t\left(\frac{g}{D}\right)^{0.5} \tag{3.32}$$

$$K_1 = \frac{V_T}{3l_T D^2} \tag{3.33}$$

$$K_2 = \frac{aU_D k_G}{h(gD^5)^{0.5}} \tag{3.34}$$

$$K_3 = \frac{\rho_{G0}\rho_L c_{vG} g D^4}{k_G \dot{m}_L} \tag{3.35}$$

and where g is the gravitational acceleration, k_G is the thermal conductivity of the gas and D is the diameter of the spray chamber.

Equation (3.28) relates the dimensionless gas pressure in the chamber, P_G and the dimensionless temperature in the transfer zone, T to dimensionless time t^* as a function of four dimensionless groups, which are now discussed in turn. The group T_0 gives the initial temperature in the spray chamber and is, for given initial conditions, a known constant. The group K_1 is determined by the geometry of the spray chamber and the configuration of the nozzles and can be regarded, to a first approximation, as a known constant. The group K_2 contains the important parameters of droplet heat transfer. It can be regarded for given experimental arrangements as a constant, but it is very difficult to determine its value *a priori*. This group is discussed later. The final group K_3 is again fixed by the geometry of the spray chamber (its diameter), the initial conditions and the mass flowrate of the injected liquid, and it can be regarded as a constant for constant mass flowrate of the injected liquid. In order to solve equation (3.28) a substitution is made for P_G, and this is determined as follows.

The complete volume of the spray chamber, V_C is given as the volume of the three zones

$$V_C = V_S + V_T + V_L \tag{3.36}$$

where, if the fraction of the injected liquid evaporated is neglected, the volume of the

liquid zone, V_L is given as

$$V_L = \frac{\dot{m}_L t}{\rho_L} \tag{3.37}$$

Substituting equations (3.36) and (3.37) into equation (3.18), and noting that the temperature in the still zone remains constant at its initial value, which is equal to the initial temperature in the transfer zone T_{T0}, the following expressions are obtained:

$$p_G(V_C - V_L) = R_G(M_{GT}T_T + M_{GS}T_{T0}) \tag{3.38}$$

$$p_{G0}V_C = R_G(M_{GT}T_{T0} + M_{GS}T_{T0}) \tag{3.39}$$

Equations (3.38) and (3.39) can be combined to express P_G as

$$P_G = \frac{(1-M)T_0 + MT}{T_0(1-Ht^*)} \tag{3.40}$$

where

$$H = \frac{\dot{m}_L}{\rho_L V_C}\left(\frac{D}{g}\right)^{0.5} \tag{3.41}$$

$$M = \frac{M_{GT}}{M_G} \tag{3.42}$$

and where M_G is the total mass of gas in the spray chamber. The dimensionless group H is set by the geometry and the flowrate of the injected liquid and is, for given conditions, a constant. The dimensionless group M gives the proportion of gas in the transfer zone and is, to a first approximation, also regarded as a constant.

Equation (3.40) is then substituted into equation (3.28) to obtain

$$\frac{(1-M)T_0 + MT}{T_0(1-Ht^*)} T_0 K_1 K_2 K_3 \frac{dT}{dt^*} = T(1-T) \tag{3.43}$$

which can be integrated to give the following equation for T as a function of t^*:

$$\frac{(1-T)^{M+(1-M)T_0}}{T^{(1-M)T_0}} = \frac{(1-T_0)^{M+(1-M)T_0}}{T_0^{(1-M)T_0}} e^{-\frac{1}{K_1K_2K_3}\left(t^* - \frac{Ht^{*2}}{2}\right)} \quad (3.44)$$

Equation (3.44) represents an equation of the type $f(T,t^*) = 0$. It is marched in time to solve for T as a function of t^*, with M, H, K_1, K_2 and K_3 taken as parameters using a simple *regula falsi* method [66].

The dimensionless gas partial pressure, P_G can then be calculated from equation (3.40). Since the initial conditions in the spray chamber are known, the initial partial gas pressure, p_{G0} can be determined as

$$p_{G0} = p_0 - p_{V0} \quad (3.45)$$

where p_0 is the initial total pressure and p_{V0} is the initial vapour partial pressure in the spray chamber. The gas partial pressure at any given time, p_G can be calculated from P_G and p_{G0}. The vapour partial pressure at any given time, p_V is given, as discussed above, by the saturation pressure at temperature T_T, which is obtained from the initial temperature T_{T0} and the dimensionless temperature T. The total pressure at any given time, p can then be obtained as

$$p = p_G + p_V \quad (3.46)$$

and the pressure ratio P can be finally obtained as

$$P = \frac{p}{p_0} \quad (3.47)$$

As discussed above, all dimensionless groups with the exception of K_2 are known *a priori* from the geometry of the spray chamber, the number and the position of the nozzles, the initial conditions and the temperature and the mass flowrate of the injected liquid. The dimensionless group K_2 is obtained by trial and error for each experimental condition by determining the value of K_2 which gives the best agreement between the theoretical solution and the experimental data.

3.4.4 Results and discussion

The dimensionless groups M and K_1 are obtained from the geometry of the spray chamber and the configuration of the spray nozzles. It should be pointed out that these two groups are regarded as constant even though in practice they are subject to some variation; the error introduced by this assumption is small. The dimensionless groups K_3 and H are obtained from the thermophysical properties of the two fluids, the geometry of the spray chamber and the mass flowrate of the injected spray liquid. It was assumed that the air in the chamber was initially saturated with water vapour. This assumption has only a second order influence for low initial air temperature in the chamber, but becomes more important as the initial air temperature increases. However, high initial air temperatures were only encountered for tests involving two or four nozzles or at low water flowrates, when some hot water entered the spray chamber from the nozzles before the commencement of the tests and the evaporation increased the water vapour pressure.

As discussed in Section 3.4.3, the governing equations are solved for values of the parameters corresponding to the experimental conditions to obtain spray chamber pressure, p, as a function of time, t, and the best value of the dimensionless group K_2 is determined by trial and error by comparing the theoretical results with the experimental data. Figures 3.23 - 3.27 indicate that, for the appropriate value of the group K_2, there is a reasonable agreement between the experimental data and the theoretical solutions for all nozzle configurations and different initial conditions covered in the test programme. Furthermore, these figures also show that for the conditions investigated in this work, the best value of the dimensionless group K_2 is independent of the size and the number of nozzles, the mass flowrate of the injected spray liquid and all other parameters, and is given by

$$K_2 \simeq 2 \times 10^{-5} \tag{3.48}$$

Figure 3.28 shows the influence of the dimensionless group K_2 on the predicted variation of pressure with time for typical experimental arrangements with one central nozzle. The figure indicates that the influence of K_2 is particularly important for short injection times, when transient effects dominate. Similarly, Figure 3.29 shows the influence of the number of nozzles on the variation of pressure with time for typical experimental arrangements

with one central nozzle, water flowrate of 20 g/s per nozzle and $K_2 = 2 \times 10^{-5}$.

All results presented show the variation of the absolute spray chamber pressure with time.

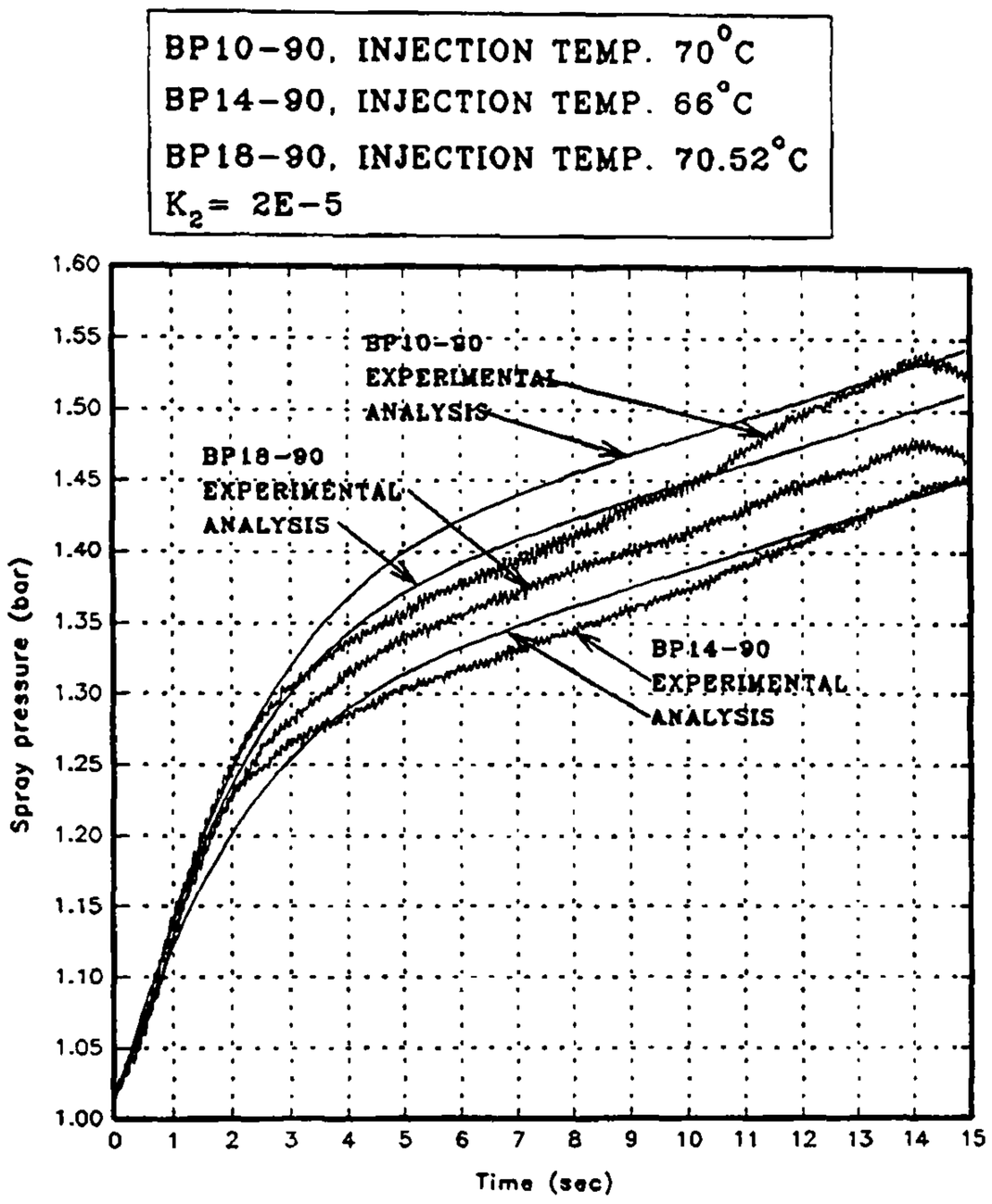

Figure 3.23 *Comparison of experimental and analytical results for different single, central nozzles, flowrate 20 g/s*

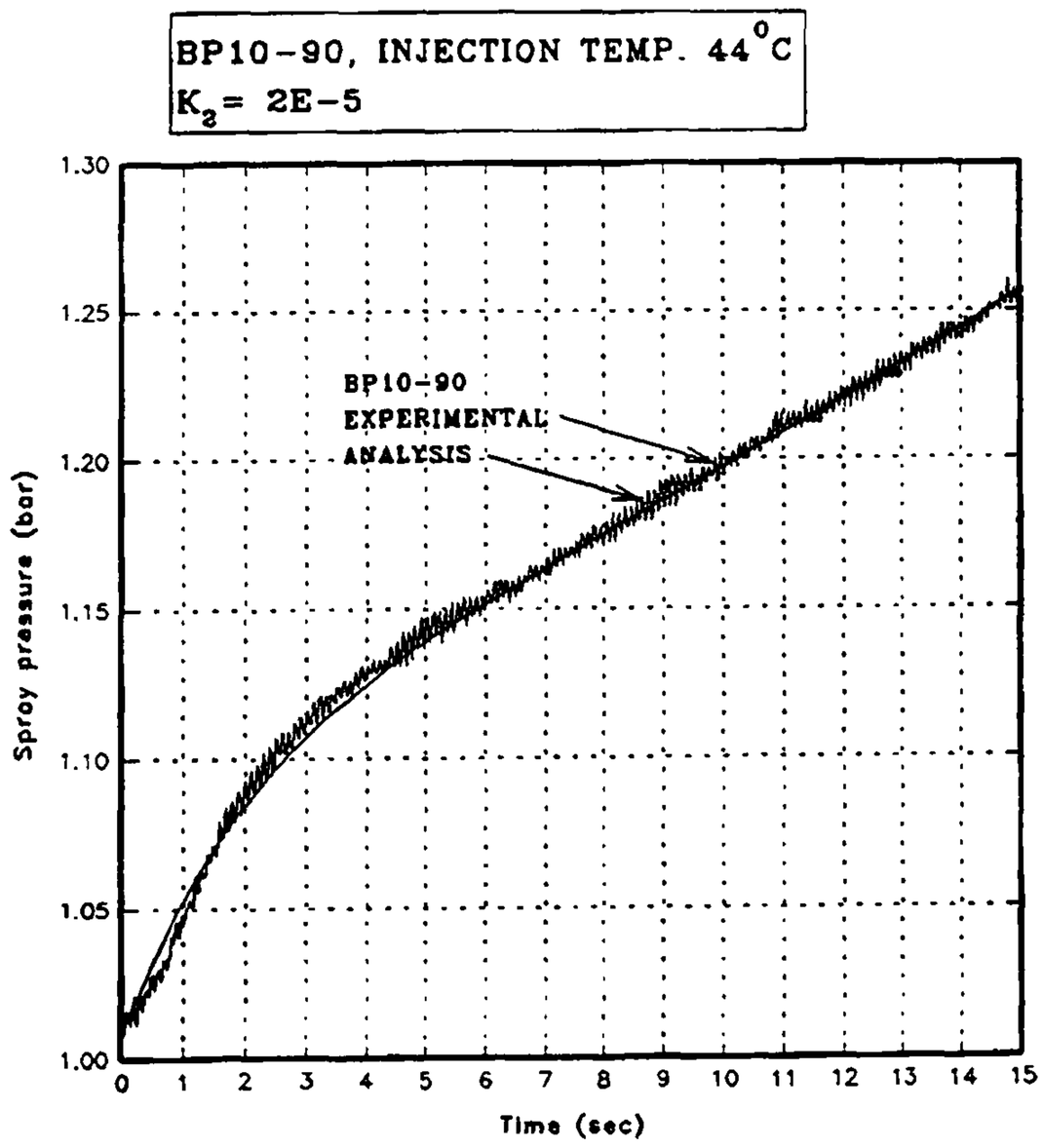

Figure 3.24 *Comparison of analytical and experimental results for one central BP10-90 nozzle, injection temperature 44°C, flowrate 20 g/s*

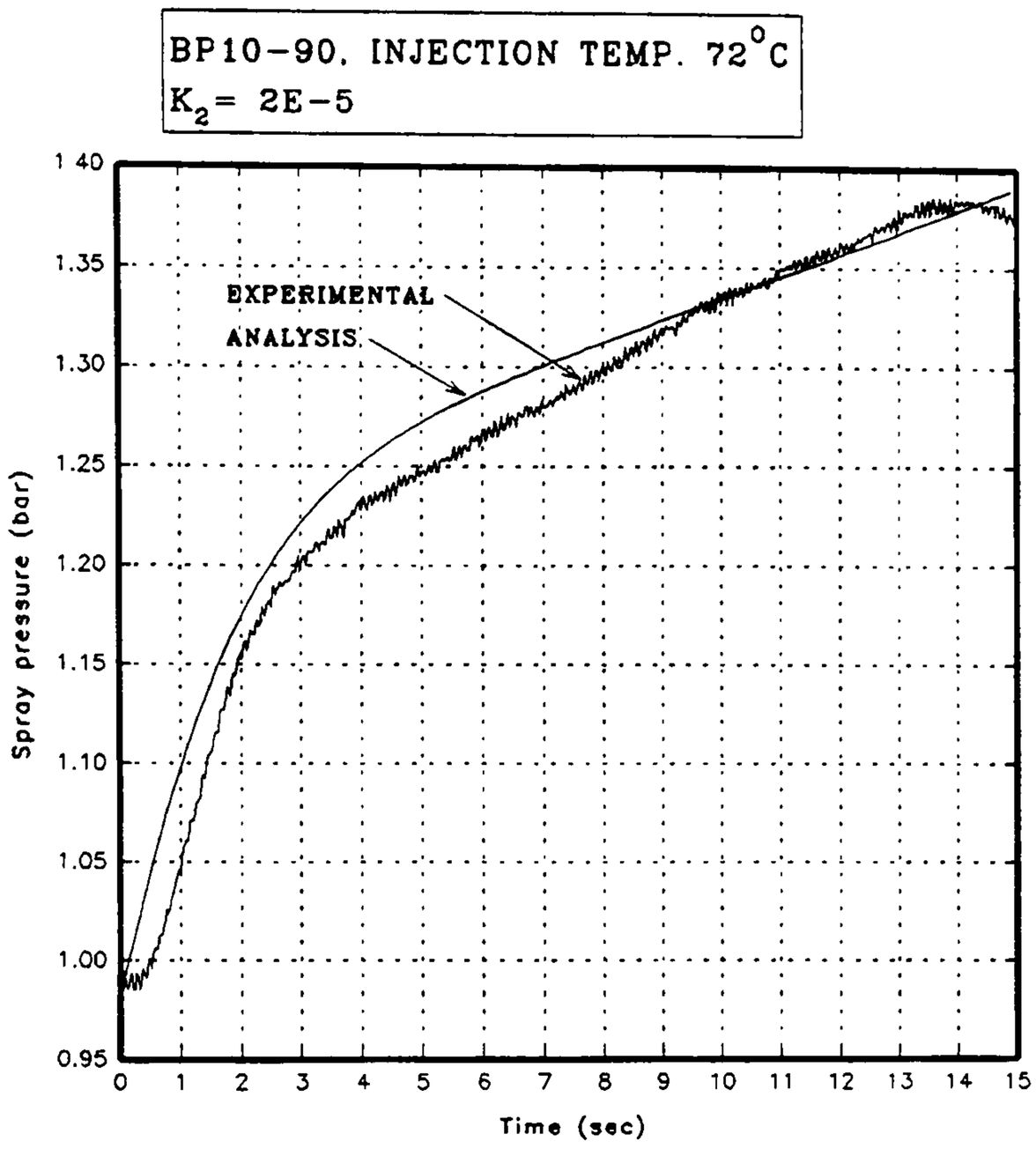

Figure 3.25 *Comparison of experimental and analytical results for 1 side BP10-90 nozzle, flowrate 20 g/s*

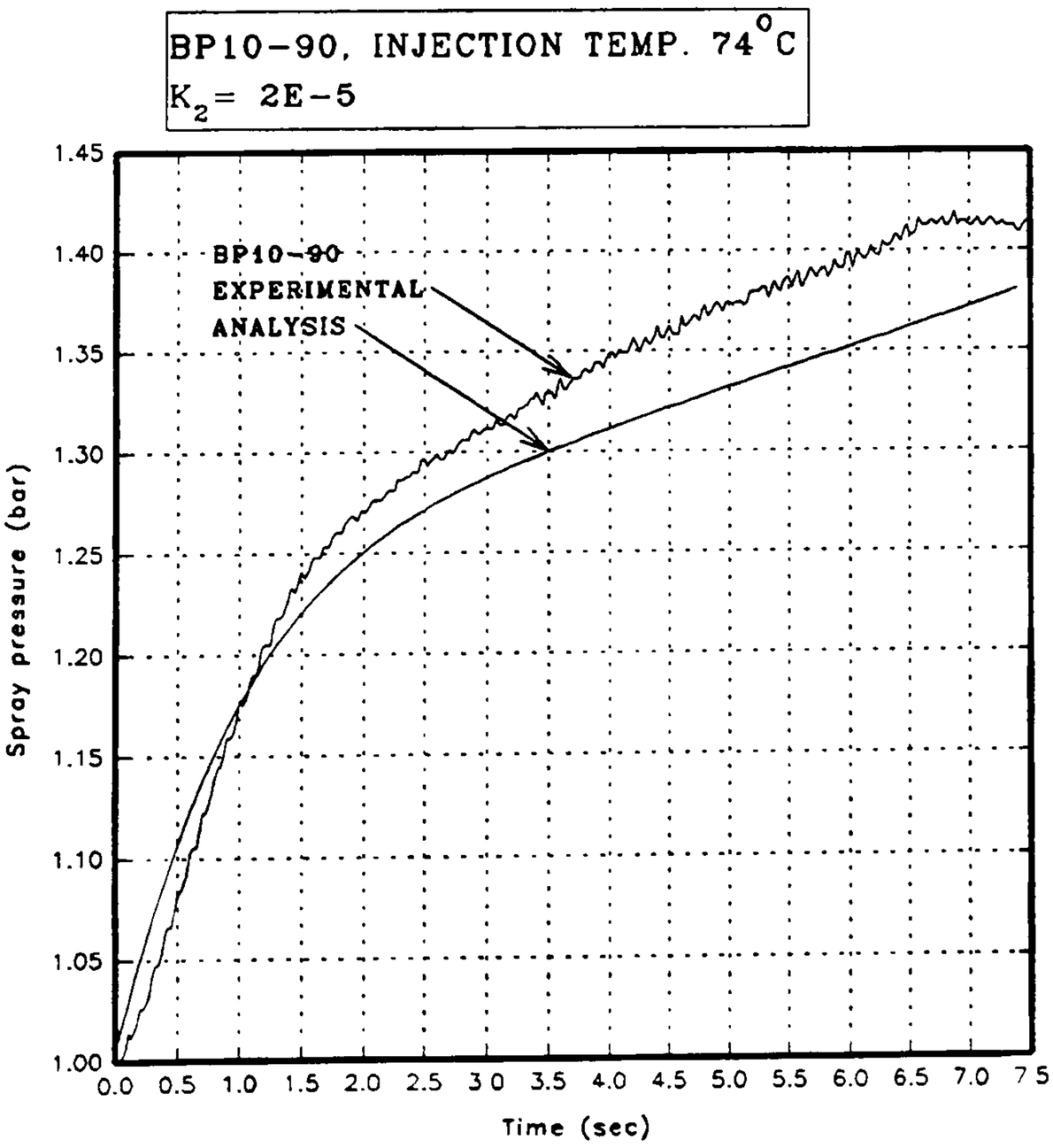

Figure 3.26 *Comparison of experimental and analytical results for 2 side BP10-90 nozzles, flowrate 20 g/s per nozzle*

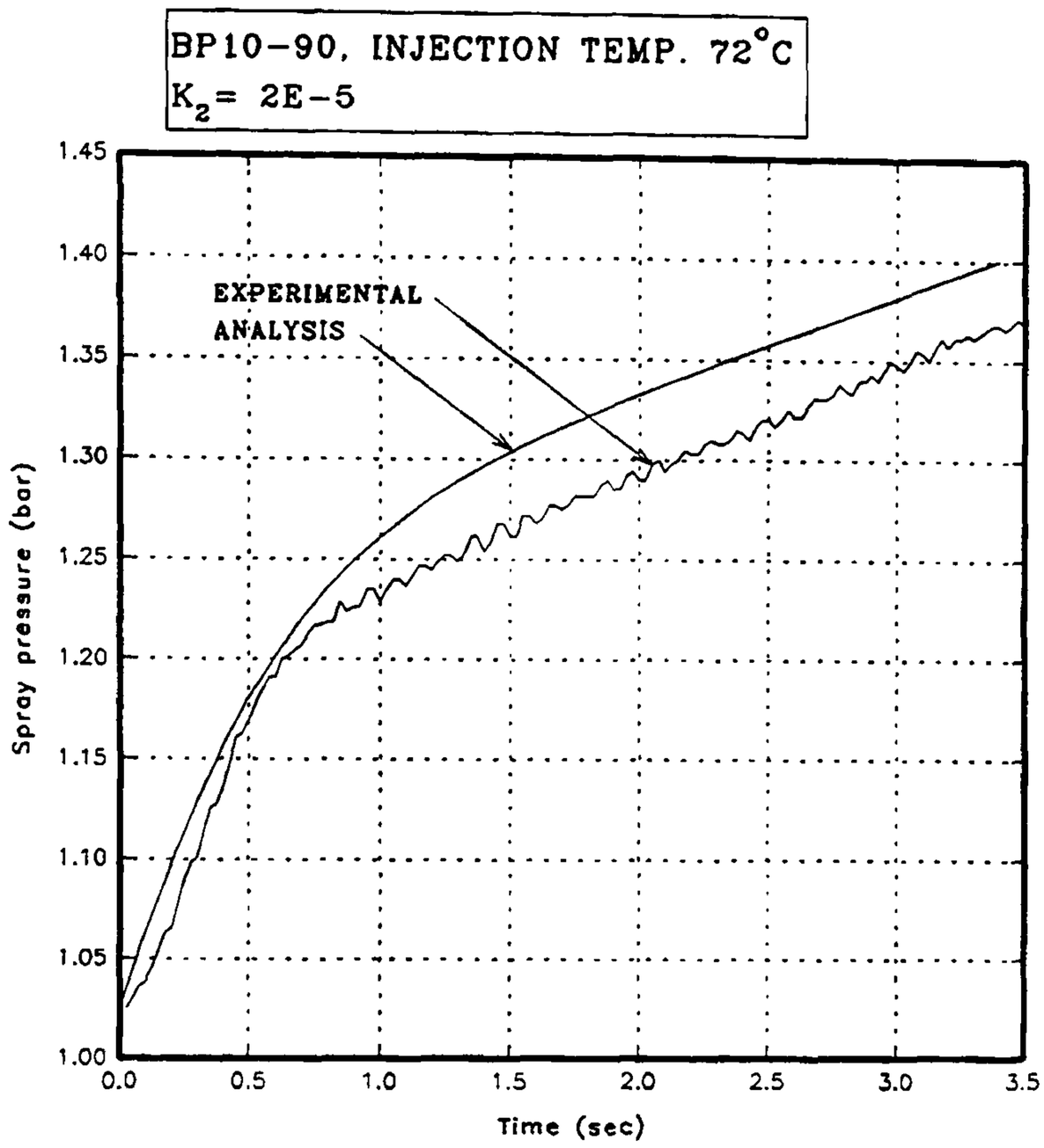

Figure 3.27 Comparison of experimental and analytical results for 4 side BP10-90 nozzles, flowrate 20 g/s per nozzle

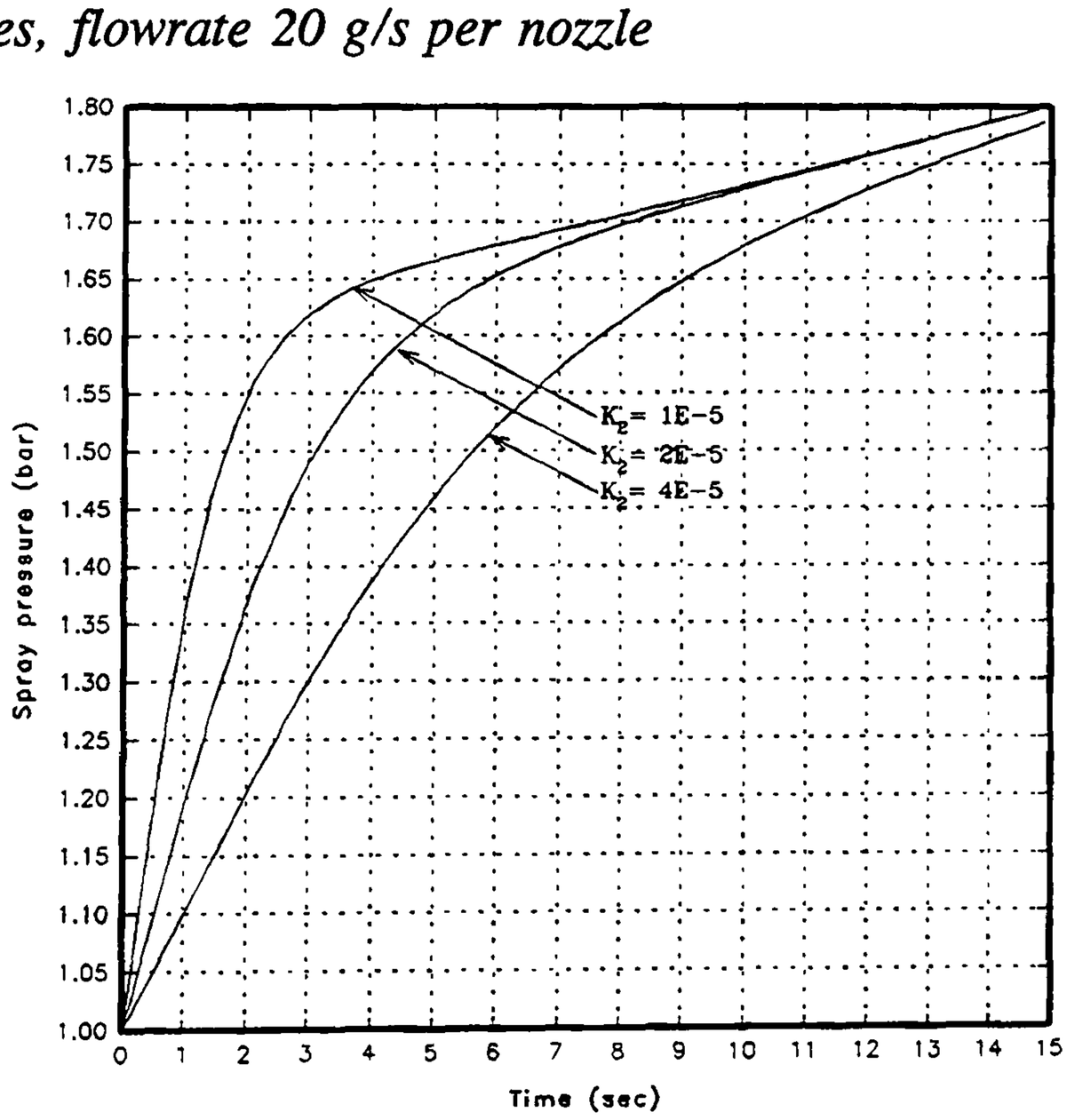

Figure 3.28 Comparison of influence of parameter K_2 on the analytical results. Single nozzle, flowrate 20 g/s, initial gas temperature 20°C, injection temperature 80°C

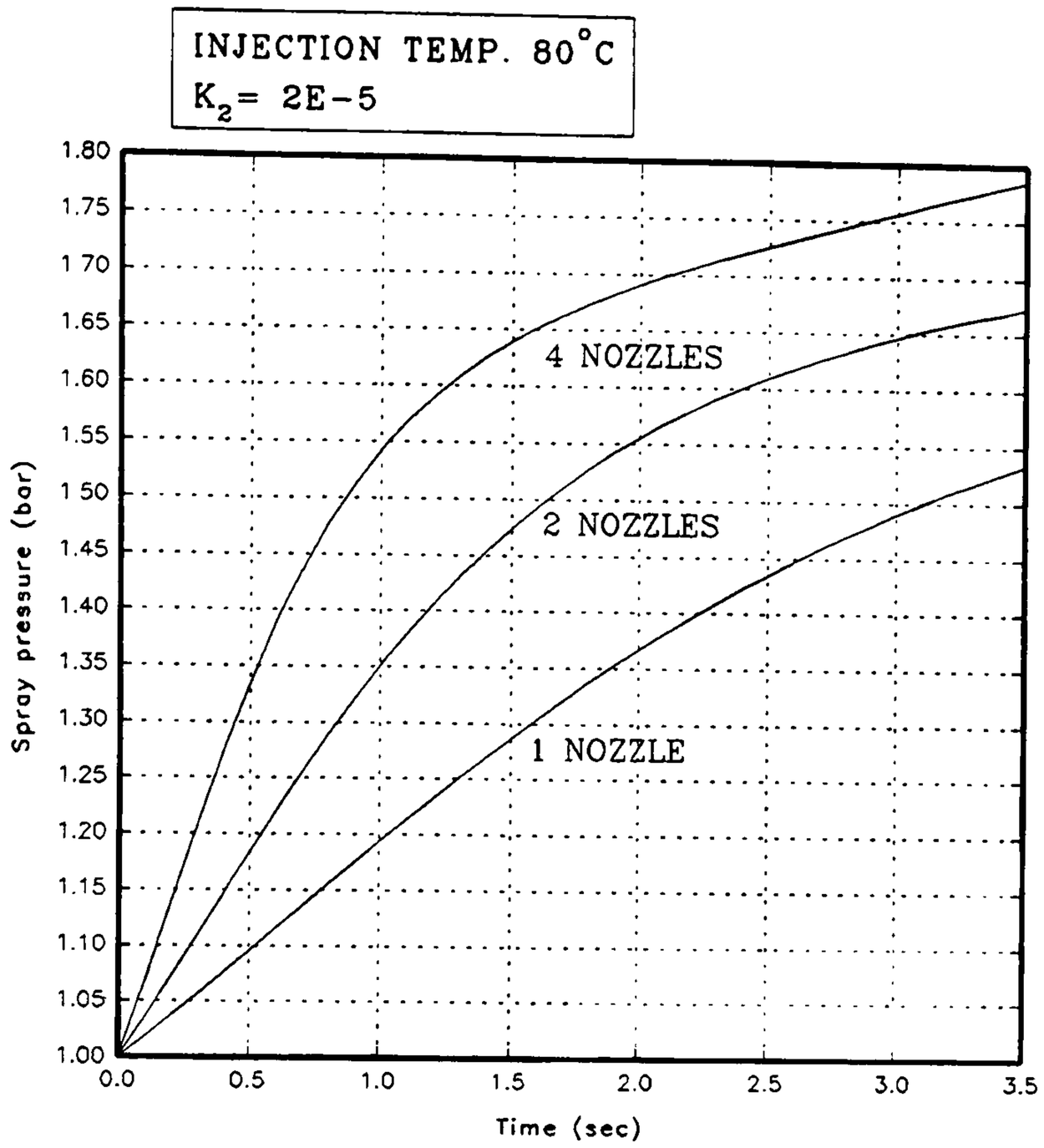

Figure 3.29 *Comparison of analytical results for 1, 2 and 4 nozzle configurations, flowrate 20 g/s per nozzle, initial gas temperature 20°C, injection temperature 80°C*

The results of the analysis presented in this work have significant implications for the modelling of transfer processes between droplet sprays and gases. The analysis, and its comparison with the experimental data, indicates that it is primarily the dimensionless group K_2, and not simply the Nusselt number, which must be used in the theoretical modelling. The present analysis recognizes that the lifetime of each droplet in the transfer zone, which depends on the typical droplet velocity U_D determines the number of spray droplets available for heat transfer at any one time.

In order to model the heat and mass transfer processes from the first principle, the droplet trajectories must be known, together with the heat and mass transfer characteristics of each individual droplet. This is complicated by the high droplet density and hence their mutual interaction. This then implies that at least two droplet parameters, typical droplet velocity and droplet heat transfer coefficient, must be known to describe fully the heat transfer processes involved. It is the single most significant advantage of the present

theoretical approach that both these parameters, U_D and h, are subsumed in one dimensionless group K_2. Furthermore, the typical droplet radius (or diameter), which is also notoriously difficult to determine is also contained only in the dimensionless group K_2.

Hence all three parameters which describe the thermo-hydraulic behaviour of spray droplets, a, U_D and h, are together characterised by the dimensionless group K_2, whose value appears to be constant and equal to about 2×10^{-5}. In any new application the value of K_2 can either be taken as 2×10^{-5} or, if the conditions are materially different from the present experimental conditions, K_2 can be determined in a single, simple experiment.

Spray injection and heat transfer performance of nozzles have been investigated, both experimentally and by developing a theoretical model. The theoretical model developed, leads to a new dimensionless group K_2, which combines the three parameters which primarily influence the heat transfer characteristics between spray droplets and gases: the typical droplet size, the typical droplet velocity and the typical droplet heat transfer coefficient. These parameters do not appear in any other dimensionless group. The model agrees reasonably well with experimental data provided the best value of this dimensionless group K_2 is used. The best value of the dimensionless group K_2 is, to a first approximation, independent of all parameters investigated in the present work, and approximately equal to about 2×10^{-5}. For all practical purposes the heat transfer characteristics between spray droplets and gases are, to a first approximation, independent of the size of the nozzles, in the range investigated in this work. The heat transfer performance depends primarily on the mass flowrate of the injected liquid.

It should be pointed out that for a typical droplet velocity of 30 m s^{-1}, computed on the basis of equation (3.1) and manufacturer's data, given in Table 3.5, for the pressure drop across the nozzle and typical droplet diameter, the resulting droplet Nusselt number is equal approximately to 1. The corresponding convective heat transfer coefficient, h, was calculated for a value of the nondimensional group $K_2 = 2 \times 10^{-5}$. This is in good agreement with analytical predictions by Kleinstreuer et al. [68] for the time averaged Nusselt number. It indicates, that for dense, evaporative sprays the effect of droplet clustering and evaporation reduces Nusselt number to levels below 2, that are reached when slip velocity between the gas phase and droplets is zero, or when the instantaneous

Reynolds number is also zero and Nusselt number, as given, for example by expressions 8. - 11. in Table 3.3 tends to 2.

3.5 SINGLE DROPLET ANALYSIS

3.5.1 General

The theoretical analysis presented in this section is based on a simultaneous solution of the energy and mass balance equations for a single evaporating liquid droplet and its associated gas phase. It is assumed that a proportion of the spray chamber volume corresponding to that one surrounding a single droplet undergoes the same transient changes as the whole spray chamber. The analysis incorporates the effect of evaporation from the droplet. Similar methods have been adopted in the works of Megahed et al. [54] and Sengupta et al. [55]. A typical control volume for a single droplet is shown in Figure 3.30.

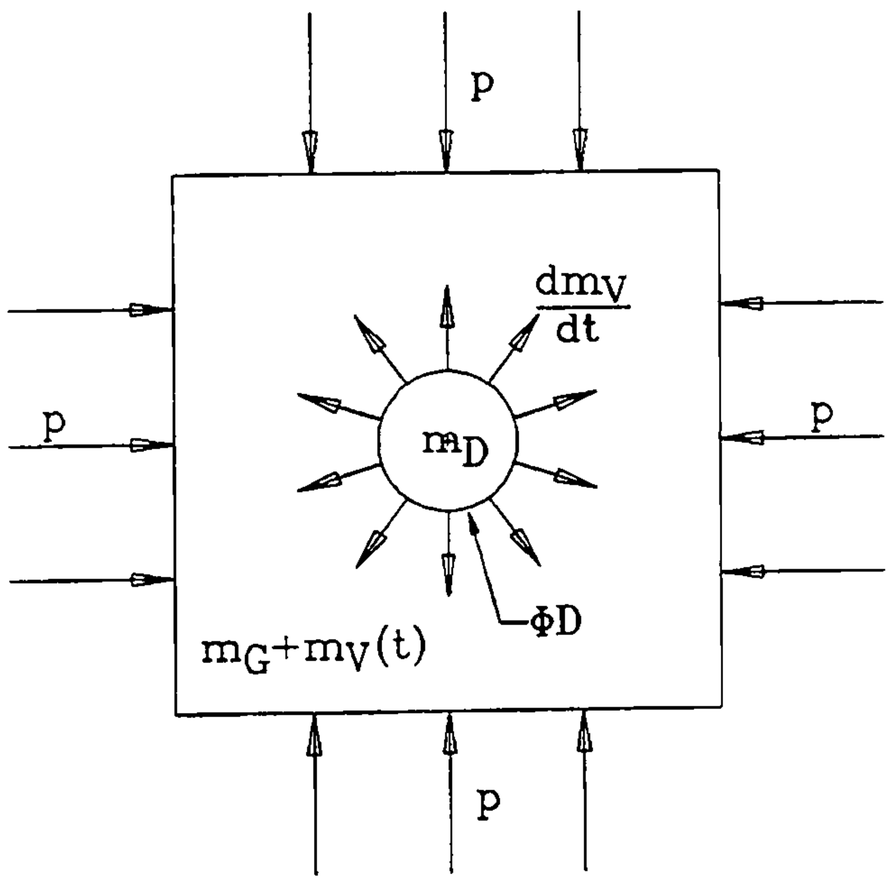

Figure 3.30 Control volume surrounding a single droplet

3.5.2 Governing equations

The energy balance for a droplet, given by equation (3.19), can be re-written as:

$$m_D c_{pD} \frac{dT_D}{dt} = h(T_G - T_D)4\pi a^2 - h_{fg}\left(\frac{dm_D}{dt}\right) \qquad (3.49)$$

The energy balance for the gas - vapour control volume surrounding a single droplet is:

$$\frac{dU_{CV}}{dt} = h(T_D - T_G)4\pi a^2 - p\frac{dV_{CV}}{dt} + \left(\frac{dm_V}{dt}\right)h_V \qquad (3.50)$$

where U_{CV} is internal energy of the gas - vapour control volume, which includes the internal energies of both the gas and the water vapour, with the mass of the latter being a function of time, t. The first term on the right hand side of Equation (3.50) represents sensible heat transfer, and the second term is due to the compression of control volume. The last term represents an increase of control volume energy due to droplet evaporation, where the specific enthalpy of the vapour, h_V, must be evaluated at the droplet temperature T_D. The rate of change of the control volume internal energy can be re-written in terms of the specific internal energies of the gas, u_G, and the vapour, u_V as:

$$m_G\frac{du_G}{dt} + m_V\frac{du_V(T_G)}{dt} + u_V\frac{dm_V}{dt} = \qquad (3.51)$$
$$h(T_D - T_G)4\pi a^2 - p\frac{dV_{CV}}{dt} + \frac{dm_V}{dt}[u_V(T_D) + pv_V]$$

where the terms on the left hand side are evaluated at the gas temperature T_G.

Defining m_m as the mass of gas - vapour mixture in the control volume

$$m_m = m_G + m_V \qquad (3.52)$$

where m_V is a function of time, the mixture specific internal energy, u_m, becomes:

$$m_m\frac{du_m}{dt} + u_m\frac{dm_m}{dt} = m_G\frac{du_G}{dt} + m_V\frac{du_V}{dt} + u_V\frac{dm_V}{dt} \qquad (3.53)$$

Substitution of equation (3.53) into equation (3.51) gives, after re-arrangement:

$$m_m\frac{du_m}{dt} = h(T_D - T_G)4\pi a^2 - p\frac{dV_{CV}}{dt} + \frac{dm_V}{dt}[u_V(T_D) - u_m] + \frac{dm_V}{dt}pv_V \qquad (3.54)$$

Taking

$$u_m = c_{vm}T_G \qquad (3.55)$$

$$u_V = c_{vV}T \qquad (3.56)$$

equation (3.54) gives:

$$m_m c_{vm} \frac{dT_G}{dt} = h(T_D - T_G)4\pi a^2 + \frac{dm_V}{dt} c_{vV}(T_D - T_G) - p\frac{dV_{CV}}{dt} + \frac{dm_V}{dt} p v_V \quad (3.57)$$

where c_{vm} is the specific heat at constant volume of the gas - vapour mixture, defined as:

$$c_{vm} = \frac{x_{GCV}\, M_G\, c_{VG} + x_{VCV}\, M_V\, c_{vCV}}{x_{GCV}\, M_G + x_{VCV}\, M_V} \quad (3.58)$$

where x_{GCV} is mole fraction of the gas in the control volume and x_{VCV} is the mole fraction of the vapour in the control volume, p is the total pressure and v is the specific volume of vapour at the droplet temperature, T_D.

The change of droplet mass due to evaporation is described by equation (3.3). This equation can be re-written in terms of mole fractions of vapour at the droplet surface and in the control volume bulk, neglecting the solubility of the gas in water, as [39]:

$$\frac{dm_D}{dt} = -\frac{\rho_G}{M_G} D_{ab}\, Sh\, \pi\, a\, \frac{x_{VD} - x_{vCV}}{1 - x_{vD}} \quad (3.59)$$

where M_G is the molecular mass of the gas, D_{ab} is the diffusivity of water vapour in air, Sh is the Sherwood number, x_{VD} is the mole fraction of vapour at the droplet surface - i. e. at the droplet temperature T_D, x_{VCV} is the mole fraction of vapour in the control volume bulk, i. e. at the control volume temperature T_G.

3.5.3 Method of solution

Equations (3.49), (3.57) and (3.59) form a system of coupled first order differential equations, that can be re-written in the form of:

$$\frac{dT_D}{dt} = f_1\,(t, T_D, T_G, m_D) \quad (3.60)$$

$$\frac{dT_G}{dt} = f_2\,(t, T_D, T_G, m_D) \quad (3.61)$$

$$\frac{dm_D}{dt} = f_3\,(t, T_D, T_G, m_D) \quad (3.62)$$

enabling a numerical solution using the fourth order Runge - Kutta formula [66] incorporated into a FORTRAN computer program. The marching scheme used for

obtaining the transient values of the dependent variables at the time step, t_{i+1} is given by:

$$T_{D\,i+1} = T_{D\,i} + \frac{\Delta t}{6}\,(l_1 + 2l_2 + 2l_3 + l_4) \tag{3.63}$$

$$T_{G\,i+1} = T_{G\,i} + \frac{\Delta t}{6}\,(q_1 + 2q_2 + 2q_3 + q_4) \tag{3.64}$$

$$m_{D\,i+1} = m_{D\,i} + \frac{\Delta t}{6}\,(r_1 + 2r_2 + 2r_3 + r_4) \tag{3.65}$$

where

$$l_1 = f_1\,(t_i, T_{D\,i}, T_{G\,i}, m_{D\,i}) \tag{3.66}$$

$$l_2 = f_1\,(t_i + \frac{\Delta t}{2}, T_{D\,i} + \frac{\Delta t}{2} l_1, T_{G\,i} + \frac{\Delta t}{2} q_1, m_{D\,i} + \frac{\Delta t}{2} r_1) \tag{3.67}$$

$$l_3 = f_1\,(t_i + \frac{\Delta t}{2}, T_{D\,i} + \frac{\Delta t}{2} l_2, T_{G\,i} + \frac{\Delta t}{2} q_2, m_{D\,i} + \frac{\Delta t}{2} r_2) \tag{3.68}$$

$$l_4 = f_1\,(t_i + \frac{\Delta t}{2}, T_{D\,i} + \Delta t\; l_3, T_{G\,i} + \Delta t\; q_3, m_{D\,i} + \Delta t\; r_3) \tag{3.69}$$

r_1, r_2, etc. are analogous to l_1, l_2, etc. . The initial conditions T_{Do}, T_{Go}, m_{Do} must be specified to start the time marching process.

The computational method allows for variations of the specific heat at constant volume of the water vapour, c_{vV} with respect to temperature using an expression fitted to data for c_{vV} tabulated in [67]. Details are given in Appendix J. An expression for the specific volume of water vapour, v, as a function of temperature, used in equation (3.57), was obtained in similar manner and details are also given in Appendix J.

Equations (3.60) - (3.62) are supplemented by an equation for pressure calculation. The initial gas - vapour pressure, p_o, is specified as an input to the computer program and the present method also allows for specification of the initial relative humidity, Φ_o, of the gas - vapour mixture contained within the spray chamber. The relative humidity is given by the ratio:

$$\Phi_o = \frac{p_{VCV}}{p_{SCV}} \tag{3.70}$$

where p_{VCV} is the partial pressure of the water vapour inside the control volume and p_{SCV} is the saturation pressure of water at the gas - vapour temperature, i.e. T_{Go}. An analytical expression for p_{SCV} as a function of temperature was derived, enabling incorporation into the present numerical method. Details of the derivation are given in Appendix J.

The initial gas partial pressure in the control volume, p_{GCV}, is then evaluated simply by:

$$p_{GCVo} = p_o - p_{VCV} \tag{3.71}$$

The typical number of droplets present in the spray chamber is calculated in the same way as given by equations (3.23) and (3.24) in Section 3.4.3 and the typical control volume size associated with a single droplet, V_{CV}, is given by:

$$V_{CV} = \frac{V_{SC}}{N} \tag{3.72}$$

where V_{SC} is the volume of the spray chamber.

The mass of water vapour evaporating into the control volume in each new time step is equal to the decrease of the liquid droplet mass. As the time marching proceeds, the ratio of the mass of water vapour, m_{VCV} in the control volume to the mass of dry gas, m_{GCV}, at any instant is expressed in terms of instantaneous specific humidity ω_i, defined as:

$$\omega_i = \frac{m_{VCV\,i}}{m_{GCV}} \tag{3.73}$$

where the total mass of the mixture, m_m, used in equation (3.57), is:

$$m_m = m_{VCV\,i} + m_{GCV} \tag{3.74}$$

The gas partial pressure during the time marching process is calculated from ideal gas law:

$$p_{GCV\,i} = \frac{m_{GCV}\, R_G\, T_{G\,i}}{V_{CV}} \tag{3.75}$$

and the total instantaneous pressure is then given by:

$$p_i = p_{GCV\,i}\left(1 + \frac{\omega_i R_G}{R_V}\right) \tag{3.76}$$

where R_G is the gas specific gas constant and R_V is water vapour specific gas constant.

Equations (3.60) - (3.69) and (3.73) - (3.75) are used to model the transient processes occurring during a typical droplet lifetime given by equation (3.24). When this time has elapsed a new, 'fresh', droplet having specified initial temperature and diameter is introduced into the control volume and the whole process repeats. This simulates continuous injection into the spray chamber.

Compression of the control volume due to incoming liquid is simulated by decreasing the control volume by the amount corresponding to volume of injected liquid rather than by the third term on the right hand side of equation (3.57).

3.5.4 Overview of the computational cycle

The calculation method above described forms a two - loop process as shown in Figure 3.31.

INPUT DATA block reads in values of the typical droplet lifetime, the total time span of calculation, the initial droplet temperature and the droplet radius as given by the manufacturers' data, the initial spray chamber pressure and temperature, the injection flowrate, the initial relative humidity, the dimensions of the spray chamber and the estimates of Nusselt and Sherwood numbers.

INITIAL AIR AND VAPOUR block performs calculation of the initial vapour and gas partial pressures and the corresponding masses of gas and vapour based on ideal gas law behaviour. Calculations for a single droplet control volume size are also performed.

NEXT DROPLET introduces a new, 'fresh', droplet having a given initial temperature and diameter into the control volume.

DROPLET LIFETIME MARCHING begins the time marching loop. The time span of this computation corresponds to the typical lifetime of a single droplet in the control volume, t_D, as given by equation (3.24).

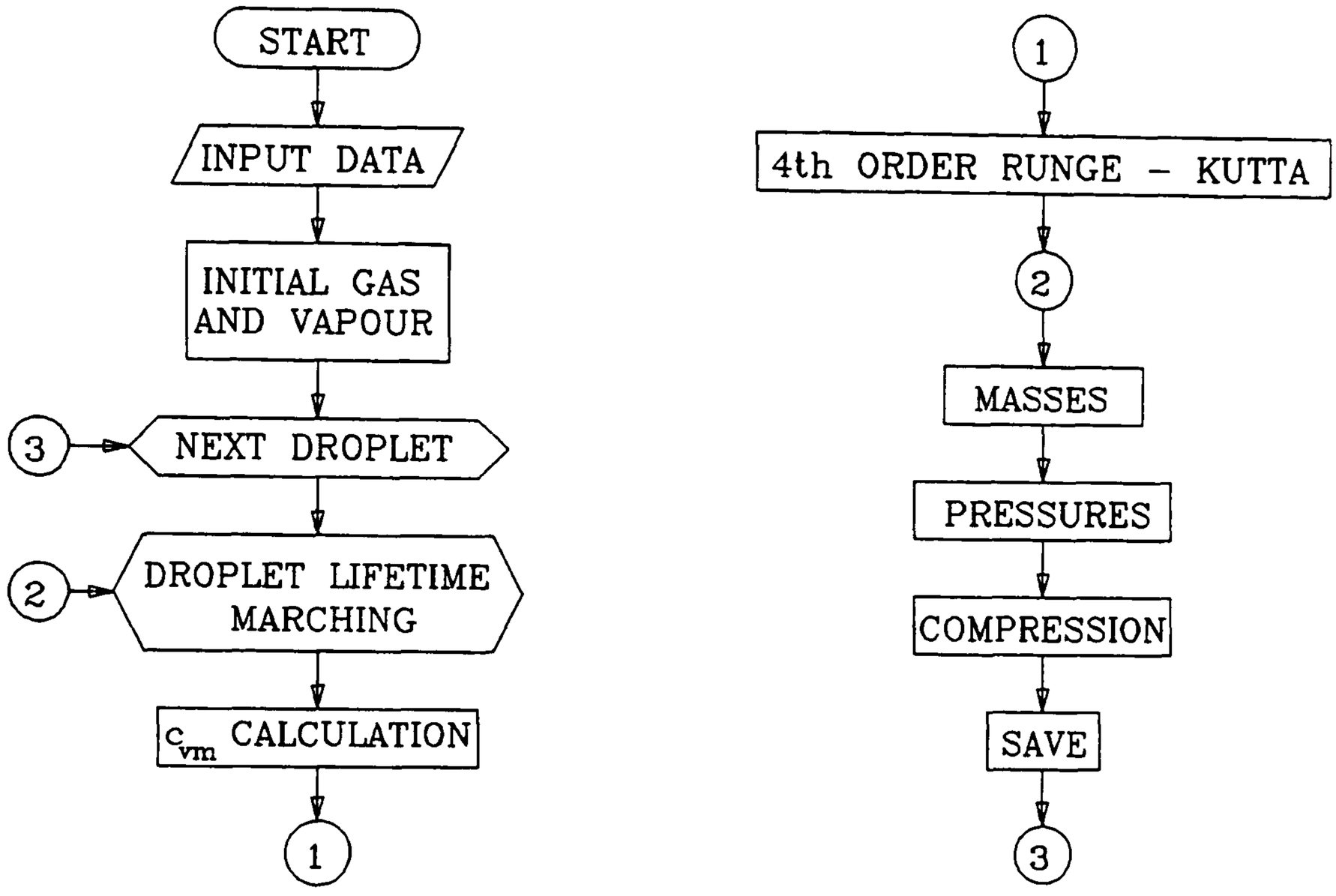

Figure 3.31 *Flow diagram of the two loop Runge - Kutta computational cycle*

c_{vm} **CALCULATION** calculates the specific heat at constant volume of the gas - vapour mixture according to equation (3.58)

4th ORDER RUNGE - KUTTA uses the time marching scheme described by equations (3.63) - (3.69) to calculate values of T_D, T_G, m_D at time t_{i+1}. The fourth order Runge - Kutta calculation performs a specified number of time steps during the droplet lifetime interval. **MASSES** block calculates the mass of the droplet after its lifetime in the control volume is finished, and also the mass content of water vapour inside the control volume. **PRESSURES** calculates the partial pressures of water vapour and gas inside the control volume as well as the total pressure.

COMPRESSION block simulates compression of the control volume due to incoming liquid.

SAVE saves computed data into a specified file and then the whole calculation is repeated until the total timespan of the calculation is marched through.

3.5.5 Results and discussion

Calculations were carried out using the single droplet analysis for a similar range of experimental conditions to those considered in Section 3.4. This enables a comparison between the bulk analysis and the single droplet analysis to be performed. Values of Nusselt number and Sherwood number were specified as an input to the computational cycle and the best agreement between the theoretical and the experimental data was sought by trial and error. The initial relative humidity in the spray chamber was chosen as 50 %. All calculations were carried out for Delavan BP10-90 nozzle as a typical representative of the range of nozzles investigated.

Figures 3.32 - 3.36 indicate that there is a reasonable agreement between the experimental data and theoretical solutions. Moreover, the results indicate that the values of heat transfer Nusselt number Nu, and Sherwood number, Sh - sometimes referred to as mass transfer Nusselt number, are both 1. This finding agrees well with the discussion of the significance of the group K_2 in Section 3.4, where it is concluded that the Nusselt number, Nu is approximately equal to 1. Figure 3.32 compares theoretical and experimental results for the influence of the liquid temperature on the variation of spray chamber pressure with time.

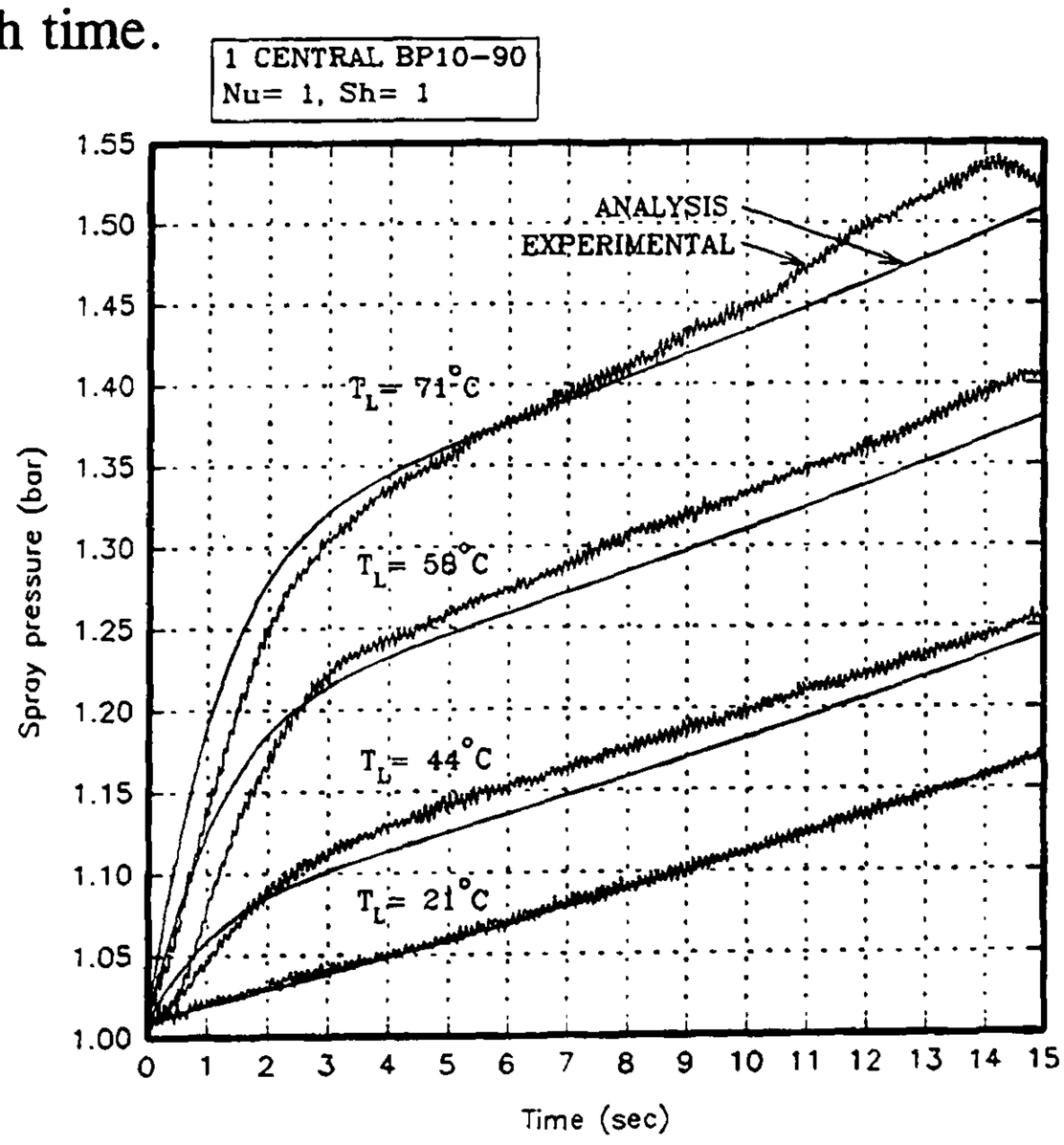

Figure 3.32 *Comparison of theoretical and experimental results investigating influence of liquid temperature with 1 central BP10-90 nozzle in air, water injection flowrate 20 g/s, p_o= 1.0004 bar, initial relative humidity 50 %*

Good agreement is found for the lowest temperature, where the pressurisation occurs only due to incoming liquid, as there are no heat or mass transfer processes taking place. This proves correct functionality of the pressure transducers and validity of the measured data. Furthermore a good match between experiment and theory, with Nu= 1 and Sh= 1, is found for higher injection temperatures.

Figures 3.33 - 3.35 compare results for different nozzle configurations. They show, once again, that for the range of conditions investigated in this work, the Nusselt number and Sherwood number are independent of the size and the number of nozzles.

Finally Figure 3.36 shows analytical result for an "ideal" case. The initial gas temperature was set to 20°C, the injection temperature to 80°C, the initial relative humidity to 0 % and the injection flowrate to 20 g/s.

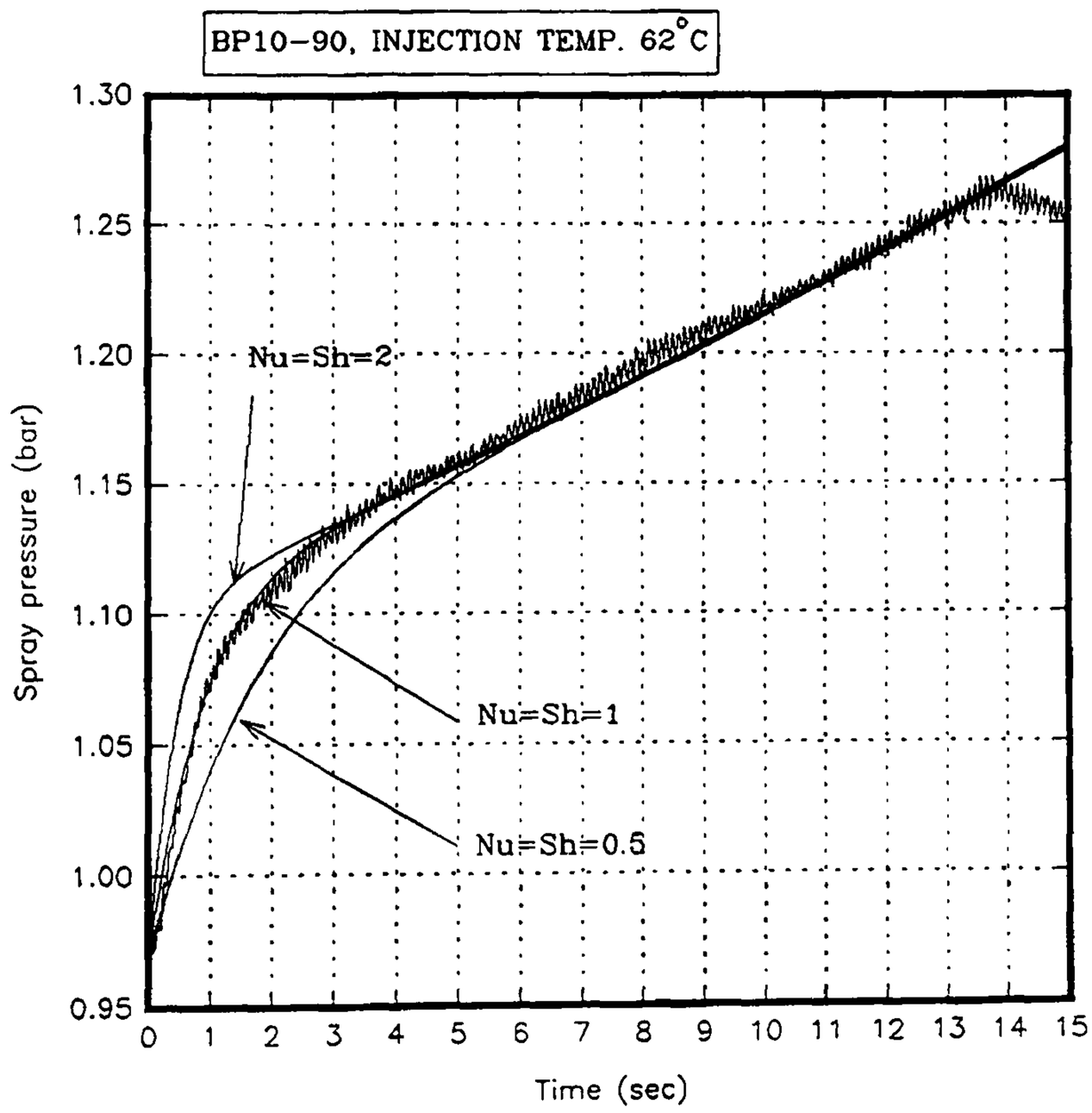

Figure 3.33 *Comparison of analytical and experimental results for one central BP10-90 nozzle, injection temperature 62°C, flowrate 20 g/s, initial relative humidity 50 %; influence of the Nusselt and Sherwood number values is also indicated*

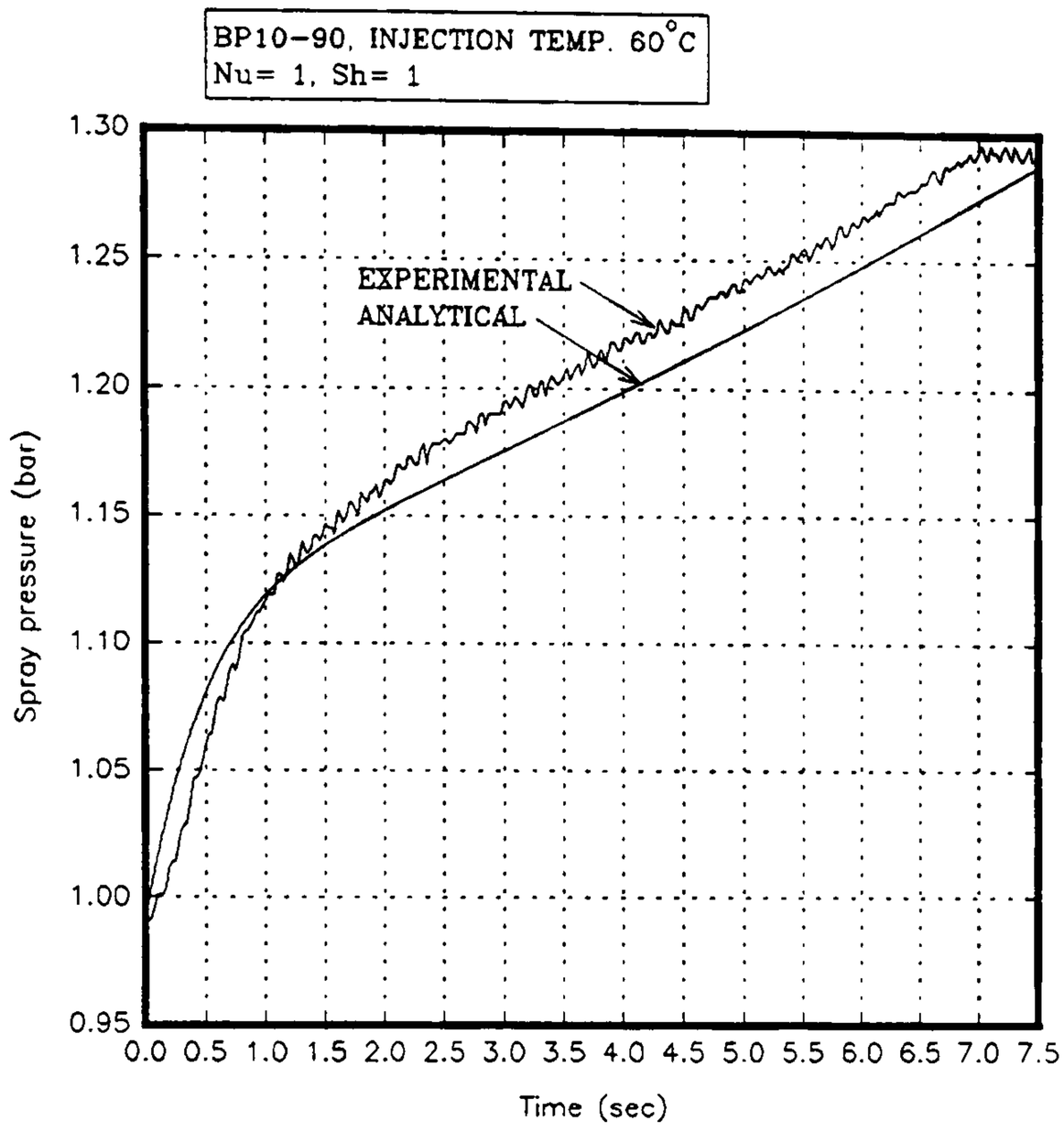

Figure 3.34 *Comparison of analytical and experimental results for two side BP10-90 nozzles, injection temperature 60°C, flowrate 20 g/s per nozzle, initial relative humidity 50 %*

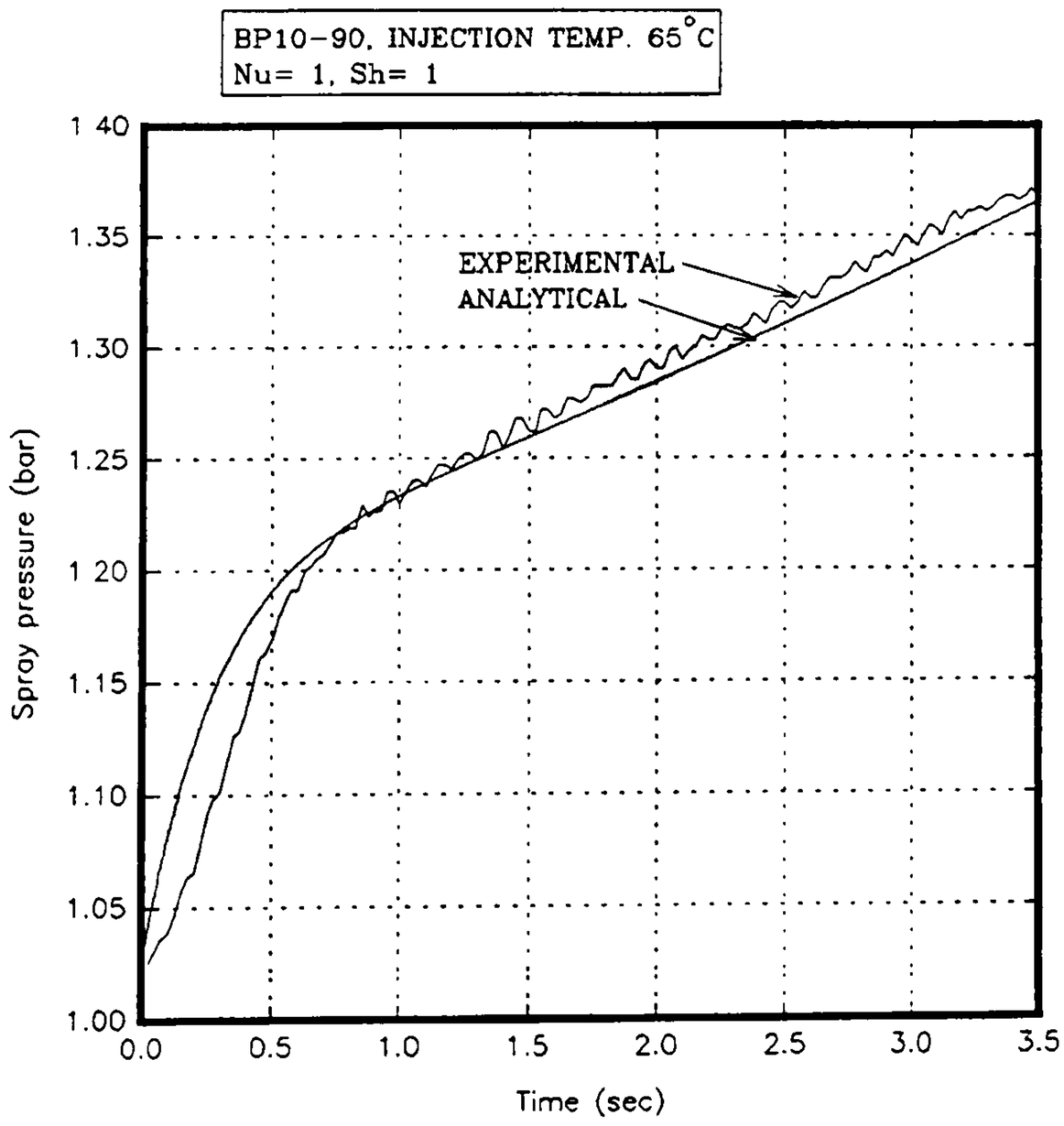

Figure 3.35 *Comparison of analytical and experimental results for four side BP10-90 nozzles, injection temperature 65°C, flowrate 20 g/s per nozzle, initial relative humidity 50 %*

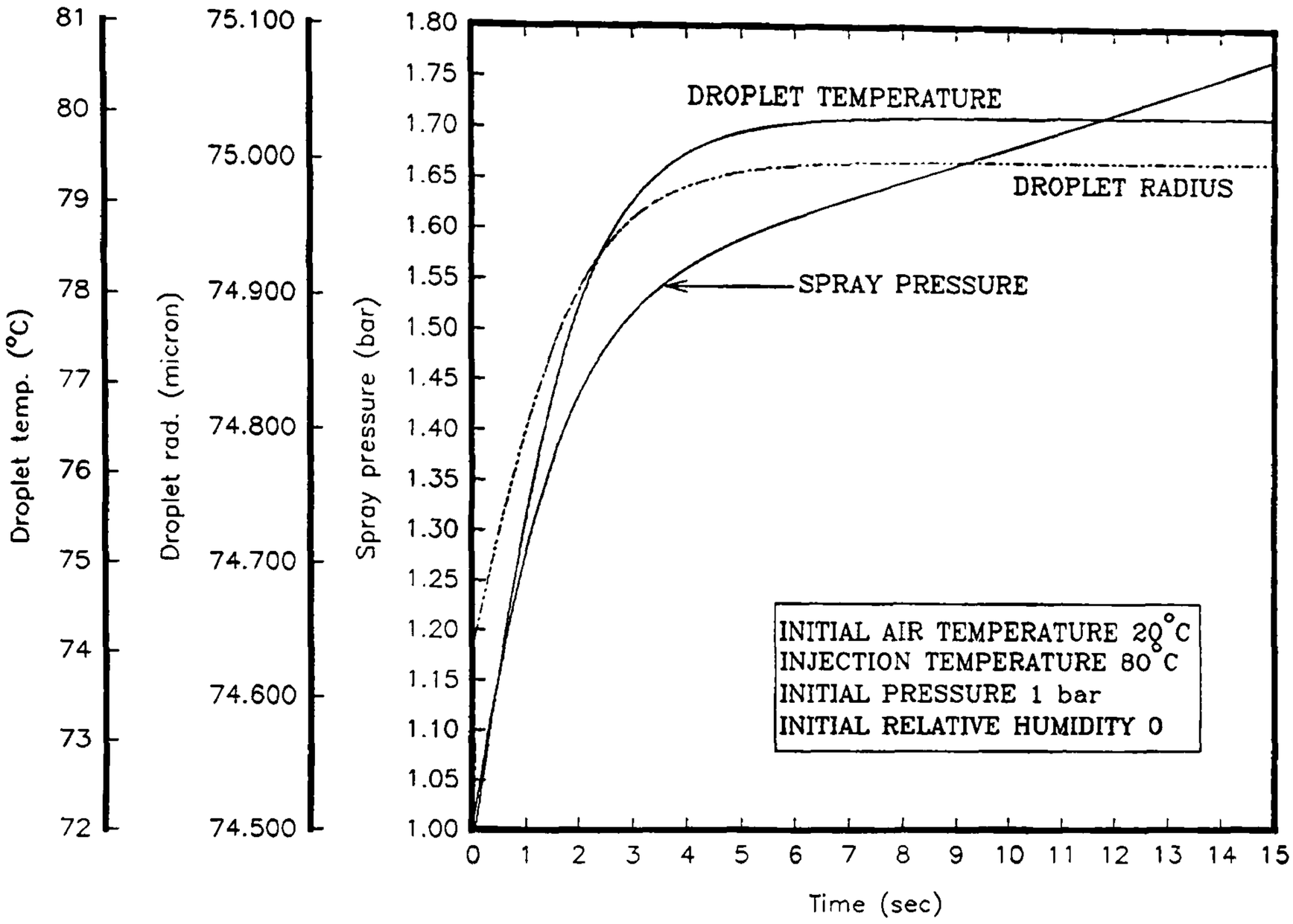

Figure 3.36 *Result of Runge - Kutta analysis, one central BP10-90 nozzle, initial gas temperature 20°C, injection temperature 80°C, flowrate 20 g/s, initial relative humidity 0 %*

In addition to the transient variation of the spray chamber pressure, Figure 3.36 also shows, the changes in droplet diameter and temperature. The values are recorded at the end of droplet lifetime interval in the control volume, thus illustrating intensity of heating and mass transfer between the gas and droplet phase. It can be seen that for this particular case the exchange processes are most rapid during the first four seconds, after that equilibrium is reached and no evaporation from droplets takes place, as droplet radius remains constant.

3.6 CONCLUSIONS

3.6.1 Summary of major findings

The experimental and theoretical work described in this chapter has been undertaken to help in the understanding of the basic mechanisms of heat and mass transfer between liquid sprays and gases. In the experimental investigation the transfer rates were investigated indirectly from transient measurements of the gas pressure variation in a closed spray chamber. Hot water spray droplets were injected from commercially available solid cone pressure swirl nozzles into a gas enclosed within a cylindrical chamber. A sophisticated data acquisition and control system enabled the transient pressure changes inside the spray chamber to be measured. A theoretical analysis of the transfer processes, based on the fundamental physical laws, has been performed and the values of unknown parameters, namely convectivity, and Nusselt and Sherwood numbers have been obtained by looking for the best agreement with the experimental data by a trial and error method.

Experimental results from the spray chamber tests, together with the simple bulk analysis were presented in two conference papers, which are included in Appendix K. The results indicate that, for this particular geometry and the range of nozzles and operating variables investigated, the heat and mass transfer characteristics are, to a first approximation independent of the size of the nozzles. The results also show that the rise of spray chamber internal pressure is directly proportional to liquid temperature and flowrate. The influence of the thermophysical properties of the gas contained in the spray chamber has also been investigated. It was found that the spray chamber pressure rises at a somewhat faster rate for helium compared to air due to the higher thermal conductivity of the helium. An agreement with the findings of Chin and Lefevbre [3] has been found regarding the influence of initial spray chamber pressure level. The results indicate that the rise in absolute spray chamber pressure is faster for higher initial spray chamber pressures. The experimental programme also included tests with different nozzle positions. Central positioning of a single nozzle is the most suitable for efficient heat and mass transfer between the gas and liquid phases. Nozzles positioned off centre cause loss of spray on the walls, and moreover the volume of the zone in which the spray droplets are

in contact with the surrounding gas is greater for the central nozzle. For all practical purposes the heat and mass transfer characteristics between the spray droplets and the enclosed gas was found to depend primarily on the mass flowrate of the injected liquid. Since the energy required for the production of spray droplets increases with the pressure drop across the nozzles, and since the size of the nozzles does not influence the heat transfer rates, it is concluded that the most efficient way of producing high heat and mass transfer rates between spray droplets and enclosed gases is to use larger nozzles. Out of the tested selection of nozzles Delavan BP18-90 nozzle, therefore, seems to be the most suitable one for the industrial application.

Good agreement has been found between the experimental results and the bulk analysis. In this analysis a new dimensionless group, denoted by the symbol K_2, is introduced. This number contains the important parameters of droplet heat transfer namely typical droplet velocity and radius, spray chamber dimensions, gravity, and conductivity and convectivity of the media. The K_2 value is, to a first approximation, independent of all parameters investigated in this work, and approximately equal to about 2×10^{-5}. The corresponding droplet - to - gas Nusselt number, calculated on the basis of the typical droplet properties given by the manufacturer's data, and the K_2 number, is equal approximately to 1. This finding agrees with the predictions given by Kleintreuer et al. [68] for the time averaged Nusselt number for dense, evaporative sprays.

The bulk analysis does not fully incorporate the effect of evaporation from the spray droplets. This drawback has been overcome using an improved analysis based on a simultaneous solution of the energy and mass balance equations for a single droplet and the gas - vapour mixture control volume associated with the drop. Good agreement has been found between the experimental results and the single droplet analysis. The values of the heat transfer Nusselt number and the mass transfer Sherwood number, found using this approach, are found to be approximately equal to 1. This finding agrees well with the results obtained using the bulk analysis.

3.6.2 Suggestions for further work

The present work provides a detailed analysis of the bulk energy transfer processes

occurring between the spray droplets and the gas - vapour mixture contained inside a closed spray chamber.

The experimental investigation could be extended to monitor time histories of droplet size using, for example, the Malvern particle analyser as shown in Figure 3.5. This would provide measurement data for comparison with the analytical predictions of the spray droplet evaporative processes. Discussions given in Sections 3.4 and 3.5 mention that the slip velocity between the droplet and gas - vapour mixture tends to zero. This could be proven by investigating a small portion of the total spray pattern using the Phase Doppler Particle Analyser (PDPA), as shown Figure 3.6, which allows slip velocities to be measured.

Transient computational CFD analysis could be applied to the present work. However, the typical timespan of the period during which the most vigorous heat and mass transfer between the phases occurs is approximately 4 seconds. With the presently available computer technology this duration is rather lengthy for a CFD analysis based on Lagrangian - Eulerian equation coupling. Nevertheless, such an approach could give a theoretical insight into the processes occurring in the spray chamber during the first couple of microseconds of spray injection.

LIST OF REFERENCES FOR CHAPTER 3

1. VALHA J. LEWIS J. S. KUBIE J., Spray Injection and Heat Transfer Performance - Literature Survey, Report MME/ETC/00/5164, Middlesex University, Energy Technology Center, September 1993

2. VALHA J. LEWIS J. S. KUBIE J., Spray Injection and Heat Transfer Performance - Final Report, MME/ETC/003/5164, Middlesex University, Energy Technology Center, September 1994

3. LEFEVBRE A. H., Atomization and Sprays, Taylor & Francis, 1989

4. BAYVEL L. ORZECHOWSKI Z., Liquid Atomization, Taylor & Francis, 1993

5. BUTTERWORTH D. SARDESAI R. G., Calculation of Droplet Size, Pressure Drop and Droplet Inlet Velocity for Spray Nozzles, HTFS Handbook, 1979

6. BAKKER N. A., Direct Contact Heat Transfer, Part 2. - Spray Condensers, HTFS DR 31, UKAEA Harwell Research Group Report, AERE-R 7497, 1975

7. RAETZO T. M. REH L., Characterisation of Three Nozzle Types for Liquid Atomisation at Industrial Scale Flow Rates up to 1000 kg/h, PARTEC 95 - 4th International Congress, Nurnberg, Germany, 21-23 March 1995

8. GORDON B., Water Spray Interaction with Air-Steam Mixture, *Experimental Thermal and Fluid Science*, 4:698-713, 1991

9. KURABAYASHI T. KARASAWA T. HAYNO K., Liquid Nitrogen Freezing Method for Measuring Spray Droplet Sizes, Proceedings ICLASS-78, Tokyo, 12-1:285-292, 1978

10. ALLEN R. F., The Mechanics of Splashing, *Journal of Colloid and Interface Science*, 124:309-316 No. 1, 1988

11. WICKS M. DUKLER A. E., Proceedings of ASME Heat Transfer Conference, 5:39, Chicago, 1966

12. DOYLE H. THOMSON J. STEVENSON W. H., Laser Velocimetry and Particle Sizing, Hemisphere Publishing Corporation, 1979

13. PARTEC 95 - 4th International Congress Optical Particle Sizing, Nurnberg, Germany, 21-23 March 1995 - Preprints

14. VASSALLO R. ASHGRIZ N., Effect of Flow Rate on the Spray Characteristics of Impinging Water Jets, *Journal of Propulsion and Power*, 8:No. 5, 1992

15. LEE S. L. YANG Z. H. HSYUA Y., Cooling of a Heated Surface by Mist Flow, *ASME Journal of Heat Transfer*, 116:167-172, 1994

16. MAYINGER F. CHAVEZ A., Measurement of Direct-Contact Condensation of Pure Saturated Vapour on an Injection Spray by Applying Pulsed Laser Holography, *International Journal of Heat and Mass Transfer*, 35:691-702 No. 3, 1992

17. ZHU H. M. SUN T. Y. CHIGIER N., Tomographical Transformation of Malvern Spray Measurements, *Atomisation and Spray Technology*, 3:89-105, 1987

18. LAMPE K. HASSE B. BAUCKHAGE K., Correlation of Droplet Size and Main Velocity Components in the Vicinity of a Swirl Pressure Burner Nozzle, Proceedings PARTEC 92, Nurnberg, 1992

19. YULE A. J. WATKINS A. P., Measurement and Modelling of Diesel Sprays, *Atomisation and Sprays*, 1:441-465, 1991

20. RANZ W. E. MARSHALL W. R., Evaporation from Drops, *Chemical Engineering Progress*, 48:173-180 & 141-146 No. 3, 1952

21. YUEN M. C. CHEN L. W., Heat Transfer Measurements of Evaporating Liquid Droplets, *International Journal of Heat and Mass Transfer*, 21:537-542, 1978

22. KULIC E. RHODES E., Heat Transfer Rates to Moving Droplets in Air-Steam Mixtures, 6th International Heat Transfer Conference, 464-474, Toronto, Ontario, 1978

23. LAW C. K. XIONG T. Y. WANG C. H., Alcohol Droplet Vaporization in Humid Air, *International Journal of Heat and Mass Transfer*, 30:1435-1443 No. 7, 1987

24. AWORONIN S. O., Evaporation Rates of Freely Falling Liquid Nitrogen Droplets to Air, *Heat Transfer Engineering*, 10:26-36 No. 1, 1989

25. HARFIELD J. P. FARRELL P. V., Droplet Vaporization in Moderate Pressure Gas, *Fluid Mechanics of Sprays, FED ASME 131*, 1991

26. BRIDGWATER J., Direct Contact Heat Transfer - Part I. : General Introduction, Report - Heat Transfer and Fluid Flow Service, Chemical Engineering Division, UKAEA Research Group, AERE Harwell, Didcot, Berks., September 1973

27. ARROWSMITH A., Direct Contact Heat Transfer - Spray Gas Coolers and Vapour Desuperheaters, Report - Heat Transfer and Fluid flow Service, Chemical Engineering Division, UKAEA Research Group, AERE Harwell, Didcot, Berks., April 1974

28. BAKKER N. A., Direct Contact Heat Transfer - Spray Condensers, Report - Thermodynamics Division, AERE, Harwell, May 1975

29. LEKIC A. FORD J. D., Direct Contact Condensation of Vapour on a Spray of Subcooled Liquid Droplets, *International Journal of Heat and Mass Transfer*, 23:1531-1537, 1980

30. GREEN P. B. JANA W. S. JOHN J. E. A., Heat Transfer from High Pressure Glycerin Sprays Produced by Fan-Jet Pressure Nozzles, 3rd International Conference on Liquid Atomisation and Spray Systems, 8-10 July 1985, Imperial College, London, 2:VII/3/1-11, 1985

31. BUGLAYEV V. T. VASILYEV F. V. STREBKOV A. S., Experimental Investigation of Heat Transfer in Evaporative Cooling of Air Flows with Fine Droplets, *Heat Transfer - Soviet Research*, 17:97-103 No. 5, 1985

32. KABALDIN G. S. IVANITSOV A. N., Heat and Energy Characteristics of Sprayers, *Heat Transfer - Soviet Research*, 17:127-135 No. 1, 1985

33. SEKINS K. M. THAYER W. J., Heat Transfer Rates in a Droplet Heat Exchanger, ASME Paper 85-HT-48, 1985

34. HWANG T. H. MOALLEMI M. K., Heat Transfer of Evaporating Droplets in Low Pressure Systems, *International Communications in Heat and Mass Transfer*, 15:635-644, 1988

35. BOGDAN S. N. GORDON B. G. UGOLEVA I. R., Experimental Study of Heat and Mass Transfer from a Vapor-Air Mixture to Water Droplets - Application to Steam Dousing Systems of Nuclear Power Plants, *Fluid Mechanics - Soviet Research*, 18:59-67 No. 3, 1989

36. UGOLEVA I. R. GORDON B. G. GRIGOREV A. S., Heat and Mass Transfer between a Flowing Steam-Air Mixture and Water Droplets, *Thermal Engineering*, 36:343-347, 1989

37. FAIR J. R., Direct Contact Gas-Liquid Heat Exchange for Energy Recovery, *Journal of Solar Energy Engineering*, 112:216-222, 1990

38. SIRIGNANO W. A., Fluid Dynamics of Sprays - 1992 Freeman Scholar Lecture, *ASME Journal of Fluids Engineering*, 115:345-378, 1993

39. BIRD R. B. STEWART W. E. LIGHTFOOT E. N., Transport Phenomena, Wiley International Edition, 1960

40. BELLAN J. HARSTAD K., Evaluation of Importance of the Relative Velocity

During Evaporation of Drops in Sprays, *International Journal of Heat and Mass Transfer*, 29:647-651 No. 4, 1986

41. BELLAN J. CUFFEL R., A Theory of Nondilute Spray Evaporation Based Upon Multiple Drop Interactions, *Combustion and Flame*, 51:55-67, 1983

42. BERLEMONT A. GRANCHER M. S. GOUESBET G., On the Lagrangian Simulation of Turbulence Influence on Droplet Evaporation, *International Journal of Heat and Mass Transfer*, 34:2805-2812 No. 11, 1991

43. CLIFT R. GRACE J. R. WEBER M. E., Bubbles, Drops and Particles, London Academic Press, 1978

44. BORMAN G. L. JOHNSON J. H., Unsteady Vaporization Histories and Trajectories of Fuel Drops Injected into Swirling Air, SAE 598D Paper, 1964

45. PATANKAR S. V., Numerical Heat Transfer and Fluid Flow, Hemisphere Publishing Corporation, 1980

46. MINKOWYCZ W. J. SPARROW E. M. SCHNEIDER G. E. PLETCHER R. H., Handbook of Numerical Heat Transfer, John Wiley & Sons Inc., 1988

47. HUBBARD G. L. DENNY E. E. MILLS A. F., Droplet Evaporation : Effects of Transients and Variable Properties, *International Journal of Heat and Mass Transfer*, 18:1003-1008, 1975

48. CHEN K. H. TREZEK G. J., Thermal Performance Models and Drift Loss Predictions for a Spray Cooling System, *ASME Journal of Heat Transfer*, 99:274-280, 1977

49. CHEN K. H. TREZEK G. J., The Effect of Heat Transfer Coefficient, Local Wet Bulb Temperature and Droplet Size Distribution Function on the Thermal Performance of Sprays, *ASME Journal of Heat Transfer*, 99:381-385, 1977

50. TANAKA M., Heat Transfer of a Spray Droplet in a Nuclear Reactor Containment, *Nuclear Technology*, 47:268-281, 1980

51. LINN J. D. M. MASKELL S. J. PATRICK M. A., A Note on Heat and Mass Transfer to a Spray Droplet, *Nuclear Technology*, 81:122-125, 1988

52. SUNDARARAJAN T. AYYASWAMY P. S., Hydrodynamics and Heat Transfer Associated with Condensation on a Moving Drop : Solutions for Intermediate Reynolds Numbers, *Journal of Fluid Mechanics*, 149:33-58, 1984

53. TONG A. Y. SIRIGNANO W. A., Multicomponent Droplet Vaporization in a High Temperature Gas, *Combustion and Flame*, 66:221-235, 1986

54. MEGAHED M. M. SAEED M. M. SOROUR M. M. MADI M. B., Unsteady Vaporization of Stationary Dodecane and Alcohol Droplets Suspended in a Hot Non-Reactive Environment, *International Journal of Heat and Mass Transfer*, 32:1299-1308 No. 7, 1989

55. SENGUPTA S. P. MITRA A. K. DASH S. K. SOM S. K., Influence of Downstream Distance on the Drop Size - Characteristics of an Evaporative Liquid Spray in a Convective Gaseous Medium, *Journal of Energy Resources Technology*, 114:70-74, 1992

56. MIGDAL D. AGOSTA V. D., A Source Flow Model for Continuum Gas-Particle Flow, *Journal of Applied Mechanics*, 860-865, 1967

57. CROWE C. T. SHARMA M. P. STOCK D. E., The Particle-Source-In-Cell Model for Gas-Droplet Flows, *ASME Journal of Fluids Engineering*, 99:326-332, 1977

58. DURST F. MILOJEVIC D. SCHONUNG B., Eulerian and Lagrangian Predictions of Particulate Two-Phase Flows : A Numerical Study, *Applied Mathematical Modelling*, 8:101-115, 1984

59. SOLOMON A. S. P. SHUEN J. S. ZHANG Q. F. FAETH G. M., Measurement and Predictions of the Structure of Evaporating Sprays, *ASME Journal of Heat Transfer*, 107:679-685, 1985

60. SOONIL NAM, Numerical Simulation of Actual Delivered Density of Sprinkler Spray Through Fire Plumes, ASME Publication FED 178/HTD 270, Fluid Mechanics and Heat Transfer in Sprays, 57-65, 1993

61. JICHA M. KARKI K. C. PATANKAR S. V., Numerical Analysis of Water Spray System in the Entrance Region of a Two-Dimensional Channel using Lagrangian Approach, *Numerical Heat Transfer*, 26:1-16/A, 1994

62. DUKOWICZ J. K., A Particle-Fluid Numerical Model for Liquid Sprays, *Journal of Computational Physics*, 35:229-253, 1980

63. CLOUTMAN L. D. DUKOWICZ J. K. RAMSHAW J. D. AMSDEN A. A., CONCHAS - SPRAY - A Computer Code for Reactive Flows with Fuel Sprays, Los Alamos National Laboratories Report LA-9294-MS, 1982

64. AMSDEN A. A. BUTLER T. D. O'ROURKE P. J. RAMSHAW J. D., KIVA - A Comprehensive Model for 2D and 3D Engine Simulations, Los Alamos National Laboratories Report LA-UR-84-4035, 1985

65. National Instruments, LabView for Windows - Data Acquisition VI Reference Manual, Part Number 320536-01, August 1993

66. PRESS W. H. TEUKOLSKY S. A. VETTERLING W. T. FLANNERY B. P., Numerical Recipes in FORTRAN - The Art of Scientific Computing, Cambridge University Press, 1992

67. MAYHEW Y. R. ROGERS G. F. C., Thermodynamic and Transport Properties of Fluids, SI Units, Oxford, Basil Blackwell, 1967

APPENDICES

APPENDIX A - PROPERTIES OF LIQUIDS USED IN INTERFACIAL INSTABILITY CALCULATIONS

The liquid property values listed in Table A.1 below were evaluated at a temperature of 20°C and atmospheric pressure of 1.013 bar. The values were found from reference [60] given in Chapter 2.

FLUID	μ [kg $m^{-1}s^{-1}$]	ρ [kg m^{-3}]	σ [N m^{-1}]
Water	0.001	1000	0.073
Ethanol	0.0017	790	0.063
Glycerol	0.83	1260	0.030

APPENDIX B - DERIVATION OF MATHIEU EQUATION STABILITY+

The Mathieu equation as given by equation (2.20) is in its canonical form. Since the coefficient of E is periodic, Floquet's theorem can be applied which states that for a differential equation of form

$$y^{(n)} + f_{n-1}(x)y^{(n-1)} + \ldots\ldots + f_1(x)y' + f_0(x)y = 0 \qquad \textbf{(B.1)}$$

in which $f_k(x)$ are holomorphic functions of the complex variable x on the whole complex plane, and are periodic with a common period ω, then there exists at least one non-zero solution $\varphi(x)$ of equation (B.1) such that for a properly chosen constant s, that is complex in general, the following relation holds:

$$\varphi(x+\omega) = s\ \varphi(x) \qquad \textbf{(B.2)}$$

The function $\varphi(x)$ with the above property is called periodic function of the second kind. Furthermore, the constant s is related to the number α by the equation

$$s = e^{\alpha\omega} \qquad \textbf{(B.3)}$$

where is α is known as the characteristic exponent. The function $\Psi(x)$ defined as

$$\psi(x) = e^{-\alpha x}\varphi(x) \qquad \textbf{(B.4)}$$

is then periodic with period ω.

Since Mathieu equation (2.20) is a second order linear homogeneous equation, it posses two linearly independent solutions $E_I(u)$ and $E_{II}(u)$. Because the forcing acceleration acting on the system is a periodic function of time with period $2\pi/\omega$, it can be, making use of Floquet theorem, shown that two solutions exist which satisfy the relations:

$$E_I(u+\pi) = K_1\ E_I(u) \qquad E_{II}(u+\pi) = K_2\ E_{II}(u) \qquad \textbf{(B.5)}$$

where K_1 and K_2, the Floquet multipliers, are either conjugate complex or real constants

+Note: symbols used in Appendix B correspond to those used in Chapter 2

which satisfy the relation:

$$K_1 K_2 = 1 \tag{B.6}$$

It can be shown that all solutions of equation (2.20) will be bounded only if:

$$|K_1| = |K_2| = 1 \tag{B.7}$$

For certain values of p and q there exist solutions for which the values of K are +1 or -1. These solutions therefore have a period of π or 2π. The pairs of values (p,q) for which such periodic solutions of equation (2.20) exist can be shown to form curves in the p-q plane. The curves divide that plane into stable regions in which equation (B.7) holds and unstable regions in which equation (B.7) does not hold. Method for determining these regions is given below.

Assuming the solution of equation (2.20) with period of π or 2π and with u replaced by z is of the form

$$E = \sum_{m=0}^{\infty} (A_m \cos mz + B_m \sin mz) \tag{B.8}$$

and substituting this expression into equation (2.20) yields:

$$\sum_{m=-2}^{\infty} [(p-m^2)A_m - q(A_{m-2}+A_{m+2})]\cos mz + \sum_{m=-1}^{\infty} [(p-m^2)B_m - q(B_{m-2}+B_{m+2})]\sin mz = 0 \tag{B.9}$$

$$A_{-m} , B_{-m} = 0 \quad \text{For m} < 0$$

Equation (B.8) can be reduced to one of four simpler types given below:

$$E_0 = \sum_{m=0}^{\infty} A_{2m+p}\cos(2m+p)z \tag{B.10}$$

$$E_1 = \sum_{m=0}^{\infty} B_{2m+p}\sin(2m+p)z \tag{B.11}$$

where p may be either 0 or 1.

If p = 0, the solution is of period π; if p = 1, the solution is of period 2π.

From equation (B.9) the following solutions can be found. Even solutions of period π:

$$\begin{aligned} \text{For } m &= 0 \ , \ pA_0 - qA_2 = 0 \\ \text{For } m &= 2 \ , \ (p-4)A_2 - q(2A_0+A_4) = 0 \\ \text{For } m &> 2 \ , \ (p-m^2)A_m - q(A_{m-2}+A_{m+2}) = 0 \end{aligned} \tag{B.12}$$

Even solutions of period 2π:

$$\begin{aligned} \text{For } m{=}1 \ , \ (p-1)A_1 - q(A_1+A_3) &= 0 \\ \text{For } m{\geq}3 \ , \ (p-m^2)A_m - q(A_{m-2}+A_{m+2}) &= 0 \end{aligned} \tag{B.13}$$

Odd solutions of period π:

$$\begin{aligned} \text{For } m{=}2 \ , \ (p-4)B_2 - qB_4 &= 0 \\ \text{For } m{\geq}3 \ , \ (p-m^2)B_m - q(B_{m-2}+B_{m+2}) &= 0 \end{aligned} \tag{B.14}$$

Odd solutions of period 2π:

$$\begin{aligned} \text{For } m{=}1 \ , \ (p-1)B_1 + q(B_1-B_3) &= 0 \\ \text{For } m{\geq}3 \ , \ (p-m^2)B_m - q(B_{m-2}+B_{m+2}) &= 0 \end{aligned} \tag{B.15}$$

Let $Ge_m = A_m/A_{m-2}$; $Go_m = B_m/B_{m-2}$

$G_m = Ge_m$ or Go_m when the same operations apply to both.

Let $V_m = (p\text{-}m^2)/q$

Then from equation (B.12):

$$\begin{aligned} Ge_2 &= V_0 \ , \ Ge_4 = V_2 - \frac{2}{Ge_2} \\ G_m &= \frac{1}{V_m - G_{m+2}} \qquad m{\geq}3 \end{aligned} \tag{B.16}$$

Similarly $V_1\text{-}1 = Ge_3$ for even solutions of period 2π, along with

$$G_m = \frac{1}{V_m - G_{m+2}} \tag{B.17}$$

$V_1{+}1 = Go_3$ for odd solutions of period 2π along with equation (B.17)

$V_2 = Go_4$ for odd solutions of period π along with equation (B.17).

The above expressions can be developed into continued fractions.

Equation (B.17) gives:

$$G_m = \frac{1}{V_m - G_{m+2}} = \frac{1}{V_m -} \frac{1}{V_{m+2} -} \frac{1}{V_{m+4} -} \ldots \quad \text{For } m \geq 3$$

$$G_{m+2} = V_m - 1/G_m = V_m - \frac{1}{V_{m-2} -} \frac{1}{V_{m-4} -} \ldots \qquad \textbf{(B.18)}$$

The characteristic values of p are divided into two major groups:

$p = a_r$, associated with even periodic solutions

$p = b_r$, associated with odd periodic solutions

Suitable combination of the above equations gives four types of continued fractions, the roots of which yield the required characteristic values:

$$V_0 - \frac{2}{V_2 -} \frac{1}{V_4 -} \frac{1}{V_6 -} \ldots = 0 \qquad \text{Roots: } a_{2r} \qquad \textbf{(B.19)}$$

$$V_1 - 1 - \frac{1}{V_3 -} \frac{1}{V_5 -} \frac{1}{V_7 -} \ldots = 0 \qquad \text{Roots: } a_{2r+1} \qquad \textbf{(B.20)}$$

$$V_2 - \frac{1}{V_4 -} \frac{1}{V_6 -} \frac{1}{V_8 -} \ldots = 0 \qquad \text{Roots: } b_{2r} \qquad \textbf{(B.21)}$$

$$V_1 + 1 - \frac{1}{V_3 -} \frac{1}{V_5 -} \frac{1}{V_7 -} \ldots = 0 \qquad \text{Roots: } b_{2r+1} \qquad \textbf{(B.22)}$$

If p is a root of equations (B.19) - (B.22) then the corresponding solution exists and is a function of u, for any values of q and with p ranging from $-\infty$ to ∞. Expansion of the continued fractions yields polynomial expressions with q acting as a parameter. Solving for the polynomial roots with a fixed value of q one comes first on the boundary curve a_0 in Figure 2.14 which begins at p= 0, 2*q= 0. Following this the next two curves are a_1 and b_1 starting at p= 1 and 2*q= 0, followed by a_2 and b_2 starting at p= 4 and 2*q= 0, etc. This process is repeated several times for increasing values of q, thus producing the stability boundaries shown in Figure 2.14. E in equation (2.20) contains frequencies which are either all odd or all even multiples of $\omega/2$, as can be seen from equations (B.10) and (B.11). The unstable regions formed by the solution of equations (B.19) - (B.22) and shown in Figure 2.14, correspond to these multiples.

APPENDIX C - FINITE DIFFERENCE APPROXIMATIONS USED IN SMAC METHOD

This appendix presents finite difference approximation of the governing equations solved by the simplified marker and cell (SMAC) numerical scheme employed in the computational study of the interfacial problem, discussed in Section 2.5. Figure C.1 shows the locations of the cell variables used in the SMAC method.

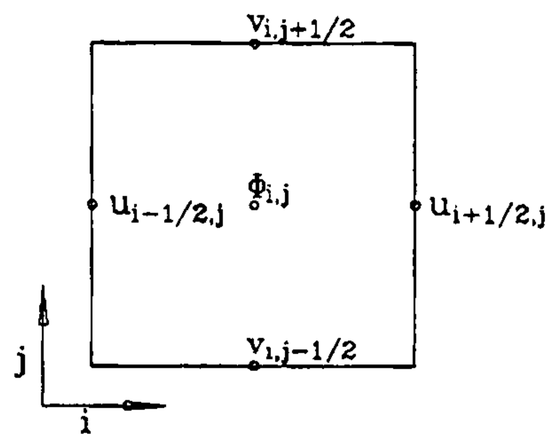

Figure C.1 SMAC finite difference cell and location of the cell variables

The continuity equation, given by equation (2.24), is re-written in finite difference form as follows:

$$D_{i,j}^{n+1} \equiv \frac{r_{i+1/2}^{\alpha} u_{i+1/2,j}^{n+1} - r_{i-1/2}^{\alpha} u_{i-1/2,j}^{n+1}}{r_i^{\alpha} \delta r} + \frac{v_{i,j+1/2}^{n+1} - v_{i,j-1/2}^{n+1}}{\delta z} = 0 \qquad \textbf{(C.1)}$$

The r-direction momentum equation (2.25) is re-written in finite difference form for an arbitrary pressure field θ and new-time $\tilde{u}$ velocities as follows:

$$\begin{aligned} \frac{\tilde{u}_{i+1/2,j}^{n+1} - u_{i+1/2,j}^{n}}{\delta t} = & \frac{r_i^{\alpha} u_{i+1/2,j}^{n} u_{i-1/2,j}^{n} - r_{i+1}^{\alpha} u_{i+3/2,j}^{n} u_{i+1/2,j}^{n}}{r_{i+1/2}^{\alpha} \delta r} \\ & + \frac{u_{i+1/2,j-1/2}^{n} v_{i+1/2,j-1/2}^{n} - u_{i+1/2,j+1/2}^{n} v_{i+1/2,j+1/2}^{n}}{\delta z} \\ & + \frac{\theta_{i,j} - \theta_{i+1,j}}{\delta r} + g_r \\ & + \nu \left[\frac{1}{\delta z^2} \left(u_{i+1/2,j+1/2}^{n} + u_{i+1/2,j-1}^{n} - 2 u_{i+1/2,j}^{n} \right) \right. \\ & \left. - \frac{1}{\delta r \delta z} \left(v_{i+1,j+1/2}^{n} - v_{i+1,j-1/2}^{n} - v_{i,j+1/2}^{n} + v_{i,j-1/2}^{n} \right) \right] \end{aligned} \qquad \textbf{(C.2)}$$

The z-direction momentum equation (2.26) is re-written in finite difference form for new-

time $\tilde{v}$ velocities in a similar fashion to equation (C.2):

$$\frac{\tilde{V}^{n+1}_{i,j+1/2} - V^{n}_{i,j+1/2}}{\delta t} = \frac{V^{n}_{i,j+1/2} V^{n}_{i,j-1/2} - V^{n}_{i,j+3/2} V^{n}_{i,j+1/2}}{\delta z}$$
$$+ \frac{r^{\alpha}_{i-1/2} u^{n}_{i-1/2,j+1/2} V^{n}_{i-1/2,j+1/2} - r^{\alpha}_{i+1/2} u^{n}_{i+1/2,j+1/2} V^{n}_{i+1/2,j+1/2}}{r^{\alpha}_{i} \delta r}$$
$$+ \frac{\theta_{i,j} - \theta_{i,j+1}}{\delta z} + g_z \qquad \text{(C.3)}$$
$$- \frac{\nu}{r^{\alpha}_{i} \delta r} [r^{\alpha}_{i+1/2} (\frac{u^{n}_{i+1/2,j+1} - u^{n}_{i+1/2,j}}{\delta z} - \frac{V^{n}_{i+1,j+1/2} - V^{n}_{i,j+1/2}}{\delta r})$$
$$- r^{\alpha}_{i-1/2} (\frac{u^{n}_{i-1/2,j+1} - u^{n}_{i-1/2,j}}{\delta z} - \frac{V^{n}_{i,j+1/2} - V^{n}_{i-1,j+1/2}}{\delta r})]$$

The finite difference form of the vorticity equation (2.28) if written as:

$$\Omega^{n}_{i+1/2,j+1/2} \equiv \frac{u^{n}_{i+1/2,j+1} - u^{n}_{i+1/2,j}}{\delta z} - \frac{V^{n}_{i+1,j+1/2} - V^{n}_{i,j+1/2}}{\delta r} \qquad \text{(C.4)}$$

In addition, the following finite difference approximations are used for the velocity products u^2 and uv:

$$(u_{i,j})^2 \simeq u_{i-1/2,j}\, u_{i+1/2,j} \qquad \text{(C.5)}$$

$$(uv)_{i+1/2,j-1/2} \simeq \left(\frac{u_{i+1/2,j} + u_{i+1/2,j-1}}{2} \right) \left(\frac{V_{i,j-1/2} + V_{i+1,j-1/2}}{2} \right) \qquad \text{(C.6)}$$

APPENDIX D - SURFACE CELL FLUID CONFIGURATIONS USED IN SMAC METHOD

Figure D.1 shows all possible arrangements of empty cells about a surface cell. During computation new surface cells may be which are identified by the reflagging section. These surface cells must satisfy the continuity equation (2.24) and cells having two adjacent empty sides (i.e. configurations 3, 6, 9, 12 in Figure D.1) must simultaneously satisfy the free-surface tangential stress condition as given by equation (2.37).

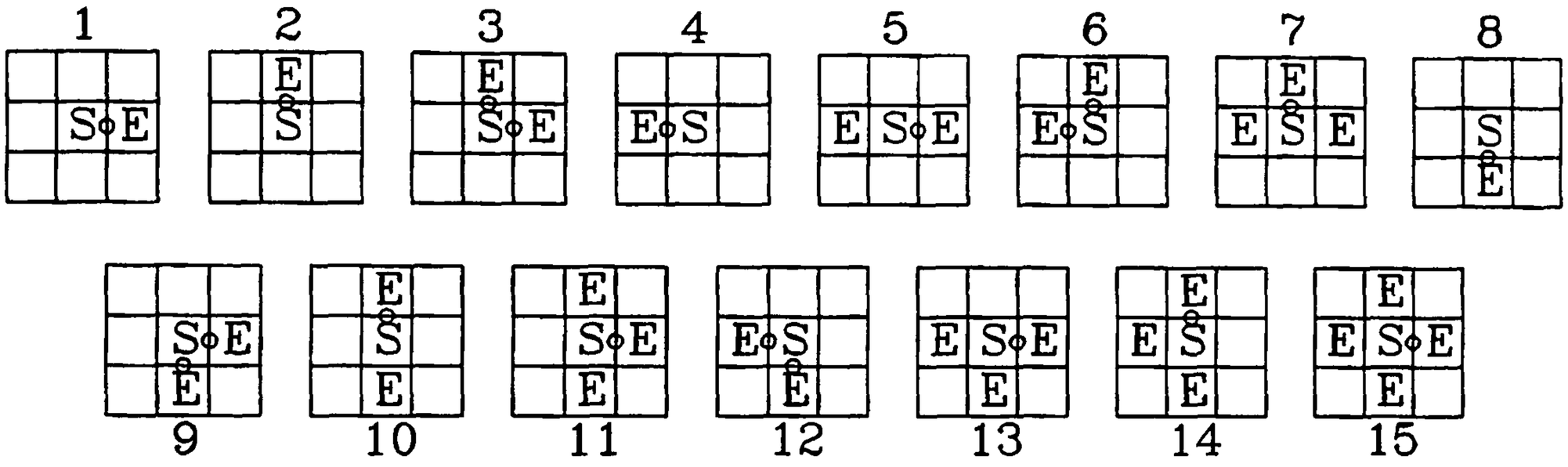

Figure D.1 *The 15 possible arrangements of empty cells about a surface cell*

This is done by resetting the normal velocities at the surface cell faces adjacent to the neighbouring empty cells. For one empty face (i.e. configurations 1, 2, 4, 8 in Figure D.1) or two adjacent empty faces (i.e. configurations 3, 6, 9, 12 in Figure D.1) the appropriate u and/or v may be calculated precisely. Configurations 5, 7, 10, 11, 13, 14, 15 in Figure D.1 involve more than one u and/or more than one v in the surface cell, and no precise treatment is available. Therefore, only one velocity is adjusted to ensure that at least the continuity equation (2.24) is satisfied in the surface cell. The velocities adjusted by this routine are indicated in Figure D.1 by small open circles. Table D.1 gives velocity equations corresponding to each of the configurations.

CONFIGURATION	VELOCITY EQUATION
1, 5, 11, 13, 15	$u_{i+1/2j} = \frac{1}{r_{i+1/2}}[u_{i-1/2j}r_{i-1/2} - \frac{r_i \delta r}{\delta z}(v_{ij+1/2} - v_{ij-1/2})]$
2, 7, 10, 14	$v_{ij+1/2} = v_{ij-1/2} - \frac{\delta z}{r_i \delta r}(u_{i+1/2j}r_{i+1/2} - u_{i-1/2j}r_{i-1/2})$
3,9	$u_{i+1/2j} = u_{i-1/2j}\left(\frac{4r_i - \delta r}{4r_i + \delta r}\right)$
4	$u_{i-1/2j} = \frac{1}{r_{i-1/2}}[u_{i+1/2j}r_{i+1/2} + \frac{r_i \delta r}{\delta z}(v_{ij+1/2} - v_{ij-1/2})]$
6,12	$u_{i-1/2j} = u_{i+1/2j}\left(\frac{4r_i + \delta r}{4r_i - \delta r}\right)$
3,6	$v_{ij+1/2} = v_{ij-1/2} - \frac{\delta z}{4r_i}(u_{i+1/2j} + u_{i-1/2j})\alpha$
8	$v_{ij-1/2} = v_{ij+1/2} + \frac{\delta z}{r_i \delta r}(u_{i+1/2j}r_{i+1/2} - u_{i-1/2j}r_{i-1/2})$
9,12	$v_{ij-1/2} = v_{ij+1/2} + \frac{\delta z}{4r_i}(u_{i+1/2j} + u_{i-1/2j})\alpha$

Table D.1 *List of velocity equations for possible surface arrangements*

APPENDIX E - CALCULATION OF PARTICLE MOVEMENTS USED IN SMAC METHOD

The purpose of this appendix is to describe the area - weighted averaging of the final cell velocities used to calculate the movement of the marker particles. Additional boundary conditions are not required for the area-weighting scheme which is based on the nearest cell velocities. With the reference to Figure E.1, the reference cell (shaded) is defined as the cell lying between the lower pair of u velocities when calculating the u of the kth particle (u_k). Similarly, the cell lying between the left-most pair of v velocities is the reference cell when calculating the v of the particle (v_k). The reference cells provide an indexing base for referencing the four u's and four v's.

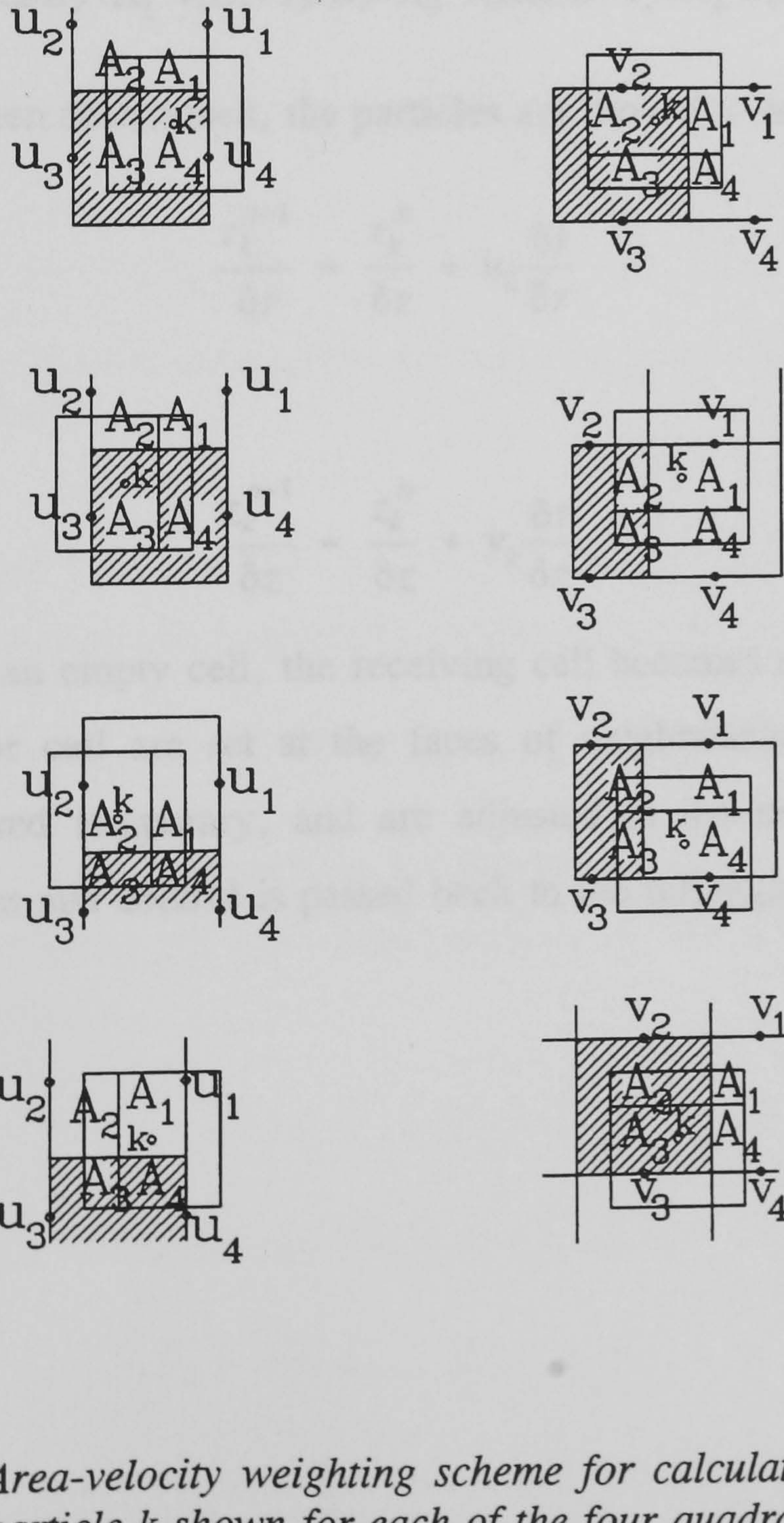

Figure E.1 *Area-velocity weighting scheme for calculation of u_k and v_k, with particle k shown for each of the four quadrants of the cell.*

The donor cell is defined as the cell containing the particle before it is moved. The donor cell velocities may be needed if the particle moves to an empty cell. There is an equal chance of the reference cell being the donor cell for either u_k or v_k. From inspection of Figure E.1, it can be seen that it is possible to calculate u_k, using indexing for donor cell ID, JD and for reference cell IR, JR as:

$$u_k = A_2\ u(ID-1,JR+1)+A_1\ u(ID,JR+1)+A_3\ u(ID-1,JR)+A_4\ u(ID,JR) \qquad \textbf{(E.1)}$$

without calculating which quadrant of the cell the particle k lies in. Similarly, v_k is calculated using IR and JD as:

$$v_k = A_2\ v(IR,JD)+A_1\ v(IR+1,JD)+A_3\ v(IR,JD-1)+A_4\ v(IR+1,JD-1) \qquad \textbf{(E.2)}$$

After u_k and v_k have been determined, the particles are moved to new positions given by:

$$\frac{r_k^{n+1}}{\delta r} = \frac{r_k^{n}}{\delta r} + u_k\frac{\delta t}{\delta r} \qquad \textbf{(E.3)}$$

and

$$\frac{z_k^{n+1}}{\delta z} = \frac{z_k^{n}}{\delta z} + v_k\frac{\delta t}{\delta z} \qquad \textbf{(E.4)}$$

If a particle moves to an empty cell, the receiving cell becomes a surface cell, and the velocities of the donor cell are set at the faces of neighbouring empty cells. These velocities are considered temporary, and are adjusted in the next cycle. This action completes the algorithm and control is passed back to the reflagging section to begin the next cycle.

APPENDIX F - SURFACE TENSION ON A PLANAR CURVE

Consider the forces due to surface tension at a point $\bar{x}_s$ on a planar curved interface separating two fluids as shown in Figure F.1. The curve is assumed to be parameterized by the arc length $s(\bar{x}_s)$, with the unit tangent $\hat{t}$ to the curve taken to be positive in the direction of increasing s.

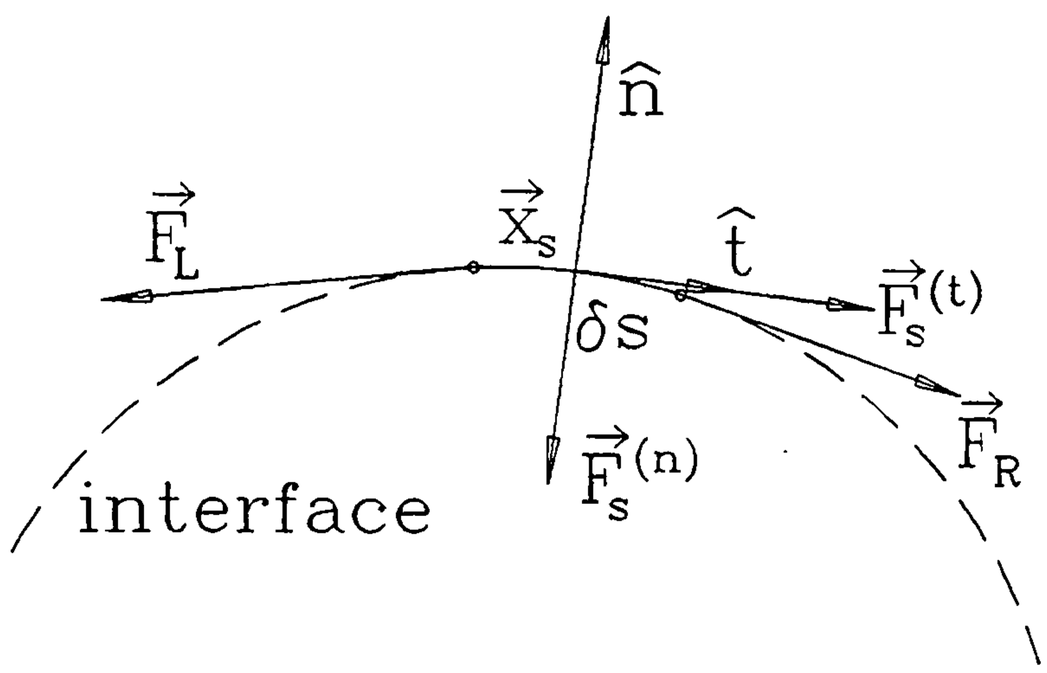

Figure F.1 *Surface tension forces exerted on a planar interface separating two fluids*

The net surface force per unit length at $\bar{x}_s$, $\bar{F}(\bar{x}_s)$, can be expressed as the vector sum of the normal and tangential components of the surface force,

$$\vec{F}_s(\vec{x}_s) = \vec{F}_s^{(n)}(\vec{x}_s) + \vec{F}_s^{(t)}(\vec{x}_s) \qquad \textbf{(F.1)}$$

The normal and tangential surface forces on an element δs can be found by computing the resultant of the tensile forces per unit length pulling on the left ($\bar{F}_L$) and right ($\bar{F}_R$) endpoints of δs, respectively:

$$\vec{F}_s(\vec{x}_s) = \vec{F}_L + \vec{F}_R \qquad \textbf{(F.2)}$$

The left and right tensile forces per unit length are given by

$$\vec{F}_L = -\sigma_L \hat{t}_L \ , \ \vec{F}_R = \sigma_R \hat{t}_R \qquad \textbf{(F.3)}$$

where σ_L, $\hat{t}_L$ and σ_R, $\hat{t}_R$ are the surface tension coefficients and unit tangent vectors at the

left and right endpoints of δs, respectively. The values of the σ and $\hat{t}$ at the left and right endpoints of element δs are estimated with Taylor series expansions in powers of δs about $\bar{x}_s$ as follows:

$$\sigma_R = \sigma(\vec{x}_s) + \frac{\delta s}{2}\frac{d\sigma}{ds}(\vec{x}_s) + \frac{\delta s^2}{8}\frac{d^2\sigma}{ds^2}(\vec{x}_s) + O(\delta s^3) \qquad \textbf{(F.4)}$$

$$\hat{t}_R = \hat{t}(\vec{x}_s) + \frac{\delta s}{2}\frac{d\hat{t}}{ds}(\vec{x}_s) + \frac{\delta s^2}{8}\frac{d^2\hat{t}}{ds^2}(\vec{x}_s) + O(\delta s^3) \qquad \textbf{(F.5)}$$

$$\sigma_L = -\sigma(\vec{x}_s) + \frac{\delta s}{2}\frac{d\sigma}{ds}(\vec{x}_s) - \frac{\delta s^2}{8}\frac{d^2\sigma}{ds^2}(\vec{x}_s) + O(\delta s^3) \qquad \textbf{(F.6)}$$

$$\hat{t}_l = -\hat{t}(\vec{x}_s) + \frac{\delta s}{2}\frac{dt}{ds}(\vec{x}_s) - \frac{\delta s^2}{8}\frac{d^2\hat{t}}{ds^2}(\vec{x}_s) + O(\delta s^3) \qquad \textbf{(F.7)}$$

With the help of the above Taylor expansions, the net surface force on δs, is found to be:

$$\begin{aligned}\vec{F}_s(\vec{x}_s) &\equiv \sigma_R\hat{t}_R - \sigma_L\hat{t}_L \\ &= \delta s\left[\sigma(\vec{x}_s)\frac{d\hat{t}}{ds}(\vec{x}_s) + \frac{d\sigma}{ds}(\vec{x}_s)\,\hat{t}(\vec{x}_s)\right] + O(\delta s^3)\end{aligned} \qquad \textbf{(F.8)}$$

The surface force per unit interfacial area, $\bar{F}_{sa}(\bar{x}_s)$, found using equation (F.8), can be expressed as:

$$\vec{F}_{sa}(\vec{x}_s) = \lim_{\delta s\to 0}\frac{\vec{F}_s(\vec{x}_s)}{\delta s} = \sigma(\vec{x}_s)\frac{d\hat{t}}{ds}(\vec{x}_s) + \frac{d\sigma}{ds}(\vec{x}_s)\,\hat{t}(\vec{x}_s) \qquad \textbf{(F.9)}$$

By comparing equation (F.9) with equation (F.1) , it is apparent that

$$\vec{F}_{sa}^{(n)}(\vec{x}_s) = \left(\sigma\frac{d\hat{t}}{ds}\right)(\vec{x}_s) \qquad \textbf{(F.10)}$$

is the normal component of the surface force, and

$$\vec{F}_{sa}^{(t)}(\vec{x}_s) = \left(\frac{d\sigma}{ds}\hat{t}\right)(\vec{x}_s) \qquad \textbf{(F.11)}$$

is the tangential component of the surface force. Note that the change in the unit tangent

vector $\hat{t}$ to the surface at $\bar{x}_s$ with respect to the arc length s along the surface, appearing in equation (F.10), is the curvature vector, $\bar{\kappa}$, given by

$$\vec{\kappa} \equiv \frac{d\hat{t}}{ds} = (\hat{t}.\nabla)\,\hat{t} \qquad \textbf{(F.12)}$$

The magnitude of $\kappa(x_s)$, the curvature, is also equal to the inverse of the radius of curvature R. That is $\bar{R}(\bar{x}_s)$

$$\kappa(\vec{x}_s) = \left(\frac{1}{R}\right)(\vec{x}_s) \qquad \textbf{(F.13)}$$

APPENDIX G - DATA ACQUISITION AND CONTROL PROGRAM FOR SPRAY CHAMBER EXPERIMENTS

Data acquisition for the transient spray heat transfer experiments and control of the spray chamber injection system were achieved using a PC - based system comprising a National Instruments Lab PC+ input/output board and associated signal conditioning modules. The purpose of this appendix is to provide a detailed description of the three program sequences used for data acquisition and control which were developed using National Instruments' graphical programming environment LabVIEW for Windows.

First, the zero sequence, shown in Figure G.1, reads the output of the millisecond timer (Oki 82C53). This does not give an absolute time value, but provides a reference for timing of the experiment, that is passed to sequence 1, as shown in Figure G.2. Sequence 1 performs the data acquisition, control and timing of the experiment. It consists of two loops. The upper one reads data from a storage buffer using the **AI READ** subroutine, a so-called virtual instrument or VI, stores the data in four arrays as a function of time and saves the arrays into an output file. The bottom loop performs control of the electric servomotor powering the liquid injection system, using the Analogue Output Single Update (**AO 1-UP**) VI, and provides the overall timing of the experimental run. The tick count is read and compared with the timer value reading from sequence 0. If the total elapsed time is less than the required total time span, the specified voltage is sent to the output channel connected to the servomotor.

Finally, sequence 2, shown in Figure G.3, performs recalculation to convert the acquired data to physical units. The data are read from the output file from sequence 1 and split into two-dimensional arrays of time versus value type. Multiplication by the appropriate conversion factors and zero offset compensation are performed, before the arrays are bundled together again and saved back to the file, over-writing the old values. The converted data are also simultaneously displayed on the front panel graphs, as shown in Figure 3.14.

Block Diagram

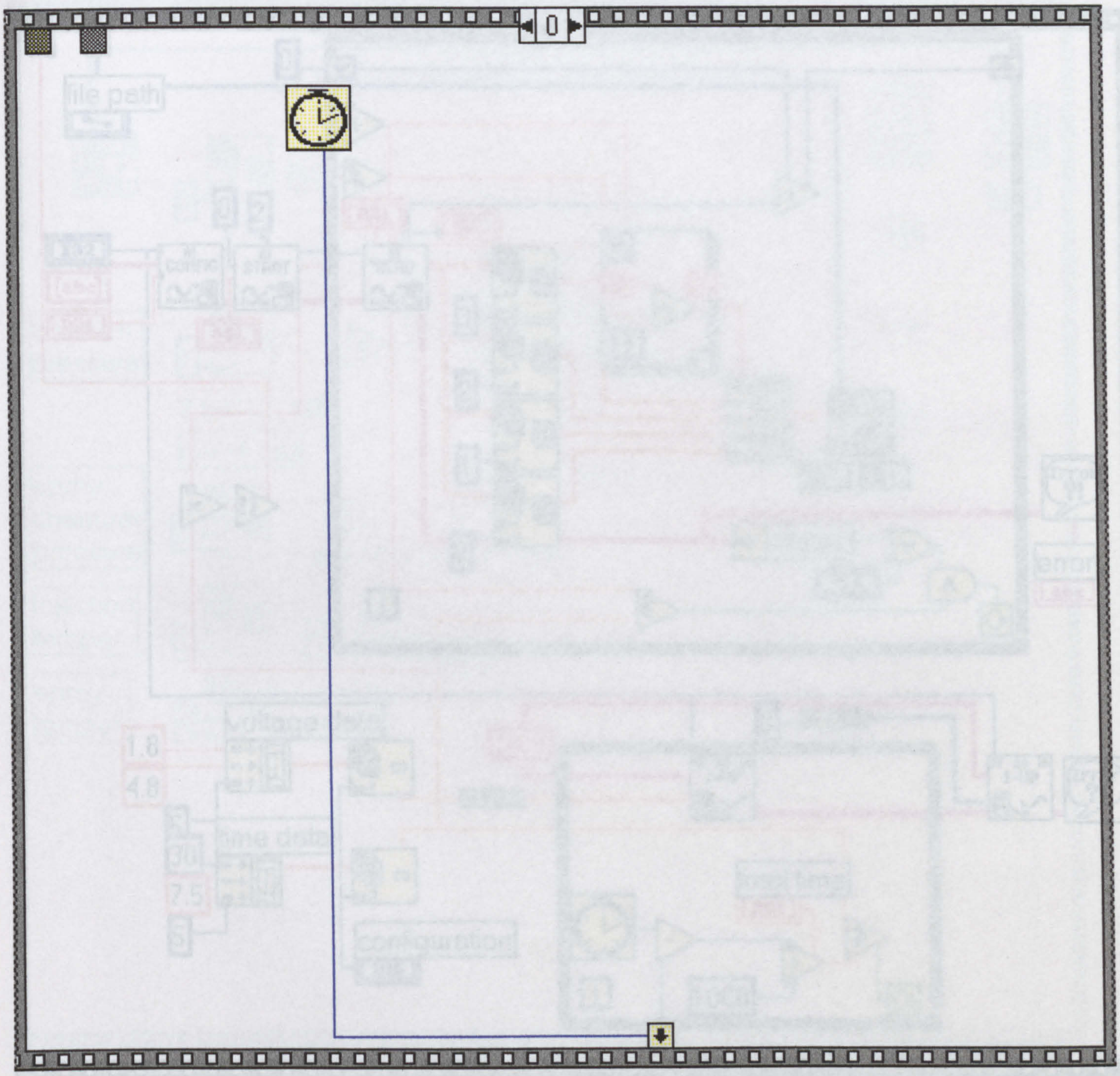

Figure G.1 *Sequence 0 - Reference Time Value Reading*

Block Diagram

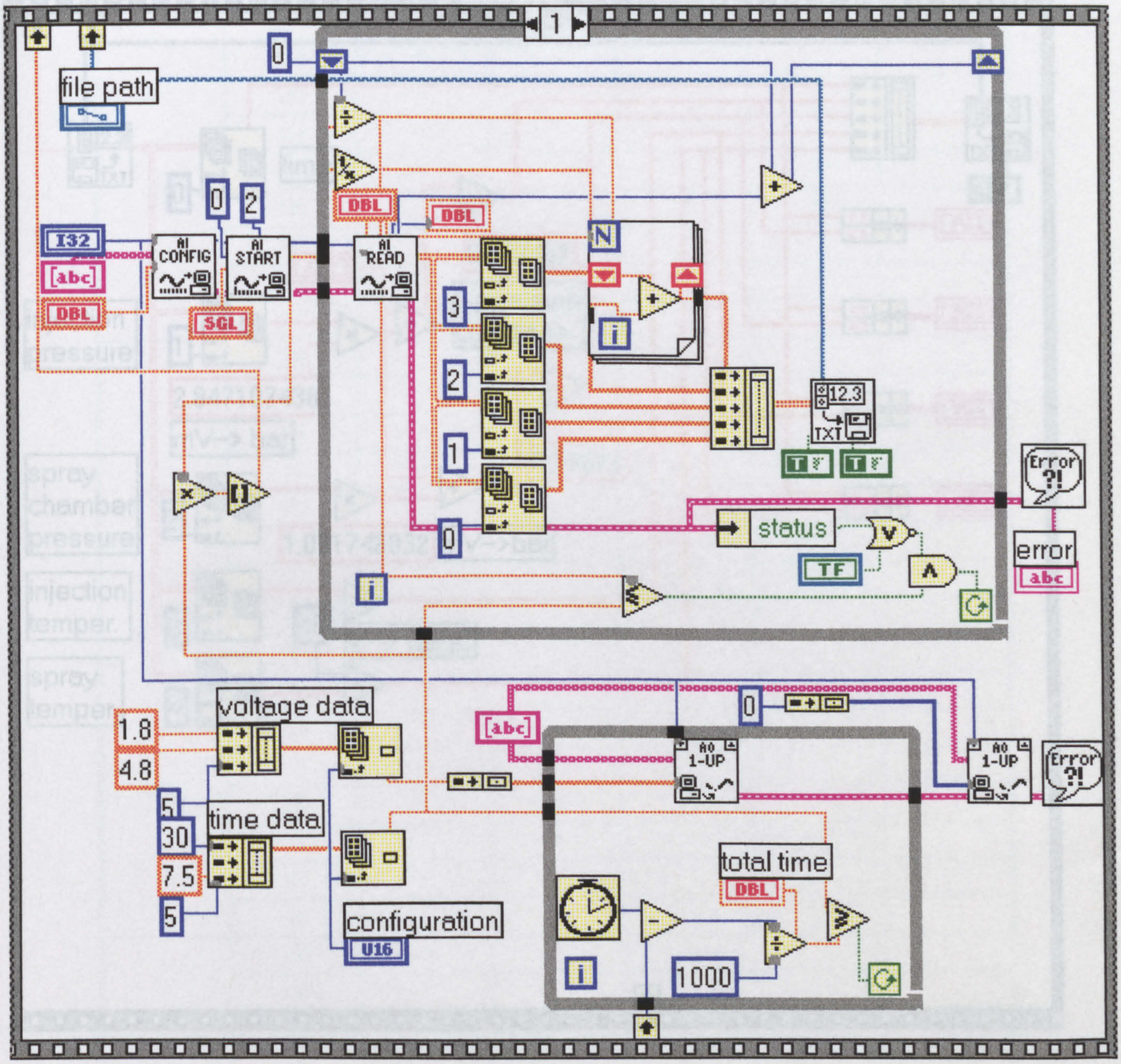

Figure G.2 *Sequence 1 - Data Acquisition and Control*

Block Diagram

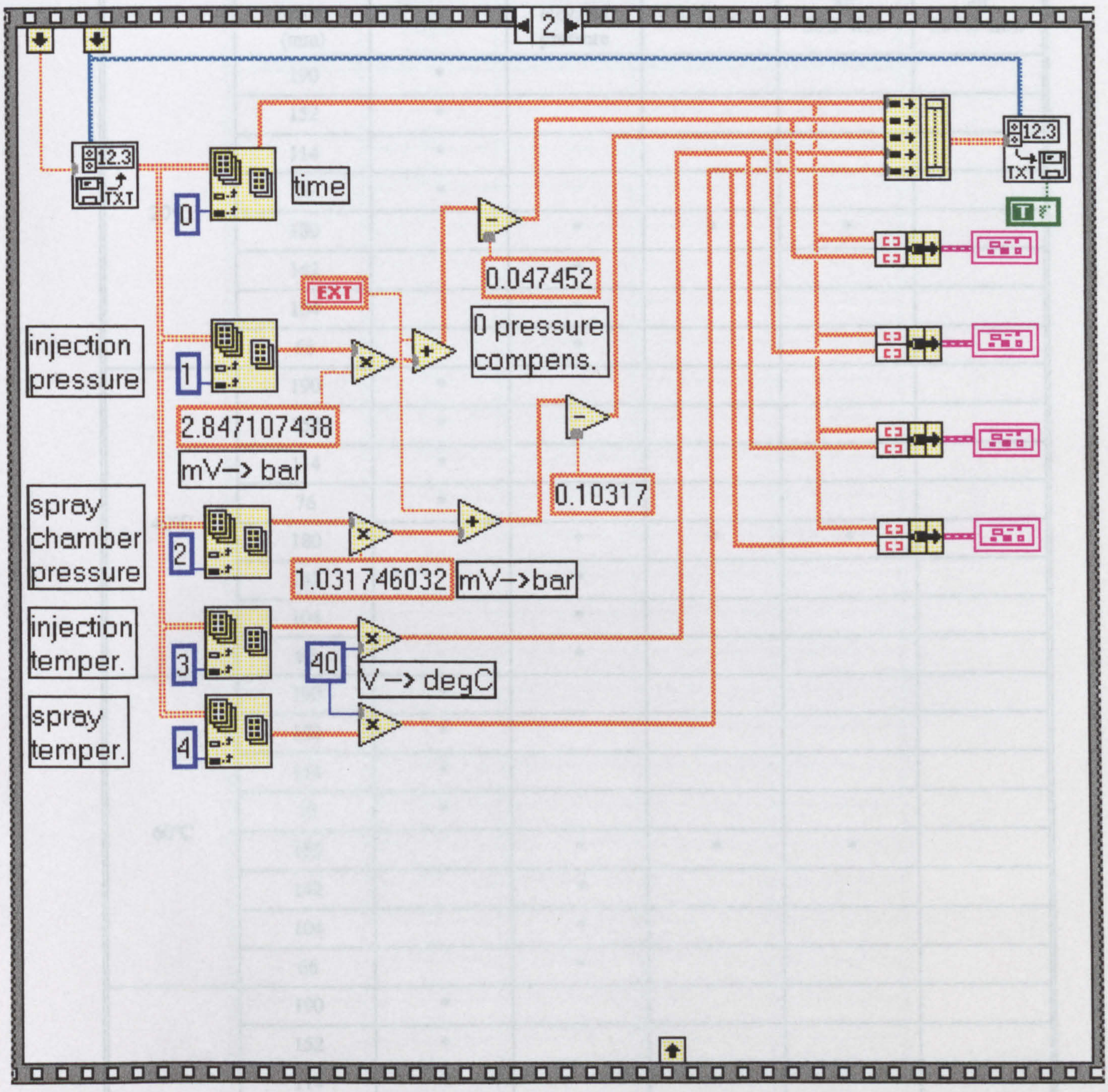

Figure G.3 *Sequence 2 - Recalculation*

		1 central BP 10-90 nozzle; 100% flow unless otherwise				
T_L	chamber height (mm)	air	air at elevated pressure	helium	air 50% flow	air 200% flow
20°C	190	*				
	152	*				
	114	*				
	76	*				
	180		*	*	*	
	142		*			
	104		*			
	66		*			
40°C	190	*				
	152	*				
	114	*				
	76	*				
	180		*	*	*	
	142		*			
	104		*			
	66		*			
60°C	190	*				
	152	*				
	114	*				
	76	*				
	180		*	*	*	
	142		*			
	104		*			
	66		*			
80°C	190	*				
	152	*				
	114	*				
	76	*				
	180		*	*	*	
	142		*			
	104		*			
	66		*			

		BP 10-90 nozzle; 100% flow		
		1 side[1]	2 side[1]	4 side[1]
T_L	chamber height (mm)	air	air	air
20°C	190			*
	152			*
	114			*
	76			*
	180			
	142			
	104			
	66			
40°C	190	*	*	*
	152	*	*	
	114	*	*	
	76	*		
	180			
	142			
	104			
	66		*	
60°C	190	*	*	*
	152	*	*	
	114	*		
	76	*		
	180			
	142			
	104		*	
	66		*	
80°C	190	*	*	*
	152	*	*	*
	114	*		*
	76	*		*
	180			
	142			
	104		*	
	66		*	

Note 1: side nozzles are placed axisymmetrically on a 60 mm diameter circle.

		1 central BP 12-90 nozzle; 100% flow			1 side[1]
T_L	chamber height (mm)	air	air at elevated pressure	helium	air
20°C	180	*	*	*	*
	142	*			
	104	*			
	66	*			
40°C	180	*	*	*	*
	142				
	104				
	66				
60°C	180	*	*	*	*
	142				
	104				
	66				
80°C	180	*	*	*	*
	142	*			
	104	*			
	66	*			

Note 1: side nozzles are placed axisymmetrically on a 60 mm diameter circle.

		1 central BP 14-90 nozzle; 100% flow			1 side[1]	2 side[1]	4 side[1]
T_L	chamber height (mm)	air	air at elevated pressure	helium	air	air	air
20°C	180	*	*	*	*	*	*
	142	*				*	*
	104	*				*	*
	66	*				*	*
40°C	180	*	*	*	*	*	*
	142						
	104						
	66						
60°C	180	*	*	*	*	*	*
	142						
	104						
	66						
80°C	180	*	*	*	*	*	*
	142	*				*	*
	104	*				*	*
	66	*				*	*

Note 1: side nozzles are placed axisymmetrically on a 60 mm diameter circle.

		1 central BP 16-90 nozzle; 100% flow unless otherwise					1 side[1]
T_L	chamber height (mm)	air	air at elevated pressure	helium	air 50% flow	air 200% flow	air
20°C	180	*	*	*	*	*	*
	142	*					
	104	*					
	66	*					
40°C	180	*	*	*			*
	142						
	104						
	66						
60°C	180	*	*	*			*
	142						
	104						
	66						
80°C	180	*	*	*	*	*	*
	142	*					
	104	*					
	66	*					

Note 1: side nozzles are placed axisymmetrically on a 60 mm diameter circle.

		1 central BP 18-90 nozzle; 100% flow			1 side[1]
T_L	chamber height (mm)	air	air at elevated pressure	helium	air
20°C	180	*	*	*	*
	142	*			
	104	*			
	66	*			
40°C	180	*	*	*	*
	142				
	104				
	66				
60°C	180	*	*	*	*
	142				
	104				
	66				
80°C	180	*	*	*	*
	142	*			
	104	*			
	66	*			

Note 1: side nozzles are placed axisymmetrically on a 60 mm diameter circle.

		Spraying Systems LN10 nozzle			
		1 central		2 side	4 side
		20 g/s	10 g/s		
T_L	chamber height (mm)	air	air	air	air
20	180	*	*	*	*
40	180	*	*	*	*
60	180	*	*	*	*
80	180	*	*	*	*

		1 central Spraying Systems LN8 nozzle	
		Air	
T_L	chamber height (mm)	20 g/s	10 g/s
20	180	*	*
40	180	*	*
60	180	*	*
80	180	*	*

APPENDIX I : COMPUTATION OF STILL ZONE GEOMETRIES AND VOLUMES USED IN SPRAY CHAMBER ANALYSIS

The still zones volumes required in the computational analysis of the transient processes occurring in the spray chamber were found using a CAD technique. Still zone geometries were drawn in the AutoCAD R12 environment for the different nozzle configurations. The AutoCAD solid modeller extension enabled the appropriate number of voxels to be generated and the calculation of the corresponding volumes. Table I.1 summarises these findings.

CONFIGURATION GEOMETRY	STILL ZONE VOLUME (m^3)	
1 CENTRAL NOZZLE	$4.638.10^{-4}$	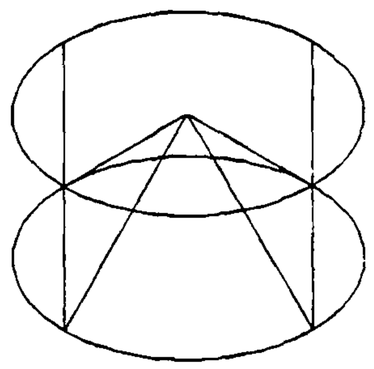
1 SIDE NOZZLE	$5.480.10^{-4}$	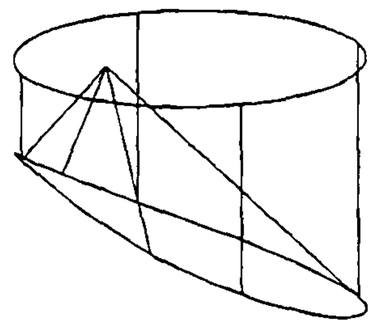
2 SIDE NOZZLES	$3.649.10^{-4}$	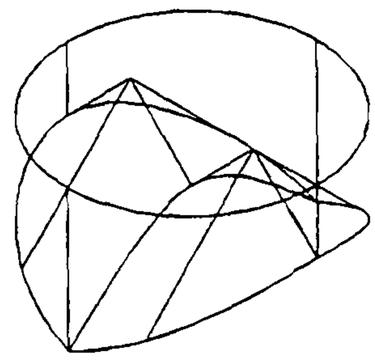
4 SIDE NOZZLES	$2.589.10^{-4}$	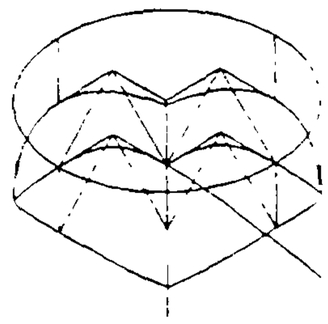

Table I.1 *Geometries and volumes of the still zones for different nozzle configurations*

APPENDIX J : ANALYTICAL EXPRESSIONS DERIVED FOR THE PROPERTIES OF WATER VAPOUR+

The FORTRAN computer program used to calculate the transient variations of the dependent variables T_D, T_G and m_D during the spray process incorporated analytical functions expressing the variations of the specific heat at constant volume, c_{vv}, and the specific volume, v, of the saturated water vapour and the saturation pressure of water, p_{SCV}, as functions of temperature.

The method of least squares incorporated within the SigmaPlot graph plotting package was used to fit analytical expressions to the data tabulated for c_{pg}, v and p_{SCV} in [67]. Figure J.1 shows the comparison between the tabulated data and the fitted function obtained for the specific heat at constant pressure of saturated water vapour, c_{pg}, as a function of temperature. Figures J.2 and J.3 show similar comparisons for the specific volume of saturated water vapour, v, and the saturation pressure of water, p_{SCV}, respectively.

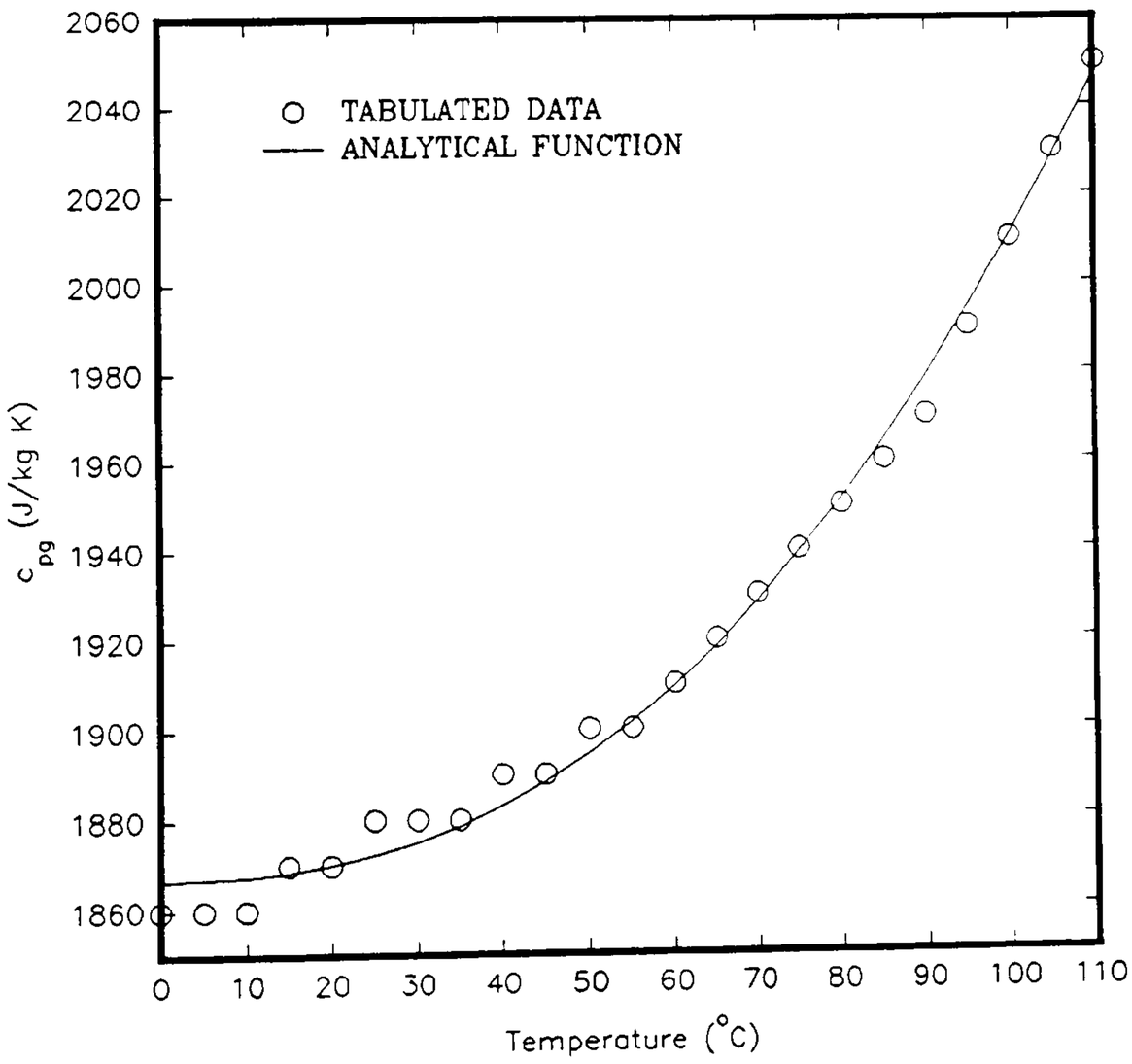

Figure J.1 *Comparison between tabulated data and fitted function for the variation of the specific heat at constant pressure, c_{pg}, of saturated water vapour with temperature.*

+ Note : The references mentioned in this Appendix refer to those for Chapter 3.

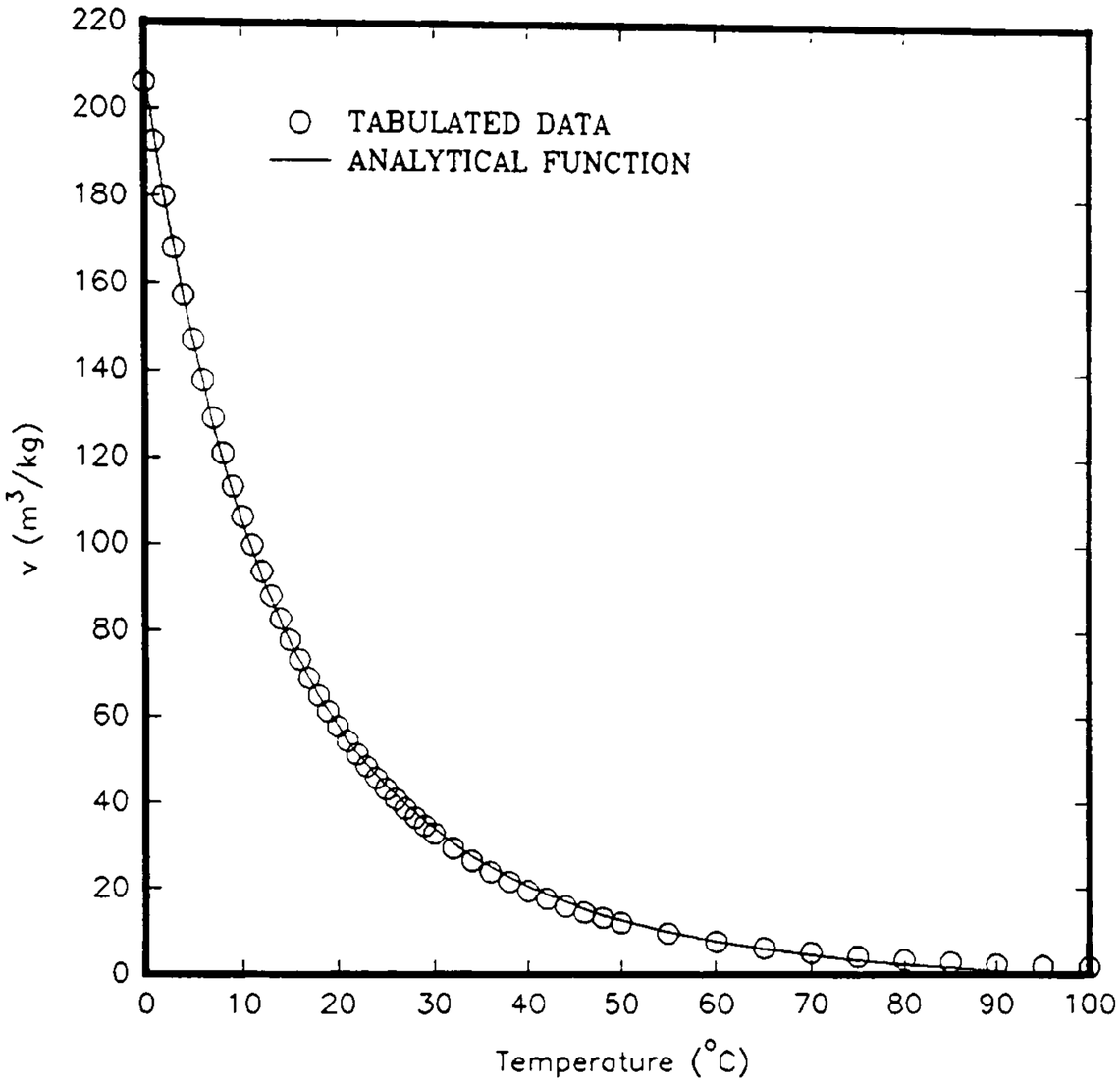

Figure J.2 *Comparison between tabulated data and fitted function for the variation of the specific volume of saturated water vapour, v, with temperature.*

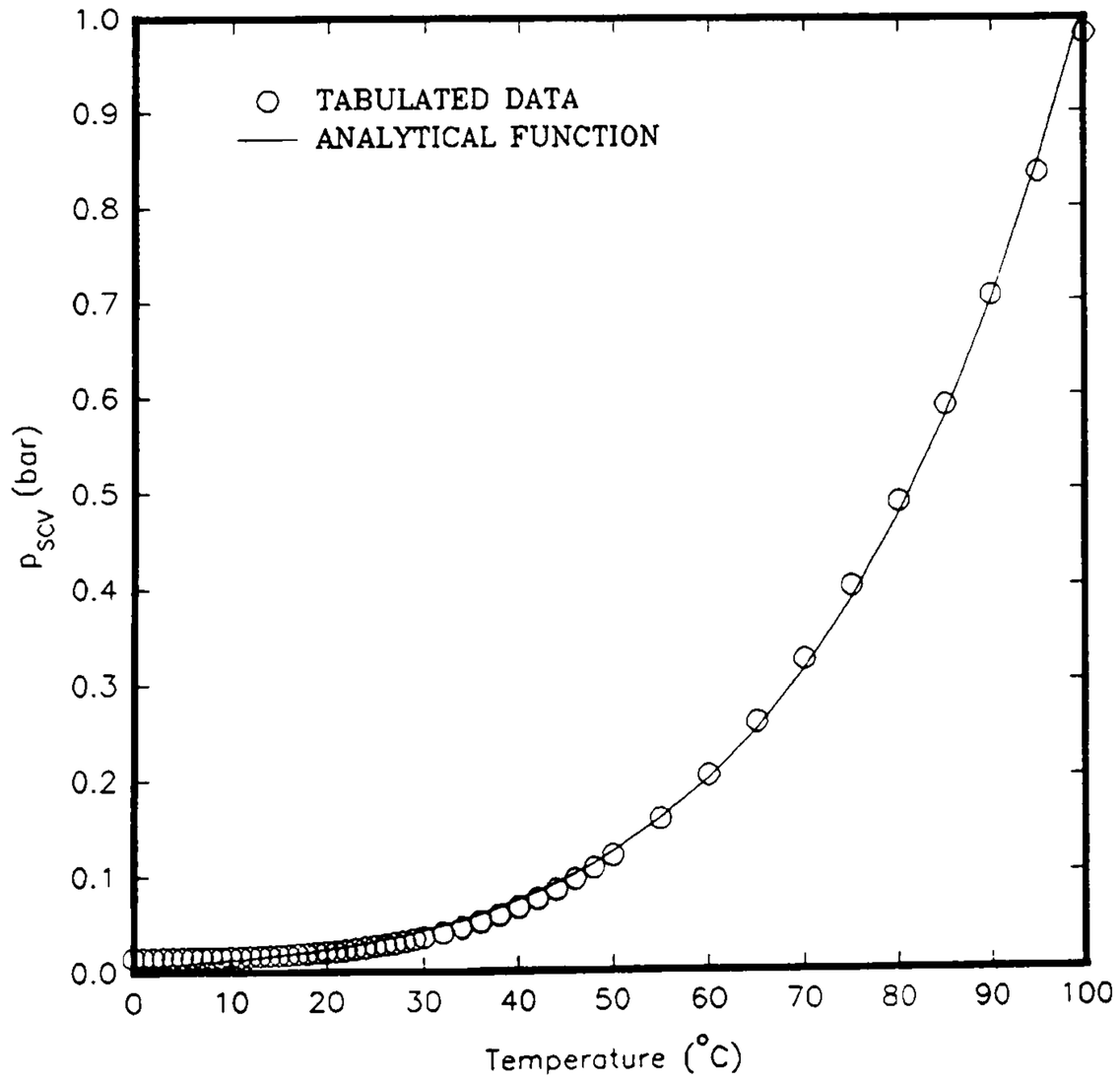

Figure J.3 *Comparison between tabulated data and fitted function for the variation of the saturation pressure of water, p_{SCV}, with temperature.*

The expression for the specific heat at constant pressure, c_{pg}, obtained by the method of least squares is given by

$$c_{pg} = 0.0025t^{2.37977} + 1866.86552 \quad \textbf{(J.1)}$$

The specific heat at constant volume, c_{vV}, can then be evaluated simply as

$$c_{vV} = c_{pg} - R_V \quad \textbf{(J.2)}$$

where c_{pg} is found using Equation (J.1) and R_V is the specific gas constant of water vapour taken equal to 461.5 J/kg K.

The variation of the specific volume of the saturated water vapour, v, with temperature is fitted by the equation

$$v = \frac{3.859\times10^{8}}{(t + 50.34)^{3.677}} - 4.184 \quad \textbf{(J.3)}$$

The following expression was found for the variation of the saturation pressure of water, p_{SCV}, with temperature:

$$p_{SCV} = 3.566\times10^{-7}t^{3.2163} + 0.01519 \quad \textbf{(J.4)}$$

It should be noted that the temperature, t, must be substituted in Equations (J.1) - (J.4) in °C. Equation (J.4) yields the saturation pressure in bar and all other properties are evaluated in basic SI units.

APPENDIX K - PUBLISHED WORKS

1. Paper presented at PARTEC 95, 11th European Conference of ILASS - Europe on Atomization and Sprays, held between 21 - 23 March 1995 in Nurnberg, Germany.

307

J. Valha, J.S. Lewis and J. Kubie

School of Mechanical and Manufacturing Engineering,
Middlesex University, Bounds Green Road,
London N11 2NQ, England

Transient Heat Transfer between Liquid Sprays and Surrounding Gas

1 Introduction

Injecting liquid in the form of a spray is an efficient form of liquid-gas contacting since a large interfacial area per unit volume is achieved with a very small gas phase pressure drop [1,2]. This is employed in many heat transfer applications, such as spray condensers, fuel sprays, spray cooling of gases, evaporative cooling and spray drying. The continuous phase can be either pure vapour or vapour-gas mixture or gas, and the liquid droplets can be either single-component or multi-component. Solid or hollow cone spray nozzles are commonly used in spray condensers. The spray produced is uniformly distributed over a relatively narrow cone (cone angles in the range 60°-90°) and drop sizes ranging from 50 to 1000 micron are common.

The most important advantages of spray heat transfer are: (i) excellent heat transfer performance, due to the large interfacial area per unit volume of liquid and the absence of a solid partition between the phases, (ii) small overall gas phase pressure drop and (iii) compactness: volumetric heat transfer rates are high and overall vessel size is correspondingly small.

The disadvantages of spray heat transfer are: (i) it is not possible to obtain true counter-current flow without using several spray sections, (ii) a large amount of liquid, often of high purity is required when vapour condensation takes place, and thus liquid pumping energy input can be significant and (iii) the liquid must be cooled (or heated) in a separate exchanger, unless an independent supply of cold liquid is available.

The work described in this paper has been undertaken to help in the understanding of the basic mechanism of heat transfer between liquid sprays and gases. An experimental investigation of heat transfer from hot water spray droplets injected into a gas enclosed within a cylinder is described. Heat transfer rates are investigated indirectly from the measurements of the gas pressure, p, in the cylinder. Experiments were conducted for 1, 2 and 4 spray nozzle configurations and the effects of liquid flowrate, initial gas pressure and volume, and type of gas, air or helium, were investigated. The experimental apparatus and test methods are described and a selection of preliminary experimental data is presented. It is shown that heat transfer rates are virtually independent of the size and number of the

nozzles, used for the production of the sprays, but depend strongly on the mass flowrate of the injected liquid.

2 Experimental Work

A diagram of the experimental apparatus is shown in Figure 1. The major components are: (i) spray chamber, (ii) spray nozzles, (iii) liquid injection system, (iv) temperature controlled circulator bath and (v) instrumentation and control system.

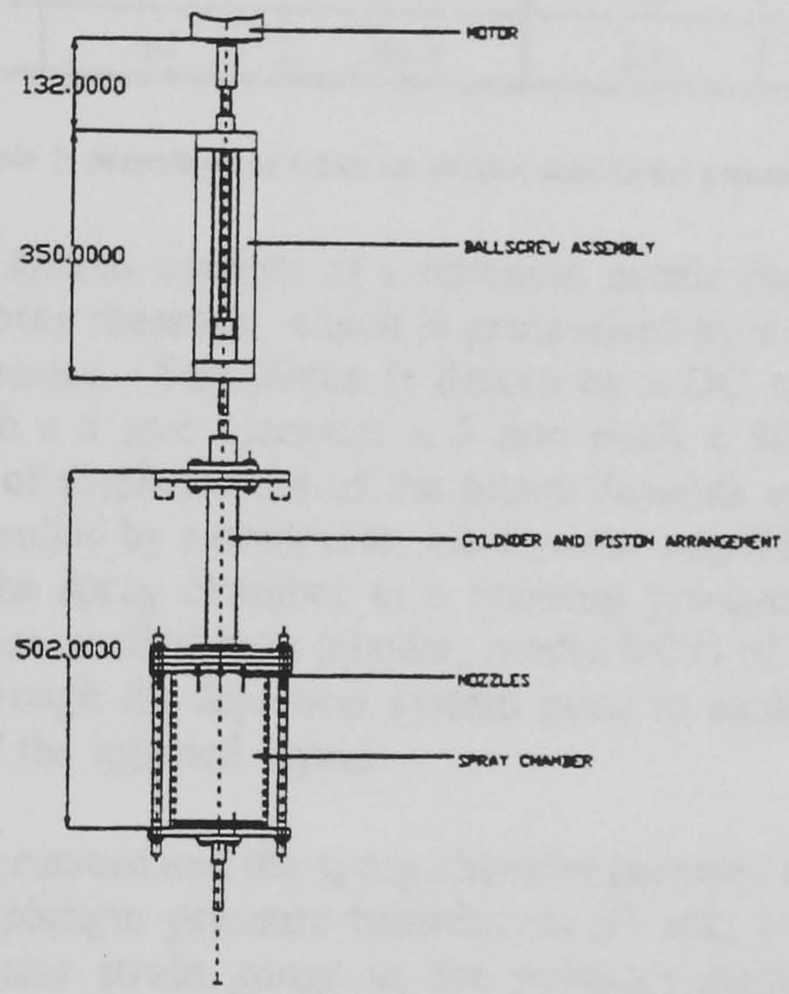

Figure 1: A diagram of the experimental apparatus

The spray chamber is constructed from a perspex cylinder, 121 mm internal diameter and 190 mm long, mounted with its axis vertical. Aluminium cover plates are fitted to both ends of the cylinder giving the chamber an enclosed volume of approximately 2 litres. The chamber is able to withstand a maximum internal pressure of about 4 bar.

Spray nozzles are installed at one or more of the five positions provided in the upper cover plate, centrally and at four equi-spaced positions on a 60 mm diameter circle, and point downwards. Solid cone nozzles, manufactured from brass by the Delavan company, were used in the experimental work. The manufacturer's data on operating pressure, spray angle and Sauter mean diameter for two different flowrates of water at 80°C, are listed in Table 1 for each type of nozzle tested.

309

Nozzle reference	Water flowrate 35 litre/hour			Water flowrate 70 litre/hour		
	Pressure	Spray angle	SMD	Pressure	Spray angle	SMD
	bar	degree	micron	bar	degree	micron
BP 10-90	1.63	90	216.0	6.55	80	150.6
BP 12-90	1.14	85	255.3	4.55	85	168.4
BP 14-90	0.83	80	296.9	3.31	90	185.2
BP 16-90	0.64	75	337.5	2.55	90	204.5
BP 18-90	0.50	65	396.5	2.0	90	224.3

Table 1: Manufacturer's data on nozzles used in the present work

The liquid injection system consists of a common nozzle feed cavity, bolted to the upper cover of the spray chamber, which is pressurised by a 40 mm diameter piston and cylinder arrangement. The piston is driven by a DC servomotor (SEM, type MT30R4-58) through a 5 mm diameter x 5 mm pitch x 300 mm long ball screw assembly. The rate of displacement of the piston depends on the servomotor input voltage which is controlled by a computer, via a power amplifier, thus enabling water to be injected into the spray chamber at a constant pre-determined flowrate. An external temperature controlled bath (Haake, model DC1) of 3 litre capacity is used to circulate water through the injection system prior to each experiment to set the initial temperature of the injected liquid.

The nozzle injection pressure and the spray chamber pressure are measured using 0-7 bar gauge silicon diaphragm pressure transducers (Druck, type PDCR 810) which employ a semiconductor strain gauge as the pressure sensing element. Mineral insulated copper-constantan thermocouples, 1.5 mm diameter, are used to measure the water temperature in the nozzle feed cavity and temperatures at four positions in the spray chamber: at the top of the chamber, and at 20 mm, 125 mm and 160 mm from the bottom of the chamber.

The data acquisition and control system is based on a multifunction input/output board (National Instruments, Lab PC+) installed in a IBM compatible 486DX personal computer. The Lab PC+ board is controlled via National Instruments' LabVIEW for Windows software (together with NI-DAQ driver software) which utilises Visual C graphical programming. A scan rate of 40 Hz was chosen for the measurement data acquisition. The system is also used to control the speed of the servomotor which determines the injected liquid flowrate. Before each new set of experiments the flowrate delivered by the piston-cylinder injection system was checked using a collection method and minor adjustments were made to the motor input voltage to ensure that the design flow rate was maintained.

Water was used as the injected liquid for all the tests reported in this work. Air was used as the working gas in the majority of the experimental work, but helium was also used in some tests. To ensure that helium in the spray chamber was not contaminated with air, the chamber was initially filled with water which was then purged with helium. The initial proportions of gas and water in the spray chamber were set by partially filling the chamber with water. Hence the height of the space occupied by the gas could be varied from 190 mm to 76 mm (four water levels were tested). In order to prevent the temperature of the gas in the spray chamber rising by conduction from the nozzle injection chamber, the gas was circulated through the spray chamber prior to each run. The initial gas temperature was nominally 30° for all experimental runs.

Each test was conducted for a given type, number and location of nozzles. The water to be injected was circulated through the external temperature controlled bath, the nozzle feed cavity and the injection cylinder until it reached the desired temperature. Nominal injected water temperatures, T_L, of 20°C, 40°C, 60°C and 80°C were used in the tests. The injection system was then isolated from the bath and circulation was stopped. The spray chamber was isolated at the same time and the initial gas temperatures in the spray chamber were noted. Water was then injected into the spray chamber at a constant pre-determined flowrate and for a pre-determined time, set and controlled by the computer-based control system. The duration of the water injection phase varied between 30 s and 3.5 s, according to the number of nozzles and the flowrate per nozzle.

The pressure in the spray chamber and the pressure in the nozzle feed cavity were continuously monitored by the data acquisition system during the water injection phase. The outputs from the thermocouples located in the nozzle feed cavity and at the top of the spray chamber were also monitored throughout each test, although the response of the thermocouples was generally too slow to follow the transient temperature variations. Consequently, the other three thermocouples in the spray chamber were only used to indicate the temperatures before and after each experimental run.

3 Experimental Results

As discussed above, experiments were conducted for 1 central nozzle, 1 perimeter nozzle, and 2 and 4 symmetrically spaced perimeter nozzle configurations, and five different nozzle sizes. Furthermore, the effects of initial gas pressure, p_o, and volume, the type of gas, air or helium, and the initial temperature difference between the injected liquid and the gas were also considered. The experimental results are presented in Figures 2 to 11 in the form of dimensionless pressure in the chamber, defined as the ratio p/p_o, against the injection time. It should be pointed out that many of the quoted parameters are nominal. For example, the temperature of the

injected liquid varied somewhat over the duration of the experiment, and hence the best estimates of temperatures are quoted. Furthermore, even though the initial pressure, p_0, was nominally atmospheric, it, once again, varied from experiment to experiment. However, all the figures do give important results in that they show accurately the rapid initial rise of pressure in the spray chamber, which is closely related to the initial rapid rate of heat transfer between droplet sprays and the surrounding gas. It should be noted that all experimental results reported in this preliminary work were obtained with the initial height of the space occupied by the gas set at 190 mm.

Figure 2 shows the influence of the liquid temperature on the variation of pressure with time (the only variable is the liquid temperature; all other parameters are constant). Figure 3 shows the influence of the thermophysical properties of the surrounding gas, either helium or air, on the variation of pressure with time. It indicates that the pressure rise is considerably faster for helium.

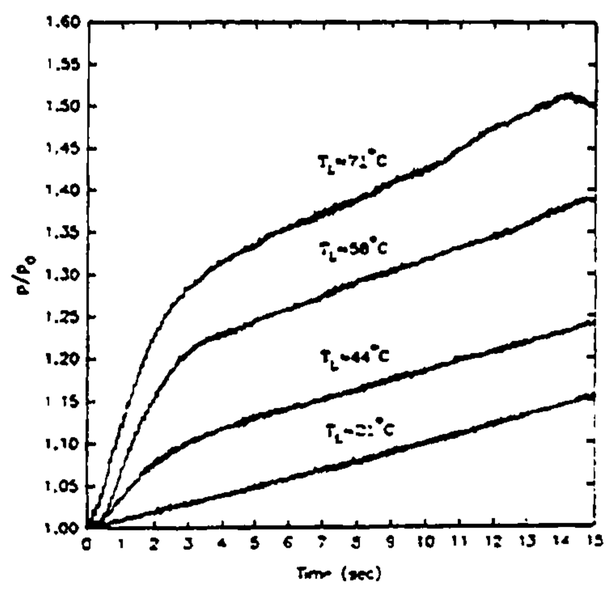

Figure 2: Influence of liquid temperature with 1 central BP10-90 nozzle in air (water flowrate 20 g/s, $p_0 \approx 1$ bar)

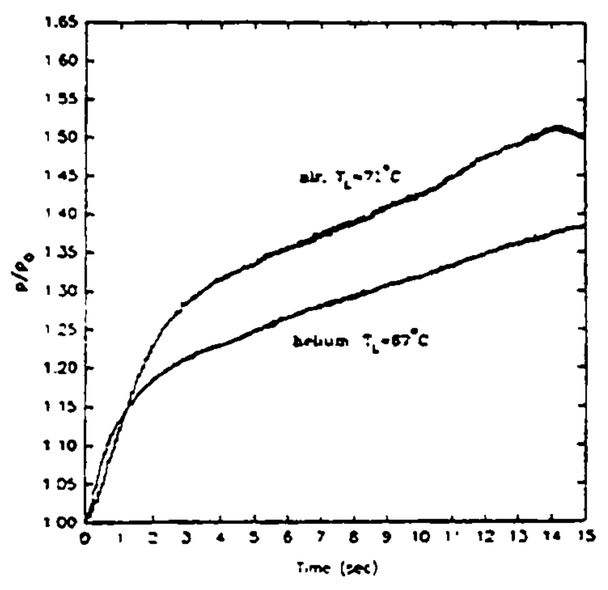

Figure 3: Influence of the surrounding gas with 1 central BP10-90 nozzle (water flowrate 20 g/s, $p_0 \approx 1$ bar)

Figure 4 shows the influence of the initial pressure in the chamber, with air as the working gas. Figure 5 shows the influence of the position of a single nozzle by comparing the pressure rise for one central nozzle and one perimeter nozzle of the same design and the same conditions. It indicates that the pressure rise is somewhat greater for the central nozzle.

Figure 6 shows the influence of the size of a single nozzle on the variation of pressure with time. The only variable is the size of the nozzle; all other parameters are constant. This figure indicates that the pressure rise depends only weakly on the size of the nozzle. Furthermore, there is no observable systematic influence of the nozzle size on the pressure rise in the chamber. Similarly, Figure 7 shows the

influence of two sets of four nozzles, four BP 10-90 nozzles and four BP 14-90 nozzles. This figure indicates, once again, no significant influence of the nozzle size on the pressure in the chamber.

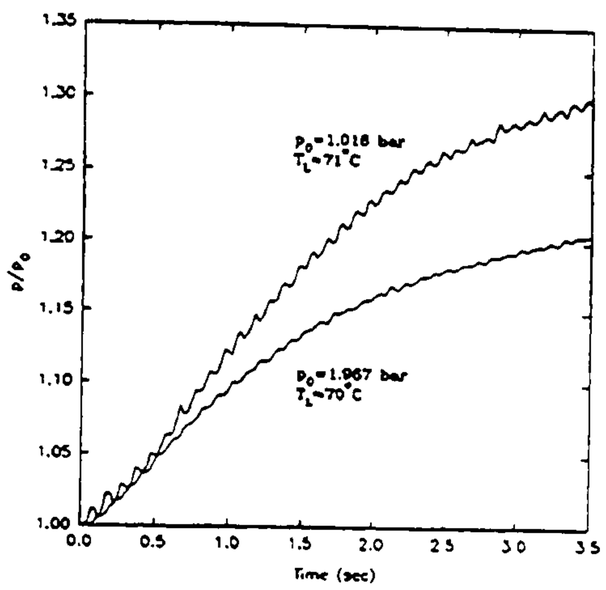

Figure 4: Influence of the initial pressure level with 1 central BP10-90 nozzle in air (water flowrate 20 g/s)

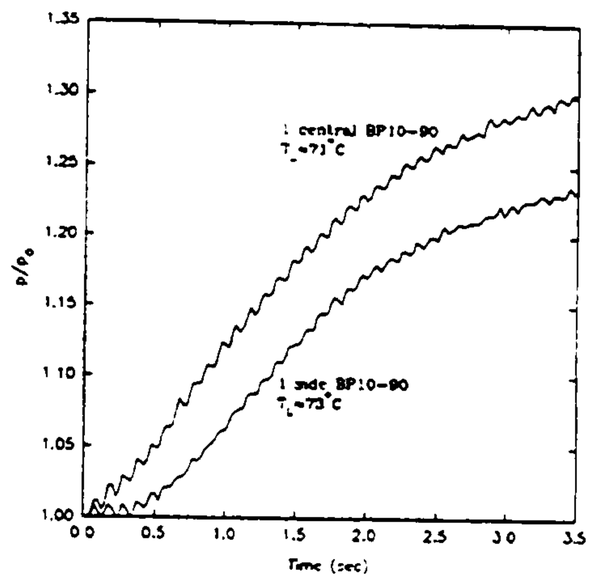

Figure 5: Influence of BP10-90 nozzle position in air (water flowrate 20 g/s, $p_0 \approx 1$ bar)

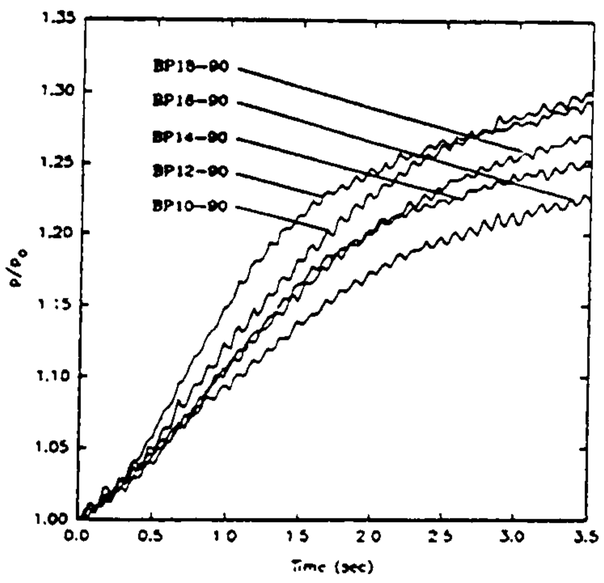

Figure 6: Comparison of nozzle performance in air (1 central nozzle, water flowrate 20 g/s per nozzle, $p_0 \approx 1$ bar, $T_L \approx 70°C$)

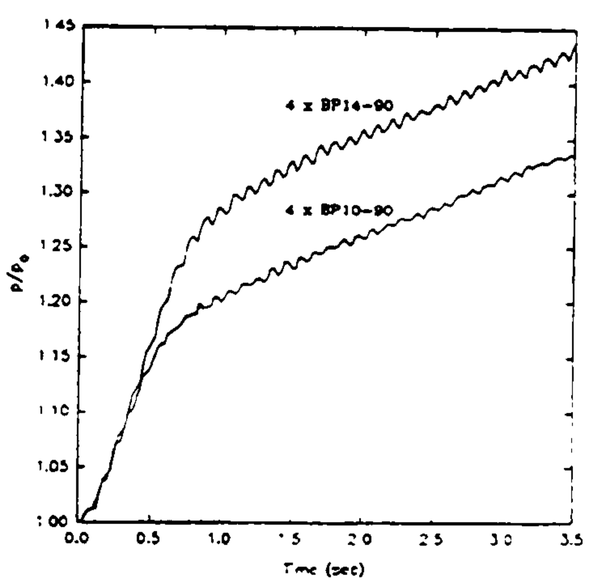

Figure 7: Comparison of nozzle performance in air (4 side nozzles, water flowrate 20 g/s per nozzle, $p_0 \approx 1$ bar, $T_L \approx 70°C$)

Figures 8 and 9 show the influence of the number of identical nozzles BP 10-90 and BP 14-90 respectively on the variation of pressure with time. Both figures compare the performance of one central nozzle, two perimeter nozzles and four perimeter nozzles. In each case the water flowrate is 20 g per second per nozzle (20 g/s for the single nozzle, 40 g/s for two nozzles and 80 g/s for four nozzles). Figure 10 shows the influence of halving the flowrate of the injected liquid for one central BP

10-90 nozzle, with all other parameters constant. Finally, Figure 11 compares the performance of one central BP 18-90 nozzle with the liquid flowrate of 20 g/s and one central BP 10-90 nozzle with the liquid flowrate of 10 g/s, with all other parameters constant. These two cases were chosen because, as indicated in Table 1, the nominal Sauter mean drop diameters are similar (224 micron and 216 micron respectively).

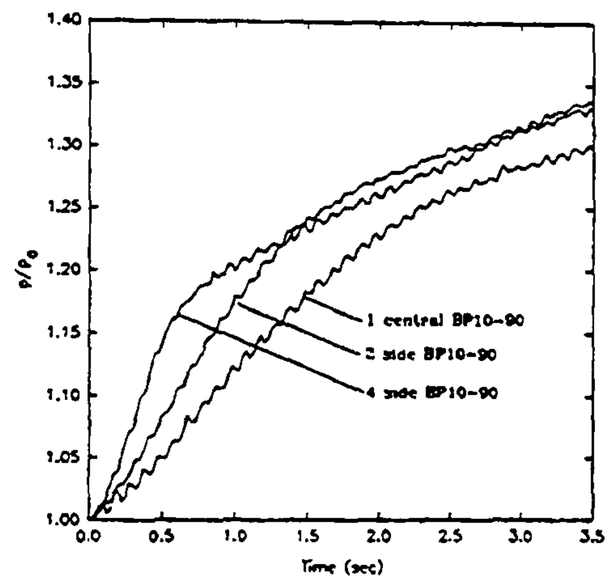

Figure 8: Influence of the number of BP10-90 nozzles in air (water flowrate 20 g/s per nozzle, $p_0 \approx 1$ bar, $T_L \approx 70°C$)

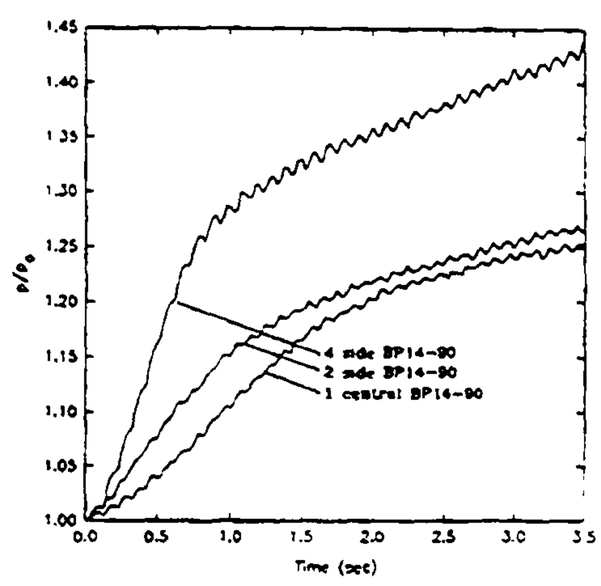

Figure 9: Influence of the number of BP14-90 nozzles in air (water flowrate 20 g/s per nozzle, $p_0 \approx 1$ bar, $T_L \approx 70°C$)

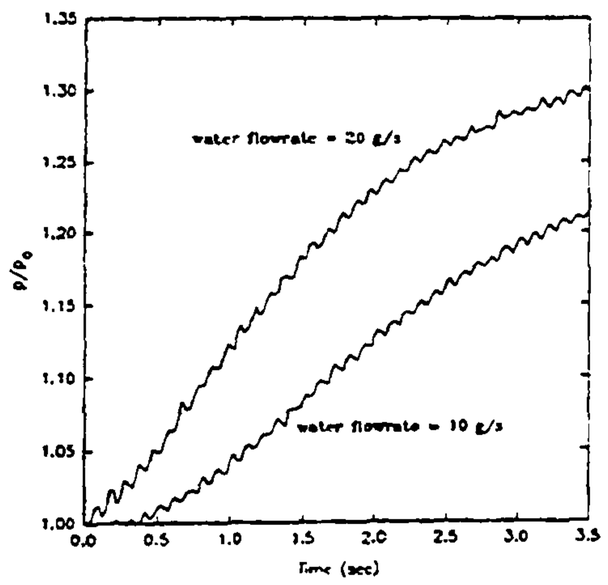

Figure 10: Influence of water flowrate with 1 central BP10-90 nozzle in air ($p_0 \approx 1$ bar, $T_L \approx 70°C$)

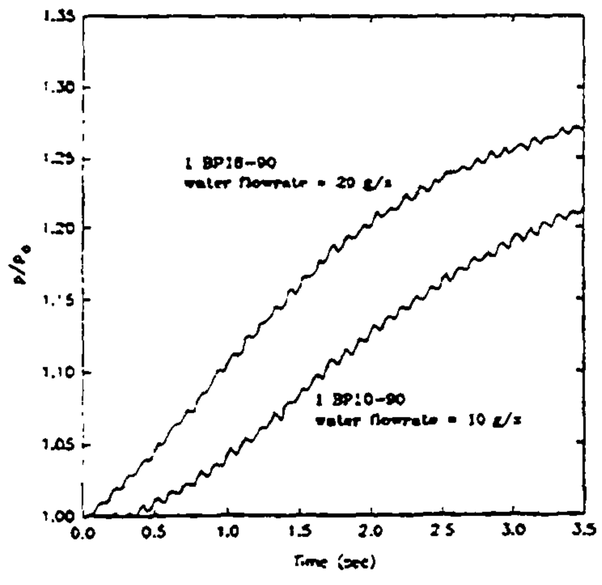

Figure 11: Influence of water flowrate with 1 central nozzle in air and SMD approximately equal for both nozzles ($p_0 \approx 1$ bar, $T_L \approx 70°C$)

4 Discussion

The pressure rise in the chamber is due to three major mechanisms: (i) increase in the temperature of the contained gas, (ii) increase in the steam partial pressure by

evaporation from the injected liquid, and (iii) decrease in the volume of the gas due to the accumulation of the injected liquid in the spray chamber. This is demonstrated in Figures 2 and 3. The initial rapid rise is predominantly due to mechanisms (i) and (ii), as the gas is heated to approach the liquid injection temperature and liquid evaporates from the droplets. As the injection period proceeds the pressure - time curves assume a lower positive slope consistent with mechanism (iii).

As expected, Figure 2 shows that the greater the difference between the temperature of the liquid and the initial gas temperature the greater the rise in pressure in the chamber. This figure demonstrates that the heat transfer process is more effective as the temperature difference increases. Similarly, Figure 3 confirms that the heat transfer increases with increasing gas thermal conductivity. Figure 4 shows that the rise in the dimensionless pressure, p/p_0, is faster for the lower initial pressure, p_0; however, the rise in the absolute pressure, p, is faster for the higher initial pressure, p_0.

Comparison of the effects of liquid injection through a single central nozzle with a single perimeter nozzle in Figure 5 suggests that the heat transfer process is more effective in the former case. This is probably due to the volume of the zone in which the spray droplet are in contact with the surrounding gas. This zone, which is defined by the volume between the spray cone, the liquid on the bottom of the chamber and the walls of the chamber, is greater for the central nozzle than for the perimeter nozzle.

The results of Figures 6 and 7 show, perhaps surprisingly, that in the nozzle range investigated the size of the nozzle has only a small effect on heat transfer between the spray droplets and the surrounding gas. Figure 6 shows that, generally speaking, the smaller the nozzle the better the heat transfer process; however, the effect is not consistent. For example, nozzles BP 10-90 and BP 12-90 indicate better heat transfer mechanism than nozzles BP 14-90, BP 16-90 and BP 18-90, but nozzle BP 12-90 gives better performance than nozzle BP 10-90, and nozzle BP 18-90 gives better performance than nozzles BP 14-90 and BP 16-90. Hence the effect of the Sauter mean diameter of the spray droplets is small in the range investigated (150 micron to 224 micron).

Figures 8 to 11 show that the flowrate of the injected liquid is of primary importance in controlling the pressure rise in the chamber and thus has a profound influence on the rate of heat transfer - the higher the flowrate the higher the rate of heat transfer.

The present experimental work shows that the heat transfer characteristics of spray droplets are, to a first approximation, independent of the size of the nozzles. For a given configuration, as determined by the size of the chamber, the thermophysical

properties of the gas and the driving temperature difference, the heat transfer rates depend almost exclusively on the mass flowrate of the injected liquid.

The energy required to inject the liquid into the spray chamber increases with the pressure drop across the nozzle and the mass flowrate of the injected liquid. Hence in order to minimise the energy requirements for the production of the spray droplets, without significant deterioration of the heat transfer rates, nozzles with low pressure drops should be used. The present work suggests that it is the largest nozzle in the range which should be employed for efficient droplet production and high heat transfer rates.

5 Conclusions

Spray injection and heat transfer performance of nozzles have been investigated experimentally. Experimental results for different sizes of nozzles indicate that the heat transfer characteristics are, to a first approximation, independent of the size of the nozzles, in the range investigated in this work. For all practical purposes the heat transfer characteristics between spray droplets and gases depend primarily on the mass flowrate of the injected liquid. Since the energy required for the production of spray droplets increases with the pressure drop across the nozzles, and since the size of the nozzles does not influence the heat transfer rates, the most efficient way of producing high heat transfer rates between spray droplets and gases is to use larger nozzles.

6 Summary

Liquid sprays provide efficient mechanism of heat and mass transfer between liquids and surrounding gases. The work described in this paper has been undertaken to help in the understanding of the basic mechanism of heat transfer between liquid sprays and gases.

An experimental apparatus has been designed which allows a close control of the parameters which affect heat transfer, such as the size, the number and the configuration of the spray producing nozzles, the flowrate of the injected liquid, and the initial temperature of the liquid and the surrounding gas. The experimental apparatus consists of a spray chamber into which the liquid is injected via a number of nozzles. The flowrate of the injected liquid is adjustable, using special injection arrangement. The experimental programme is computer controlled, which allows for rapid evaluation of the experimental data.

Experimental results for different sizes of nozzles indicate that the heat transfer characteristics are, to a first approximation, independent of the size of the nozzles, in the range investigated in this work. For all practical purposes the heat transfer characteristics between spray droplets and gases depend primarily on the mass flowrate of the injected liquid.

316

7 References

[1] K. Suzuki, K. Nakabe, T. Yamanaka, Heat Transfer Accompanied by Evaporation to a Recirculating Turbulent Flow, PhysicoChemical Hydrodynamics 6(1985)311-327.

[2] V.T. Buglayev, F.V. Vasilyev, A.S. Strebkov, Experimental Investigation of Heat Transfer in Evaporative Cooling of Air Flows with Fine Droplets, Heat Transfer - Soviet Research 17(1985)97-103.

8 Acknowledgement

This work was sponsored by National Power Plc.

2. Paper presented at the 4th UK National Conference on Heat Transfer, held 26th-27th September 1995 in Manchester, Paper No. C510-007-95

C510/007/95

Analysis of transient heat transfer between liquid sprays and surrounding gas

J VALHA BEng J S LEWIS DCAe, PhD, CEng, MIMechE, MRAeS, and J KUBIE BSc, PhD, CEng, FIMechE
School of Mechanical and Manufacturing Engineering, Middlesex University, London, UK

SYNOPSIS

Liquid sprays provide efficient mechanism of heat and mass transfer between liquids and surrounding gases. The work described in this paper has been undertaken to analyse the basic mechanism of heat transfer between liquid sprays and gases. An experimental apparatus has been designed which allows a close control of the parameters which affect heat transfer. Analysis of the experimental data has indicated that the transient heat transfer process is efficient, but not as efficient as previous scoping analyses might suggest.

NOTATION

a	radius of a typical droplet
B	dimensionless parameter defined by equation (8)
D	diameter of the chamber
h	coefficient of heat transfer between a droplet and surrounding gas
k_{G0}	thermal conductivity of gas at initial temperature
U_D	typical droplet velocity

1 INTRODUCTION

Injecting liquids in the form of sprays is an efficient form of liquid-gas contacting since a large interfacial area per unit volume is achieved with a very small gas phase pressure drop. The large interfacial area and the lack of a solid partition between the phases are responsible for excellent heat transfer performance between liquid sprays and surrounding gases. In this work we analyse heat transfer from hot water spray droplets injected into a gas enclosed within a cylindrical chamber. Heat transfer rates are investigated indirectly from the measurements of the gas pressure, p, in the cylindrical chamber. The aim of this investigation is to analyse the processes occurring in the bulk volume, rather than the heat transfer processes for a single droplet, which have been investigated previously by many authors.

The performance of Delavan solid cone nozzles was investigated in the first stage of this work and is reported elsewhere (1). The Sauter mean droplet diameter for the experimental conditions ranged from about 150 micron to about 250 micron (as given by the manufacturer's data). Experimental results for different sizes of nozzles indicate that the heat transfer characteristics are, to a first approximation, independent of the size of the nozzles, in the range investigated in this work. For all practical purposes the heat transfer characteristics between spray droplets and gases depend primarily on the mass flowrate of the injected liquid.

Theoretical work is being undertaken along two parallel lines. An analytical model is being developed, which considers the major parameters of the problem, and this is supported by full computational fluid dynamics (CFD) of the processes involved. In this paper we describe our preliminary analytical model.

2 EXPERIMENTAL WORK

An experimental apparatus has been designed which allows a close control of the parameters which affect heat transfer, such as the size, the number and the configuration of the spray producing nozzles, the flowrate of the injected liquid, and the initial temperature of the liquid and the surrounding gas. The experimental apparatus, shown in Figure 1, consists of a spray chamber, 121 mm internal diameter, D, and 190 mm long, into which the liquid is injected via a number of nozzles. The flowrate of the injected liquid is adjustable, using special injection arrangement. The experimental programme is computer controlled, which allows for rapid evaluation of the experimental data. Further details are reported in reference (1).

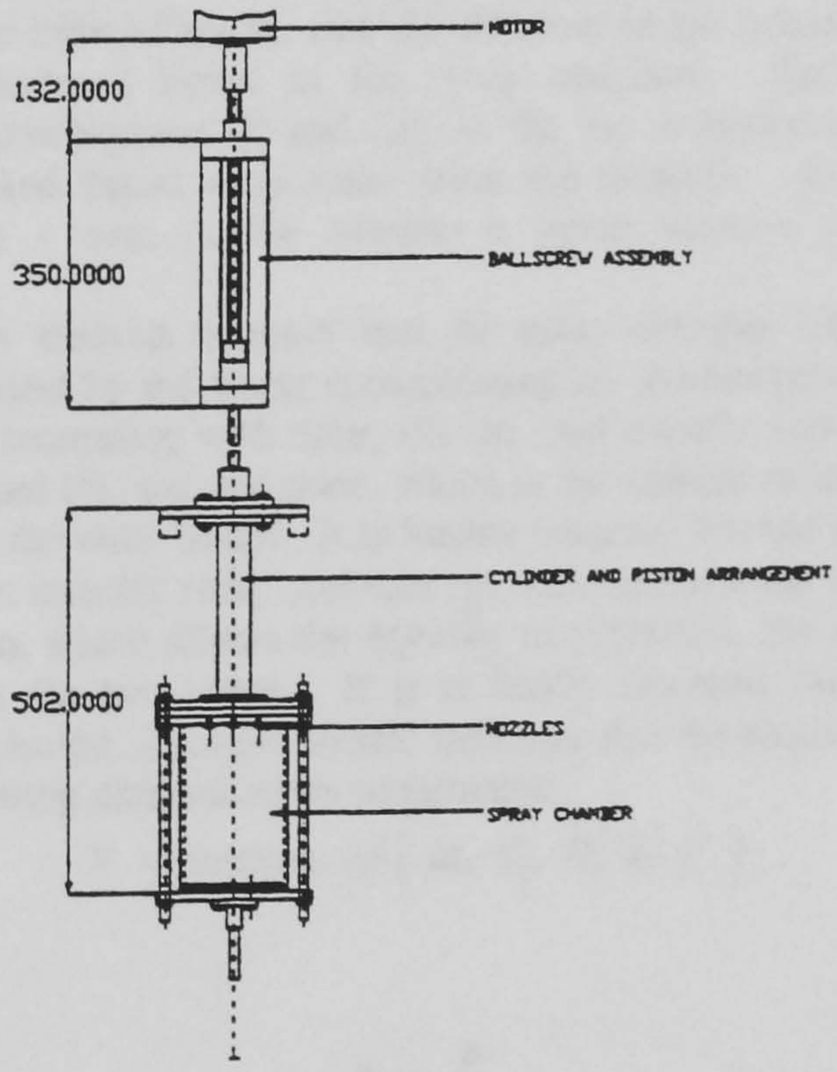

Figure 1: A diagram of the experimental apparatus

Figure 2 shows typical experimental data on the influence of the size of a single nozzle on the variation of the pressure in the chamber with time.

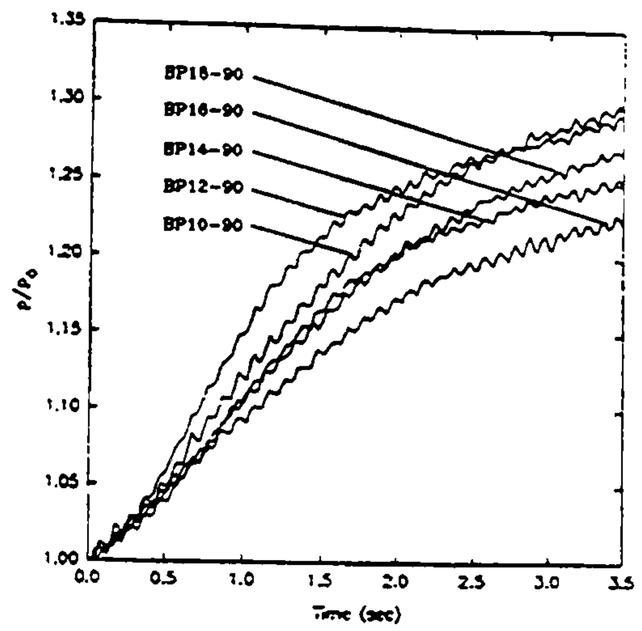

Figure 2: Comparison of nozzle performance in air (1 central Delavan BP nozzle, water flowrate 20 g/s per nozzle, $p_0 \approx 1$ bar, $T_L \approx 70°C$)

3 PRELIMINARY THEORETICAL WORK

The pressure rise in the chamber, shown in Figure 2, is due to three major mechanisms: (i) increase in the temperature of the contained gas, (ii) increase in the steam partial pressure by evaporation from the injected liquid, and (iii) decrease in the volume of the gas due to the accumulation of the injected liquid in the spray chamber. The initial rapid rise is predominantly due to mechanisms (i) and (ii), as the gas is heated to approach the liquid injection temperature and liquid evaporates from the droplets. As the injection period proceeds the pressure - time curves assume a lower positive slope consistent with mechanism (iii).

The preliminary analysis assumes that the spray chamber consists of three zones: (i) the water zone, formed by the water accumulating on the bottom of the spray chamber, whose volume will be increasing with time, (ii) the heat transfer zone, formed by the solid cone and the cylinder and (iii) the still zone, which is the volume of the chamber outside the heat transfer zone (and the water zone). It is further assumed that the heat transfer processes are confined to the heat transfer zone, and that the still zone and the heat transfer zones are separated by a partition, which allows the equality of pressures, but does not allow heat or mass transfer between the two zones. If it is finally assumed that in the initial stages evaporation can be neglected, a simple model indicates that the dimensionless pressure P is a function of the following dimensionless parameters:

$$P = \textit{function of} \left(M, T_0, H, K, t^* \right) \tag{1}$$

where

$$P = \frac{p}{p_0} \tag{2}$$

$$M = \frac{M_H}{M_T} \tag{3}$$

$$T_0 = \frac{T_{H0}}{T_L} \tag{4}$$

$$H = \frac{\dot{m}_w}{\rho_L V_T}\left(\frac{D}{g}\right)^{0.5} \tag{5}$$

$$K = \frac{V_H}{l_H D^2} \quad \frac{aU_D k_{G0}}{h(gD^5)^{0.5}} \quad \frac{\rho_{G0}\rho_L c_{VG0} g D^4}{3k_{G0}\dot{m}_w} \tag{6}$$

$$t^* = t\left(\frac{g}{D}\right)^{0.5} \tag{7}$$

and where p and p_0 is the pressure and the intimal pressure in the chamber respectively, M_H is the mass of the gas in the heat transfer zone, M_T is the total mass of gas in the spray chamber, T_{H0} is the initial temperature of the gas, T_L is the temperature of the injected liquid, $\dot{m}_w$ is the mass flowrate of the injected spray water, V_T is the volume of the spray chamber, V_H is the volume of the heat transfer zone, l_H is the length of the heat transfer zone, t is time, and where other parameters are either defined in Notation or have their usual meaning.

Equation (6) shows that the dimensionless parameter K is itself a product of three dimensionless groups. The first and the third group are fixed by the geometry of the vessel, the initial conditions and the mass flowrate of the injected liquid. It is the second group, B, which is of interest in heat transfer calculations, and which contains the important parameters of droplet spray heat transfer, such as h, U_D, a and k_{G0}:

$$B = \frac{aU_D k_{G0}}{h(gD^5)^{0.5}} \tag{8}$$

The dimensionless group B is obtained by trial and error for each experimental condition by determining the value of B which gives the best agreement between the theoretical solution and the experimental data. The typical comparison between the theoretical solution and the experimental data is shown in Figure 3.

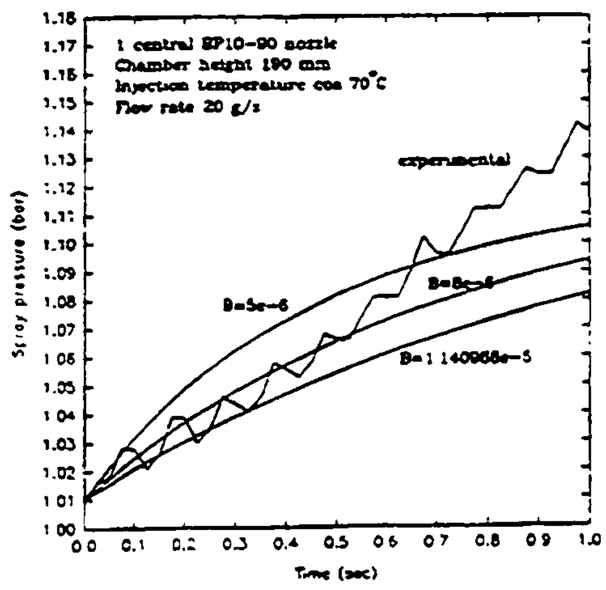

Figure 3: Comparison of the theoretical results with the experimental data.

Experimental results indicate that for the appropriate value of the dimensionless group B, there is a reasonable agreement between the theoretical predictions and experimental data for times of up to about 1 second. Furthermore, the data also show that in the ranges investigated, the best value of the dimensionless group B is independent of the size and number of the nozzles, the mass flowrate, and all other parameters, and given by

$$B \approx 0.5 \times 10^{-5} \tag{9}$$

The value of B given by equation (9) was further examined for the case of one BP-10 nozzle. This value could be obtained with the Nusselt number equal to 2, provided the typical droplet velocity was about 15 m/s. This value of the velocity is about half of the velocity with which the droplets leave the nozzles, but about ten times higher than the approximate terminal droplet velocity, which is attained within a very short distance from the nozzle. Using the typical terminal droplet velocity of about 1 m/s implies that the Nusselt number is of the order of 0.2, or substantially smaller than its value for an isolated rigid sphere of 2.

The fact that the dimensionless group B appears to remain constant for different nozzle sizes implies that any decrease in the droplet heat transfer coefficient h associated with larger nozzles (and hence larger droplets), is compensated by other factors, such as the possible decrease in the typical droplet velocity U_D.

4 CONCLUSIONS

The preliminary results presented in this work have significant implications for the modelling of heat transfer processes between droplet sprays and gases. The analysis, and comparison with the experimental data, indicates that it is primarily the dimensionless group B, and not the Nusselt number, which must be used in the theoretical modelling. The use of the Nusselt number as the primary dimensionless group in the modelling of heat transfer implies that, generally, all droplets are in suspension and that their lifetime is determined by the duration of the overall heat transfer process. The present analysis indicates that the lifetime of each droplet depends on the typical droplet velocity U_D. Hence, in other words, the number of spray droplets available for heat transfer at any one time is substantially smaller that the number which is obtained or implied by neglecting the typical droplet velocity U_D. It should be noted that all three parameters which describe the thermo-hydraulic behaviour of spray droplets, a, U_D and h, are together characterised by the dimensionless group B, whose value appears to be constant and equal to about 0.5×10^{-5}. In any new application this value can either be assumed or, if the conditions are materially different from the present experimental conditions, determined in a single, simple experiment.

REFERENCES

1. VALHA, J., LEWIS J.S. and KUBIE, J. Transient heat transfer between liquid sprays and surrounding gas, Intern. Conf. PARTEC'95/ILASS-Europe, March 1995, Nurnberg, Germany

Acknowledgement
This work was sponsored by National Power Plc.